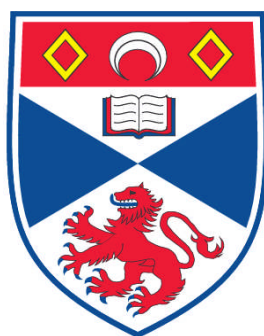# NOVEL METAL ORGANIC FRAMEWORKS:
SYNTHESIS, CHARACTERIZATION AND FUNCTIONS

Mohamed Infas Haja Mohideen

A Thesis Submitted for the Degree of PhD
at the
University of St. Andrews

2011

**Full metadata for this item is available in
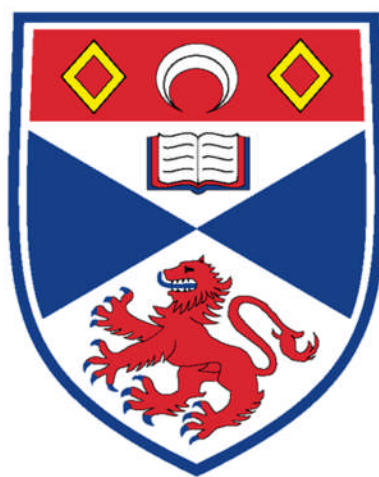Research@StAndrews:FullText
at:
http://research-repository.st-andrews.ac.uk/**

**Please use this identifier to cite or link to this item:
http://hdl.handle.net/10023/1892**

Novel Metal Organic Frameworks: Synthesis, Characterization and Functions

University of St Andrews

A thesis presented for the degree of
Doctor of Philosphy
In the Faculty of Science of the University of St. Andrews

By

Mohamed Infas Haja Mohideen, Grad. Chem., MRes.

April 2011

Acknowledgements

Firstly I would like to thank Professor Russell Morris for his excellent supervision and guidance throughout the course of my Ph.D studies. He has been an enormous help and has always been available with lots of enthusiastic ideas. A big thank you to the past and present members of the Morris group for their help, especially Dr Paul Wheatley, Dr Bo Xiao, Dr David Aldous and Dr Alistair McKinlay.

Thanks are also owed to our collaborators in the University of Edinburgh, Dr Tina Düren, Dr David Fairen-Jimenez and Naomi Cessford, Dr Paul Wright and his group at the University of St Andrews. Many thanks to Prof. Mark Thomas, Xuebo Zhao and Rachel Gill at the Newcastle University.

I am grateful to several academic staff whom without their guidance this thesis would not have been a success: Prof. Alex Slawin and Dr Yang Li for the collection of single crystal data, Dr Sharon Ashbrook, Dr John Griffin and Daniel Dawson for solid state NMR work. Thanks are also due to the technical staff at the University of St Andrews, in particular, Mrs S. Williamson (TG-MS, ICP and CHN analysis), Mrs M. Smith (NMR) and Mr R. Blackley (PXRD).

A big thank you also goes to Dr Dave Aldous, Morven Duncan and Phoebe Allan for proof reading my thesis and for your invaluable suggestions.

On a personal note, I would like to thank my wife for helping and supporting me throughout the years of my study and my lovely son whose smile always cheers me up. Also all my brothers and sisters have been invaluable for helping me continue with my studies and all of my friends in and out of chemistry for their support, friendship and guidance.

Publications from this work

Protecting group and switchable pore-discrminating adsorption properties of a hydrophilic-hydrophobic metal-organic framework.

M. Infas H. Mohideen, Bo Xiao, Paul S. Wheatley, Alistair C. McKinlay, Yang Li, Alexandra M. Z. Slawin, David W. Aldous, Naomi F. Cessford, Tina Düren, Xuebo Zhao, Rachel Gill, K. Mark Thomas, John Griffin, Sharon E. Ashbrook and Russell E. Morris, *Nature Chemistry*, **2011**, 3, 304-310.

Abstract

The synthesis and properties of novel Metal Organic Frameworks were investigated and reported in this thesis. Thirteen new materials have been synthesized and their properties have been discussed with nine of the structures being solved. The most interesting and useful MOF among the thirteen materials is STAM-1, a copper-based Metal Organic Framework in which the starting linker (Benzene-1,3,5-tricarboxylic acid) undergoes selective *in situ* monoesterification during the synthesis. The monoesterified BTC can be recovered easily from the MOF, opening up MOF synthesis as a "protection" tool for unexpected selectivity in preparative chemistry that is difficult to accomplish using standard organic chemistry approaches. The selective linker derivatisation leads to the formation of a porous MOF with two types of accessible channel; one hydrophilic lined by copper and the other hydrophobic, lined by the ester groups.

The unique structure of the pores leads to unprecedented adsorption behaviour, which reacts differently to gases or vapours of dissimilar chemistry and allows them to access different parts of the structure. The structural flexibility of STAM-1 shows significant differences in the kinetics of O_2 and N_2 adsorption, showing potential for new materials to be developed for air separation. Having two types of channel systems, adsorption can be switched between the two channels by judicious choice of the conditions; a thermal trigger to open the hydrophilic channel and a chemical trigger to open the hydrophobic channel.

The storage and release capability of NO in STAM-1 was investigated for use in biomedical applications. Successful studies showed the strength of the antibacterial effects of NO loaded STAM-1, by using three different bacterial strains as a test of performance and were found to be bactericidal. Furthermore the antibacterial effects of NO free STAM-1 were also probed and found to be bactericidal even with low concentrations of the material such as 5 wt%.

STAM-1 showed some complex magnetic behaviour by displaying strong antiferromagnetic properties at room temperature and ferromagnetic properties at lower temperatures. The antiferromagnetic coupling was observed within the dimer and ferromagnetic coupling between the dimers. This property of ferromagnetism can only be attributed to the corporation of magnetic dimers in the framework. STAM-2 displays a different magnetic behaviour than STAM-1 which shows paramagnetic properties at room temperature and antiferromagnetic properties at lower temperatures.

Other novel MOFs were also successfully characterised and their properties were investigated for potential applications.

Table of Contents

Abbreviations used throughout this thesis

MOF	Metal Organic Framework
STAM	St Andrews MOF
HKUST	Hong Kong University of Science and Technology
IRMOF	Isoreticular Metal Organic Framewoeks
MIL	Materials of Institut Lavoisier
CPO	Coordination polymer of Oslo
PCN	Porous Coordination Network
SBU	Secondary building unit
PSM	Post synthetic modifications
BTC	1,3,5-Benzenetricarboxylic acid
mmBTC	monomethyl benzenetricarboxylic acid
BTB	1,3,5-tris(4-carboxyphenyl) benzene
BDC	1,4-Benzenedicarboxylic acid
bpy	4,4-bipyridine
bpe	1,2-trans-(4-pyridyl)ethane
tpct	1,2,3,4-tetrakis(4-pyridyl)cyclobutane

BDOA	benzene-1,4-dioxylacetate
dabco	1,4-diazabicyclo[2.2.2]octane
tatb	4,4',4''-s-triazine-2,4,6-triyltribenzoate
TGA	Thermogravimetric analysis
XRD	X-ray diffraction
IR	Infrared
NMR	Nuclear Magnetic Resonance
SEM	Scanning Electron Microscope
EDX	Electron Dispersive X-ray spectroscopy
SQUID	Superconducting Quantum Interference Device
ICP	Inductively Coupled Plasma
NO	Nitric oxide
CUS	Coordinatively unsaturated metal site
STP	Standard temperature and pressure
DMF	Dimethylformamide
BET	Brunauer, Emmett and Teller
PTFE	polytetrafluoroethylene

Chapter 1   Metal Organic Frameworks

1.1.   Introduction

Porous solids are of scientific interest because of their beneficial applications. These solids are classified as microporous, mesoporous and macroporous based on the size of the pores. Solids which have a pore size of 2 nm or below are known as microporous.[1] The mesoporous solids are in the range of 2 nm – 50 nm and above 50 nm are known as macroporous.[2,3] Zeolites which are crystalline aluminosilicates are the prime example of the microporous materials.[4] Usually zeolites occur as natural minerals, but a wide variety of synthetic zeolites also can be made and have been used in various applications. Catalytic cracking and xylene isomerization are large scale examples of the application of zeolites.[5,6] Ion exchange is another property of zeolites which allows them to be used as detergents and water softners.[4] Recently many other zeolite-like materials have been synthesised, including materials such as aluminophosphates, zinc phosphates or arsenates.[4,7]

Metal Organic Frameworks (MOFs), also known as coordination polymers, are a class of crystalline materials that are currently attracting a tremendous amount of interest due to their attractive properties. The backbone of the compound is constructed from metal ions which act as connectors and organic bridging ligands as linkers. The formation of the desired architectural, chemical, and physical properties of MOFs depend on the chemical structure of the ligand and the

properties of the connecting metals.[8] A huge range of network topologies are designed by aggregating molecular building blocks to achieve a specific structure and objective. MOFs are infinite one-, two-, and three dimensional (1D, 2D, and 3D) networks (Figure 1.1). The 2D and 3D structures of MOFs can exhibit small cavities or open channels. Record-high surface areas, high porosity, structural regularity and ''fine-tunability'' are among the well-known features of the MOFs.[9-13]
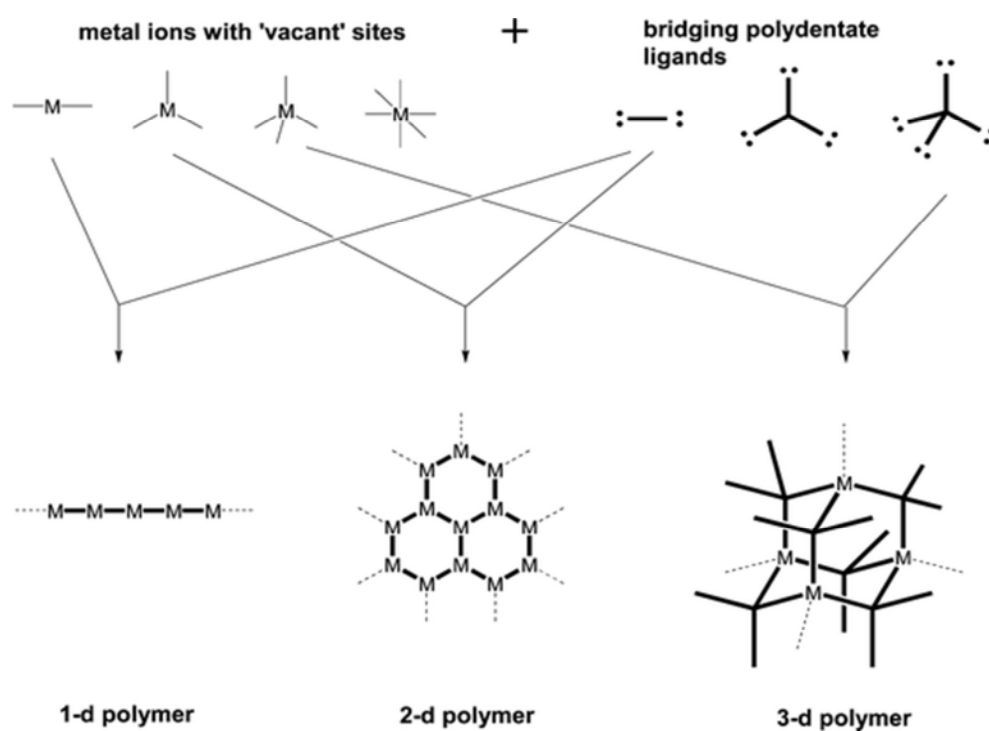
Figure 1.1.   The building block, or 'modular', principle behind forming

coordination polymers.[8]

Initially the main interest of MOFs was gas storage.[13] However, now several other applications such as gas purification, gas separation, catalysis, nonlinear optics,

magnetism and biological applications are of interest.[13-20] These critical applications have motivated the synthetic strategies of MOFs immensely. Many different synthetic approaches have been reported in the literature. Solution and hydrothermal reactions are the most important techniques used when dealing with MOFs.

1.2.   Synthetic methods

1.2.1. Solution and hydrothermal synthesis

Hydrothermal synthesis includes the various techniques of crystallizing substances from high-temperature aqueous solutions at high vapour pressures.[21] Most of the reported MOF materials have been synthesized using solvothermal and hydrothermal synthetic conditions, often by using sealed autoclaves. Hydrothermal synthesis, where water is used as the solvent and solvothermal synthesis, where other solvents except water are used as solvents are accompanied with high temperatures and increased pressure. Other than the pure hydro or solvothermal methods, mixtures of water and other solvents also have been used to synthesize various MOFs. Compared to the solution reactions hydrothermal techniques plays an important role in preparing robust and stable MOF compounds.[22] Unlike solution reactions, the solubility of the reactants increases under hydrothermal methods which makes the reaction more likely to occur at lower temperatures than is expected. This ''soft-chemistry'' approach enables the formation of polymeric units through molecular building blocks.[23] Small changes

in one or more of the reaction variables, such as; temperature, time, pH or the solvent type can have a profound influence on the product. In some cases organic amines or alkylammonium cations are used as templates in the crystallization process.[24] The disadvantage of this approach is that these templates tend to block the pores of the resulting framework. Recently it was revealed that this technique can also be used in preparation of MOFs which undergo *in situ* ligand synthesis.[25]

1.2.2. Ionothermal synthesis

In ionothermal synthesis, ionic liquids or eutectic mixtures are used as solvents. The ionic liquids are a class of organic solvents with high polarity and pre-organized solvent structure.[26] These are made up with essentially only ions and are fluid at near ambient temperature (less than ~100 ºC).[27] A eutectic mixture is a mixture of two or more compounds which has a lower melting point than either of its constituents.[26] Usually high vapour pressures are generated in solvothermal methods but the most fascinating feature of ionic liquids is that they possess a very low vapour pressure which in turn is more safe than the solvothermal methods.[27] Also they have excellent solvating properties and high thermal stabilities.[28] Easy preparation of the pure state and their non-reactivity towards water are the advantage of the eutectic mixtures over the ionic liquids. The other important feature of these ionic liquids is that they are not only acting as solvent but can also act as structure directing agents as well.[29] Also these ionic liquids can be recycled for further use.[26] Some of the specific examples of ionic liquids which were used in this course of research are discussed in Chapter 7.

1.3.   *In situ* and post synthetic modification methods

1.3.1. *In situ* ligand synthesis

Metal Organic Frameworks (MOFs) are usually obtained by using pre-designed linkers, which either is commercially available or synthesized prior to use. Recently, a new strategy has been developed by chemists, in which ligands are synthesised, *in situ*, under hydrothermal conditions. In this approach, ligand precursors are used in the place of ligands to produce MOFs. This method is of great interest in both organic as well as coordination chemistry for the preparation of coordination complexes, the discovery of new reactions and the understanding their associated mechanisms.[25] Hydrothermal-driven *in situ* ligand synthesis provides alternative pathways to crystalline complexes which are difficult to obtain by routine synthetic methods. For example, rigid tetradentate ligand 2,2'-biphenanthroline is not easy to obtain from 1,10-phenanthroline but formed automatically under hydrothermal conditions (Figure 1.2).[30]
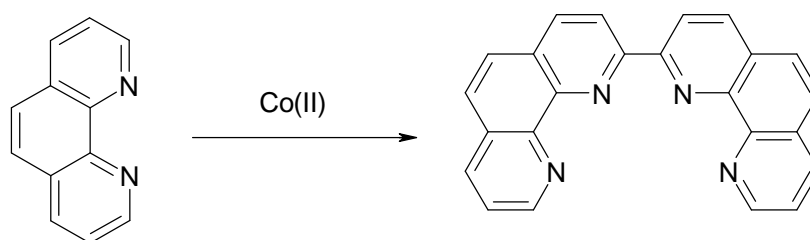
Figure 1.2.   *In situ* synthesis of 2,2'biphenanthroline[30]

In situ ligand synthesis has the following benefits in the crystal engineering process:[25]

1. In this approach, ligand precursors are used instead of the final ligand, simplifying the synthetic steps

2. Single crystal X-ray quality crystals can result due to the *in situ* slow formation of the ligand which allows for easier structural determinations

3. Environmental friendliness

Carbon-carbon bond formation has an important role in the organic chemistry. The *in situ* cyclisation reaction of 1,2-trans-(4-piridyl)ethane (bpe) to yield 1,2,3,4-tetrakis(4-pyridyl)cyclobutane (tpct) was observed in 1997 by Champness and Schröder which was the first *in situ* ligand synthesis reported in crystal engineering.[31] The 3D coordination polymer {Ag[tpct]BF$_4$}was formed in the reaction between AgBF$_4$ and bpe in a MeCN/CH$_2$Cl$_2$ solution system in the presence of light (Figure 1.3).[31]

Figure 1.3. *In situ* synthesis of tpct[31]

It was found that Ag(I) ions play a key role in the preparation of the complex but there is still a question as to whether the cyclisation occurred in the solution or solid state. Interestingly *in situ* cyclisation of bpe in the reaction produced only a single isomer of the tpct ligand whereas the photochemical reaction yields two isomers of the ligand. Which means *in situ* ligand synthesis may provide an alternative pathway of isolating the ligand isomers. Following this success a variety of reactions which involves *in situ* ligand synthesis have been reported. These include Oxidative coupling, Hydroxylation, Acylation, Decarboxylation and Tetrazole formation.[32-36]

Although hydro/solvothermal *in situ* syntheses are useful methods for the preparation of unusual ligands or complexes that are not easily obtained in normal conditions, unexpected results may occur because many factors including metal ions, pH and temperature have significant influence on the resulting products.[25] In the literature there appears to have been no attempts to isolate any of these uncommon ligands such as 2,2'-biphenanthroline, 2,2';6,2'';6'';2'''-quaterpyridine and tpct found in MOFs.[30,31,37] Therefore while discovering different types of *in situ* synthetic reactions, future research should be focussed on mechanistic studies of these reactions, isolation of these uncommon ligands and their utilization in different other applications. The i*n situ* preparation of mono-methyl benzene tricarboxylic acid is discussed in Chapter 5 with its isolation, mechanism and applications in synthesis.

1.3.2. Post Synthetic Modifications

Metal Organic Frameworks are usually obtained from a ''one pot'' synthesis[38] where there is no opportunity available for the adjustment of the properties during the formation of the material. Therefore functionalized networks can be prepared by undertaking reactions on preformed MOFs. The phrase ''Post Synthetic Modification'' (PSM) is used to describe this approach in reference to the process of ''Post Translational Modification of proteins''.[38] Therefore PSM can be defined as chemical derivatization of MOFs after their formation (Figure 1.4).
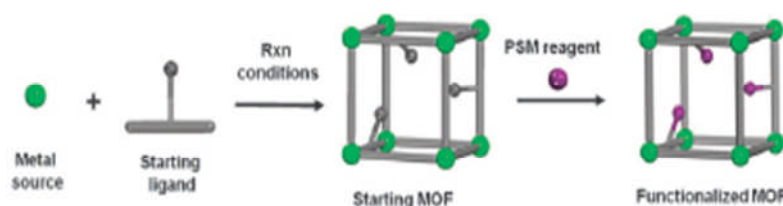
Figure 1.4.   A generic scheme for the postsynthetic modification (PSM) of

MOFs.[39]

The following benefits have been identified from the PSM of MOFs:[38,40,41]

- The pore architecture of the preformed MOF can be tailored by PSM for a specific purpose in order to ''tune'' the material for selective adsorption and catalysis.

- PSM facilitates the incorporation of a diverse range of functional groups in to MOFs which cannot survive the conditions of the initial synthesis (e.g. temperature and pH)

- The functional groups that might compete with the donor groups or the bridging ligands can be introduced after the formation of MOF via PSM method.

- A large number of materials which are topologically identical but functionally diverse can be obtained by modifying a given MOF with different reagents.

PSM can be done in the following ways;[38,39]

- PSM of MOFs by non-covalent interactions

  Guest removal, Guest exchange and ion exchange are the most common forms of non-covalent modifications. Ion exchange is limited to the charged frameworks whereas other two types are more generally applicable.

- PSM of MOFs by coordinative interactions

  Two different approaches have been used for MOFs with metal ligand interactions. This is to either target the exposed metal sites of MOFs or explore the coordination chemistry of the organic component.[38] Unsaturated metal centres can provide modification sites for

functionalization. For example HKUST-1 which consists with Cu-paddlewheel Secondary Building Units (SBU) have axial aqua ligands on the Cu centres.[42] These aqua ligands can be replaced by the other molecules without collapse of the framework. Treatment of the dehydrated HKUST-1 with dry pyridine results in a different formulation of the MOF while the 3D lattice remains intact. Pyridine serves as the new axial ligand in this new framework.[42]

- PSM of MOFs by covalent bonds

  In this approach organic components allow MOFs to be readily modified with a wide array of covalent transformations under mild conditions. This should be challenging to preserve the framework when considering the strength of the covalent bonds. But MOFs show high thermal and chemical stability due to the periodic arrangements.[38] Recent findings show that amide coupling, imine condensation, urea formation, N-alkylation and click chemistry are suitable for MOF modifications.[38,39,43] IRMOF-3 which is constructed from Zn_4O SBU's and 2-amino-1,4-benzenedicarboxylic acid linkers can be modified with alkyl anhydrides to generate a alkyl functionalized material (Figure 1.5).[39]
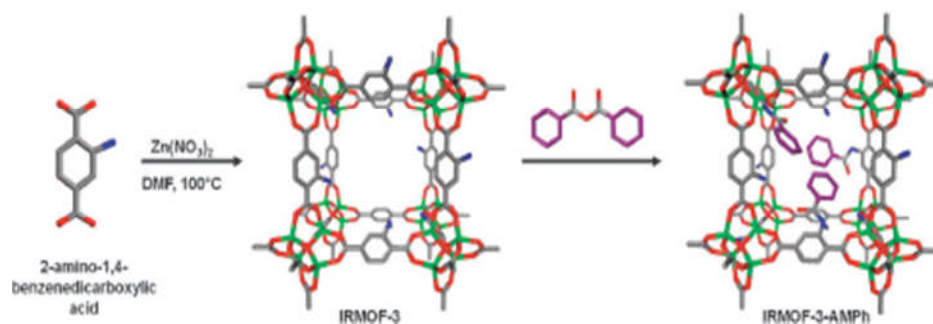
Figure 1.5. A specific example of PSM on IRMOF-3 with benzoic anhydride.[39]

Apart from the methods mentioned above, new methodologies based on the different forms of chemical modulations such as step-wise tandem modifications and doping with metals have also been demonstrated in various systems.[38-40,44] Since higher numbers of MOFs reported in the literature and a large number of suitable organic reactions available, there should be plenty of opportunities for PSM in order to engineer the physical and chemical properties of MOFs.

1.4. Network Geometry

Metal coordination and the properties of the organic ligand play a vital role in predicting the network geometry. Specifically, by changing the bridge or its functionalization, new MOFs can be designed without changing the underlying topology.[45] Transition metal ions provide coordination sites for the organic ligands. The oxidation state and coordination numbers of the metal ion play a significant role in giving rise to various geometries, which can be linear, T- or Y-shaped, tetrahedral, square-planar, square-pyramidal, trigonal-bipyramidal,

octahedral, trigonal-prismatic, pentagonal-bipyramidal, and the corresponding distorted forms.[46]

Linkers are normally multidentate bridging ligands. These contain a wide variety of linking sites or donor atoms, with binding strength and directionality of the ligand unique to its structure.[8] For example, rigid ligands will be in control of the structural topologies during the synthesis process.[47] The physical properties of the MOFs are highly dependent on the organic ligand, so it is worthwhile studying them carefully. The length of the ligand, its flexibility and number of binding sites are considered important when selecting a ligand for the synthesis of a certain network.[47] The most frequently reported problem with the bridging ligand is its flexibility. When a ligand has several probable conformations this could lead to unexpected and unpredictable structures. In order to overcome this problem rigid ligands have been introduced. Rigid backbones such as in 4,4′-bipyridine can be used to restrict the free rotation of the ligand lone pairs.[8] Rigid ligands are mostly used in the assembly of MOFs to avoid complications in the expected product. Multidentate ligands containing N and O donors are widely used in constructing these structures.[48] Some common examples of N-donor and O-donor ligands are given in Figure 1.6.
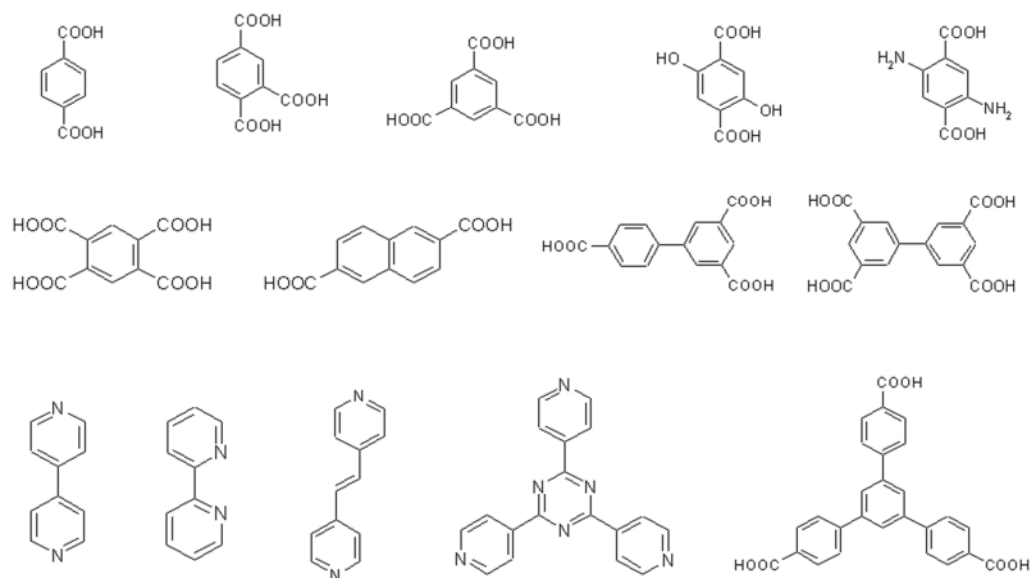
Figure 1.6.   Some of the common ligands used in the synthesis of MOFs

The strength of the resulting frameworks arises from the following intrinsic properties of metal-carboxylate bond.[45]

- The energy of the framework is relatively large due to the electrostatic attraction

- Metal-carboxylate chelation produce rigid clusters

Ligands containing N-donors have the following advantages.[49]

- N-donor ligands are mostly neutral which makes the resulting MOFs cationic. Some of the zeolites reported anionic properties which enables these MOFs to be utilised in anion exchange.

- These ligands have rich structural properties, various types and configuration.

The main shortcoming is that due to the low metal-nitrogen bond strengths the resulting frameworks of most N donor ligands have low thermal stability, especially upon removal of guests' molecules.[49]

Researchers in this area have undertaken the challenge of synthesizing different rigid ligands. Long bridging ligands with appropriate spacers have been used as linear linkers.[46] Ligand concentration, type of anion, solubility, solvent polarity and temperature are important factors in determining the character of the product.[45] They can be result in different topologies such as, diamond, NBO net, Pt_3O_4 net, primitive cubic network and body centered cubic network and especially zeolite topologies.[9,42,50-52]

1.5. Interpenetration

The synthesis of porous MOFs creates cavities or channels which are usually occupied by solvent molecules. As the size of the pores is increased by extending the length of the linker, interpenetration occurs by forming sub lattices within the existing frameworks. This will lead to a high reduction in size of the pores. The main characteristic feature of these interpenetrated frameworks is that these sub-lattices can be removed only by breaking the internal connections.[53] It can also be reasoned that if strong enough interactions between the framework and guest molecules exist, then the framework cavities may preferentially be filled with guests rather than with additional polymer strands.[8] These interpenetrated network structures falls into the category of infinite, polycatenanes or polyrotaxanes.[53]

Examination of M-4,4'-bipyridine (bpy), (M = Ni, Zn) frameworks reveals that the rod-like bpy has a greater tendency to form interpenetrated structures in the absence of either large guest molecules or hydrogen-bonded and solvated ion guest aggregates.   Robson *et al.* previously showed that the polymer $Zn(bpy)_2(H_2O)_2SiF_6$ has pores of dimension 11 by 11 Å which is large enough for interpenetration to occur.[54] This is exemplified in the structure of $Ni(bipy)_{2.5}(H_2O)_2.(bpy)_{1.5}(ClO_4)_2(H_2O)_2$, (Figure 1.7) which is constructed from large square shaped building units of four $Ni(H_2O)_2^{2+}$ centers linked by bpy.[55] Extension of these units in one dimension forms a porous cationic $Ni[(bpy)_{2.5}(H_2O)_2]^{2+}$ structure with a railroad-like topology. There are 12 large pores of 11 by 11 Å dimension exist despite their tendency to be interpenetrated. Instead, no interpenetration had occurred and the pores are found to be occupied by hydrogen-bonded perchlorate anions, water molecules and additional, uncoordinated bpy.[55]
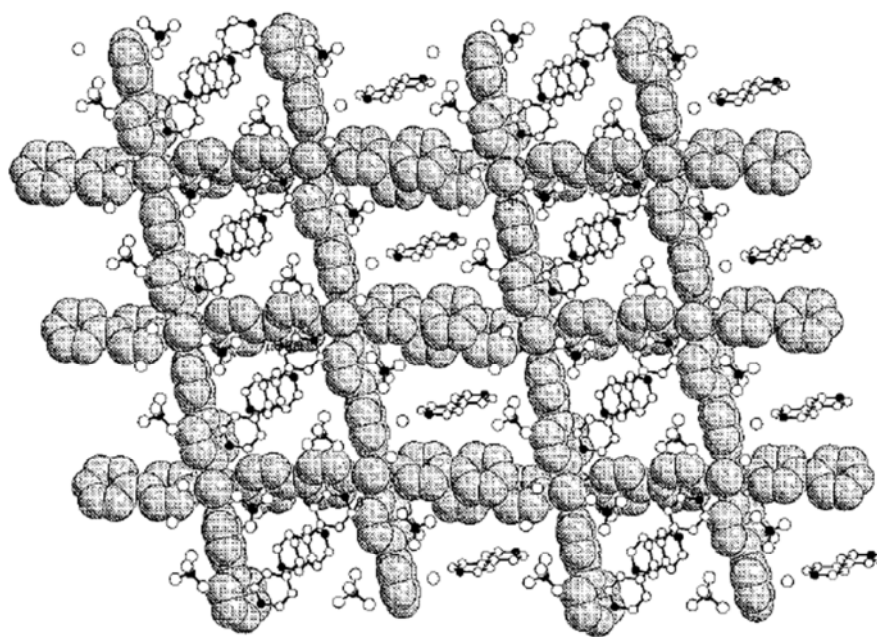
Figure 1.7.   View of the solid-state structure of

$Ni(bipy)_{2.5}(H_2O)_2.(bpy)_{1.5}(ClO_4)_2(H_2O)_2$ along the *a-axis*. The Ni-bpy framework

is shown in space-filling shaded representation, while the guests in the channels

are shown in stick and ball representation with C and O, open and Cl and N,

dark.[55]

In order for interpenetration to occur the diameter of the polymer strand must be

less than the size of the cavity. Therefore interpenetration can be prevented by

using bulkier vertices. Metal clusters and cages, as opposed to single metal ions,

are therefore of interest as building units. Yaghi *et al.* introduced this idea by

introducing the concept of secondary building units to Metal Organic

Frameworks.   This was done by introducing an approximately cubic terbium

dicarboxylate network, using 4,4′-azodibenzoate as the dicarboxylate linker,

where the octahedral $Tb_2(carboxylate)_6$ SBU shown in Figure 1.8 was adopted.[56]
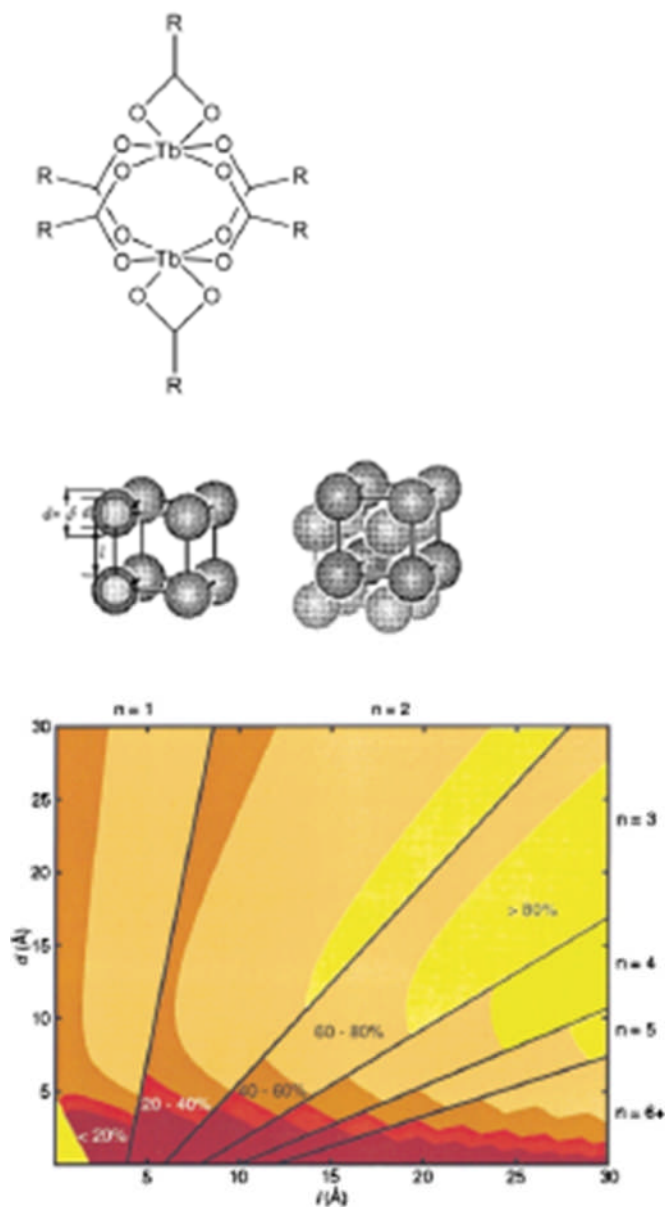
Figure 1.8.   Bulky *pseudo*-octahedral $Tb_2(carboxylate)_6$ SBU (top), geometrical

model used to relate vertex bulk and spacer length to the degree of

interpenetration, *n*, in interpenetrated cubes (middle), and the extrapolation of this

relationship to show how percentage free volume relates to SBU diameter, *d*, and

linker length, *l*.[56]

1.6.   Secondary building units

The intense interest in this field can be attributed to the potential use of designed materials in a wide variety of technologically important applications. Therefore the synthesis of MOFs should not just be the selection of some raw materials and their synthesis but should have some foresight as how the final solid is formed by the assembling of the raw materials. An emerging approach in the rational assembly of networks is through the use of secondary building units (SBUs). The concept of ''Secondary Building Units'' as structural entities of MOFs was adopted from zeolite structure analysis.[57] These are molecular complexes and cluster entities that are linked together by the organic linkers to form extended porous networks. This approach has allowed the synthesis and use of a large number of inorganic and organic SBUs with varying geometries (Figure 1.9).
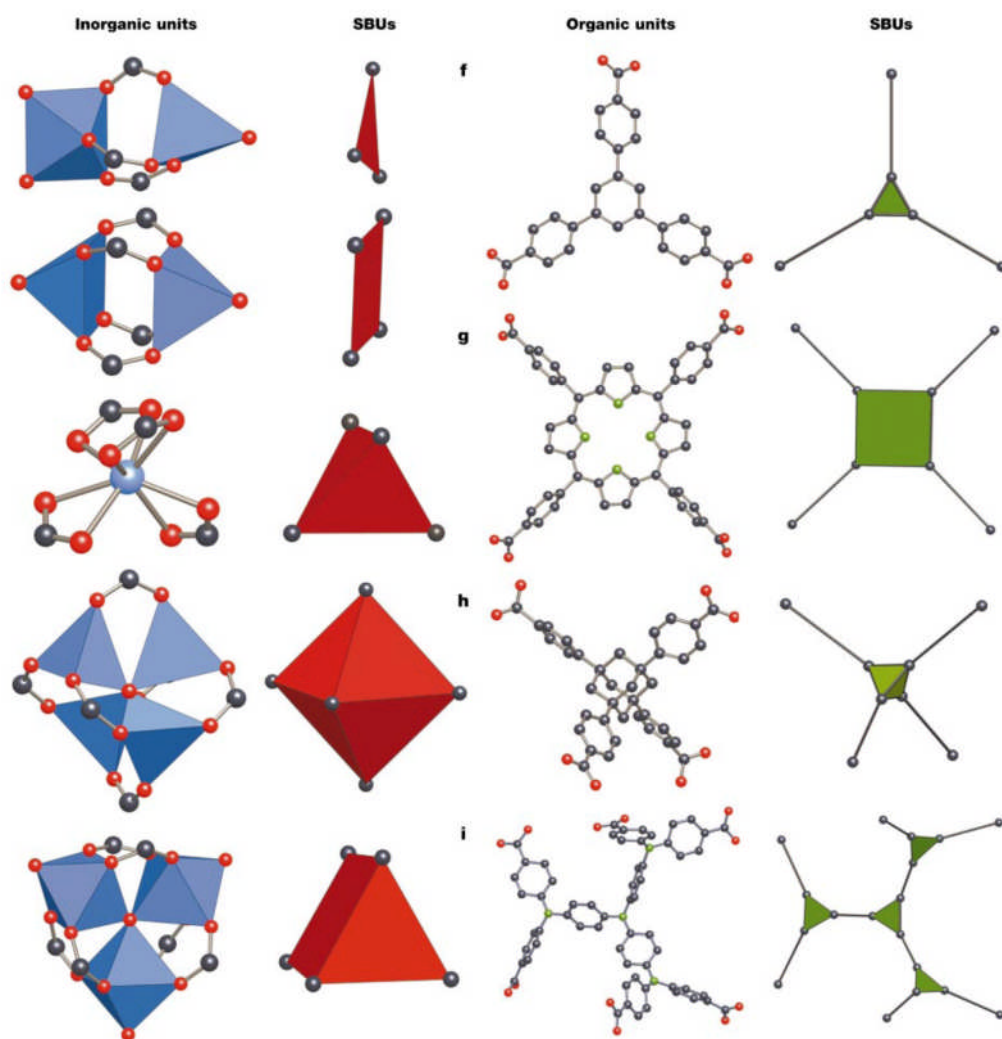
Figure 1.9.   Examples of SBUs from carboxylate MOFs. O – red; N – green; C – black. In inorganic units metal-oxygen polyhedral are blue and the polygon or polyhedron defined by carboxylate carbon atoms (SBUs) are red. In organic SBUs the polygons or polyhedrons to which linkers (all –C_6H_4- units in these examples) attached are shown in green.[58]

The use of SBUs is attractive in part because of their steric requirements and rigidity, which dramatically reduce the number of possible network topologies arising for a given node/linker combination.[59] This is analogous to aluminosilicate

zeolite chemistry, where nine SBUs based on tetrahedral AlO_4 and SiO_4 primary

building units have been classified.[59] Although many of the SBUs can be observed

in molecular form, they are not generally introduced directly but these specific

SBUs can be generated *in situ* under the correct chemical conditions. As the metal

ions are locked into their positions by carboxylate groups (Figure 1.10), the SBUs

are sufficiently rigid to produce extended frameworks of high structural stability.

In clusters with terminal ligands, the reactivity of the metal site can be studied

through the removal of these ligands, which frees a coordination site.[59]
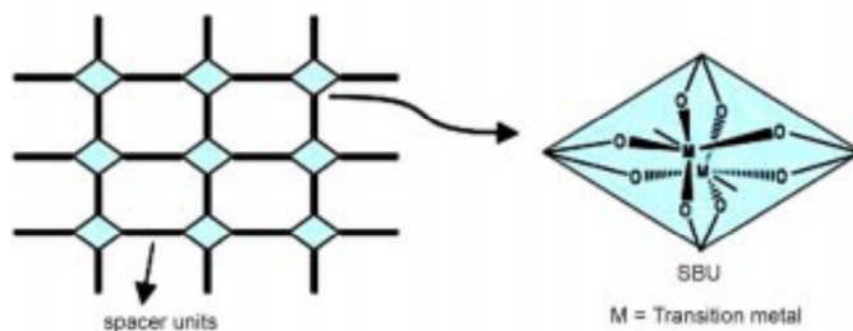
Figure 1.10.   Part of the two-dimensional coordination polymer built with 1,4-

benzene dicarboxylate spacer and the SBU (paddlewheel cluster).[59]

One of the common metal carboxylate cluster used in MOFs is the bimetallic

"paddlewheel" unit. This SBU is generated *in situ* by combining two cations with

four carboxylates. These cations can be Cu^{2+}, Zn^{2+}, Mo^{2+}, Fe^{2+} etc. each metal ion

on the paddlewheel SBU can be capped by a solvent molecule.[45] For example,

MOF-2 generated by Yaghi *et al* has a square paddle wheel containing two zinc

atoms linked in a periodic square array.[60] HKUST-1 which was synthesised by

William *et al* has a Paddle wheel SBU which contains Cu dimers.[42]

However the concept of SBUs has been useful in designing MOFs structures. In particular this strategy has allowed synthesising a number of SBUs with varying geometries. This approach has made the control of the coordination number of the SBUs easy and therefore it is critical to identify different geometric shapes which expected to form networks.

1.7.   Reticular synthesis

Once identified the SBUs, the next step is to try to arrange them to generate a desired structure. A better understanding of the mechanistic stability of the framework is needed to design a MOF. The challenge of synthesizing these materials is to change the chemical composition, functionality and molecular dimensions without changing the underlying topology. Thus on designing a target structure the following factors should be considered.[11]

1. Whether the starting material exhibits the relevant features which are expected to be in the product.
2. Appropriate techniques should be used to obtain different functionalities and dimensions by having the same skeleton.
3. The product should be highly crystalline in nature.

Reticular synthesis is designing experiments to produce materials of predetermined ordered structures.[58] This technique was developed as a way of identifying the principles governing the way target frameworks assemble, and

these principles are then used to develop new frameworks with similar topologies, but varying functional groups and properties.[61] This is different from retrosynthesis of organic compounds because the structural integrity and rigidity of the building blocks in reticular synthesis remain unaltered.[45] Yaghi *et al* has produced a series of 16 isoreticular metal–organic frameworks (IRMOFs) in crystalline form, differing in the polarity, reactivity, and bulk of the pendant groups on the aromatic link (Figure 1.11).[45] These IRMOFs demonstrates the design of the porous structures in which pore size and functionality varied systematically.
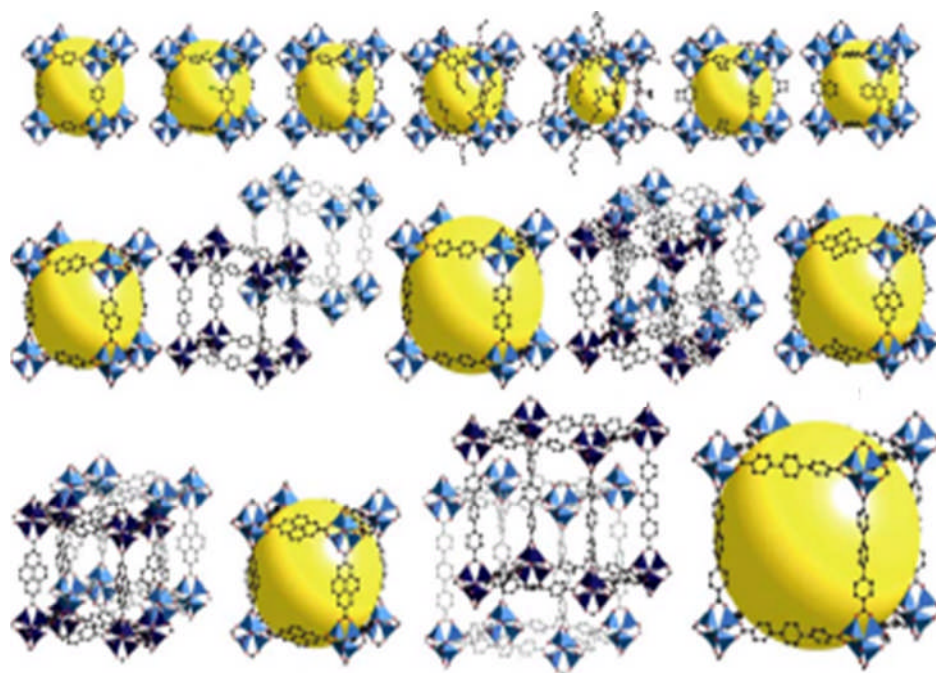
Figure 1.11.   A large series of isoreticular metal–organic frameworks (IRMOFs) has been produced in which each member shares the same cubic topology.[45]

1.8.   Rigidity and flexibility of the framework

One of the main problems faced in the early stage of MOF chemistry was to preserve the structural stability after the removal of the guest molecules. Therefore multidentate rigid ligands were incorporated in MOFs in order to obtain stable frameworks.[59] These rigid organic links were able to produce robust MOFs of high structural stability. As described above Yaghi *et al* has synthesised a series of MOFs (IRMOF series) that represents the concept of reticular design. Since some of the linkers used in the series were long bridging ligands the catenation was resulted with decreasing the void space. In addressing this issue, Kitagawa *et al* have proposed a ''pillared layer construction'' for the synthesis of MOFs which were referred as CPL-*n* compounds.[62] These MOFs show some structural transformation after guest molecule accommodation. This means MOFs can respond to external stimuli which are unique characteristics of MOFs which make it special in comparison to rigid zeolites or activated carbon. Based on this, MOFs have been classified into three classes as follows:[62,63]

- First generation MOFs – where the framework collapse irreversibly upon removal of guest molecules.

- Second generation MOFs – these are non-conformationally changeable frameworks which maintain their robustness even after the removal of guest molecules.

- Third generation MOFs - these frameworks exhibit flexibility and dynamic functionalities, leading to guest responsive adsorption behaviours.

Therefore second generation MOFs are known as robust MOFs while the third generation MOFs are referred as flexible MOFs. Flexible MOFs undergo reversible structural transformations upon applying external stimuli such as guest molecule removal or inclusion, heat, magnetic and electric fields, whereas the robust MOFs do not show any transformations. MOF-5 and HKUST-1 are the well-known examples for robust MOFs while MIL-53 and MIL-88 belong to the category of flexible MOFs.[9,42,64,65] Both robust and flexible MOFs have their own advantages in various applications. High porosity and surface area combined with permanent pore size and shape are the assets of robust MOFs for gas storage applications.[62] The unique property of the flexible MOFs is the flexibility of the framework which is an advantage in gas separation applications.[62]

One of the main stimuli that affect the structural transformation in flexible MOFs is guest molecules. These can either induce crystal to amorphous transformation or crystal to crystal transformation when considering the guest induces distortion phenomena of flexible MOFs.

Crystal to amorphous transformation was seen in the lanthanide (III) coordination polymers $\{[M_2(BDOA)_3(H_2O)]\cdot 6H_2O\}n$ (where M = Tb, Gd and Sm; BDOA = benzene-1,4-dioxylacetate).[66] The crystalline nature of these frameworks was lost after the removal of guest molecules but was regained after soaking them in water.

Interestingly the 3D MOF, $\{[Zn_2(1,4\text{-}BDC)_2(dabco)]\cdot 4DMF\cdot 0.5H_2O\}n$, (1,4-BDC = 1,4-benzenedicarboxylate and dabco = 1,4-diazabicyclo[2.2.2]octane), adapts to

two other different structures in the guest free state and the benzene included state.[67] In the guest free state, it has a formula of $\{Zn_2(1,4\text{-}BDC)_2(dabco)\}n$ and the formula of the benzene included state is $\{[Zn_2(1,4\text{-}BDC)_2(dabco)]\cdot 2C_6H_6\}n$.[67] This is a good example for guest induced crystal to crystal transformation since in all three cases the crystalline nature of the framework is preserved.

Guest induced structural transformation of flexible MOFs occurs due to the following factors:[62,63]

- Rotation of bridging ligand – here ligand molecules undergo a partial motion such as rotation. This happens when the MOF has high void space which sterically allows the movements of the ligands.

- Shrinking, swelling and shape-responsive fitting – MOF is held together with various types of bonding including coordination bonds, H- bonds and other weak nonbonding interactions. Slight adjustments of these interactions can result small structural changes such as shrinkage or expansion. This usually happens in order to accommodate the guest molecules.

- Interdigitation and interpenetration – If the resultant framework has higher void space then catenation occurs as described earlier. In these interpenetrated networks, the cooperative motion between the frameworks can be seen which results a mutual sliding.

1.9.   Properties and Applications

MOFs have several applications including gas storage, gas separation, magnetic, non-linear optical properties, catalysis and biomedical applications.[13-20] Synthesis of MOFs is done in a way that the product exhibits the relevant attributes of the starting materials. Therefore when synthesising MOFs the starting materials should be carefully chosen in order to get the desired properties. This is quite similar to the synthesis of organic polymers, where nature of the monomer determines the properties of the polymer such as its processability, physical and optical characteristics.[45] In similar way it is the building units of the network connectivity which governs the properties of MOF.[45] This includes magnetic exchange, acentricity for non-linear optical (NLO) applications, availability of large channels for gas storage and biological applications. Some applications such as gas storage and separation, magnetic properties and biomedical applications will be discussed in this chapter.

1.9.1. Hydrogen Storage

Climate change and global warming dominate the news today. Due to the high consumption of hydrocarbons which results in the emission of carbon dioxide and other pollutants, it is said that global warming will be the highest threat to the environment in the near future.[68,69] Considering these threats, the palpable solution would be to employ an alternative energy source that is widely available and does not produce pollutants. The solution: hydrogen. The fact that the

combustion product of hydrogen with air is water, hydrogen emphasizes the advocates of hydrogen economy. The development of hydrogen-fueled vehicles and portable electronics will require new materials that can store large amounts of hydrogen at ambient temperature and relatively low pressures with small volume, low weight, and fast kinetics for recharging.[13] The U.S. Department of Energy targets for a hydrogen storage system are as follows,[13,70]

- A capacity of 45 g H_2 per L

- Re-fuelling time of 10 min or less

- Life time of 1000 refuelling cycles

- Ability to operate within the temperature range of -30 to 50 ºC

These targets are set for the entire storage system. Therefore practically a material should have a higher capacity to store hydrogen when considering the weight and the regeneration system. However the size and the weight of these components depend on the operational conditions such as whether it goes through chemisorption or physisorption mechanism.[13] Physisorption correlates with surface area, with greater gas uptake favored by higher surface area. As MOFs have higher surface areas and low densities, they are one of the attractive candidates for hydrogen storage. However since dispersive forces cannot assist to uptake considerable amount of hydrogen, MOFs need to accommodate new functionalities to enhance the storage properties.

A vast variety of research has been done on computational studies to model H_2 adsorption in MOFs.[71-73] MOF-5 and its isoreticular series have received much attention for this purpose. These computed isotherms and binding energies usually agree with the experimental results. Van der Waals type interactions between H_2 and frameworks are employed in this regard. These types of materials where physisorption dominates the adsorption, storage capacity depends on the size of the pore. In graphites and carbon nanotubes it was predicted that the maximal uptake takes place with the materials having pores around 7 Å wide.[13] This will allow one layer of H_2 molecules to adsorb on opposing surface without leaving any space in between.

Increasing the H_2 binding energy within MOFs is the most important challenge for creating hydrogen adsorbents that operate at 298 K. The desired binding energy to be achieved is *ca.* 20 kJ mol^{-1}.[74] Therefore mostly in MOF systems strong orbital interactions will be avoided and move to simple charge-induced dipole interactions. The H_2 adsorption enthalpy in MOF systems can probably be increased by introducing open metal sites on the surfaces.[75]

MOFs that consist of large pores may not be good enough for H_2 storage due to the poor attraction from the surface of pore walls experienced by the H_2 molecules in the center of the pores. Therefore MOFs with pores just bigger than the kinetic diameter of the H_2 would be an ideal storage material.[76] Interpenetration is a tool which can be used to reduce the number of large voids in a given structure. But it is not easy to control the level of interpenetration when synthesizing a MOF

material. There is only one example known in the literature which is $Cu_3(tatb)_2$ ($tatb^{3-}$= 4,4',4''-s-triazine-2,4,6-triyltribenzoate) where the catenated and the noncatenated versions of the same framework is compared for H_2 storage.[77] The catenated version adsorb 1.9 wt% of H_2 at 1 bar and 77 K whereas the non catenated version adsorbs only 1.3 wt%.[77]

One of the best examples of MOFs for H_2 storage reported today is MOF-5, which is a cubic Zn-terephthalate based network (Figure 1.12).[9] At 77 K it shows a gravimetric uptake of about 1.3 wt% at 1 bar and 5.1 wt% at 5 bar.[78,79] This variation is due to the incomplete evacuation of guest molecules from the channels as well as partial decomposition of the framework upon exposure to air. It was reported that upon complete activation and protection of the sample from water and air, the H_2 uptake observed was 7.1 wt% at 77 K and 40 bar. This amount increased to 10 wt% at 100 bar (Figure 1.13) which corresponds to the volumetric storage density of 66 g L^{-1}.[80] More interestingly it was reported that hydrogen can be loaded into a cold sample of the compound within 2 minutes, and 24 cycles of adsorption and desorption has taken place without loss of capacity.[80]
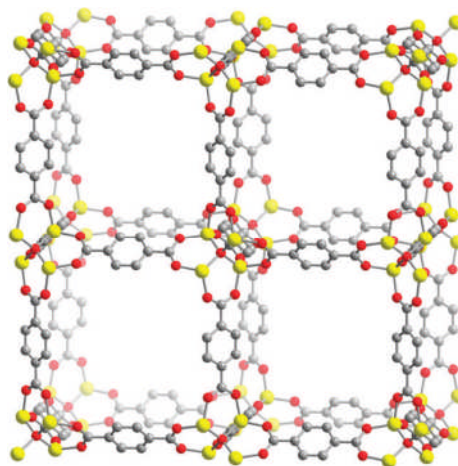
Figure 1.12.   Crystal structure of MOF-5. Yellow, gray and red spheres

represent Zn, C, and O atoms, respectively. H atoms are omitted for clarity.[13]
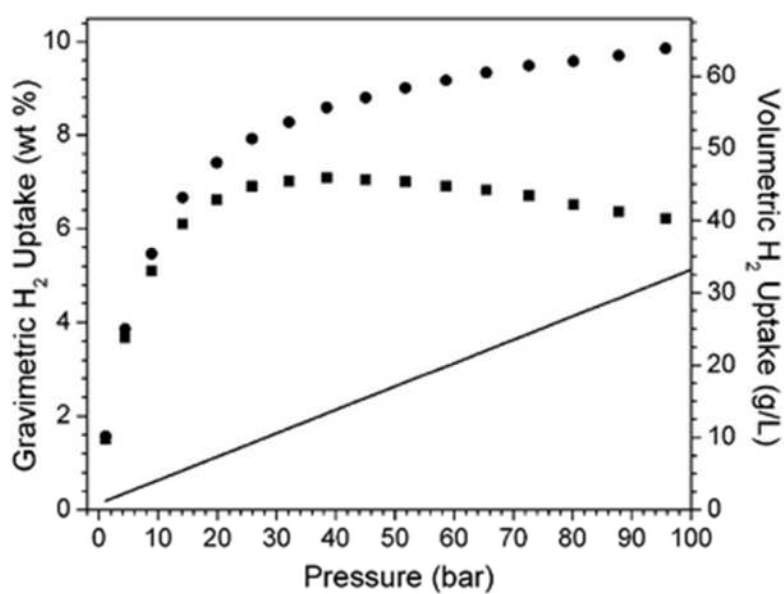
Figure 1.13.   Excess (squares) and total (circles) hydrogen uptake for MOF-5 at

77 K. The solid line represents the density of compressed hydrogen over the given

pressure range at this temperature.[13]

Although MOF-5 shows high storage capacity at 77 K, it doesn't show a good uptake at 298 K due to weak interactions between H_2 and the framework. The volumetric capacity of MOF-5 at 298 K and 100 bar is about 9.1 g L^{-1} whereas compressed H_2 has a value of 7.7 g L^{-1} under the same conditions.[80] This suggests that MOF -5 is not a good storage material for H_2 at room temperature.

$Mn_3[(Mn_4Cl)_3(BTT)_8]_2$, which contains open Mn^{2+} coordination sites has a volumetric storage capacity of 60 g L^{-1} at 77 K and 90 bar and 12.1 g L^{-1} at 298 K and 90 bar which is 77 % greater than the density of compressed gas under same conditions.[81] This is the highest storage capacity reported for MOFs under these conditions. The isosteric heat of adsorption of H_2 for this MOF is 10.1 kJ mol^{-1} at zero coverage.[81] According to the powder neutron diffraction data, strong $Mn-D_2$ interactions can be seen with a separation of 2.27 Å between metal and the center of the D_2 molecule.[82] This is a much shorter distance observed for physisorbed hydrogen and may have an effect on efficient packing of hydrogen molecules in channels.

MOFs have a number of key characteristics which show promise for exceptional hydrogen storage properties such as high surface area and fine tunable pore architectures. However so far none of them meet all the criteria set by U.S. Department of Energy and the hydrogen economy is yet to flourish.

1.9.2. Methane Storage

Methane is another candidate which can be considered as an alternative fuel due to its profusion and availability. However, the lack of effective and safe on-board system is one of the major hurdles to overcome when considering methane to compete with gasoline. Usually methane is stored as compressed natural gas in pressure vessels at 20.7 MPa.[83] An attractive alternative is a porous material where methane could be stored by physisorption at lower pressure. The Department of Energy of U.S. set a target as 180 v (STP)/ v at 298 K and 35 bar (STP : 298 K, 0.1 MPa) for material-based adsorbed methane storage.[83,84] Various materials have been studied for methane storage which includes carbon nanotubes, zeolites and activated carbon.[85-87] Although significant effort has been made on studying these materials, it seems that there is still a long way to go. Recently MOFs have been considered as a potential candidate for methane storage due to the high surface area and pore volume.

The first demonstration of MOFs on methane storage was reported by Kitagawa *et al.* In their studies, a cobalt containing MOF which has a formula of $\{Co_2(4,4'\text{-bpy})_3(NO_3)_4 \cdot 4H_2O\}n$, was found to have a gravimetric methane uptake of 52 cm^3 (STP) g^{-1} at 298 K and 30 bar.[88] HKUST-1 has been studied for methane storage and reported to have an uptake of ~160 cm^3 (STP) cm^{-3}.[89]

PCN-14 (Figure 1.14) made by Zhou *et al* which is composed of clusters of nano sized cages is the first MOF reported to meet the DOE target. This MOF is

showing a methane uptake of 230 cm^3 (STP) cm^{-3} at 290 K and 35 bar (Figure 1.15).[90] This exceptional behaviour was attributed to the following structural features of the PCN-14 framework:[90]

- The aromatic rings of the linker were good enough for the binding of methane.
- Size and the geometry of nanopores.
- Coordinatively unsaturated metal ions.
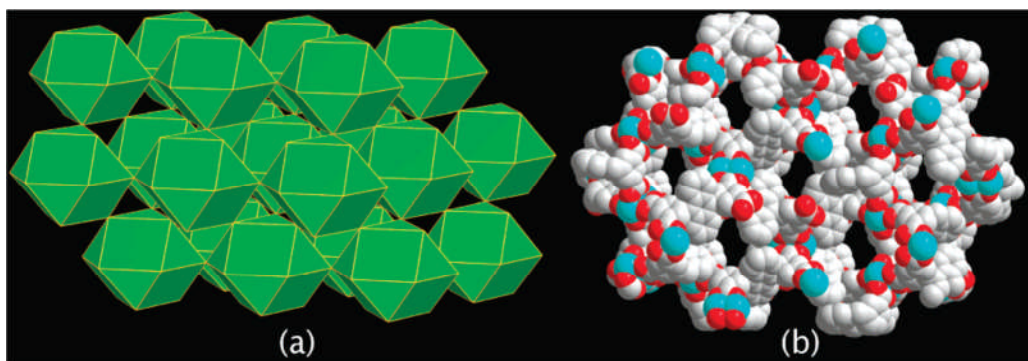
Figure 1.14. 3D framework of PCN-14 viewed as a (a) cuboctahedral net and (b) space filling model on the [1 0 3] plane.[87]
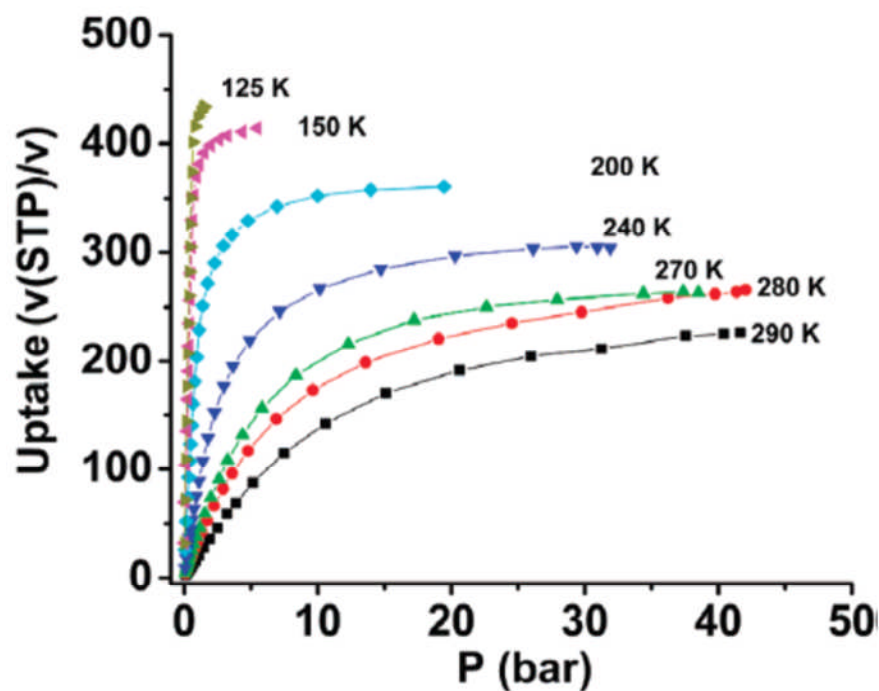
Figure 1.15. High pressure methane sorption isotherms at various

temperatures.[83]

Although the number of methane adsorption studies on MOFs is increasing, detailed investigations on the adsorption mechanism in MOFs are limited. Usually gas adsorption on MOFs has a strong relationship with the surface area. Since the interactions between the methane molecules and the surface of the MOF occur due to van der Waals forces,[83] a relatively homogenous pore coverage can be seen upon methane adsorption. Therefore higher adsorption capacity of methane can be obtained by increasing the surface area of the MOF. On the other hand if the MOF contains open metal sites, it can strongly attract methane molecules through the Coulombic interactions.[83]

In a short period of time the progress made by MOFs on methane adsorption is remarkable. While considering the outstanding storage capacities reported for some of the MOFs such as PCN-14, it is clear that MOFs are promising materials for methane storage.

1.9.3. Gas Separation

Separation is a process that divides a mixture into its components.[14] This can be achieved by selective adsorption since it is based on different affinities at the given condition. Different techniques are used for gas separation which includes cryogenic distillation, pressure or thermal swing adsorption and membrane based separations.[91] Notable examples are nitrogen-oxygen (air), H_2 and CH_4 purification, CO_2 capture and noble gas (Kr-Xe) separations.[91,92] Development of adsorption based separations have become a key in the gas separation industry some of which use zeolitic adsorbents.[92] This has induced the research on new porous materials to overcome the demand for the adsorptive separation. Adsorptive separation is meant to be two types: bulk separation and purification.

Gas adsorptive separation depends on the following mechanisms;[14]

- Molecular sieving effect
- Thermodynamic equilibrium effect
- Kinetic effect
- Quantum sieving effect

Molecular sieving effect happens according to size and shape exclusion. Some of the components in the gas mixture cannot enter the material due to the size and shape of the pore structure of the material. This depends on the size of the pore and the kinetic diameter of the molecule. Separation of normal paraffin from isoparaffin using zeolite 5A is one of the most common examples for molecular sieving effect.[92] Once a gas stream entered the channel system the interactions between the adsorbate and adsorbent is crucial in determining the separation efficiency. This phenomenon is known as thermodynamic equilibrium effect.

The kinetic separation is known as ''partial molecular sieving effect''.[14,93] Because of the different diffusing rates, certain components adsorb faster than the others which leads to the separation. Quantum sieve effect also allows separation based on difference in the diffusion speeds, but it is discussed mainly for the light molecules such as H_2, D_2 penetration,[14,94] where pore sizes become comparable with the *de* Broglie wave length of these molecules at low temperature.

Metal Organic Frameworks are ideal candidates for gas separation due to higher surface area, adjustable pore sizes and controllable surface properties. The tunability of MOFs makes it unique because in zeolites pores are difficult to alter due to its rigid tetrahedral oxide skeletons. Currently, investigation of MOFs for gas separation is in its early stage.

The adsorptive gas separation or purification can be done by passing streams of gas mixture through a column packed with adsorbents followed by a strong desorption. This will lead a product rich with weakly adsorbed component. MOFs can be used as the adsorbents in this context and possibly used to remove ppm-traces of components from various gases.[95] For example, removal of tetrahydrothiophene (THT) from natural gas has been studied at room temperature.[95] Electrochemically prepared fixed bed reactor has been used for this purpose which is filled with Cu-EMOF. About 10-15 ppm traces of sulphur was able to capture down to less than 1ppm from this process.[95] MOFs with accessible open metal sites are well suited for the separation process.[14]

Adsorptive selectivity of rigid MOFs (Figure 1.16) is different than flexible MOFs (Figure 1.17). In rigid MOFs, guest inclusion has a limitation with the kinetic size of the guest molecule and the diameter of the pore window of the MOF. Therefore similar to zeolites, the separation occurs due to the molecular sieving effect and /or different strengths of the interactions between adsorbent-adsorbate as well as adsorbate-adsorbate.[96] In flexible MOFs guest molecules act as external stimuli on the structural transformation process.[97,98] Therefore certain guests are preferentially recognized than the others. ''Gate effect'' occurs when the structural transformation happened during the adsorption from a closed structure to an open structure.[97] In the closed state the pores are usually not available for guest molecules but it expands and become available when certain type of guest molecules is introduced. This process is known as ''gate opening process'' and the pressure at that point is called ''gate opening pressure'' which generates a

sigmoidal adsorption profile.[97] Therefore in flexible MOFs, same factors govern the separation efficiency but unlike rigid MOFs these factors are combined with the structural re-arrangement effect.[14] Few examples for gas separation in different MOFs are discussed in the following section.
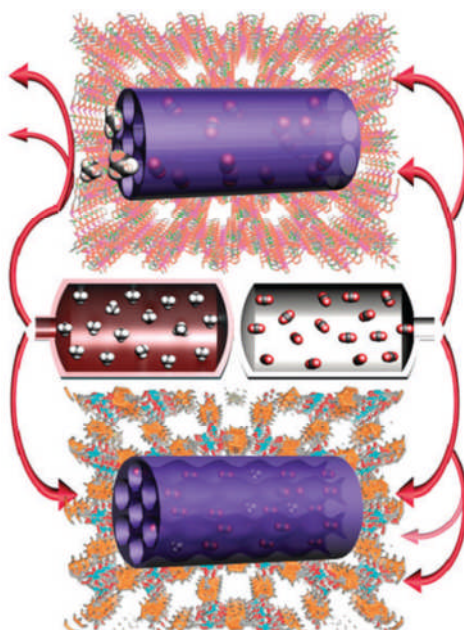
Figure 1.16.   Schematic illustration of selective gas adsorption in rigid MOFs (top: the molecular sieving effect, bottom: preferential adsorption).[14]
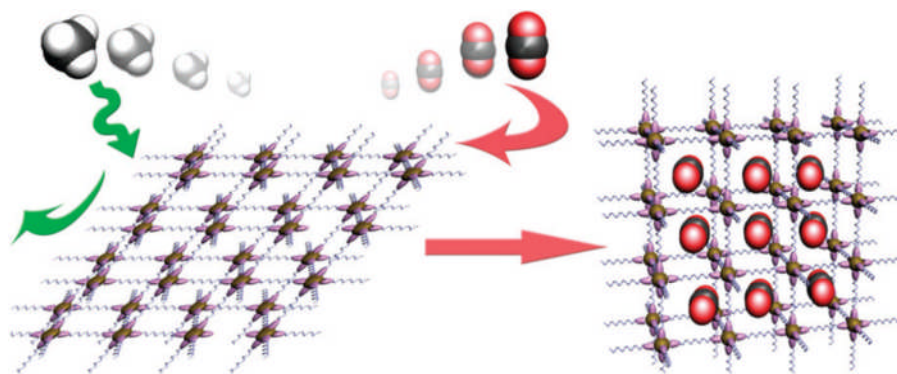
Figure 1.17.   Schematic illustration of selective gas adsorption in a

flexible MOF.[14]

Examples for gas separation using rigid MOFs:

The separation of carbon dioxide from methane is important in natural gas upgrading since CO_2 reduces the energy content in natural gas and induces pipeline corrosion. Separation of CO_2/CH_4 mixtures have been studied by Snurr *et al* using a carborane based MOF with and without coordinatively unsaturated open metal sites.[96] The study has confirmed the selective adsorption of CO_2 over CH_4 with a selectivity factor of ~ 17.[96] The separation occurred according to adsorbate-surface interactions and shows that the open metal sites have an influence in separation of quadrapolar and non-polar gas pairs.[96]

A 3D MOF based on manganese and formate, which has 1D channel, has been studied for gas separation.[99] The structure contains larger cages connected by small windows. Experiments show that, at 78 K the material selectively adsorbs H_2 over N_2 and at 195 K it has selectivity towards CO_2 over CH_4.[99] The

adsorption capacities of the excluded gases N_2 and CH_4 were almost zero. The selective sorption of H_2 and CO_2 is attributed to the small aperture of the channels which discriminates these gases with small kinetic diameters from other gases which have larger kinetic diameters. This is a good example for molecular sieving effect. Also it should be noted that the adsorption properties may be distinct at different temperatures as the MOF exhibits different selectivity at different temperature.[99]

Examples for gas separation using flexible MOFs:

Surface properties of pores play a critical role in determining the adsorption selectivity in flexible MOFs. MIL-53 has a 3D structure which has 1D channel (Figure 1.18a).[98] The material exhibits a breathing phenomenon upon hydration and dehydration. The hydrated version has slightly deformed pores due to hydrogen bonding interactions between H_2O molecules and the framework. It has little uptake of CO_2 below 10 bar but it showed a distinct high uptake between the pressure range of 12-18 bar. Below 20 bar, there was no uptake of CH_4 and this was due to the non-polarity and the repulsive forces of water molecules in the framework.[98] Interestingly the dehydrated version shows different adsorption behaviours towards CH_4 and CO_2. CH_4 has a typical adsorption isotherm for microporous materials but CO_2 has a different shape of isotherm. CO_2 adsorption takes place in two steps. Above the first step, CO_2 exceed the adsorption capacity of CH_4 in the low pressure region (Figure 1.18b). Quadrapole moment of the CO_2 is the reason for this difference in the isotherms.[98]
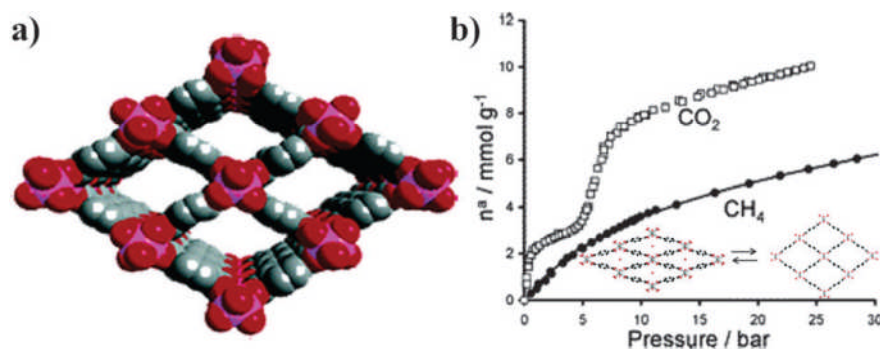
Figure 1.18.   (a) Framework structure of MIL-53. (b) Gas adsorption isotherms

of MIL-53(Cr) at 304 K (inset, schematic illustration of the ''breathing'' effect in

MIL-53(Cr))[14]

Another 1D channels containing 2D MOF with the formula of $Cu(dhbc)_2(4,4'$-

bpy) (dhbc = 2,4-dihydroxybenzoic acid) shows some interesting selective gas

adsorption properties.[97] This framework is mutually interdigitated and interlayer

π----π stacking interactions can be seen. This compound shows zero adsorption

towards N_2 and O_2 in the low pressure region.[97] Then at a point it has a sudden

increase of adsorption which is referred to as gate opening pressure and there is a

sudden decrease of adsorption at the gate closing pressure which gives a

hysteresis. Interestingly the gate opening pressure and the gate closing pressure

for both gases are different. This may be related to the intermolecular interactions

of the gas molecules.[97]

Environmental friendly and cost effective gas separation system is the need today.

Exploitation of new adsorbents is critical but difficult due to the industrial and

environmental requirements. As potential adsorbents not only have MOFs

attracted a great deal of interest but also it has made good progress within a short period.

1.9.4. Magnetic Properties of MOFs

Since magnetism is another potential application of Metal Organic Frameworks, the construction of MOFs with fascinating topologies and the study of their magnetic properties has become an important subject. The research is focussed on ways to improve the properties of magnets and to explore new functions in combination with other useful phenomena.[15] In MOFs, paramagnetic metal ions are linked with diamagnetic organic ligands which can be used efficiently in transmitting magnetic exchange.[15] Therefore the magnetic properties in MOFs depend on the properties of both metal and ligands as well as the structural organization of the resulting network. Mostly the paramagnetic centres will be first row transition metals such as V, Cr, Mn, Fe , Co, Ni, and Cu, but lanthanides also have been used for the same purpose. Spin quantum number and magnetic anisotropy are important parameters of these metal ions which are often associated with their oxidation states.[17] Close-shell ligands usually give weak magnetic interactions.[100-102] Therefore oxo, cyano and azido bridges are used in order to get a strong coupling between the metal centres.[15] Polycarboxylic ligands are also good candidates for this purpose. Not only they can make flexible structure by bridging with two or more metal centres but also can adapt to different bridging modes which can influence the magnetic properties.[103,104] Magnetism also can be induced in non-magnetic frameworks by introducing guest

molecules.[17] Magnetic properties such as ferromagnetic, anti-ferromagnetic and ferrimagnetic properties that have arisen from MOFs will be discussed in this section.

1.9.4.1.   Ferromagnetic Properties

Ferromagnetism arises with parallel coupling of the spins. A chiral 3D Ni-Glutarate, $[Ni_{20}(H_2O)_8(C_5H_6O_4)_{20} \cdot 40H_2O]$ has been synthesized with helices of edge sharing octahedra connected to four parallel neighboring ones through a Nickel octahedron.[105] The framework is walled by two independent glutarate anions. This framework shows ferromagnetic behavior with a Curie temperature of 4 K. The low value of Tc is due to the weak ferromagnetic interactions of larger Ni-O-Ni angle.[105]

1.9.4.2.   Antiferromagnetic Properties

A MOF structure that allows antiparallel coupling of the spin metal ions or organic free radical entities within the structure generates the antiferromagnetic properties. Yu *et al* has reported a cobalt MOF which has a formula of $Co_3(tatb)_2(H_2O)_2 \cdot 2DMA \cdot 3H_2O$ (Figure 1.19a).[106] In this structure, trimetallic cobalt clusters are extended by the tatb ligand pairs to form non interpenetrated porous network. Magnetic susceptibility measurements revealed the presence of paramagnetic properties within the temperature range of 2-300 K. The

antiferromagnetic coupling was seen between the neighbouring Co^{2+} ions (Figure 1.19b).[106]
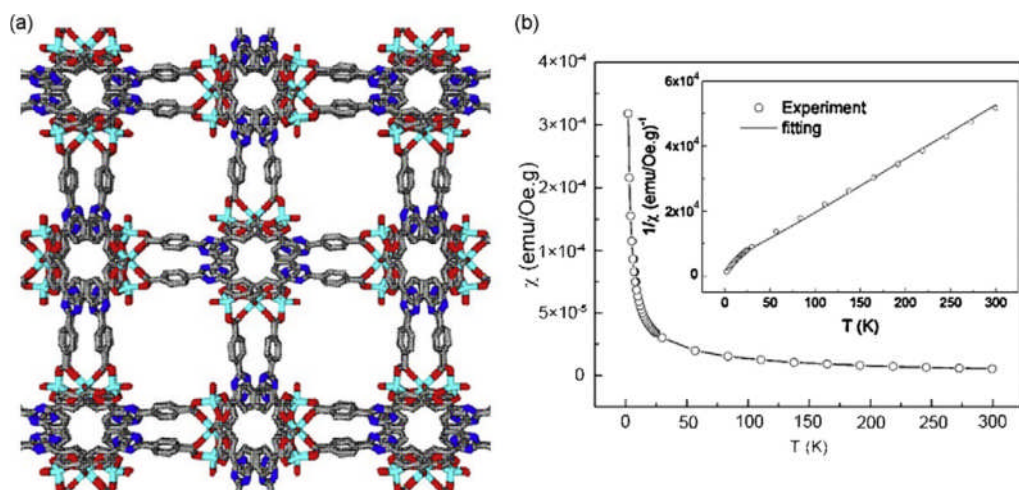
Figure 1.19.   (a) 3D framework structure of $Co_3(tatb)_2(H_2O)_2$. (b) Susceptibility as function of temperature (inset shows the $1/\chi$ vs T curve along with a theoretical fitting).[15,106]

Zhang *et al* reported the antiferromagnetic properties of HKUST-1. The structure consists of dimeric Cu paddle wheel units (Figure 1.20) with a Cu-Cu separation of 2.6 Å.[107] The temperature dependant magnetization was analysed and fitted with the Bleaney Bower model (Figure 1.21). At high temperatures the material is antiferromagnetic and below 65 K it shows weak ferromagnetic interactions.[107]
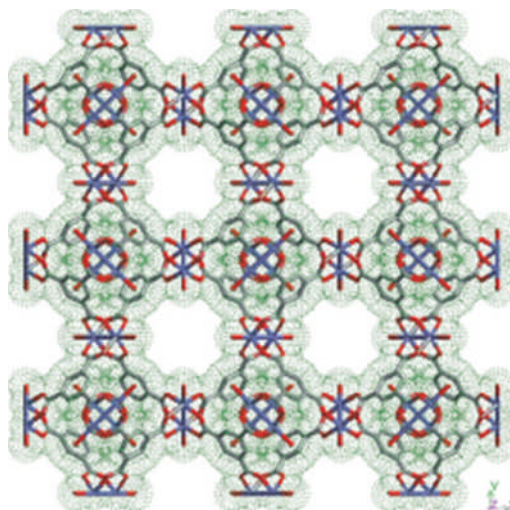
Figure 1.20.   3D Framework of HKUST-1, showing the neighbouring dimeric

Cu paddle wheel units.[42,107]
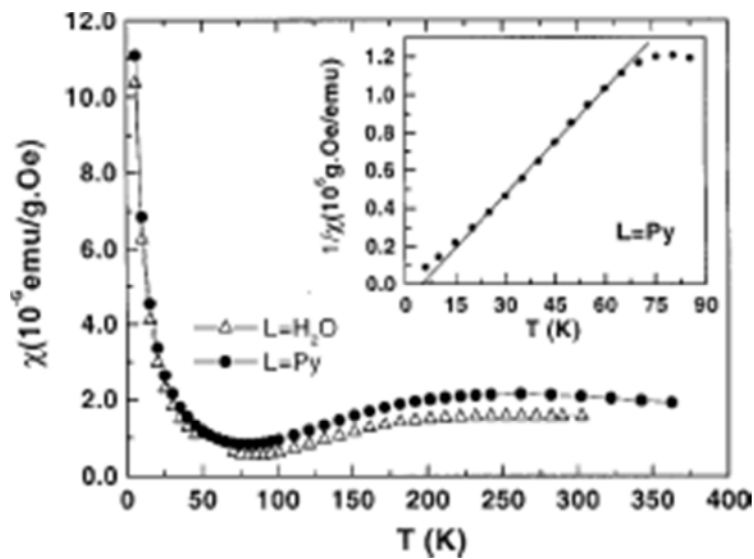
Figure 1.21.   Temperature dependent magnetic susceptibility of HKUST-1,

(inset - low T Curie–Weiss behavior for L= Py).[107]

1.9.4.3.   Ferrimagnetic Properties

In ferrimagnets, usually two kinds of spin carriers can be seen, which alternate regularly and interact antiferromagnetically.[108] The exchange coupling among the paramagnetic centres of MOFs can lead to either ferromagnetic or antiferromagnetic behaviour. MIL-9 $[Co_5(OH)_2(C_4H_4O_4)_4]$, framework is reported with ferrimagnetic properties (Figure 1.22a).[108] The 2D zig-zag metal oxide layers are covalently connected through succinates to make the 3D network (Figure 1.22b). The edge sharing cobalt octahedra produce pentamers and 12 membered ring cavities. The ligands act as bridges between the sheets. Obviously the edge sharing Co^{2+} octahedra should have a vital effect on the magnetic properties of the compound. The $1/\chi$ vs temperature plot has a linear fit with Curie Weiss law above 50 K (Figure 1.23). The remarkable change occurs below 25 K as compound tends to show ferrimagnetic properties. This behavior can be reasoned as,

- Anti-ferromagnetic coupling within the pentamers
- Ferromagnetic coupling between the pentamers to avoid the compensation of the moments.
- Ferromagnetic coupling between the layers.
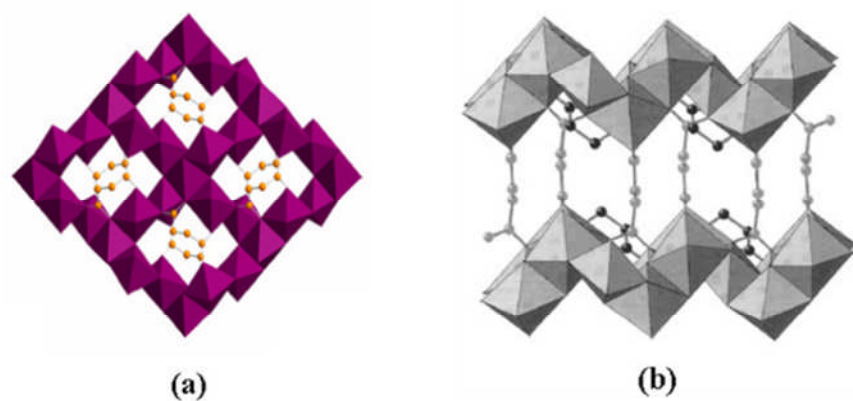
Figure 1.22. (a) View of the 2D inorganic layer in a 3D cobalt succinate

$[Co_5(OH)_2(C_4H_4O_4)_4]$ and (b) a view of the 3D structure where 2D layers are

connected by succinate anions.[108]
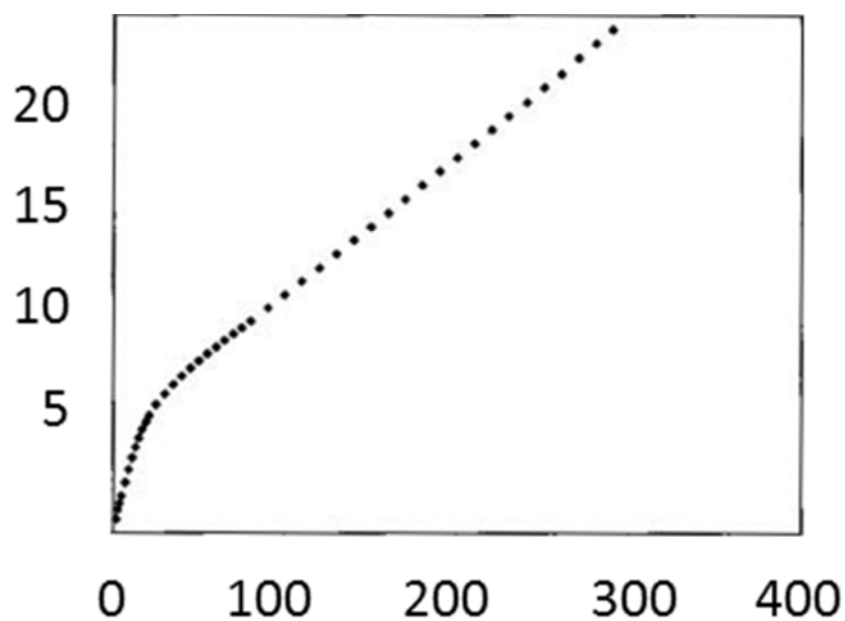
Figure 1.23. Temperature dependence of $1/\chi$ of $[Co_5(OH)_2(C_4H_4O_4)_4]$.[108]

Recently MOFs have moved another step forward by introducing multiferroic MOFs. Four MOF structures $[(CH_3)_2NH_2]M(HCOO)_3$, (M = Mn, Fe, Co, and Ni) have been reported by Jain *et al* as multiferroic frameworks.[109] Multiferroic materials are where magnetic and electrical ordering co-exists. It is difficult to achieve in the same material since, cooperative phenomena required different molecular interactions that are hard to incorporate in the same compound. MOFs have been able to overcome this hurdle by combining host lattice magnetic ordering with ferroelectric behaviour due to guest/solvent molecule ordering at low temperatures in the nanopores.[109]

Magnetic MOFs explored so far illustrate the potential of producing magnets of many different types; ferromagnets, antiferromagnets and ferrimagnets. The new approach to the creation of multiferroic system opens up opportunities for the production of lead-free multiferroic structures tailored for specific applications. Clearly, magnetic properties of MOFs offer much scope for further research.

1.9.5. Biomedical Applications of MOFs

The applications of MOFs in the field of biomedical science have recently been explored. The initial studies of MOFs in this field show a promise for biomedical applications. Stability and the toxicology of the material are the main issues that should be concerned when MOFs are used in this field. Since a large number of MOFs have been synthesized to date, it is hard to make a general comment on the stability of the MOFs. For example Fe-MIL-100 and Fe-MIL-101[110] are stable in

biological solutions for extended periods whereas MOF-5 is only partially stable in humid environments.[111] The toxicology studies of MOFs have started recently and some of the toxicological experiments carried out on iron carboxylate materials are extremely encouraging. For example Hinks *et al* reported iron fumarate which has the same chemical composition as MIL-88A, is approved as an oral iron supplement.[65] The biomedical applications of MOFs can be categorized into two different areas:

- Use of MOFs for drug delivery
- Use of MOFs as active materials themselves

1.9.5.1.   MOFs as drug delivery vehicles

The requirements for a material to be considered as a potential novel drug carrier are: [112]

- Non toxicity and bio-compatibility
- High drug loading capacity
- Efficient delivery, control the release and avoid the ''burst effect''
- Control matrix degradation and surface engineering

The high porosity of MOFs can be utilized for drug delivery. For example, MIL-100 and MIL-101 have been studied by Horcajada *et al* by loading anti-inflammatory drug Ibuprofen into the pores.[112] The attempt was succeeded by loading of 0.35 g of Ibuprofen per gram of MIL-100 and 1.4 g of Ibuprofen per

gram of MIL-101. Both MOFs were stable with the drug and complete guest release was achieved in approximately 3 days by MIL-100 and 6 days by MIL-101 into a simulated body fluid solution.[112]

NO is an important biological signalling agent and its delivery is attractive for many in vitro and in vivo antibacterial, antithrombotic, and wound healing applications.[113] Since MOFs have a great potential in storage of gases due to high surface area they are being considered for NO storage and delivery. Xiao *et al* reported NO adsorption capacity of 9 mmolg^{-1} at 196 K and 3 mmolg^{-1} at 298 K in HKUST-1.[114] Desorption of NO from HKUST-1 occurred in contact with moisture but was a very small amount. McKinlay *et al* showed that Ni-CPO-27 and Co-CPO-27 has a greater uptake of NO at room temperature with a perfect release upon exposure to the moisture.[113] M-CPO-27 (M = Ni, Co) delivered a significant amount of NO in the adsorption-storage-delivery cycle (Figure 1.24) and this flux of NO was shown to be active in the vasodilation of porcine arteries.[113] A lesser flux of NO released by HKUST-1 was shown to be active for antiplatelet activities.[114]
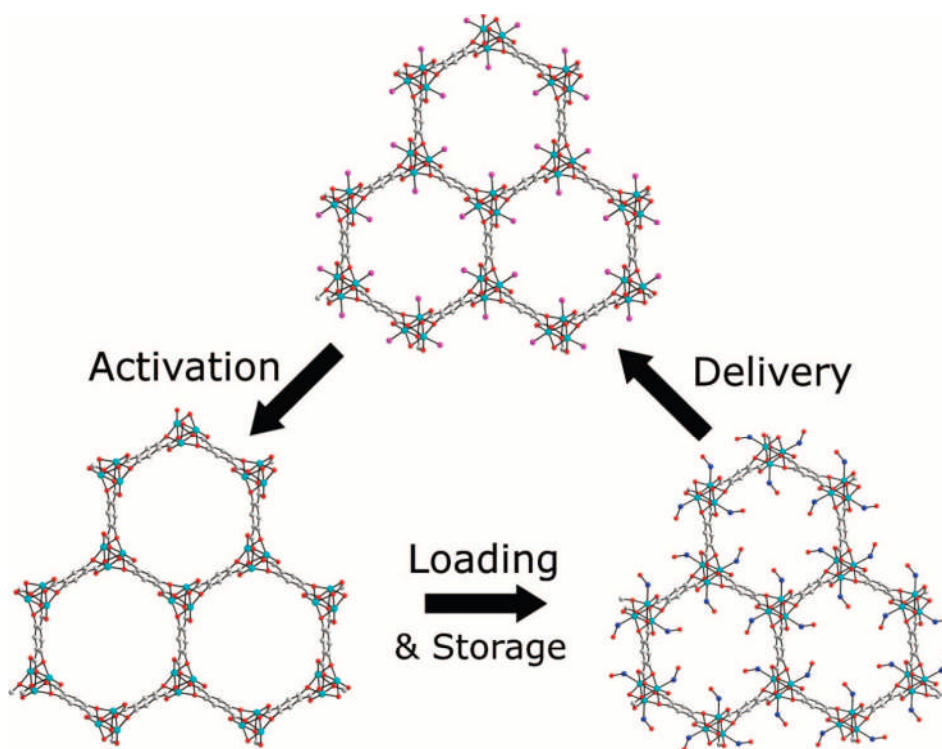
Figure 1.24.   NO adsorption-storage-delivery cycle of CPO-27.[113]

1.9.5.2.   MOFs as active materials themselves

MOFs are used as contrast agents for magnetic resonance imaging. Lin *et al* has synthesized lanthanide MOFs which has nanoparticle morphology.[115] These nanoparticle MOFs (NMOFs) can be dispersed in solution. Since it contains lanthanides, these NMOFs can be used as imaging agents. According to the study, Gadolinium NMOFs have shown high relaxivity which exceeds the other agents such as gadolinium containing liposomes.[115] Further improvement of these NMOFs comes with both magnetic resonance and luminescence properties. This was achieved by doping the gadolinium NMOFs with 5% terbium or 5% europium, where terbium gives green and europium gives red.[115] Even though

these doped NMOFs proposed as multimodal imaging agents, few questions to be answered such as biocompatibility and stability to validate the concept.

Research on biomedical applications of MOFs gaining momentum and it looks as if MOFs will replace the traditional nanoporous materials in drug delivery and storage applications. Since these studies are in the preliminary stage, more research is needed to get a better understanding about the use of MOFs in this field, especially about the toxicology and the biocompatibility of MOFs.

1.10. References

(1)   Davis, M. E. *Nature* **2002**, *417*, 813.

(2)   Inagaki, S.; Fukushima, Y.; Kuroda, K. *J Chem Soc Chem Comm* **1993**, 680.

(3)   Imhof, A.; Pine, D. J. *Nature* **1997**, *389*, 948.

(4)   Cundy, C. S.; Cox, P. A. *Chem Rev* **2003**, *103*, 663.

(5)   Cappellazzo, O.; Cao, G.; Messina, G.; Morbidelli, M. *Ind Eng Chem Res* **1991**, *30*, 2280.

(6)   Degnan, T. F.; Chitnis, G. K.; Schipper, P. H. *Micropor Mesopor Mat* **2000**, *35-6*, 245.

(7)   Wilson, S. T.; Lok, B. M.; Messina, C. A.; Cannan, T. R.; Flanigen, E. M. *J Am Chem Soc* **1982**, *104*, 1146.

(8)   James, S. L. *Chem Soc Rev* **2003**, *32*, 276.

(9)   Li, H.; Eddaoudi, M.; O'Keeffe, M.; Yaghi, O. M. *Nature* **1999**, *402*, 276.

(10)   Chae, H. K.; Siberio-Perez, D. Y.; Kim, J.; Go, Y.; Eddaoudi, M.; Matzger, A. J.; O'Keeffe, M.; Yaghi, O. M. *Nature* **2004**, *427*, 523.

(11)   Eddaoudi, M.; Kim, J.; Rosi, N.; Vodak, D.; Wachter, J.; O'Keeffe, M.; Yaghi, O. M. *Science* **2002**, *295*, 469.

(12)   Furukawa, H.; Ko, N.; Go, Y. B.; Aratani, N.; Choi, S. B.; Choi, E.; Yazaydin, A. O.; Snurr, R. Q.; O'Keeffe, M.; Kim, J.; Yaghi, O. M. *Science* **2010**, *329*, 424.

(13)   Murray, L. J.; Dinca, M.; Long, J. R. *Chem Soc Rev* **2009**, *38*, 1294.

(14)   Li, J. R.; Kuppler, R. J.; Zhou, H. C. *Chem Soc Rev* **2009**, *38*, 1477.

(15)   Kuppler, R. J.; Timmons, D. J.; Fang, Q. R.; Li, J. R.; Makal, T. A.; Young, M. D.; Yuan, D. Q.; Zhao, D.; Zhuang, W. J.; Zhou, H. C. *Coordin Chem Rev* **2009**, *253*, 3042.

(16)   Czaja, A. U.; Trukhan, N.; Muller, U. *Chem Soc Rev* **2009**, *38*, 1284.

(17)   Kurmoo, M. *Chem Soc Rev* **2009**, *38*, 1353.

(18)   Allendorf, M. D.; Bauer, C. A.; Bhakta, R. K.; Houk, R. J. T. *Chem Soc Rev* **2009**, *38*, 1330.

(19)   Ma, L. Q.; Abney, C.; Lin, W. B. *Chem Soc Rev* **2009**, *38*, 1248.

(20)   McKinlay, A. C.; Morris, R. E.; Horcajada, P.; Ferey, G.; Gref, R.; Couvreur, P.; Serre, C. *Angew Chem Int Edit* **2010**, *49*, 6260.

(21)   Bian, Z. F.; Zhu, J.; Cao, F. L.; Lu, Y. F.; Li, H. X. *Chem Commun* **2009**, 3789.

(22)   Zhao, X. X.; Ma, J. P.; Dong, Y. B.; Huang, R. Q. *Cryst Growth Des* **2007**, *7*, 1058.

(23)   Jiang, T.; Lough, A.; Ozin, G. A.; Bedard, R. L. *J Mater Chem* **1998**, *8*, 733.

(24)   Cheetham, A. K.; Ferey, G.; Loiseau, T. *Angew Chem Int Edit* **1999**, *38*, 3268.

(25)   Zhang, X. M. *Coordin Chem Rev* **2005**, *249*, 1201.

(26)   Del Popolo, M. G.; Voth, G. A. *J Phys Chem B* **2004**, *108*, 1744.

(27)   Parnham, E. R.; Morris, R. E. *Accounts Chem Res* **2007**, *40*, 1005.

(28)   Wasserscheid, P.; Keim, W. *Angew Chem Int Edit* **2000**, *39*, 3772.

(29)   Parnham, E. R.; Morris, R. E. *J Am Chem Soc* **2006**, *128*, 2204.

(30)   Liu, C. M.; Gao, S.; Kou, H. Z. *Chem Commun* **2001**, 1670.

(31)   Blake, A. J.; Champness, N. R.; Chung, S. S. M.; Li, W. S.; Schroder, M. *Chem Commun* **1997**, 1675.

(32)   Wei, Q. H.; Zhang, L. Y.; Yin, G. Q.; Shi, L. X.; Chen, Z. N. *J Am Chem Soc* **2004**, *126*, 9940.

(33)   Zhang, X. M.; Tong, M. L.; Chen, X. M. *Angew Chem Int Edit* **2002**, *41*, 1029.

(34)   Hu, X. X.; Pan, C. L.; Xu, J. Q.; Cui, X. B.; Yang, G. D.; Wang, T. G. *Eur J Inorg Chem* **2004**, 1566.

(35)   Xiong, R. G.; Zhang, J.; Chen, Z. F.; You, X. Z.; Che, C. M.; Fun, H. K. *J Chem Soc Dalton* **2001**, 780.

(36)   Xiong, R. G.; You, X. Z.; Abrahams, B. F.; Xue, Z. L.; Che, C. M. *Angew Chem Int Edit* **2001**, *40*, 4422.

(37)   Xiao, D. R.; Hou, Y.; Wang, E. B.; Lu, J.; Li, Y. G.; Xu, L.; Hu, C. W. *Inorg Chem Commun* **2004**, *7*, 437.

(38)   Wang, Z. Q.; Cohen, S. M. *Chem Soc Rev* **2009**, *38*, 1315.

(39)   Tanabe, K. K.; Cohen, S. M. *Chem Soc Rev* **2011**, *40*, 498.

(40)   Burrows, A. D.; Frost, C. G.; Mahon, M. F.; Richardson, C. *Angew Chem Int Edit* **2008**, *47*, 8482.

(41)   Doonan, C. J.; Morris, W.; Furukawa, H.; Yaghi, O. M. *J Am Chem Soc* **2009**, *131*, 9492.

(42)   Chui, S. S. Y.; Lo, S. M. F.; Charmant, J. P. H.; Orpen, A. G.; Williams, I. D. *Science* **1999**, *283*, 1148.

(43)   Song, Y. F.; Cronin, L. *Angew Chem Int Edit* **2008**, *47*, 4635.

(44)   Jee, B.; Eisinger, K.; Gul-E-Noor, F.; Bertmer, M.; Hartmann, M.; Himsl, D.; Poppl, A. *J Phys Chem C* **2010**, *114*, 16630.

(45)   Rowsell, J. L. C.; Yaghi, O. M. *Micropor Mesopor Mat* **2004**, *73*, 3.

(46)   Kitagawa, S.; Kitaura, R.; Noro, S. *Angew Chem Int Edit* **2004**, *43*, 2334.

(47)   Janiak, C. *Dalton T* **2003**, 2781.

(48)   Li, X. J.; Cao, R.; Sun, Y. Q.; Bi, W. H.; Li, X.; Wang, Y. Q. *Eur J Inorg Chem* **2005**, 321.

(49)   Sun, F. X.; Zhu, G. S.; Fang, Q. R.; Qiu, S. L. *Inorg Chem Commun* **2007**, *10*, 649.

(50)   Evans, O. R.; Xiong, R. G.; Wang, Z. Y.; Wong, G. K.; Lin, W. B. *Angew Chem Int Edit* **1999**, *38*, 536.

(51)   Chen, B. L.; Ockwig, N. W.; Millward, A. R.; Contreras, D. S.; Yaghi, O. M. *Angew Chem Int Edit* **2005**, *44*, 4745.

(52)   Luo, T. T.; Tsai, H. L.; Yang, S. L.; Liu, Y. H.; Yaday, R. D.; Su, C. C.; Ueng, C. H.; Lin, L. G.; Lu, K. L. *Angew Chem Int Edit* **2005**, *44*, 6063.

(53)   Batten, S. R.; Robson, R. *Angew Chem Int Edit* **1998**, *37*, 1460.

(54)   Gable, R. W.; Hoskins, B. F.; Robson, R. *J Chem Soc Chem Comm* **1990**, 1677.

(55)   Yaghi, O. M.; Li, H. L.; Groy, T. L. *Inorg Chem* **1997**, *36*, 4292.

(56)   Reineke, T. M.; Eddaoudi, M.; Moler, D.; O'Keeffe, M.; Yaghi, O. M. *J Am Chem Soc* **2000**, *122*, 4843.

(57)   Baerlocher, C.; Meier, W. M.; Olson, D. *Atlas of zeolite framework types*; 5th rev. ed.; Elsevier: Amsterdam ; New York, 2001.

(58)   Yaghi, O. M.; O'Keeffe, M.; Ockwig, N. W.; Chae, H. K.; Eddaoudi, M.; Kim, J. *Nature* **2003**, *423*, 705.

(59)   Eddaoudi, M.; Moler, D. B.; Li, H. L.; Chen, B. L.; Reineke, T. M.; O'Keeffe, M.; Yaghi, O. M. *Accounts Chem Res* **2001**, *34*, 319.

(60)   Li, H.; Eddaoudi, M.; Groy, T. L.; Yaghi, O. M. *J Am Chem Soc* **1998**, *120*, 8571.

(61)   Zaworotko, M. J. *Chem Commun* **2001**, 1.

(62)   Bureekaew, S.; Shimomura, S.; Kitagawa, S. *Sci Technol Adv Mat* **2008**, *9*.

(63)   Horike, S.; Shimomura, S.; Kitagawa, S. *Nat Chem* **2009**, *1*, 695.

(64)   Serre, C.; Millange, F.; Thouvenot, C.; Nogues, M.; Marsolier, G.; Louer, D.; Ferey, G. *J Am Chem Soc* **2002**, *124*, 13519.

(65)   Chalati, T.; Horcajada, P.; Gref, R.; Couvreur, P.; Serre, C. *J Mater Chem* **2011**, *21*, 2220.

(66)   Hong, X. L.; Li, Y. Z.; Hu, H. M.; Pan, Y.; Bai, J. F.; You, X. Z. *Cryst Growth Des* **2006**, *6*, 1221.

(67)   Dybtsev, D. N.; Chun, H.; Kim, K. *Angew Chem Int Edit* **2004**, *43*, 5033.

(68)   National Research Council (U.S.). Committee on Alternatives and Strategies for Future Hydrogen Production and Use.; National Academy of Engineering.; National Academy of Sciences (U.S.) *The hydrogen economy : opportunities, costs, barriers, and R&D needs*; National Academies Press: Washington, D.C., 2004.

(69)   Ball, M.; Wietschel, M. *The hydrogen economy : opportunities and challenges*; Cambridge University Press: Cambridge, UK ; New York, 2009.

(70)   http://www.eere.energy.gov/hydrogenandfuelcells/mypp.

(71)   Lochan, R. C.; Head-Gordon, M. *Phys Chem Chem Phys* **2006**, *8*, 1357.

(72)   Frost, H.; Duren, T.; Snurr, R. Q. *J Phys Chem B* **2006**, *110*, 9565.

(73)   Duren, T.; Snurr, R. Q. *J Phys Chem B* **2004**, *108*, 15703.

(74)   Sun, Y. Y.; Kim, Y. H.; Zhang, S. B. *J Am Chem Soc* **2007**, *129*, 12606.

(75)   Dinca, M.; Han, W. S.; Liu, Y.; Dailly, A.; Brown, C. M.; Long, J. R. *Angew Chem Int Edit* **2007**, *46*, 1419.

(76)   Stern, A. C.; Belof, J. L.; Eddaoudi, M.; Space, B. *Abstr Pap Am Chem S* **2007**, *233*.

(77)   Sun, D. F.; Ma, S. Q.; Ke, Y. X.; Collins, D. J.; Zhou, H. C. *J Am Chem Soc* **2006**, *128*, 3896.

(78)   Rowsell, J. L. C.; Millward, A. R.; Park, K. S.; Yaghi, O. M. *J Am Chem Soc* **2004**, *126*, 5666.

(79)   Panella, B.; Hirscher, M.; Putter, H.; Muller, U. *Adv Funct Mater* **2006**, *16*, 520.

(80)   Kaye, S. S.; Dailly, A.; Yaghi, O. M.; Long, J. R. *J Am Chem Soc* **2007**, *129*, 14176.

(81)   Dinca, M.; Long, J. R. *J Am Chem Soc* **2005**, *127*, 9376.

(82)   Spencer, E. C.; Howard, J. A. K.; McIntyre, G. J.; Rowsell, J. L. C.; Yaghi, O. M. *Chem Commun* **2006**, 278.

(83)   Zhou, W. *Chem Rec* **2010**, *10*, 200.

(84)   http://www.afdc.energy.gov/afdc/fuels/natural_gas.html.

(85)   Menon, V. C.; Komarneni, S.; Park, M.; Schmucker, M.; Schneider, H. *J Sol-Gel Sci Techn* **1998**, *11*, 7.

(86)   Lozano-Castello, D.; Alcaniz-Monge, J.; de la Casa-Lillo, M. A.; Cazorla-Amoros, D.; Linares-Solano, A. *Fuel* **2002**, *81*, 1777.

(87)   Pfeifer, P.; Burress, J. W.; Wood, M. B.; Lapilli, C. M.; Barker, S. A.; Pobst, J. S.; Cepell, R. J.; Wexler, C.; Shah, P. S.; Gordon, M. J.; Sup-Pes, G. J.; Buckley, S. P.; Radke, D. J.; Ilavsky, J.; Dillon,

A. C.; Parilla, P. A.; Benham, M. C.; Roth, M. W. *Mater Res Soc Symp P* **2008**, *1041*, 63.

(88)   Kondo, M.; Yoshitomi, T.; Seki, K.; Matsuzaka, H.; Kitagawa, S. *Angew Chem Int Edit* **1997**, *36*, 1725.

(89)   Senkovska, I.; Kaskel, S. *Micropor Mesopor Mat* **2008**, *112*, 108.

(90)   Ma, S. Q.; Sun, D. F.; Simmons, J. M.; Collier, C. D.; Yuan, D. Q.; Zhou, H. C. *J Am Chem Soc* **2008**, *130*, 1012.

(91)   Karger, B. L.; Snyder, L. R.; Horváth, C. *An introduction to separation science*; Wiley: New York,, 1973.

(92)   Yang, R. T. *Adsorbents: Fundermentals and Applications*; John Wiley & Sons, 2003.

(93)   Cavenati, S.; Grande, C. A.; Rodrigues, A. E. *Energ Fuel* **2006**, *20*, 2648.

(94)   Beenakker, J. J. M.; Borman, V. D.; Krylov, S. Y. *Chem Phys Lett* **1995**, *232*, 379.

(95)   Mueller, U.; Schubert, M.; Teich, F.; Puetter, H.; Schierle-Arndt, K.; Pastre, J. *J Mater Chem* **2006**, *16*, 626.

(96)   Bae, Y. S.; Farha, O. K.; Spokoyny, A. M.; Mirkin, C. A.; Hupp, J. T.; Snurr, R. Q. *Chem Commun* **2008**, 4135.

(97)   Kitaura, R.; Seki, K.; Akiyama, G.; Kitagawa, S. *Angew Chem Int Edit* **2003**, *42*, 428.

(98)   Bourrelly, S.; Llewellyn, P. L.; Serre, C.; Millange, F.; Loiseau, T.; Ferey, G. *J Am Chem Soc* **2005**, *127*, 13519.

(99)   Dybtsev, D. N.; Chun, H.; Yoon, S. H.; Kim, D.; Kim, K. *J Am Chem Soc* **2004**, *126*, 32.

(100)   Ribas, J.; Escuer, A.; Monfort, M.; Vicente, R.; Cortes, R.; Lezama, L.; Rojo, T. *Coordin Chem Rev* **1999**, *195*, 1027.

(101)   Wang, X. Y.; Wang, Z. M.; Gao, S. *Chem Commun* **2008**, 281.

(102)   Beltran, L. M. C.; Long, J. R. *Accounts Chem Res* **2005**, *38*, 325.

(103)   Colacio, E.; Dominguez-Vera, J. M.; Ghazi, M.; Kivekas, R.; Klinga, M.; Moreno, J. M. *Eur J Inorg Chem* **1999**, 441.

(104)   Qi, C. M.; Zhang, D.; Gao, S.; Ma, H.; He, Y.; Ma, S. L.; Chen, Y. F.; Yang, X. J. *J Mol Struct* **2008**, *891*, 357.

(105)   Guillou, N.; Livage, C.; Drillon, M.; Ferey, G. *Angew Chem Int Edit* **2003**, *42*, 5314.

(106)   Yu, C. T.; Ma, S. Q.; Pechan, M. J.; Zhou, H. C. *J Appl Phys* **2007**, *101*.

(107)   Zhang, X. X.; Chui, S. S. Y.; Williams, I. D. *J Appl Phys* **2000**, *87*, 6007.

(108)   Livage, C.; Egger, C.; Nogues, M.; Ferey, G. *J Mater Chem* **1998**, *8*, 2743.

(109)   Jain, P.; Ramachandran, V.; Clark, R. J.; Zhou, H. D.; Toby, B. H.; Dalal, N. S.; Kroto, H. W.; Cheetham, A. K. *J Am Chem Soc* **2009**, *131*, 13625.

(110)   Ferey, G.; Mellot-Draznieks, C.; Serre, C.; Millange, F.; Dutour, J.; Surble, S.; Margiolaki, I. *Science* **2005**, *309*, 2040.

(111) Huang, L. M.; Wang, H. T.; Chen, J. X.; Wang, Z. B.; Sun, J. Y.; Zhao, D. Y.; Yan, Y. S. *Micropor Mesopor Mat* **2003**, *58*, 105.

(112) Horcajada, P.; Chalati, T.; Serre, C.; Gillet, B.; Sebrie, C.; Baati, T.; Eubank, J. F.; Heurtaux, D.; Clayette, P.; Kreuz, C.; Chang, J. S.; Hwang, Y. K.; Marsaud, V.; Bories, P. N.; Cynober, L.; Gil, S.; Ferey, G.; Couvreur, P.; Gref, R. *Nat Mater* **2010**, *9*, 172.

(113) McKinlay, A. C.; Xiao, B.; Wragg, D. S.; Wheatley, P. S.; Megson, I. L.; Morris, R. E. *J Am Chem Soc* **2008**, *130*, 10440.

(114) Xiao, B.; Wheatley, P. S.; Zhao, X. B.; Fletcher, A. J.; Fox, S.; Rossi, A. G.; Megson, I. L.; Bordiga, S.; Regli, L.; Thomas, K. M.; Morris, R. E. *J Am Chem Soc* **2007**, *129*, 1203.

(115) Rieter, W. J.; Taylor, K. M. L.; An, H. Y.; Lin, W. L.; Lin, W. B. *J Am Chem Soc* **2006**, *128*, 9024.

Chapter 2   Aims of the Project

Metal Organic Frameworks (MOFs) exhibit a wide variety of structural types and chemical composition and hence a diverse range of properties leading to many different potential applications (far more so than traditional porous solids such as zeolites and activated carbon).[1-9] The overall objective of this thesis is to design and prepare novel MOFs which show new properties for different applications. Following successful synthesis of these new MOFs, various characterisation techniques will be employed to investigate their properties and subsequently be evaluated in a number of prospective applications.

Taking a closer look at the specific properties of MOFs, it is clear that their high surface area, tuneable pore architectures combined with structural flexibility makes these materials useful in such applications as adsorption, separation and purification.[7,10-13] Another aim of this project therefore, is to investigate the gas adsorption and separation properties of the synthesized MOFs in relation to their flexible chemical and structural composition.

Porous MOFs can be considered for application in healthcare and medical sectors. For example, recently MOFs have been explored for their storage and delivery of gases and pharmaceuticals.[8,14-16] Nitric Oxide (NO) has a number of well characterised immunomodulatory and antimicrobial effects.[14,17] Due to their porous nature, NO can be impregnated into MOFs and its release controlled by the structure of the MOF.[14,15] Another aim of this project is thus to synthesise MOFs

which can store and release biologically significant amounts of NO for possible use in medical applications.

In addition, research on the magnetic properties of MOFs is gaining momentum, due to their ability to host various transition metal elements in the framework.[9,18,19] By tuning the distances between the different magnetic ions via bridging ligands, MOFs can serve as unique candidates for magnetic materials. Another aim of the project therefore was to investigate any interesting magnetic properties exhibited by the novel synthesized MOFs.

2.1. References

(1)   Li, H.; Eddaoudi, M.; O'Keeffe, M.; Yaghi, O. M. *Nature* **1999**, *402*, 276.

(2)   Eddaoudi, M.; Kim, J.; Rosi, N.; Vodak, D.; Wachter, J.; O'Keeffe, M.; Yaghi, O. M. *Science* **2002**, *295*, 469.

(3)   Rowsell, J. L. C.; Yaghi, O. M. *Micropor Mesopor Mat* **2004**, *73*, 3.

(4)   Chui, S. S. Y.; Lo, S. M. F.; Charmant, J. P. H.; Orpen, A. G.; Williams, I. D. *Science* **1999**, *283*, 1148.

(5)   Murray, L. J.; Dinca, M.; Long, J. R. *Chem Soc Rev* **2009**, *38*, 1294.

(6)   Kuppler, R. J.; Timmons, D. J.; Fang, Q. R.; Li, J. R.; Makal, T. A.; Young, M. D.; Yuan, D. Q.; Zhao, D.; Zhuang, W. J.; Zhou, H. C. *Coordin Chem Rev* **2009**, *253*, 3042.

(7)   Li, J. R.; Kuppler, R. J.; Zhou, H. C. *Chem Soc Rev* **2009**, *38*, 1477.

(8)   McKinlay, A. C.; Morris, R. E.; Horcajada, P.; Ferey, G.; Gref, R.; Couvreur, P.; Serre, C. *Angew Chem Int Edit* **2010**, *49*, 6260.

(9)   Kurmoo, M. *Chem Soc Rev* **2009**, *38*, 1353.

(10)   Chen, B. L.; Ockwig, N. W.; Millward, A. R.; Contreras, D. S.; Yaghi, O. M. *Angew Chem Int Edit* **2005**, *44*, 4745.

(11)   Bureekaew, S.; Shimomura, S.; Kitagawa, S. *Sci Technol Adv Mat* **2008**, *9*.

(12)   Kondo, M.; Okubo, T.; Asami, A.; Noro, S.; Yoshitomi, T.; Kitagawa, S.; Ishii, T.; Matsuzaka, H.; Seki, K. *Angew Chem Int Edit* **1999**, *38*, 140.

(13)   Horike, S.; Tanaka, D.; Nakagawa, K.; Kitagawa, S. *Chem Commun* **2007**, 3395.

(14)   McKinlay, A. C.; Xiao, B.; Wragg, D. S.; Wheatley, P. S.; Megson, I. L.; Morris, R. E. *J Am Chem Soc* **2008**, *130*, 10440.

(15)   Xiao, B.; Wheatley, P. S.; Zhao, X. B.; Fletcher, A. J.; Fox, S.; Rossi, A. G.; Megson, I. L.; Bordiga, S.; Regli, L.; Thomas, K. M.; Morris, R. E. *J Am Chem Soc* **2007**, *129*, 1203.

(16)   Horcajada, P.; Chalati, T.; Serre, C.; Gillet, B.; Sebrie, C.; Baati, T.; Eubank, J. F.; Heurtaux, D.; Clayette, P.; Kreuz, C.; Chang, J. S.; Hwang, Y. K.; Marsaud, V.; Bories, P. N.; Cynober, L.; Gil, S.; Ferey, G.; Couvreur, P.; Gref, R. *Nat Mater* **2010**, *9*, 172.

(17)   Zhu, H. F.; Ka, B.; Murad, F. *World J Surg* **2007**, *31*, 624.

(18)   Zhang, X. X.; Chui, S. S. Y.; Williams, I. D. *J Appl Phys* **2000**, *87*,

         6007.

(19)   Livage, C.; Egger, C.; Nogues, M.; Ferey, G. *J Mater Chem* **1998**,

         8, 2743.

Chapter 3:   Techniques

3.1.   Introduction

A variety of experimental techniques were used in the synthesis and characterisation of the Metal Organic Frameworks (MOFs). The MOFs were synthesized using either hydro/solvothermal or ionothermal routes and characterised using a combination of the following techniques : X-ray diffraction, Infra-red spectroscopy (IR), Nuclear Magnetic Resonance spectroscopy (NMR), Scanning Electron Microscopy (SEM), Electron Dispersive X-ray spectroscopy (EDX), Thermogravimetric Analysis (TGA), Elemental Analysis, Inductively Coupled Plasma method (ICP), gas adsorption measurements and magnetic measurements. The main scope of this chapter is to discuss the background of these experimental techniques used in this work.

3.2.   Hydrothermal, Solvothermal and Ionothermal Synthesis

Most of the MOFs reported today are synthesized using hydrothermal or solvothermal methods. Under hydrothermal conditions, the reaction occurs at high temperatures and pressures in an aqueous medium in a closed system. In solvothermal method, the same methodology applies with non-aqueous solvent. In ionothermal synthesis, the reaction occurs at high temperatures using ionic liquids as the solvent. Since ionic liquids possess lower vapour pressures, these reactions

eliminate the dangers associated with high pressure. All the reactions were carried out in Teflon-lined stainless steel autoclaves.

3.3.   Basic Crystallography[1-4]

A crystal structure can be defined as a particular repeating arrangement of atoms (molecules or ions) and as a lattice exhibiting a long-range order and symmetry. The unit cell is the smallest repeat unit which shows the full symmetry of the crystal structure. The unit cell can be classified into 4 categories depending on the positions of the lattice points within the unit cell, (Figure 3.1). When the lattice points occupy the corners of the unit cell, the cell is known as a primitive (P) cell. If there is a lattice point in the centre of a primitive cell it is called body centred (I), if there are lattice points in the centre of each face of a primitive cell, it is called face centred (F) and if one additional lattice point at the centre of each of one pair of the cell faces of a primitive cell it is known as base centred (A, B or C).
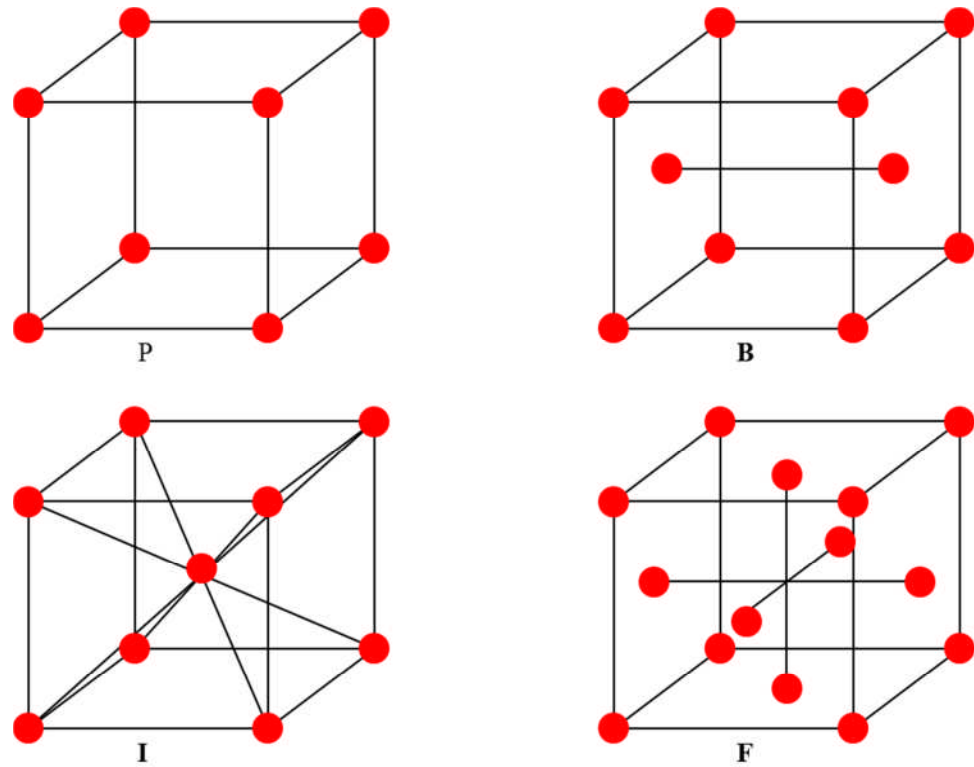
Figure 3.1. Possible Lattice point positions. (B shows the lattice point centred

on the B plane.)

The size and the shape of the unit cell is described in terms of its unit cell

parameters. These are the edge lengths (a, b and c) and the angles of the unit cell

(α, β and γ). There are 7 possible combinations of lengths and angles which give

rise to seven crystal systems (Table 3.1).

Table 3.1.   Seven Crystal Systems.

Crystal System	Lengths	Angles	Characteristic Symmetry
Triclinic	$a \neq b \neq c$	$\alpha \neq \beta \neq \gamma \neq 90°$	$1\times$ 1-fold
Monoclinic	$a \neq b \neq c$	$\alpha = \gamma = 90°$ $\beta \neq 90°$	$1\times$ 2-fold
Orthorhombic	$a \neq b \neq c$	$\alpha = \beta = \gamma = 90°$	$3\times$ 2-fold
Tetragonol	$a = b \neq c$	$\alpha = \beta = \gamma = 90°$	$1\times$ 4-fold
Trigonal	$a = b \neq c$	$\alpha = \beta = 90°$ $\gamma = 120°$	$1\times$ 3-fold
Hexagonal	$a = b \neq c$	$\alpha = \beta = 90°$ $\gamma = 120°$	$1\times$ 6-fold
Cubic	$a = b = c$	$\alpha = \beta = \gamma = 90°$	$4\times$ 3-fold

The number of lattices that can fill 2D or 3D space with periodically repeating units without leaving gaps or overlaps is limited. These so called Bravais lattices are distinct lattice types which when repeated fill the whole space. There are 14 Bravais lattices (Table 3.2) formed by a combination of the crystal systems and the lattice types. All crystal structures have translational symmetry. In addition, it is possible to have point symmetry or symmetry which has both point and translational symmetry. The elements of point symmetry which can be observed in crystal systems are rotation axes, inversion axes and mirror planes. The elements of point and translational symmetry are screw axes (rotation + translation) and glide planes (reflection + translation). These symmetry elements may occur either alone or in combination to give a total of 32 possible crystallographic point groups. The combination of possible symmetry operators

within the 14 Bravais lattices results in 230 space groups. Space groups are mathematical descriptions of the symmetry, to which all crystalline materials belong.

There is a specific notation for describing space groups: the first descriptor defines the lattice type (P, B, F, I), the following descriptors describe the point group symmetry of which the principal axis (if present) is noted first. For the remaining characters, different rules apply for different crystal systems. Each space group is fully described in the International Tables for Crystallographers.[5,6]

The asymmetric unit is the smallest part of the crystal structure which cannot be projected on to itself by applying symmetry operations. On applying symmetry operators to the asymmetric unit gives all the atomic positions within one unit cell. On repeating the unit cell this gives all atomic positions in the crystal.

Table 3.2.   Bravais Lattices and Symmetry Elements.

Bravais Lattice	Crystal System
P	Triclinic, Monoclinic, Orthorhombic, Tetragonal, Trigonal, Hexagonal, Cubic
C	Monoclinic, Orthorhombic
I	Orthorhombic, Tetragonal, Cubic
F	Orthorhombic, Cubic
Symmetry Element	**Symbol**
Centre of Inversion	-1
Mirror Plane	m
Glide Plane	a, b, c, n, d
Rotation Axis	2, 3, 4, 6
Screw Axis	2_1, 3_1, 3_2, 4_1, 4_2, 4_3, 6_1, 6_2, 6_3, 6_4, 6_5
Inversion Axis	-3, -4, -6

3.3.2. X-ray Diffraction[1-4]

As crystals have a regular repeating structure they can diffract radiation that has a wavelength similar to the interatomic distances. X-rays have a wavelength in the order of a few angstroms which is comparable to typical interatomic distance in crystalline solids. When X-rays are scattered from a crystal lattice, the scattered/diffracted beams can interfere either constructively or destructively.

Only the reflected beams that satisfy the following conditions are in phase and interfere constructively are observed. (Figure 3.2):

- The angle of incidence = angle of scattering.

- The path length difference is equal to an integer number of wavelength.
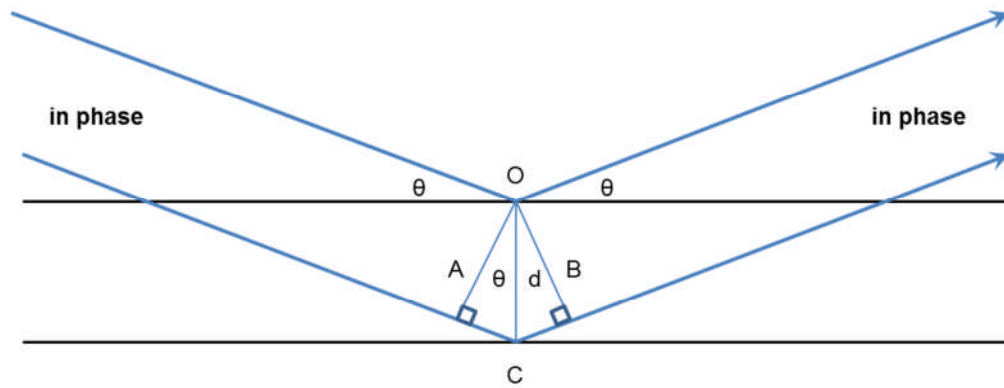
Figure 3.2:   X-rays reflecting off adjacent planes.

The relationship of the angle at which a beam of X-rays of a particular wavelength diffracts from a crystalline surface is described by Bragg's Law which is given in Equation 3.1.

2nd wave in phase after reflection only if:

$AC + CB$ is an integer multiple of λ (e.g. n λ)

Since $AC = CB$; $2AC = n\lambda$

$sin\theta = AC /d$; $AC = d\ sin\ \theta$

Therefore, $2d\ sin\theta = n\lambda$ **(3.1)**

Where;

λ = wavelength of the X-ray beam

θ = scattering angle

n = integer representing the order of the diffraction peak

d = inter-planar distance

Bragg's law shows that the diffraction angle (*sin θ*) is inversely related to the lattice spacing (*d*) in a crystalline sample.

Miller indices describe the position that the plane intersects the main crystallographic axes of the unit cell. They are defined by 3 integers (h, k and l). Combining these two approaches gives a relationship between the interplanar distance and lattice spacing. For example, for the cubic system the relationship is given by the following Equation 3.2:

$$d = \frac{a}{\sqrt{h^2 + k^2 + l^2}}$$ (**3.2**)

Where,

a = lattice spacing of the cubic crystal

h, k, l = Miller indices of the Bragg plane

Therefore by combining the Equation 2.2 with Bragg's Law (Equation 2.1), the following relation can be obtained (Equation 3.3):

$$\left(\frac{\lambda}{2a}\right)^2 = \frac{sin^2\,\theta}{h^2+k^2+l^2} \qquad\qquad \textbf{(3.3)}$$

By applying an inverse Fourier Transform to the diffraction pattern we can obtain an electron density map.

3.3.3. Single Crystal Method[1,3]

Single crystal X-ray diffraction is a non-destructive analytical technique which provides detailed information to facilitate the determination of the structure of a material. The information collected includes; crystal symmetry, unit cell dimensions, details of site-ordering, atomic positions and space group. These unit cell parameters can be used to verify if a structure is new or known in the literature by comparing this data with online databases.[7]

Rigaku SCX Mini diffractometer and Rigaku Mercury CCD diffractometer were used to collect the data presented in this thesis. When crystallite size was small, data was collected on Station 11.3.1 of the Advanced Light Source, Berkeley National Laboratory, Berkeley, CA, USA, a synchrotron radiation source.

For single crystal XRD work, a suitable crystal had to be selected; one with straight edges which extinguishes light uniformly under polarized light was chosen. The crystal is mounted in the instrument such that all orientations of the lattice planes can be accessed by changing the geometry of the incident X-rays as

well as the orientation of the crystal in relation to the detector. Once a data set is collected, the data is integrated to correct intensities for each *hkl* value. *hkl* values are assigned to each spot in the diffraction pattern. The data is also corrected for adsorption and polarization. The experimental intensity data is related to the structure factor by the following equation:

$$I \propto |F(hkl)|^2 \qquad\qquad \textbf{(3.4)}$$

The amplitude of the diffracted beams are obtained from these results however, there is no information gleaned as to the phase. This is known as the phase problem. On solving the phase problem a unique set of phases is obtained which, when combined with the structure factors, allows the diffraction data to be converted into a 3D map of electron density. There are two methods for solving the crystal structures using the electron density map, the Patterson method and direct methods.

3.3.4. Patterson Methods[1-3]

This method is usually used when the unit cell contains heavy atoms. The peaks in the Patterson map are the interatomic distances; their weights are proportional to the product of the electron densities at the tips of the vectors in the real cell. In this method, the amplitude of the square of the structure factor which is taken from the diffraction data is used to overcome the phase problem as shown in the following expression:

$$Puvw = \frac{1}{v} \sum_{hkl} |F_{hkl}|^2 \cos 2\pi \; (hu + kv + lw) \qquad\qquad (3.5)$$

3.3.5. Direct Methods[1,3]

This method is the most commonly used to determine the crystal structures. It deals with the structure factor phases directly from the observed F_{hkl} using mathematical models. This method is derived based on two main properties of electron density function. They are:

- Electron density is always positive

- It is composed of discrete atoms

The principle of positivity of electron density may be extended to three dimensions and given below:

$$s(h_1,k_1,l_1) \; s(h_2,k_2,l_2) \approx s(h_1 + h_2, \; k_1 + k_2, \; l_1 + l_2) \qquad\qquad (3.6)$$

Where,

s = sign of the phase in question.

(h_1,k_1,l_1), (h_2,k_2,l_2), $(h_1 + h_2, k_1 + k_2, l_1 + l_2)$ = strong reflections.

It is often possible to derive phases for almost all strong reflections and to determine the structure from the resulting electron density map, although there are limitations to the possible phase angles for individual reflections.

3.3.6. Structure Refinement[1]

Once a suitable model has been constructed the model is refined to a best fit of the experimental data using a least squares refinement program. The structure solution program SHELXL-97[8] has been used to carry out the least squares refinement. This program compares the calculated intensities from the structural model with the experimentally measured intensities in order to obtain the best model to minimize M:

$$M = \sum w \, (F_o^2 - F_c^2)^2 \qquad (3.7)$$

Where,

M = minimization function

w = weighing factor

F_o = Observed structure factor

F_c = Calculated structure factor

The quality of the model is determined by using various residual factors which are known as R-factors. The R-factor should attain a minimum during the refinement. The weighted R-factor is given by the following equation:

$$wR = \left[\frac{\sum w (F_o^2 - F_c^2)^2}{\sum w (F_o^2)^2} \right]^{1/2} \qquad (3.8)$$

The un-weighted residual factor R can be obtained from the F values as follows:

$$R = \frac{\sum ||F_o| - |F_c||}{\sum |F_o|} \qquad (3.9)$$

Based on F^2 the goodness of fit, GoF or S can be obtained as follows:

$$S = \left[\frac{\sum w(F_o{}^2 - F_c{}^2)^2}{(N_R - N_P)}\right]^{1/2} \qquad (3.10)$$

Where,

N_R = number of independent reflections

N_P = number of refined parameters

Once the refinement is complete the goodness of fit should be close to 1.0. A goodness of fit of $S < 1$ suggests that the model is better than the data. The R index for F should be below 5%. However it is possible to get a low R-value although the structure is not correct therefore it is always important to make sure that the structure makes chemical sense with sensible bond lengths, bond angles and site occupancy.

3.3.7. Powder X-ray Diffraction Method[2,4]

Powder X-ray diffraction is a rapid analytical technique which is used for characterisation of crystalline materials. The sample is typically a powdered (polycrystalline) material which is composed of many small crystallites, thus it is possible that more than one crystal can satisfy Bragg's law. Hence from a powder, the diffracted beams are cones of electron density reflected from the Miller planes

(hkl), which resemble rings on the screen. These rings can be indexed and integrated to obtain a powder pattern. This technique is primarily used for phase identification as the powder pattern can be seen as a finger print of a specific structure. The resultant experimental patterns recorded were compared with simulated patterns from solved single crystal data to check for sample purity. The experimental data was compared with known powder diffraction patterns in the literature to find out whether novel structures had been prepared.

Powder X-ray diffraction patterns were collected on a STOE STADI-P powder diffractometer using a copper anode, which produced monochromated X-rays at 1.5406 Å (Figure 3.3) and using synchrotron radiation in station I 11, Diamond Light Source, UK (Figure 3.4).

In a synchrotron, a high energy electron beam is accelerated in a closed orbit for a period of several hours while the beam is bent by multiple magnets to produce synchrotron light (high intensity X-rays). The required wavelength for each station is selected by a monochromator and focused by a magnetic field. Diamond Light Source is a source of synchrotron radiation in the UK. Synchrotron radiation has the following advantages: the very high intensity of X-rays and very low divergence allows smaller samples to be run over shorter time periods, tuneable wavelengths and higher degree of polarization.

a   **b**

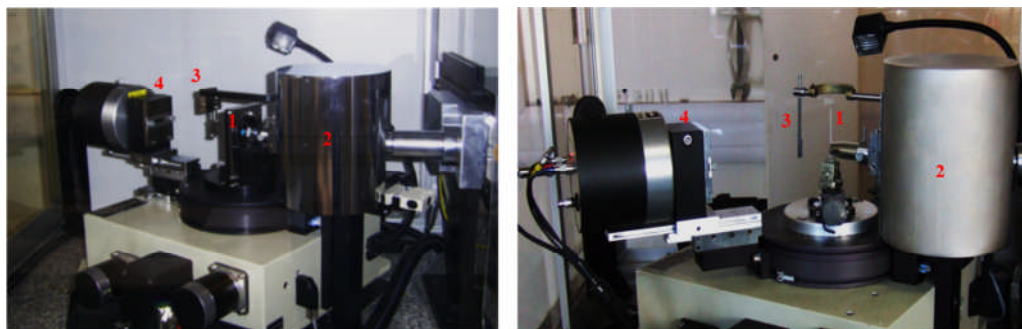**Figure 3.3.** Two of the X-ray powder diffractometers used in house. (a) for thin film discs, and (b) for glass capillaries. (1- sample holder, 2- X-ray source, 3- beam stop, 4- detector).
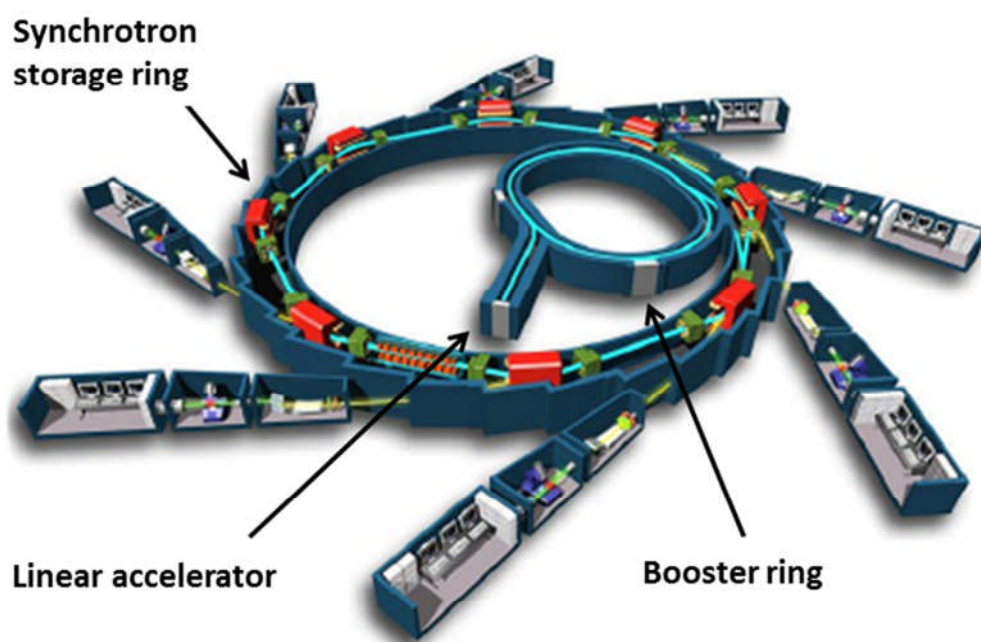

Figure 3.4. A schematic diagram of a synchrotron facility.[9]

For unknown structures, when suitable single crystals are not available then PXRD was used to determine the crystal structure of the powder. The program

DICVOL91[10] was used to index the diffraction peaks in the PXRD pattern to obtain the unit cell parameters. The indexing is used to identify the space group of the structure and this data can be input into a program EXPO2009[11] to give a structural model. This model is used by the program GSAS[12] to refine the model against the experimental data to give crystal structure parameters.

3.4.   Infrared Spectroscopy[13]

Fourier transform infrared (IR) spectroscopy is one of the most common spectroscopic techniques used by organic and inorganic chemists. Infrared radiation is passed through the sample and a detector measures the energy of the transmitted radiation. Examination of this transmitted light shows how much energy has been absorbed at each wavelength. The spectrum produced shows at which particular wavelength the sample absorbed which in turn reveals details regarding the molecular structure of the material since different functional groups absorb at known characteristic frequencies. IR is used here to determine the types of functional groups present in the MOFs.

The concept is based on the notion that most adsorptions occurring at different energies which in turn correspond to the energies involved in bond vibrations. In covalent bonds, atoms are not joined by rigid links. The two atoms are held together because both nuclei are attracted to the same pair of electrons. Such nuclei can have movements which are known as molecular vibrations. For example in a diatomic molecule the two atoms are joined by a covalent bond

which can undergo a stretching vibration where the atoms move back and forth. These stretching vibrations can be either symmetric or asymmetric (Figure 3.5). In addition to stretching vibrations, polyatomic molecules can have bending type vibrational modes (Figure 3.5).

(a) Symmetric stretch   (b) Asymmetric stretch   (c) bending
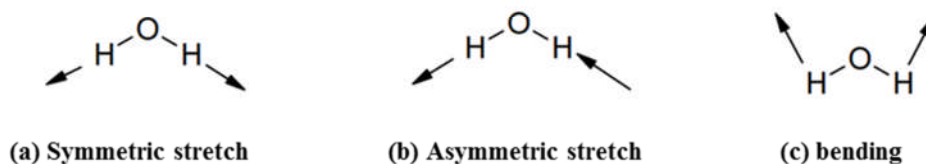
Figure 3.5.   Stretching and bending modes of H_2O molecule.

The stretching frequency of a bond is related to the masses of the two atoms involved in the bond and to the bond strength. The strength of a bond is related to its force constant. The stretching frequency of a bond in a diatomic molecule can be given in the following equation:

$$\bar{\upsilon} = \frac{1}{2\pi c}\left[\frac{f(m_1+m_2)}{m_1 m_2}\right]^{1/2}$$

(3.11)

Where,

$\bar{\upsilon}$ = frequency (cm^{-1})

c = velocity of light

f = force constant (Nm^{-1})

m_1, m_2 = masses of two atoms

In this work, IR spectra were collected on a Perkin Elmer Spectrum GX FT-IR spectrometer, 16 scans were taken using a resolution of 4 cm^{-1}. The IR spectra gave an insight into the nature of the functional groups of the organic linker molecules forming the framework structure of the MOFs. Namely, whether the carboxylic groups were free or bonded within the structure.

3.5.   Nuclear Magnetic Resonance Spectroscopy[13]

Nuclear Magnetic Resonance (NMR) spectroscopy is another form of absorption spectroscopy, whereby the energy of radio waves are absorbed by nuclei in the molecule, when placed in a strong magnetic field. The interaction of the nuclei with the magnetic field results in a transition between nuclear spin states. Not all nuclei however have nuclear spin. Some nuclei have integral spins (e.g. $I = 1, 2, 3$), some have fractional spins (e.g. $I = 1/2, 3/2, 5/2$), and a few have no spin, $I = 0$ (e.g. ^{12}C, ^{16}O, ^{32}S). It is only the nuclei which have nuclear spin that show the NMR phenomenon and give rise to a NMR spectrum. The nuclear spin of a particular isotope can be described in terms of its spin quantum number I and will have $2I + 1$ orientations. A nucleus with spin ½ will have 2 possible orientations. In the absence of an external magnetic field, these orientations are of equal energy whereas in a presence of a magnetic field these energy levels split (Figure 3.6). Each level is given a magnetic quantum number, m.
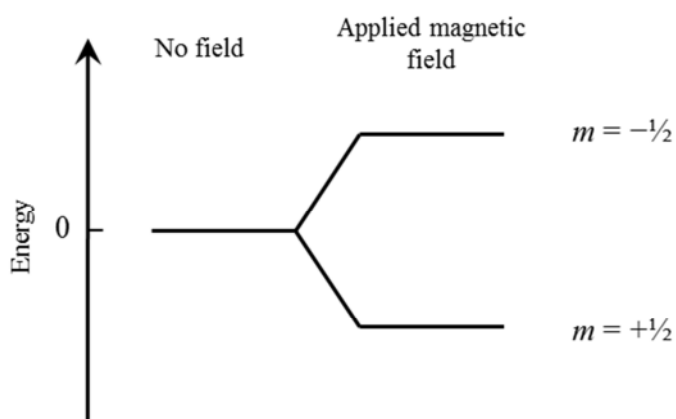
Figure 3.6.   Energy levels for a nucleus with spin quantum number ½.

This energy difference (ΔE) is a function of the strength of the applied magnetic field B_0. The stronger the applied field, the greater is the energy differences between the two spin states. This energy difference is given by the following equation:

$$\Delta E = \left(\frac{h}{2\pi}\right) \gamma B_0$$

(3.12)

Where; h = Planck's constant and γ = magnetogyric ratio of the nucleus.

The frequency of the radiation (ν) that is required to bring about spin flipping or nuclear magnetic resonance can be given by:

$$\nu = \left(\frac{1}{2\pi}\right) \gamma B_0$$

(3.13)

NMR spectroscopy is an important physical technique which is widely used to obtain chemical and structural information. The technique can be used to glean structural information in both solution and in the solid state. Both solution and solid state NMR techniques were used in the course of this research to analyse various structural features of MOFs. NMR was also used to determine the purity of the ionic liquids prepared.

3.5.1. Solution Phase NMR

Bruker Avance 300 and Bruker Avance II 400 spectrometers were used to analyse the samples. These two spectrometers operate at frequencies of 300 MHz and 400 MHz respectively. Topspin 2 NMR software was used to analyse the data collected from these spectrometers. In this work, solution phase NMR was useful in the characterisation and phase purity of the ionic liquids and ligands.

3.5.2. Solid State NMR Techniques[13]

Most of the MOFs prepared are insoluble in typical NMR solvents, thus solid state NMR proved to be a very useful technique for MOF characterization. Broad peaks are typically observed in solid state NMR spectra due to the anisotropic effects or orientation dependent-interactions. However these effects can be supressed by introducing artificial motion on the solid. This technique involves spinning the solid sample rapidly at an angle of 54.7º (magic angle) to the magnetic field. This is known as ''magic-angle spinning'' and it is used to make the line widths

narrower. A 600 MHz Bruker Avance III solid state spectrometer was used in this work to characterize the functional groups (e.g. presence of ester groups) present in different MOFs.

3.6.   Scanning Electron Microscopy and Energy Dispersive X-ray Spectroscopy

The Scanning Electron Microscope (SEM) uses a focused beam of high energy electrons to scan the surface of a solid specimen. The electrons interact with the atoms at the surface producing signals which allows an image to be created by analysis of the secondary and backscattered electrons. The electron-sample interactions reveal information regarding morphology, composition and electrical conductivity of the surface of the sample. SEM has many advantages over traditional light microscopes: higher magnification as well as higher resolution and a larger depth of field yielding a characteristic three-dimensional appearance useful for understanding the surface structure of a sample.

The interaction of an electron beam with a sample produces a variety of emissions including X-rays, these X-rays can be used to determine the abundance of specific elements in the sample. This technique is known as Energy Dispersive X-ray Spectroscopy. The X-rays generated are from a region about 2 microns in depth and thus EDX is not a surface science technique. The elemental ratios can be determined from the spectra and hence this data can be used to examine the level of doping of metals into the MOF structures.

3.7. Thermogravimetric Analysis and Thermogravimetry Coupled with Mass Spectrometry

Thermogravimetric analysis (TGA) measures the mass change in a sample as a function of temperature, under a controlled atmosphere. It provides a quantitative measurement of the mass changes in a material associated with both material transitions and thermal degradation and thus can be used in the determination of the thermal stability and decomposition products of a material. The instrument used was a TA Instruments NETZSCH TG 209 cell with simultaneous TGA/DTA furnace. Samples were heated at a rate of 10 °C min^{-1} to a maximum temperature of 600 °C in a flowing atmosphere of argon. In this work TGA was used to analyse the mass changes occurring on the degradation of the MOF structure.

Though the TGA which combines with differential thermal analysis (DTA) is widely used for material characterisation, it is a limited technique as it cannot distinguish the actual nature of the material evolved in the course of the process and it is not easy to resolve overlapped thermal events. Therefore a large number of gas analytical techniques such as FT-IR, Gas Chromatography and Mass spectroscopy are used for interfacing with TGA. Thermogravimetry coupled with mass spectrometry (TG-MS) was also accompanied in this work in order to understand the actual material evolved at different temperatures. TG-MS was performed on STA 449 C NETZSCH thermal analysis instrument coupled with Thermostar PFEIFFER vacuum mass spectrometer. Especially this technique was very useful in order to analyse the liquid phase experiments carried out for

STAM-1. It provided solid proof that STAM-1 is capable of adsorbing different liquids (for example hexane and methanol or hexane and water) at the same time.

3.8.   Elemental Analysis

Elemental analysis has been used to elucidate the empirical formula of the MOF structures. Two different techniques have been employed to determine the complex formulation of these MOFs, the organic component by CHN analysis and the metal content by ICP.

3.8.1 CHN Analysis

CHN has been used to quantify the percentage amounts of carbon, nitrogen and hydrogen in the MOF structures. CHN analysis was performed using a Carlo Erba EA1110 analyser. Typical sample mass was 50 mg.

3.8.2 Inductively Coupled Plasma

Inductively Coupled Plasma (ICP) is an analytical technique which can be used to determine the quantity of each metal present in a sample. This is a highly sensitive technique which can provide information in the ppm range. In this work an ICP-MS Agilent 7500 series instrument was used with New Wave UP-213 Laser Ablation system. ICP was conducted by mixing the samples with Teflon.

ICP was used in the determination of the empirical formulae of the different MOF materials, especially effective in evaluating the quantity of doping levels in the mixed metal materials.

3.10. Gas and Vapour Adsorption[14-16]

At a gas/solid interface, the excess concentration of gas at the surface is referred to as being adsorbed and the solid is known as the adsorbent and the gas as adsorbate. In the case of porous adsorbents, gas molecules can diffuse through the pores and adsorb on the walls, with the amount of gas adsorbed being dependant on a number of parameters namely, temperature, pressure, chemical and physical properties of both adsorbate and adsorbent. Gas molecules can also penetrate through the surface. This is known as absorption. A process combining both absorption and adsorption is called sorption.

Some definitions: physisorption is an interaction via van der Waals forces of adsorbate and adsorbent and chemisorption is a chemical reaction between adsorbate molecules and the array of surface atoms. In addition, there are some other key differences differentiating physisorption and chemisorption:

- In physisorption, the heat of adsorption is of the same order of magnitude as the heats of condensation of gases whereas for chemisorption it is the heats of chemical reactions.
- The rate of adsorption in physisorption is rapid whereas in chemisorption the rate is dependent on the energy of activation of the chemical reaction.

- The adsorption isotherm in chemisorption is always a unimolecular process whereas in physisorption it can be either a unimolecular or multimolecular process.

The measurement of adsorption of gases and vapours is widely used to determine properties such as the surface area, pore volume and pore size distribution of solids. There are two different ways in which the gas or vapour adsorption can be measured, namely volumetrically or gravimetrically.   In a volumetric measurement the amount of adsorption is determined by measuring the volume the gas occupies, this is obtained by the pressure difference before and after the data point. In a gravimetric measurement the increase in the weight of the sample is correlated to the amount of gas or vapour adsorbed. The experimental measurements of the amount adsorbed, v, as a function of pressure and temperature can be plotted in the form of an adsorption isotherm as expressed in the following equation:

$$v = f(P)_T \qquad\qquad\qquad (3.14)$$

The adsorption isotherms have been classified into 5 types by Brunauer *et al*.[13] The adsorption of gas on a solid typically will follow one of these adsorption isotherms shown in Figure 3.7. Adsorption isotherms are plotted as an equivalent volume at standard pressure against the equilibrium pressure (P/P_0) at constant temperature.
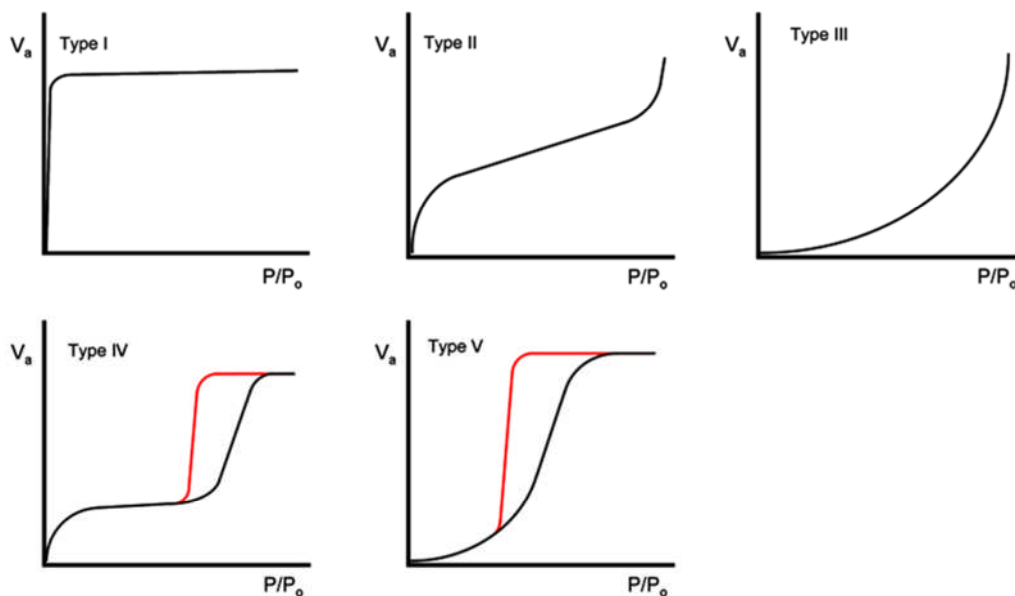
Figure 3.7.   The five types of physical adsorption isotherms classified by Brunauer. The red lines indicate desorption hysteresis loops for Types IV and V.

Type I shown in Figure 3.7 is associated with systems where adsorption does not proceed beyond a monomolecular layer. All other types involve multilayer adsorption, types II and III are characteristic of multilayer adsorption onto open surfaces and types IV and V are characteristic of multilayer adsorption on highly porous solids.

3.10.1.   Determination of Surface Area and Porosity

A Micromeritics ASAP 2020 surface area and porosity analyser was used for all nitrogen adsorption experiments. ∼ 0.1 g of sample was degassed at 393 K under vacuum for 3 hours prior to N_2 adsorption. All the N_2 adsorption experiments were then carried out at 77 K and results were analysed using Langmuir and BET theories.

3.10.1.1.   Langmuir Theory[14-16]

Whenever a gas is in contact with a solid, equilibrium will be established between the gaseous phase and the adsorbed gases bound on the surface of the solid. The Langmuir theory describes the relationship between the number of active sites for adsorption on the surface as a function of pressure. The surface coverage can be calculated by the Langmuir equation which states:

$$\theta = \frac{KP}{1+KP} \qquad\qquad (3.15)$$

The same equation can be expressed in terms of pressure:

$$\frac{P}{V} = \frac{P}{V_{mono}} + \frac{1}{KV_{mono}} \qquad\qquad (3.16)$$

However, the Langmuir equation is more applicable to chemisorption than physisorption as it assumes that the gas will only form a monolayer on the solid.

Moreover for the Langmuir equation to give an accurate measurement, the adsorbed gas has to behave ideally in the vapour phase, which can be fulfilled only at low pressures.

3.10.1.2.   BET Theory[14,16]

BET theory, proposed by Brunauer, Emmett and Teller is an extension of the Langmuir theory as it incorporates the concept of multimolecular layer adsorption. The BET equation is given below:

$$\frac{x}{v(1-x)} = \frac{1}{v_{mon}c} + \frac{x(c-1)}{v_{mon}c} \qquad (3.17)$$

where, $x = P/P_0$, v is the STP volume of adsorbate, v_{mon} is STP volume of the amount of adsorbate required to form a monolayer, c is the equilibrium constant.

A key assumption used in deriving the BET equation is that the successive heats of adsorption for all layers except the first are equal to the heats of condensation of the adsorbate. It also assumes that there are no lateral interactions between adsorbed species. Hence, BET theory models the process of physisorption better than the Langmuir theory although it is generally still not a good model for adsorption on microporous materials.

3.10.2.   Adsorption/Desorption of NO and CO_2

Adsorption and desorption of NO gas on samples was measured using a gravimetric adsorption system. A CI Instruments microbalance was thermally stabilized to eliminate effects from the external environment. The microbalance had a sensitivity of 0.1 μg and a reproducibility of 0.01% of the load. The sample (~25 mg) was initially degassed at 393 K under a pressure of 1×10^{-4} mbar until no further mass loss was observed. The sample temperature was decreased to 298 K and thereafter remained constant at 298 K throughout the experiment. The counterbalance temperature was kept the same as that of the sample in order to minimize the influence of temperature differences on the mass readings. The sample temperature was monitored using a K-type thermocouple located close to the sample bucket (<5 mm). The variation in sample temperature was minimal (<0.1 K). In the NO adsorption procedure, NO gas was introduced into the adsorption system until the desired pressure was achieved. The mass uptake of the sample was measured as a function of time until adsorption equilibrium was achieved and this was plotted as an adsorption isotherm. Desorption isotherm of the NO gas adsorbed in the sample was obtained by gradually decreasing the system pressure to 2×10^{-2} mbar and noting the sample mass.

CO_2 measurements were carried out using a similar procedure. In this case after activating the sample to 393 K, the sample temperature was decreased to 273 K and kept constant throughout the experiment.

3.10.3.   Measurement of NO Release by Chemiluminescence

Sievers NOA 280i chemiluminescence Nitric Oxide analyser was used to determine the amount of NO that could be recovered from a MOF. It has a highly sensitive detector for NO based on ozone-chemiluminescence technology. NO release was measured by passing nitrogen gas of known humidity over the sample. The resultant gas was then directed to the analyser to determine the concentration of NO. The concentration was recorded as parts per million (PPM) or parts per billion (PPB). The flow rate of N_2 was set to 200 mL/min with a cell pressure of 8.5 Torr and an oxygen pressure of 6.1 psig.

3.10.4.   Isosteric Heats of Adsorption[14-16]

When the addition of the differential amount of component i dn_i^{σ} or dn_i^{s} effected at constant pressure p, the differential molar enthalpy of adsorption, $\Delta_a H_i^{\sigma}$ or $\Delta_a H_i^{s}$ also called the isosteric enthalpy of adsorption (q^{st}) is defined as:

$$\Delta_a H_i^{\sigma} = - q^{st,\sigma} = U_i^{\sigma} - H_i^{g} \tag{3.18}$$

$$\Delta_a H_i^{s} = - q^{st,\sigma} = U_i^{\sigma} - H_i^{g} \tag{3.19}$$

Where, $H_i^{s} = (\partial H^{s}/\partial n_i^{s})T,p,m,n_j^{s}$ and H_i^{g} is the partial molar enthalpy of component i in the gas phase.

Gas adsorption is an exothermic process whereas desorption is an endothermic process. The temperature change of the adsorbent during the adsorption and desorption process is known as the isosteric heat of adsorption. This value gives an insight into understanding the type of interactions taking place between the adsorbate and adsorbent as well as to the kinetics of the process and a measure of the adsorption equilibrium. Experimentally it can be determined using calorimetric methods. Isosteric heats of adsorption of the components of a gas mixture are used as key thermodynamic values for the design of practical gas separation processes such as pressure swing and thermal swing adsorption.

3.11. Magnetism[17]

Magnetic fields are created by the movement of the protons and electrons in the atom. The hydrogen atom has a net nuclear spin which creates a magnetic field, as does electron spin and also a magnetic field arises due to the electron moving around the nucleus.

Some atoms show a zero net magnetic moment due to the pairing up of all the electrons, this pairing effectively cancels the moments. Materials that show no net magnetic moment are called diamagnetic materials. Most materials have one or more unpaired electrons and therefore exhibit some magnetism. The magnitude of the magnetic moment is the magnetic flux density (B) of a material which is given by Equation 3.20.

$$B = \mu H \qquad\qquad (3.20)$$

Where,

B = Magentic flux density

H = Field Strength

μ = absolute permeability of the medium

The magnetic susceptibility of a material is the degree of magnetization shown by a material when an external magnetic field is applied. The magnetic susceptibly is given by Equation 3.21.

$$M = \chi H \qquad\qquad (3.21)$$

Where,

M = intensity of magnetization induced by H

χ = Magnetic susceptibility

Experimentally, the magnetic susceptibility is measured as a function of temperature. The data obtained is then corrected for diamagnetic interactions using Pascal constants. The data can then be used to describe the type of magnetic interactions occurring in the material. The types of magnetic interactions can be classified as paramagnetic, ferromagnetic, antiferromagnetic and ferrimagnetic. Paramagnetic materials are those with unpaired electron spins, where each atom acts independently, resulting in relatively weak magnetic properties. Ferromagnetic materials also have unpaired electron spins but the magnetic

moment of each atom is coupled to the others such that the electrons become parallel. A spontaneous magnetization can be seen in these materials even in absence of an external field. Antiferromagnetic materials contain unpaired electrons which are held in such an alignment that results in an equal number of spins in each direction, therefore there is no net magnetization. Lastly, in ferrimagnetic materials the arrangement of spins are similar to antiferromagnetic materials but the sub lattices have unequal magnetic moments, this results in high magnetic susceptibilities in these materials.

3.11.1.   Magnetic measurements

The magnetic measurements were carried out on a Quantum Design MPMS SQUID magnetometer. A SQUID magnetometer measures the magnetic moment of a material from which the magnetization and magnetic susceptibility can be determined. It is highly sensitive to the magnetic changes occurring in the sample as a function of temperature when an external magnetic field is applied.

Data was collected in a field of 5000 Oe in the temperature range 2 to 300 K and from 300K to 2 K in 5 K steps. The data was recorded using zero field cooling (ZFC) as well as field cooling (FC) cycles. All data sets were corrected for diamagnetism through the use of Pascal constants.

3.12. References

(1)   Müller, P. *Crystal structure refinement : a crystallographers guide to SHELXL*; Oxford University Press: Oxford ; New York, 2006.

(2)   West, A. R. *Basic solid state chemistry*; 2nd ed.; John Wiley & Sons: New York, 1999.

(3)   Bennett, D. W. *Understanding single-crystal x-ray crystallography*; Wiley-VCH: Weinheim, 2010.

(4)   Clegg, W. *Crystal structure determination*; Oxford University Press: Oxford ; New York, 1998.

(5)   Hahn, T.; International Union of Crystallography. *International tables for crystallography. Brief teaching edition of volume A, Space-group symmetry*; 3rd, rev. and enl. ed.; Published for the International Union of Crystallography by Kluwer Academic Publishers: Dordrecht ; Boston, 1993.

(6)   Hahn, T.; Shmueli, U.; Wilson, A. J. C.; International Union of Crystallography. *International tables for crystallography*; D. Reidel Pub. Co. ;

        Sold and distributed in the U.S.A. and Canada by Kluwer Academic Publishers Group: Dordrecht, Holland ; Boston, U.S.A.Hingham, MA, 1984.

(7)   Fletcher, D. A.; McMeeking, R. F.; Parkin, D. *J Chem Inf Comp Sci* **1996**, *36*, 746.

(8)   Farrugia, L. J., p WinGX Version 1.70.01.

(9)   Synchrotron Soleil, p Schéma de Principe Copyright © Chaix &
        Morel et Associés.

(10)   Dichotomy, D. L., R. Shirley, p DICVOL91.

(11)   A. Altomare, M. C., Cuocci, C. Giacovazzo, A. Moliterni, R. Rizzi
        2009, p Expo2009 version 1.9.10.

(12)   Dreele, A. C. L. a. R. B. V.; Los Alamos National Laboratory
        Report LAUR 86-748 (1994). p General Structure Analysis System
        (GSAS).

(13)   Brisdon, A. K. *Inorganic spectroscopic methods*; Oxford
        University Press: Oxford ; New York, 1998.

(14)   Brunauer, S. *The adsorption of gases and vapors*; Princeton
        University Press;

        H. Milford: Princeton, London,, 1943.

(15)   Miller, A. R. *The Adsorption of Gases on Solids*; Cambridge
        University Press, 1949.

(16)   Crowell, D. M. Y. a. A. D. *Physical Adsorption of Gases*; Butter
        Worths, 1962.

(17)   Blundell, S. *Magnetism in condensed matter*; Oxford University
        Press: Oxford ; New York, 2001.

Chapter 4   Experimental

4.1. General Procedure

All Metal Organic Frameworks were synthesised using hydrothermal, solvothermal or ionothermal synthetic methods in an oven at temperatures above 100 ºC using Teflon-lined stainless steel sealed autoclaves unless otherwise stated. All chemicals were purchased from commercial sources and used without further purification.

4.2. Synthetic procedure of STAM-1

2.0 mmol of $Cu(NO_3)_2.3(H_2O)$ (0.483 g) and 2.0 mmol of 1,3,5-Benzenetricarboxylic acid (H_3BTC) (0.421 g) were dissolved in 20 ml of $MeOH/H_2O$ (50:50) solution in a Teflon-lined steel autoclave. The solution was stirred for 15 minutes at ambient temperature prior to be heated in an oven preheated at 383 K, followed by heated at 383 K for 7 days. After the reaction, the autoclave was naturally cooled down to room temperature. Large blue crystals were isolated by Buchner filtration, washed with water and acetone and dried in air. The yield was 95%.

4.3.   Synthetic procedure of Cu/Zn STAM-1

2.0 mmol of $Cu(NO_3)_2.3(H_2O)$ (0.483 g), 2.0 mmol of $Zn(NO_3)_2.6(H_2O)$ (0.595 g) and 4.0 mmol of 1,3,5-Benzenetricarboxylic acid (H_3BTC) (0.842g) were dissolved in 20 ml of $MeOH/H_2O$ (50:50) solution in a Teflon-lined steel autoclave. This solution was stirred for 15 minutes at ambient temperature prior to be heated in an oven preheated at 383 K, followed by heated at 383K for 7 days. After the reaction, the autoclave was naturally cooled down to room temperature. Large blue crystals were isolated by Buchner filtration, washed with water and acetone and dried in air.

4.4.   Synthetic procedure of STAM-2

STAM-1 solids were suspended in water and irradiated with ultrasound for 260 min (Branson Digital Sonifier 250, 20 KHz ultrasound, 50% intensity pulsed at 3 secs on, 1 sec off). The resultant blue nanoparticulate powder was recovered by centrifugation.

4.5.   Synthetic procedure of STAM-3

2.0 mmol of $Cu(NO_3)_2.3(H_2O)$ (0.483 g) and 2.0 mmol of 1,3,5-benzenetricarboxylic acid (0.421 g) were dissolved in 20 ml of $MeOH/H_2O$ (50:50) and irradiated with ultrasound for 64 min (Branson Digital Sonifier 250,

20 KHz ultrasound, 50% intensity pulsed at 3 secs on, 1 sec off). The resultant blue nanoparticulate powder was recovered by centrifugation.

4.6.　Synthetic procedure of In-BDC MOF

This MOF was synthesized using the method as described in the literature.[1] 0.50 mmol of $In(NO_3)_3.5H_2O$ (0.195 g), 1.50 mmol of 1,3,4-benzenetricarboxylic acid (0.316 g) and 3.0 mmol piperazine (0.258 g) were dissolved in 10 mL of water in a Teflon-lined steel autoclave. This solution was stirred for 15 minutes at ambient temperature prior to be heated in an oven preheated at 443 K, followed by heated at 443 K for 2 days. After the reaction, the autoclave was naturally cooled down to room temperature. The resultant off white solid was isolated by Buchner filtration, washed with water and acetone and dried in air.

4.7.　Synthetic procedure of STAM-6

1.0 mmol of $(CH_3CO_2)_2Ni \cdot 4H_2O$ (0.248 g), 1.0 mmol of pyromellitic dianhydride (0.218 g) and 2.0 mmol of 4,4' bipyridine (0.312 g) were dissolved in 20 mL of MeOH in a Teflon-lined steel autoclave. This solution was stirred for 15 minutes at ambient temperature prior to be heated in an oven preheated at 383 K, followed by heated at 383 K for 24 h. After the reaction, the autoclave was naturally cooled down to room temperature. Blue crystals were isolated by Buchner filtration, washed with water and acetone and dried in air.

4.8.   Synthetic procedure of STAM-7

1.0 mmol of 1,3,5-tris(4-carboxyphenyl)benzene (H$_3$BTB) (0.438 g) and 1.0 mmol of Cu(NO$_3$)$_2$.3(H$_2$O) (0.241.5 g) were dissolved in 10 mL of MeOH/H$_2$O (50:50) solution in a Teflon-lined steel autoclave. This solution was stirred for 15 minutes at ambient temperature prior to be heated in an oven preheated at 383 K, followed by heated at 383 K for 7 days. After the reaction, the autoclave was naturally cooled down to room temperature. Small bluish green crystals were isolated by Buchner filtration, washed with water and acetone and dried in air.

4.9.   Synthetic procedure of STAM-8

3.0 mmol of (CH$_3$CO$_2$)$_2$Cu·H$_2$O (0.597 g) and 1.0 mmol of 1,3,5-benzenetricarboxylic (0.210 g) acid were dissolved in 15 mL of pyridine in a Teflon-lined steel autoclave. The mixture was first acidified to pH 5 using few drops of HCl and stirred for 15 minutes at ambient temperature prior to be heated in an oven preheated at 383 K, followed by heated at 383 K for 7 days. After the reaction, the autoclave was naturally cooled down to room temperature. Blue crystals were isolated by Buchner filtration, washed with water and acetone and dried in air.

4.10. Synthetic procedure of STAM-9

3.0 mmol of Cu(NO$_3$)$_2$.3(H$_2$O) (0.716 g), 1.0 mmol of 1,3,5-benzenetricarboxylic acid (0.210 g) and 1.0 mmol of 4,4-bipyridine (0.158 g) were dissolved in 10 mL of ethanol in a Teflon-lined steel autoclave. This solution was stirred for 15 minutes at ambient temperature prior to be heated in an oven preheated at 383 K, followed by heated at 383K for 7 days. After the reaction, the autoclave was naturally cooled down to room temperature. Bluish green crystals were isolated by Buchner filtration, washed with water and acetone and dried in air.

4.11. Synthetic procedure of STAM-10

3.0 mmol of Zn(NO$_3$)$_2$.6(H$_2$O) (0.892 g), 1 mmol of 1,4-benzenedicarboxylic acid (0.166 g) and 1 mmol of 4,4-bipyridine (0.156 g) were dissolved in 20 mL of EtOH/H$_2$O (50:50) in a Teflon-lined steel autoclave. This solution was stirred for 15 minutes at ambient temperature prior to be heated in an oven preheated at 383 K, followed by heated at 383K for 3 days. After the reaction, the autoclave was naturally cooled down to room temperature. Colourless crystals were isolated by Buchner filtration, washed with water and acetone and dried in air.

4.12. Synthetic procedure of STAM-11

2.0 mmol of Zn(NO$_3$)$_2$.6(H$_2$O) (0.594 g) and 1.0 mmol of 1,4-Benzenedicarboxylic acid (0.166 g) were mixed with 4.5 g of EMIMBr in a

Teflon-lined steel autoclave. The mixture was then heated at 423 K for 3 days . After crystallization the autoclave was naturally cooled down to room temperature. Colourless crystals were isolated by Buchner filtration, washed with ethanol and dried in air.

4.13. Separation of 1,3,5-Benezenetricarboxylic Acid, Monomethyl Ester

5-Methoxycarbonylbenzene-1,3-dicarboxylic acid (mmBTC) was extracted from STAM-1 by the following procedure. 3.50 g of STAM-1 was suspended in 50 ml of water. Under stirring, 17.5 ml of 1 M NaOH was added slowly dropwise and the mixture was allowed to stir for 5 h. The solution was filtered and white powder was recovered. Since NaOH was used in the reaction the product obtained was the sodium salt of the 5-Methoxycarbonylbenzene-1,3-dicarboxylic acid (Na_2mmBTC). The yield was 70 %.

4.14. Synthetic procedure of Co-Na_2mmBTC

2.0 mmol of $Co(NO_3)_2.6(H_2O)$ (0.582 g) and 1.0 mmol of Na_2mmBTC (0.268 g) were dissolved in 20 mL of MeOH/H_2O (50:50) solution in a Teflon-lined steel autoclave. The solution was stirred for 15 minutes at ambient temperature prior to be heated in an oven preheated at 383 K, followed by heated at 383 K for 3 days. After the reaction, the autoclave was naturally cooled down to room temperature.

A pink product was recovered by Buchner filtration, washed with water and acetone and dried in air.

4.15. Synthetic procedure of Ni-Na$_2$mmBTC

2.0 mmol of Ni(NO$_3$)$_2$.6(H$_2$O) (0.581 g) and 1.0 mmol of Na$_2$mmBTC (0.268 g) were dissolved in 14 mL of MeOH/H$_2$O (50:50) solution in a Teflon-lined steel autoclave. The solution was stirred for 15 minutes at ambient temperature prior to be heated in an oven preheated at 383 K, followed by heated at 383 K for 7 days. After the reaction, the autoclave was naturally cooled down to room temperature. Bluish green crystals were isolated by Buchner filtration, washed with water and acetone and dried in air.

4.16. Synthetic procedure of Zn-Na$_2$mmBTC

2.0 mmol of Zn(NO$_3$)$_2$.6(H$_2$O) (0.595 g) and 1.0 mmol of Na$_2$mmBTC (0.268 g) were dissolved in 20 mL of EtOH/H$_2$O (50:50) solution in a Teflon-lined steel autoclave. The solution was stirred for 15 minutes at ambient temperature prior to be heated in an oven preheated at 383 K, followed by heated at 383 K for 24 h. After the reaction, the autoclave was naturally cooled down to room temperature. A white crystalline product was recovered by Buchner filtration, washed with water and acetone and dried in air.

4.17. Synthetic procedure of Cu-Na₂mmBTC

2.0 mmol of Cu(NO₃)₂.3(H₂O) (0.483 g) and 1.0 mmol of Na₂mmBTC (0.268 g) were dissolved in 14 mL of EtOH/H₂O (50:50) solution in a Teflon-lined steel autoclave. The solution was stirred for 15 minutes at ambient temperature prior to be heated in an oven preheated at 383 K, followed by heated at 383 K for 3 days. After the reaction, the autoclave was naturally cooled down to room temperature. Small blue crystals were isolated by Buchner filtration, washed with water and acetone and dried in air.

4.18. Synthesis of Ionic liquids

Ionic liquids were prepared according to Literature procedures.[2]

4.18.1.   Preparation of 1-Ethyl-3-methylimidazolium Bromide

45.30 g of 1-methylimidazole (0.59 mol) was placed in a two-necked 500 mL round bottom flask which was equipped with a reflux condenser. 70.9 g of Bromoethane (0.65 mol) was then transferred slowly into the flask as this addition gave rise to an increase in temperature. The resulting solution was stirred for 30 mins and then refluxed for 3 h. After cooling the reaction mixture to room temperature, it was washed with ethyl acetate (5 X 40 ml) to remove any unreacted starting material. The volatile materials were removed under high vacuum to obtain the product.

4.18.2.   Preparation of 1-Butyl-3-methylimidazolium Bromide

76.23 g of 1-methylimidazole (0.90 mol) was placed in a two-necked 500 mL round bottom flask which was equipped with a reflux condenser. 130.0 g of Bromobutane (slightly higher than 0.90 mol) was then transferred slowly into the flask as this addition gave rise to an increase in temperature. The resulting solution was stirred for 30 mins and then refluxed for 3 h. After cooling the reaction mixture to room temperature, it was washed with ethyl acetate (5 X 40 ml) to remove any unreacted starting material. The volatile materials were removed under high vacuum to obtain the product.

4.18.3.   Preparation   of   1-Isopropyl-3-methylimidazolium Bromide

50.0 g of 1-methylimidazole (0.61 mol) was placed in a two-necked 500 mL round bottom flask which was equipped with a reflux condenser. 79.90 g of Bromopropane (0.65 mol) was then transferred slowly into the flask as this addition gave rise to an increase in temperature. The resulting solution was stirred for 30 mins and then refluxed for 7 h. After cooling the reaction mixture to room temperature, it was washed with ethyl acetate (5 X 40 ml) to remove any unreacted starting material. The volatile materials were removed under high vacuum to obtain the product.

4.19. References

(1)   Han, Z. B.; Song, Y. J.; Ji, J. W.; Zhang, W.; Han, G. X. *J Solid State Chem* **2009**, *182*, 3067.

(2)   Bonhote, P.; Dias, A. P.; Papageorgiou, N.; Kalyanasundaram, K.; Gratzel, M. *Inorg Chem* **1996**, *35*, 1168.

Chapter 5 Synthesis and Characterisation of STAM-1 and Related Materials

5.1. Introduction

As described in Chapter 1 the *in situ* ligand synthesis is of growing interest as a new approach for the synthesis of Metal Organic Frameworks. The simplicity, effectiveness and environmentally friendliness have made it a promising approach in the preparation of MOF compounds. Since hydrothermal reactions occur at relatively strong conditions it has more chances to undergo some of the *in situ* ligand reactions than the conventional synthetic methods. Many different types[1-5] of *in situ* ligand reactions have been found to date and as mentioned in Chapter 1 some of the ligands obtained from this approach are not easy to synthesize using the conventional organic synthetic methods.[6] The other important feature of the *in situ* approach is the ease of obtaining the ligand isomers.[7] Some of the organic ligands exist in isomeric form. Therefore usually during the synthesis of these ligands all the isomers will be resulted with a need of separation. But interestingly, only one of these isomers might arise from the *in situ* synthesis of the metal complex, which simplifies the synthesis by providing an alternative pathway to isolate the ligand isomers. For example *in situ* cyclisation reaction of 1,2-trans-(4-piridyl)ethane (bpe) to yield 1,2,3,4-tetrakis(4-pyridyl)cyclobutane (tpct) has produced only a single isomer of the tpct ligand.[7]

In the preparation of coordination complexes, the *in situ* ligand approach is suitable to obtain novel MOFs with beautiful topologies and excellent properties, directly from metal ions and organic precursors which might not be accessible from a direct reaction of metal salts and ligands. However, it is still difficult to anticipate the target organic compounds and the structural topologies of MOFs generated by *in situ* reactions.

5.2.   Synthesis of STAM-1

There are many examples of the use of 1,3,5-Benzenetricarboxilic acid (BTC) in the preparation of MOFs, utilising many different metals. Copper (II) ions in combination with BTC form several different materials,[8,11] depending on the protonation state of the incorporated linker. The most important of these materials is HKUST-1, a highly porous cubic MOF synthesised by Williams *et al*.[8] Since the original synthesis there have been many variants on the preparative procedure, including microwave[9] and electrochemical[10] methods, and it is clear that the facile synthesis of HKUST-1 is one of its advantages. Described herein is a small modification to the synthesis procedure giving rise to a new MOF with unique properties.

The common solvent used for the preparation of HKUST-1 is 50:50 ethanol:water. However, changing the solvent to a 50:50 methanol:water mix leads to the formation of a new material which has a formula of $Cu(C_{10}H_6O_6)(H_2O) \cdot 1.66H_2O$, and named as STAM-1 (St Andrews MOF-1).

The unusual feature of STAM-1 is that the BTC linker has undergone esterification during the solvothermal reaction to selectively form, the mono methyl derivative in a quantitative yield, with respect to both linker and metal (Figure 5.1). This direct monoesterification of BTC is unknown, adding to the considerable surprise that STAM-1 forms at all, and also opens up the use of MOFs as protecting groups to enable selectivity that is difficult to achieve in organic chemistry.
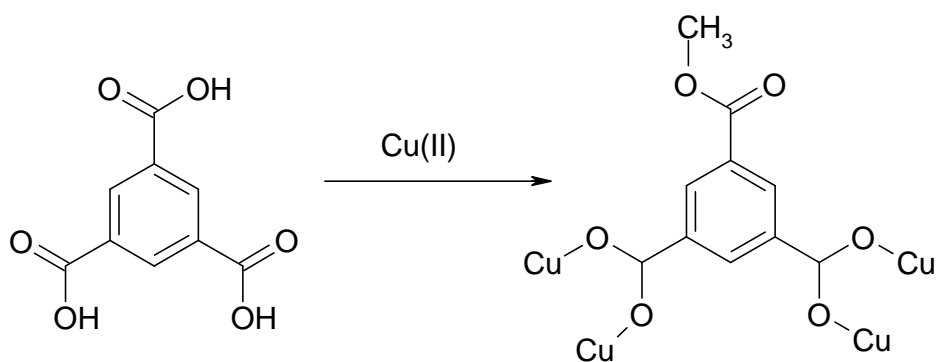

Figure 5.1.   Selective monomethyl esterification of BTC

5.3.   Structure Analysis of STAM-1

One of the major challenges within the field of MOFs is the control of dimensionality. When polyfunctional ligands are employed low dimensionality will be resulted due to ancillary ligation of the water or other solvent molecules. For example, in the reaction between Cu^{2+} and BTC one dimensional chain polymers $[Cu(BTC-H)(H_2O)_3]_n$ [11] or $[NaCu(BTC)(H_2O)_5]$ [12] are formed from

alcoholic solutions at room temperature (RT). The same reaction in ethanol resulted in producing 3D HKUST-1 at higher temperatures.[8] When it comes to STAM-1 the same conditions made a 2D solid with the only difference being the choice of alcohol, from ethanol to methanol.

Single-crystal X-ray diffraction revealed that the structure of STAM-1 (Figure 5.2) contains the same Cu paddle wheel unit that is seen in HKUST-1. The paddle wheel is composed of dimeric cupric tetracarboxylate units (Figure 5.3), with a short Cu-Cu internuclear separation of 2.6212(3) Å (number in parentheses is the estimated standard deviation of the final significant digit). The framework is electrically neutral; the 12 carboxylate oxygens from the three BTC ligands bind to four coordination sites for each of the three Cu ions in the formula unit, whereas the remaining two carboxylates undergo the monomethyl esterification with the methanol in the solvent system. Each metal completes its pseudooctahedral coordination sphere with an axial aqua ligand opposite to the Cu-Cu vector. Such bimetallic tetracarboxylate units are a common and often a highly stable arrangement found not just for Cu but also for many other transition metal carboxylates such as Co[13] and Zn.[14]
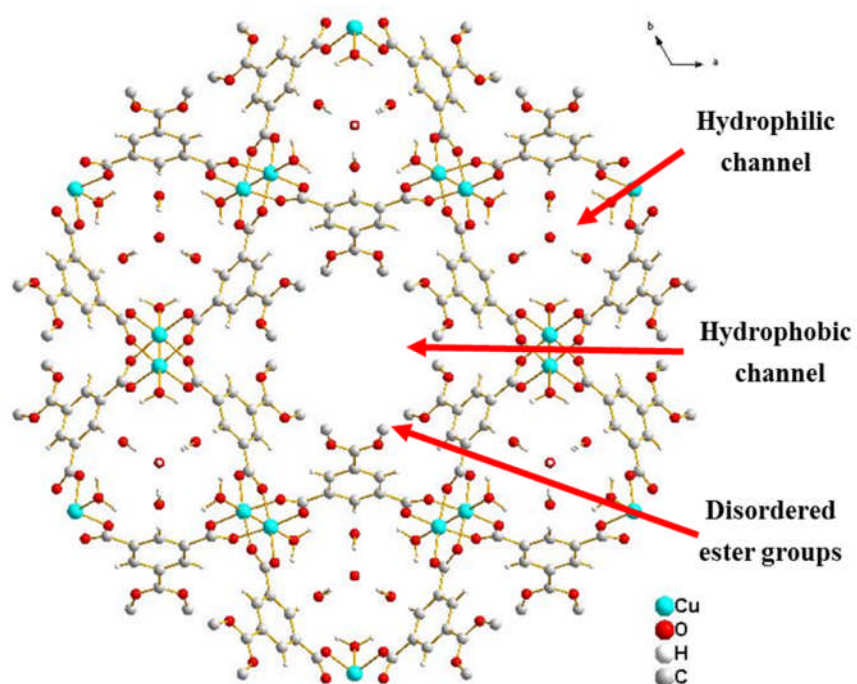
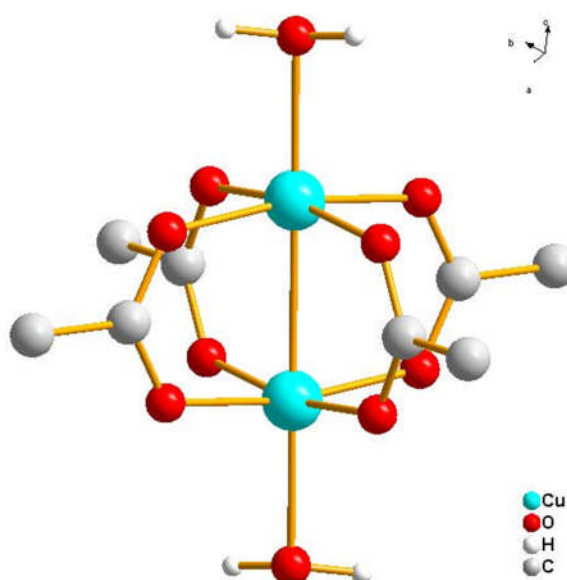**Figure 5.2.**   Structure of the STAM-1 along the *c*-axis

Figure 5.3.   Cu-Paddle wheel unit of STAM-1

The paddle wheels are connected into approximately triangular 'cups' (Figure 5.4) reminiscent of calixarenes,[15,16] with the paddle wheels at the narrow end of the cup, and the wide end delimited by the ester groups. The cups are arranged in a hexagonal pattern with alternating up-down-up orientations to form the layered structures shown in Figure 5.5. This arrangement leads to hydrophilic space lined by metal ions inside the cups and hydrophobic cavities lined only by organic groups between the cups. The hydrophobic/hydrophilic nature of the material is clear from the single crystal X-ray diffraction experiments – the hydrophilic channel contains ordered water molecules while no ordered scattering can be found in the hydrophobic channel (Figure 5.6).

The layers stack directly on top of each other to yield the final structure. The hydrophilic channels are therefore formed by stacked cups, leading to channels that undulate parallel to the crystallographic c-axis with a largest diameter, calculated from molecular modelling studies, of around 5.65 Å and windows into the pores of ~4 Å diameter (Figure 5.7). The hydrophobic channels are best described as pseudo-cubic cages stacked on top of one another, with triangular entrance windows formed by the ester groups. The windows are approximately the same size (~4 Å) as those in the hydrophilic channels.
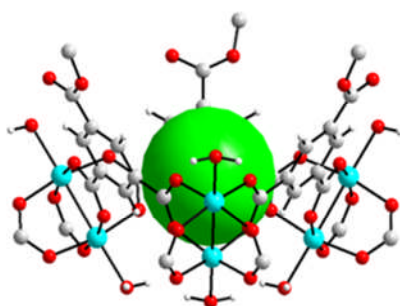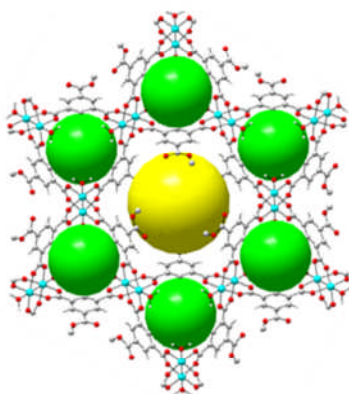
Figure 5.4.   Triangular Cup motif in STAM-1

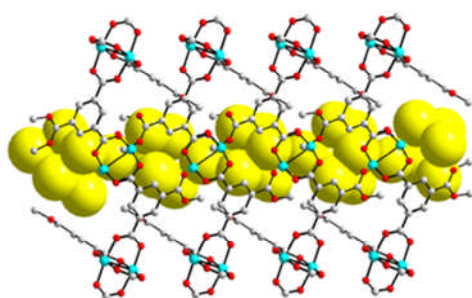**Figure 5.5.**   Arrangement of alternating toroic hydrophilic channels in STAM-1

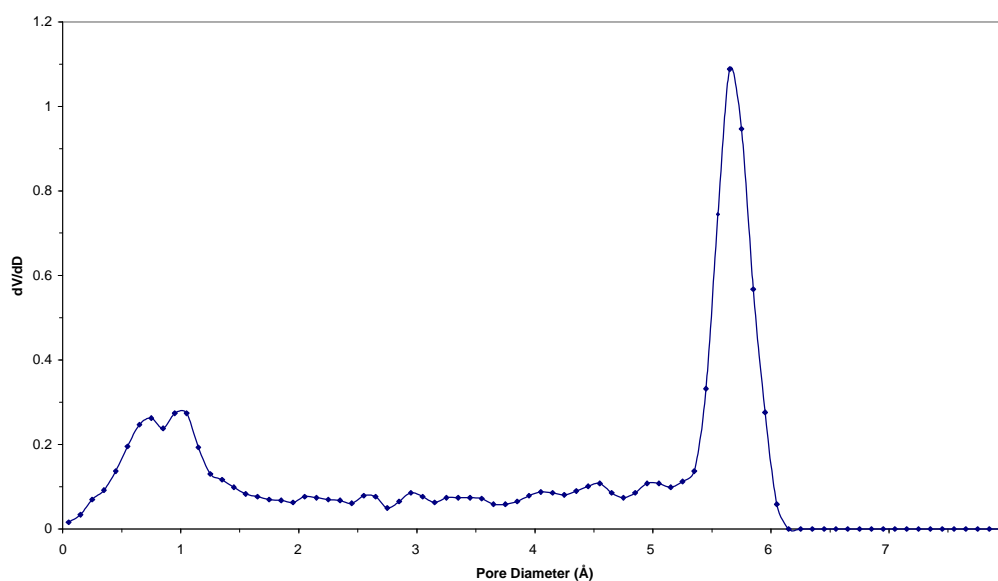**Figure 5.6.**   Hydrophilic and hydrophobic arrangement in STAM-1 in side view

Figure 5.7.   Pore size distribution for STAM-1

5.4.   Characterization of STAM-1

The synthesis of STAM-1 (see Chapter 4.2) involves heating $Cu(NO_3)_2 \cdot 3H_2O$ and

BTC in methanol/water at 110 $^\circ$C for seven days to obtain a highly crystalline

sample. At the end of the seven days material consists of blue, hexagonal-plate

crystals (Figure 5.8 and 5.9) with maximum dimensions around 0.1 to 0.2 mm.

The structure was solved using single crystal X-ray diffraction data and the final

crystallographic parameters are shown in table 5.1.
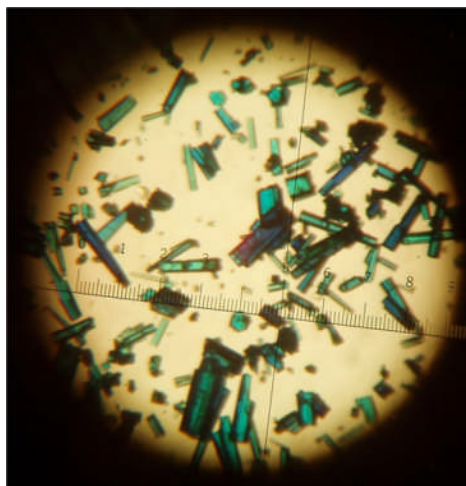
Figure 5.8.   STAM-1 crystals
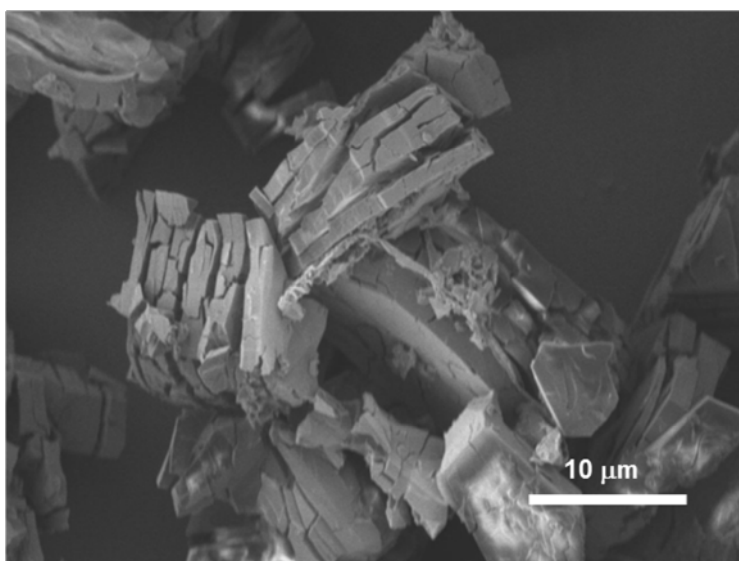
Figure 5.9.   SEM micrograph of STAM-1 crystals

Table 5.1. Crystal data from the structural determination of STAM-1 (Full

details of the refinement can be found in the cif in the Appendix 1)

Identification code	STAM-1
Empirical formula	$Cu(C_{10}H_6O_6)(H_2O)\cdot1.66H_2O$
Formula weight	333.6
Temperature	293(2) K*
Wavelength	0.71073 Å
Crystal system, space group	Trigonal,P-3m1
Unit cell dimensions	a=18.6500(17) Å
	b= 18.6500(17) Å
	c= 6.8329(9) Å
Volume	2058.2(4) Å^3
Z	6
Calculated density	1.615 g cm^{-1}
Absorption coefficient	1.628 mm^{-1}
F(000)	1018
Crystal size	0.09 x 0.08 x 0.05 mm
Theta range for data collection	3.24 to 27.38 deg.
Limiting indices	-24<=h<=19, -22<=k<=24, -8<=l<=6
Reflections collected/unique	14358/1647[R(int) = 0.0689]
Completeness to theta = 27.38	96.7 %
R1 (I > 2σ(I), wR2 (All data)	0.056, 0.1415

* Structure has been confirmed at 100 K using synchrotron radiation

This novel material, yielded 95% and has a formula of $Cu(C_{10}H_6O_6)(H_2O)\cdot1.66H_2O$. Elemental analysis [Calculated for $(CuC_{10}H_8O_7)_3(H_2O)_5$: C, 35.99; H, 3.42. found: C, 36.84; H, 3.44.] and Powder X-Ray Diffraction (PXRD) measurements were carried out to find out the purity of the product. The experimental PXRD pattern perfectly matched the simulated pattern (Figure 5.10) based on the single-crystal X-ray data although a small amount of HKUST-1 was present as an impurity.
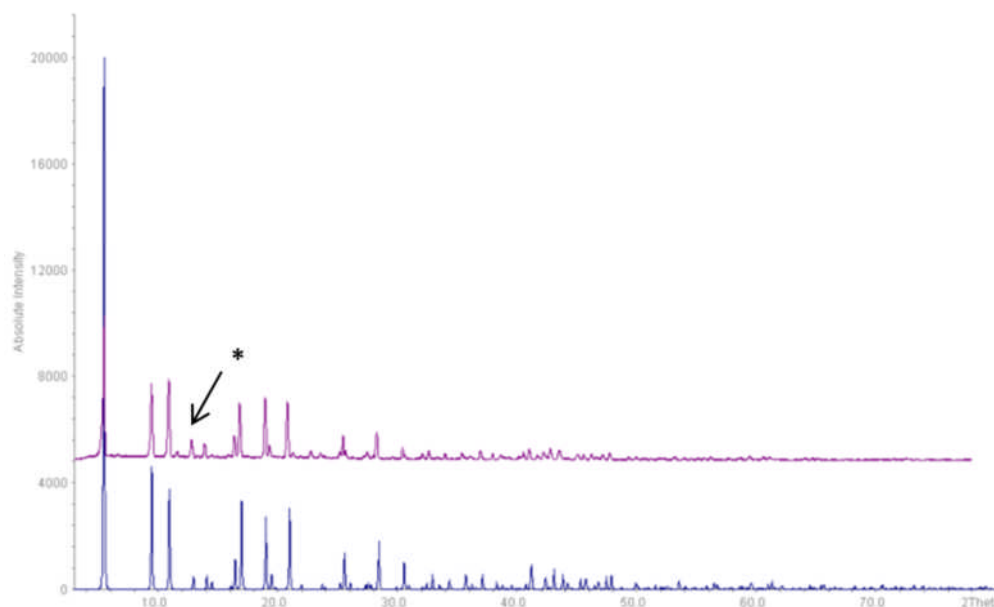

Figure 5.10.   A comparison of experimental (top) and calculated (bottom) PXRD patterns for STAM-1. The calculated pattern is based upon the single crystal X-ray diffraction data; See the relevant cif in the appendix for details. ***** shows the impurity of HKUST-1 present in the PXRD of STAM-1

Single crystal X-ray diffraction reveals the presence of the methyl ester of BTC, which is further, confirmed by the ester peak at 1731 cm^{-1} in the infrared spectroscopy (Figure 5.11) and methylated peak at 49 ppm in the solid-state ^{13}C MAS NMR studies (Figure 5.12). However the carbonyl peak of the ester group also can be seen around 170-180 ppm, which is overlapping with the aromatic carbon peaks in the same region making their differentiation difficult. It is notable that this is one of the very few copper-containing MOFs that have been studied using solid-state NMR.[17]
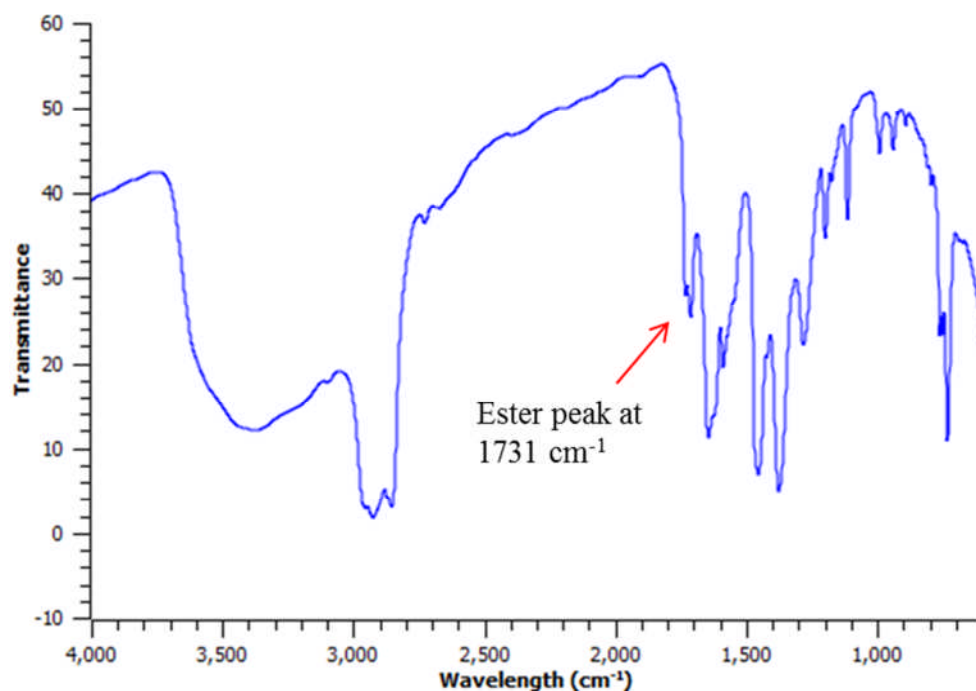

Figure 5.11. The Infrared spectrum of STAM-1

Methylated peak
indicating the presence
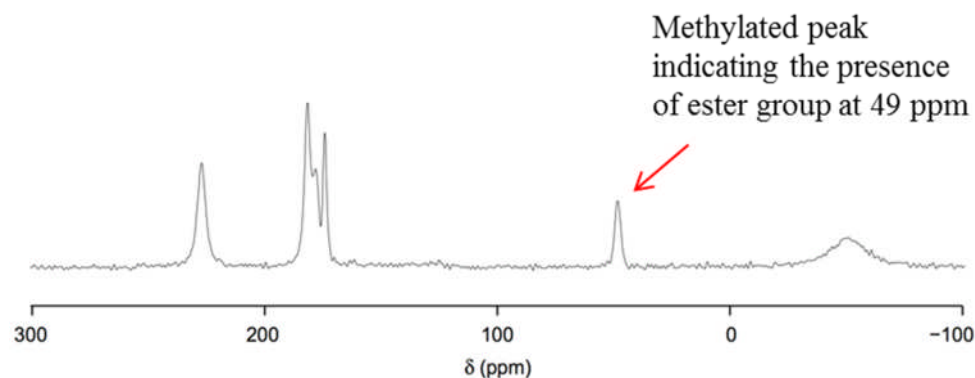of ester group at 49 ppm

Figure 5.12. The ^{13}C MAS NMR spectrum of STAM-1

5.5.   Mechanism

It is interesting to think about why such an unusual structure is formed from this reaction. From the large amount of previous work in a similar area it would be expected that HKUST-1 (or a similar BTC-derived MOF) would be the major product. However, ^{1}H NMR studies of the synthesis solution at an early stage, before any solid is formed, show a mixture of the monomethyl, dimethyl and trimethyl esters of BTC (Figure 5.13). This effectively precludes any formation of HKUST-1 or other MOFs that only contain the BTC linker. The NMR studies suggest that the esterification takes place with no special selectivity in the synthesis solution, and the selectivity towards the monomethyl BTC-containing STAM-1 solid occurs during precipitation/crystallisation. The peak at 1731 cm^{-1} indicates the presence of the ester group in all solids recovered, even at the very earliest stages of the reaction (Figure 5.14).
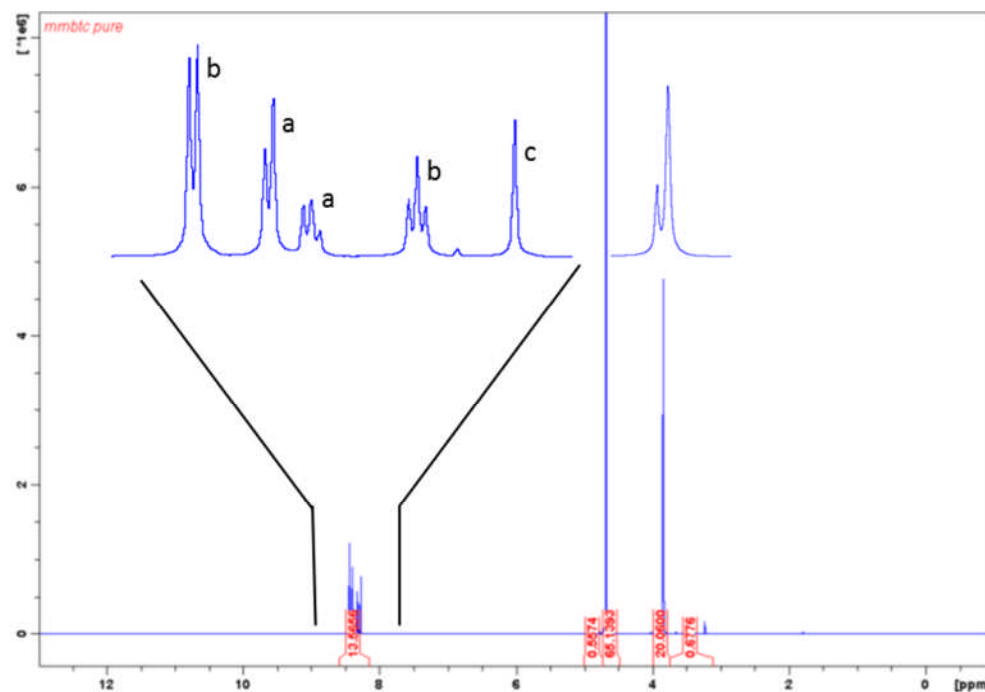
Figure 5.13. ^{1}H-NMR spectrum of the synthesis solution prior to any solid

forming. The nature of the solution inside the autoclave was probed by stopping

the reaction after certain amounts of time and characterising the species present.

The diagram shows the ^{1}H spectrum stopped after 2 hours of heating, which is

before any significant amount of solid was formed. Solution evaporated and the

resulting solid were treated with NaOH in order to remove the copper ions. The

expanded region of the diagram shows the aromatic region of the ^{1}H spectrum,

clearly showing a mixture monomethyl(a), dimethyl(b) and tri-methyl(c) ester

derivatives of BTC. [**^{1}H-NMR** (400 MHz, D_2O, 25 ºC): δ = 3.80 (s, 3H), 3.85 (s,

3H), 8.28 (s, 3H), 8.33 (t, 1H), 8.39 (t, 1H), 8.41 (d, 2H), 8.44 (d, 2H)].

From studies of the reaction carried out using NMR on the solution, IR and PXRD

of the solid, it seems that the equilibrium between the esters is set up very quickly

in the solution, and the relative amounts remain effectively constant until nucleation of the solid occurs. Infrared spectroscopy shows that the earliest solid formed contains the ester group and PXRD shows that the initial solid is rather poorly crystalline (Figure 5.15). STAM-1 forms over the following few days, with highly crystalline samples available after four days. At the end of seven days the material consists of blue, hexagonal-plate crystals with maximum dimensions around 0.1 to 0.2 mm.
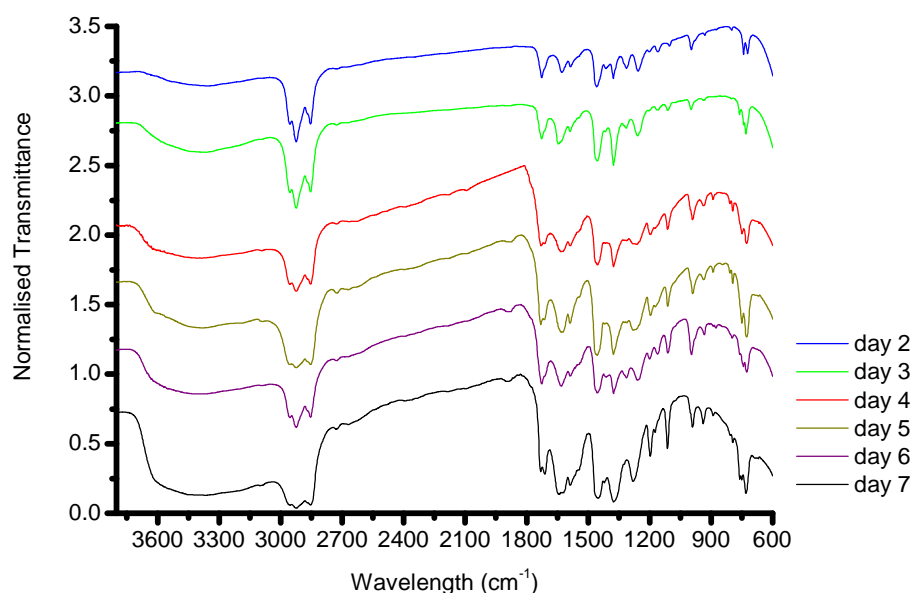

Figure 5.14. The infrared spectrum of STAM-1 recovered after different reaction times.
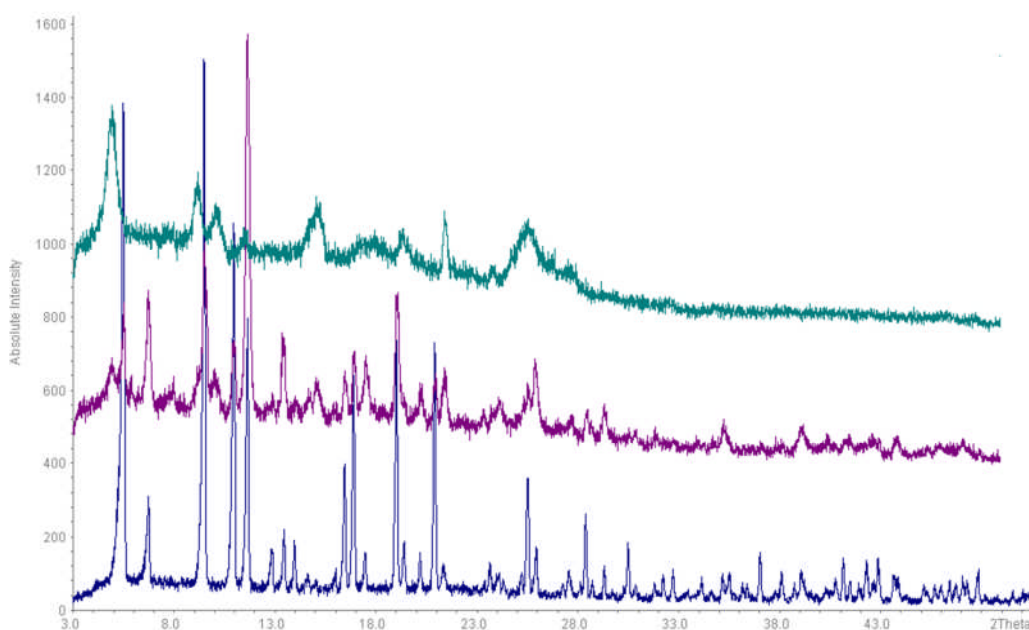
Figure 5.15. The X-ray diffraction patterns of the solid STAM-1 recorded at

different times after the reaction had been started. The time steps used in the

reaction show are 2 days (top), 3 days (middle) and 4 days (bottom). The initial

sample is very poorly crystalline and probably not of the same structure as

STAM-1.

By considering the above facts the following mechanism can be suggested for the

formation of STAM-1:

The BTC starting material undergoes a copper ion-promoted esterification to give

a mixture of mono-, di- and tri-methyl esters of BTC, which are in equilibrium.

The copper metal ions seem to be vital to this process, as replacing copper with

other metals does not lead to the same esterification process. The well-known

reversibility of esterification reactions means that this equilibrium is set up

relatively quickly. Importantly, the solution state NMR studies (Figure 5.13) indicate that there is very little unreacted BTC in the sample. This selectivity can be explained given the structure of the three competing esters. The trimethyl BTC ester has no free carboxylate groups available to interact with the metals in solution, and therefore cannot form a metal-carboxylate MOF. The dimethyl BTC ester has only one free carboxylate group that can coordinate to a metal, and so any such complex is likely to remain in solution as it cannot form a polymeric material. The monomethyl BTC ester has two available carboxylate groups and when it interacts with the metals present it precipitates out of solution to form a coordination polymer solid, STAM-1. A graphical depiction of this is shown in Figure 5.16. This perturbs the equilibrium in the solution, leading to more of the monoester BTC being formed and a depletion of the other two esters, and further precipitation of STAM-1. Since the solid is formed in essentially 100% yield, this process continues until all of the BTC has been transformed into the monoester and precipitated out as STAM-1.
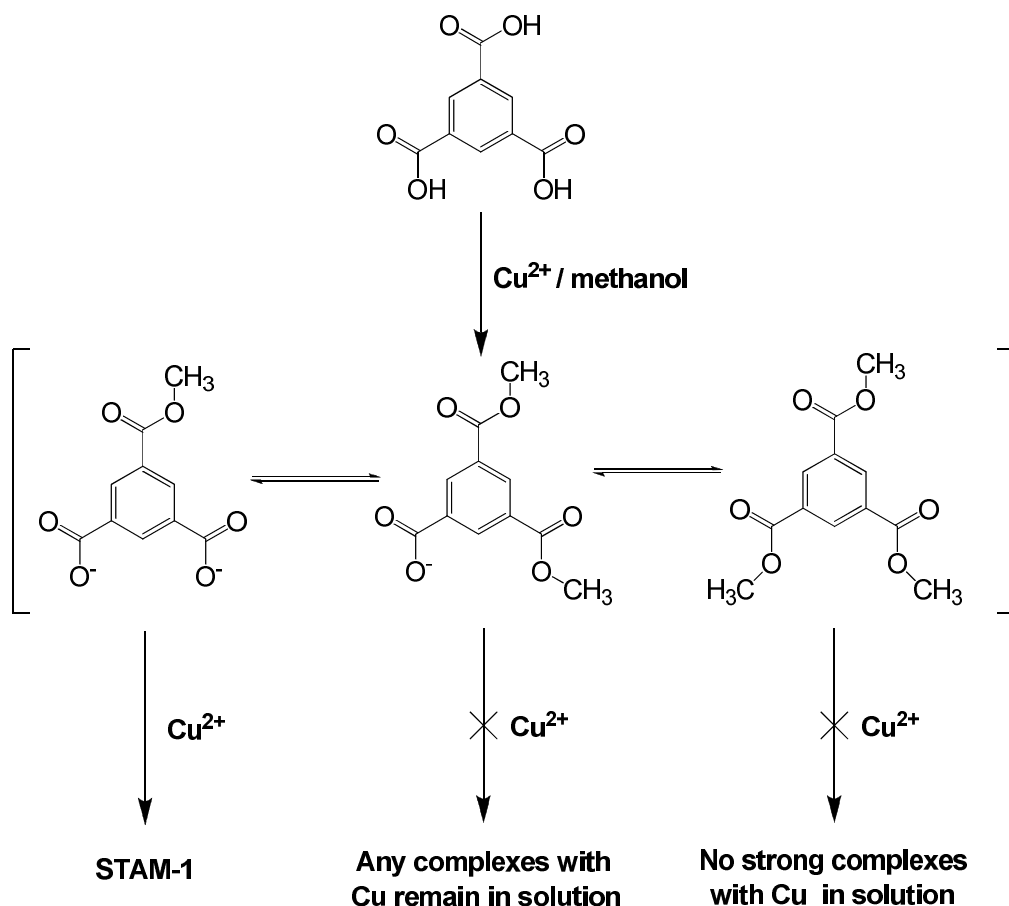
Figure 5.16. The proposed mechanism for the synthesis of STAM-1.

5.6.   Stability of STAM-1

Stability of the framework is important when considering its applications. Some of the MOFs reported today are not stable in many solvents. For example, MOF-5 is one of the very famous MOFs synthesised by Yaghi *et al* in the early stage of MOF development.[18] This material shows many interesting properties including hydrogen uptake and exceptional surface area. However recently it was reported that MOF-5 is unstable in water.[19] On the other hand, STAM-1 is stable in water

at neutral pH, as well as in many other solvents. Stability of STAM-1 in various solvents is listed below in Table 5.2.

Table 5.2. Stability of STAM-1 in various solvents

Solvent	Stability
Water	Yes
Methanol	Yes
Ethanol	Yes
DCM	Yes
Acetone	Yes
Acetonitrile	Yes
THF	No
DMF	No
DMSO	No

5.7.   Cu(II) substitution by Zn(II) in STAM-1

STAM-1 shows excellent properties in various applications, which is discussed in the later chapters. Within the wide variety of possible applications for STAM-1, it is of particular interest to tune its physical and chemical properties while maintaining the structural features. This can be achieved by manipulating the organic linker molecule which will be discussed later in this chapter or by modifying the inorganic building unit, the Cu paddle wheel unit. One way of achieving this is by substituting the metal species to a certain degree.

Modification of the inorganic building unit of a MOF is rare and has been reported for the HKUST-1.[20] By applying the same method, partially Zn(II) substituted STAM-1 was synthesized with the aim to form binuclear Cu-Zn paddle wheel SBU (Figure 5.17).
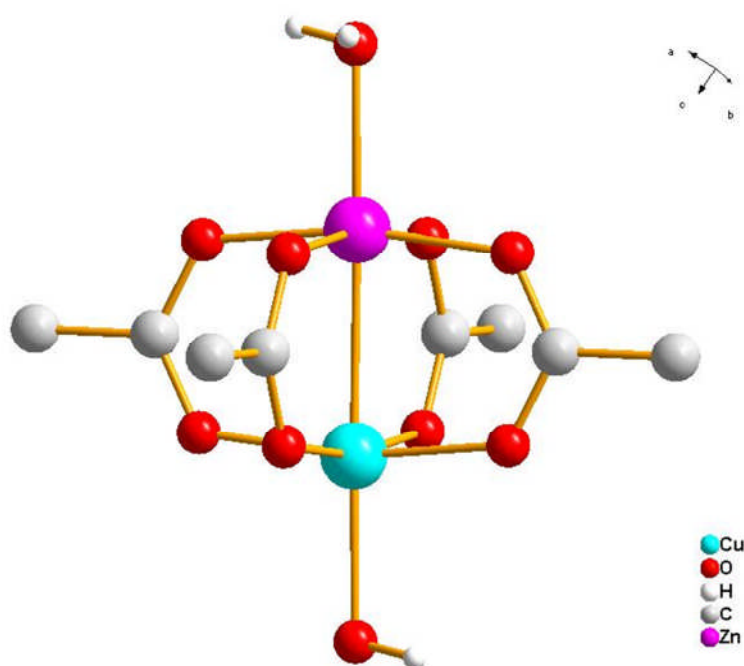

Figure 5.17. Schematic representation of the structure of a binuclear Cu/Zn-

Paddle wheel unit

$Zn(NO_3)_2$ was used along with the $Cu(NO_3)_2$ in 1 : 1 molar ratio and keeping all other conditions the same as used in the parental STAM-1 synthesis. The resulting product was characterized using PXRD (Figure 5.18). The powder pattern confirms that the framework of the Zn doped STAM-1 has a similar pattern of that of the STAM-1 parent material. Presence of the Zn in the paddle wheel was

examined by using ^{13}C MAS NMR spectroscopic methods (Figure 5.19). Despite the presence of paramagnetic copper ions, the ^{13}C MAS NMR spectra show highly resolved signals. The methylated peak at 49 ppm of parental STAM-1 can be seen as two peaks in the Zn/Cu doped STAM-1 material due to the differences in their respective chemical environments. The resonance at 227 ppm in the parental STAM-1 also was split into two in the spectrum of the mix metal sample due to the different chemical environment experienced by the mix metal STAM-1. This indicates that the Paddle wheel unit in the Zn doped STAM-1 has a different chemical environment than the parental STAM-1 which influences the signals to be split. Therefore it is evident that instead of having a Cu-Cu paddle wheel unit as in parental STAM-1, the SBU of the mix metal MOF is a Cu-Zn paddle wheel.

Other than the solid state NMR technique, EDX (Figure 5.20) and ICP (37% Cu and 0.5% Zn) methods were accompanied to show the incorporation of Zn in the material. But the results of these two techniques were different. ICP states the percentage of Zn incorporation as 0.5% whereas EDX shows about 2.3% of Zn inside the material. Although the exact amount of doped Zn into the structure cannot be calculated precisely from the outcome as both of the techniques used were semi-quantitative, at least the incorporation of Zn within the structure is proved from both techniques. Also it should be noted that although a 50% of Zn source was initially used as a reactant along with Cu, a very small amount of Zn was doped in the material.
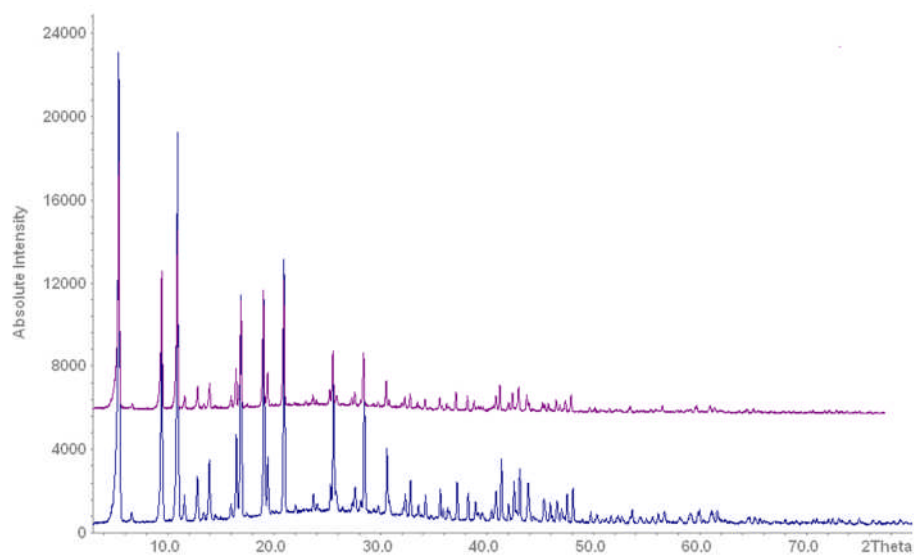
Figure 5.18. A comparison of PXRD pattern for Zn/Cu-STAM-1 (top) and PXRD
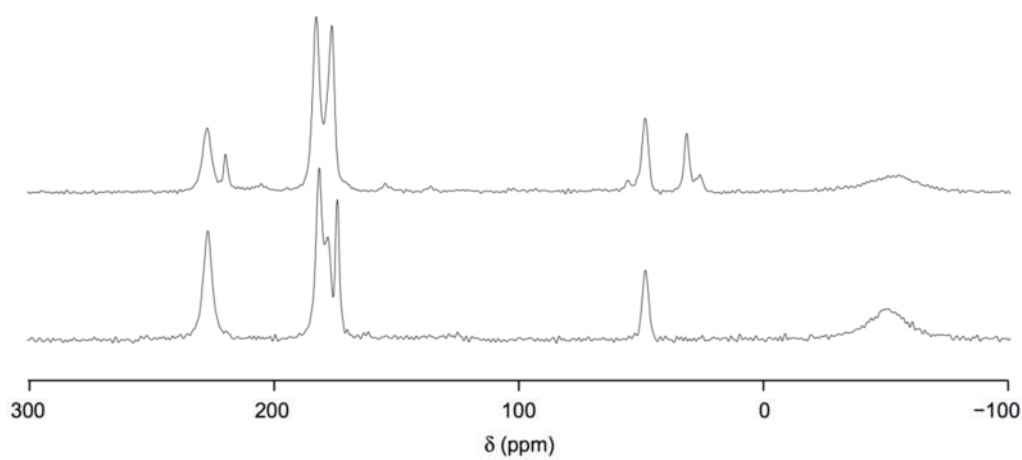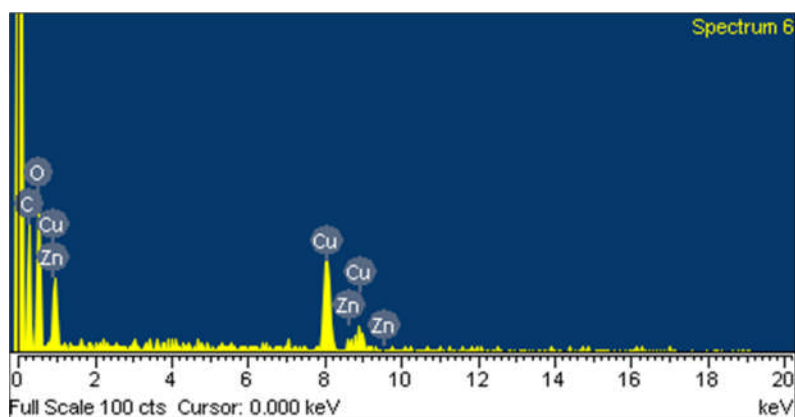
pattern for Cu-STAM-1 (bottom).

Figure 5.19. A comparison of ^{13}C MAS NMR spectrum of Zn/Cu-STAM-1(top)

with Cu-STAM-1(bottom)

Element	Weight%	Atomic%
C	36.47	54.85
O	32.08	36.23
Cu	29.09	8.27
Zn	2.36	0.65
Totals	100.00	

Figure 5.20. The EDX data of Zn/Cu-STAM-1

^{13}C MAS NMR results clearly show that we have successfully substituted paramagnetic Cu(II) ions in the paddle wheel units of STAM-1 by diamagnetic Zn(II) ions. Furthermore PXRD and the TGA measurements (see Appendix 7, A7.1) are similar to that of pure Cu-STAM-1 which is a clear evidence that doping of STAM-1 by Zn(II) conserves the framework structure and its stability. Therefore this confirms that the synthesis of mixed metal STAM-1 structure is in principal feasible.

5.8.   Synthesis of STAM-2

MOFs with different functionalities can be obtained by post synthetic modifications. As described in Chapter 1, MOFs which contain functional groups in the bridging ligand can be modified by means of a simple chemical reaction. These modifications are usually covalent in nature, based on the chemical reaction that takes place.

STAM-2 was obtained from STAM-1 in a similar way. However in this case instead of introducing a chemical reaction, STAM-1 was irradiated with ultra sound. Ultrasonication is a technique which has recently been used to synthesize MOFs,[21] which is a rapid, facile and environmentally friendly method, already widely used in organic synthesis.

As described in detail in Chapter 4.4, 50% intensity of ultrasound (US) was introduced (from a 250 W digital sonifier) to the STAM-1 with 3 seconds pulse and 1 second no pulse for 260 minutes in water. The resultant product was filtered, air dried and analysed using PXRD (Figure 5.21). The powder pattern of the product was different to that of STAM-1, which suggested a preparation of a new material. This material was named as STAM-2 and has a formula of $Cu_2(OH)_2(C_{10}O_6H_6)$.
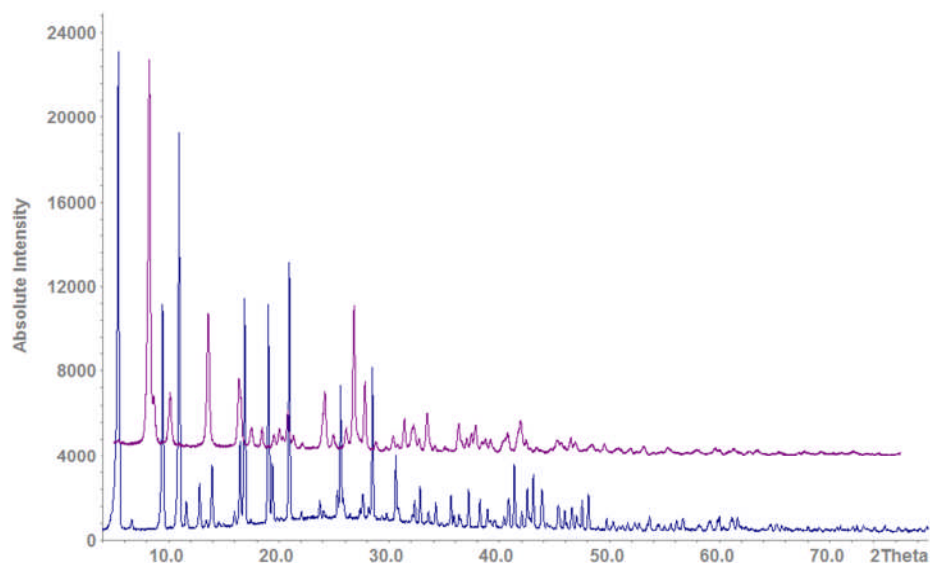
Figure 5.21.   A comparison of PXRD patterns for STAM-2 (top) and STAM-1

(bottom)

As STAM-1 was irradiated with US, structural re-arrangement has occurred

within the material to result in a completely new architecture. It appears that this

is the first time a new MOF has been synthesized from an existing MOF using

US. When US was applied to a layered structure like STAM-1, the interactions

between the layers break and facilitate the structural changes that occur.   The

structure of STAM-2 was solved from PXRD data using a ''Charge Flipping

algorithm''.[22] The structure solution was carried out by Prof. Russell Morris.

Various analyses such as pair distribution function analysis, solid state NMR and

IR were carried out in order to identify the building units and the functional

groups of the new material. The comparison of the experimental PXRD of

STAM-2 with the theoretical pattern generated from its crystallographic data

indicates a presence of another phase (Figure 5.22). This unidentified phase could

be an impurity resulting from the incomplete structural transformation. The crystallographic data and atomic coordinates are given in the Table 5.3 and Table 5.4.
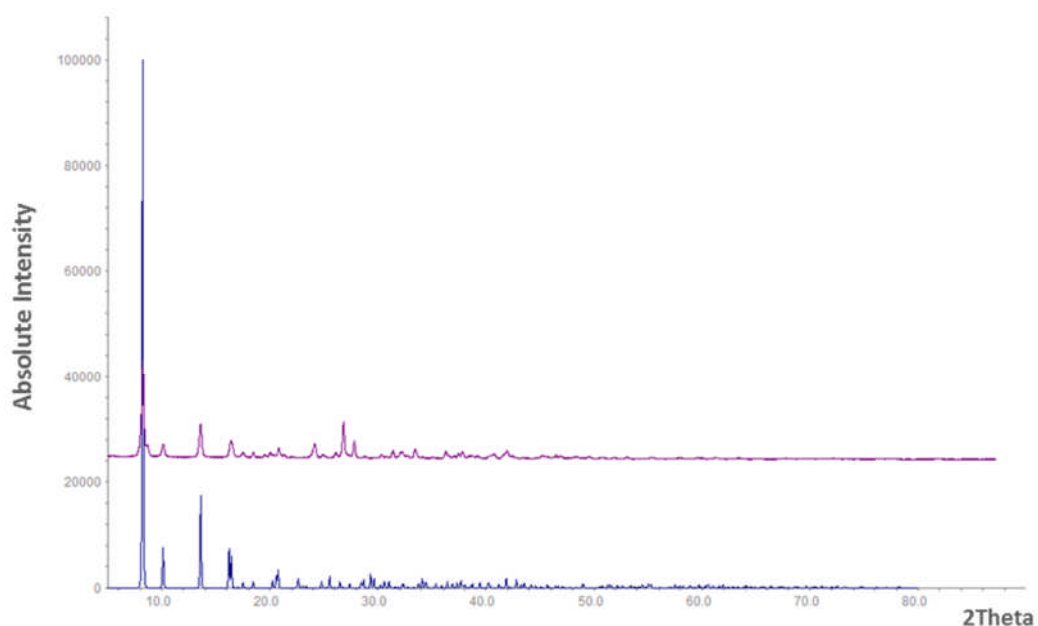

Figure 5.22.   A comparison of experimental (top) and calculated (bottom) PXRD patterns for STAM-2. The calculated pattern is based upon the crystallographic data, details of which are given in table 5.3

Table 5.3.   Crystal data for structure determination of STAM-2

Identification code	STAM-2
Empirical formula	$Cu_2(OH)_2(C_{10}O_6H_6)$
Formula weight	386.28
Crystal system, space group	Triclinic, P -1
Unit cell dimensions	a=11.2519(17) Å
	b= 10.6141(17) Å
	c= 5.7446(9) Å
	α=86.58
	β=97.72
	γ=106.83

Table 5.4.   Atomic coordinates of STAM-2

Atom	X	Y	Z	Occupancy	Uiso
CU1	0	0	0	0.5	0.019235
CU2	-0.041087	0.139742	0.524525	1	0.019235
O1	0.869719	0.114591	0.899289	1	0.019235
O2	1.000023	0.259928	0.239795	1	0.019235
O3	0.985077	0.684227	0.310408	1	0.019235
O4	0.801091	0.731688	0.187893	1	0.019235
O5	0.591122	0.291891	0.378024	1	0.019235
O6	0.613777	0.511877	0.380251	1	0.019235
O7	0.03365	0.002294	0.683741	1	0.019235
O8	0.092233	0.167312	0.306886	1	0.019235
C1	0.633027	0.406392	0.465445	1	0.019235
C2	0.89145	0.207845	0.079904	1	0.019235
C3	0.82709	0.316258	1.01014	1	0.019235
C4	0.893086	0.442743	0.098886	1	0.019235
C5	0.839018	0.545605	1.023418	1	0.019235
C6	0.769695	0.539811	0.797898	1	0.019235
C7	0.712445	0.415132	0.699853	1	0.019235
C8	0.762633	0.310789	0.775705	1	0.019235
C9	0.887672	0.676157	0.142429	1	0.019235

Pair distribution function (PDF) analysis was used to identify the SBU present in STAM-2. As can be seen in Figure 5.23 the PDF data of STAM-2 is similar to STAM-1 below 2.5 Å, suggesting that all the interactions between C-C, C-H, C-O, and O-H are similar in both materials. However STAM-2 tends to differ from STAM-1 after 2.5 Å; STAM-1 has a peak at around 2.6 Å related to the bond length between Cu-Cu in the paddle wheel unit. However there is no peak at 2.6 Å in STAM-2 suggesting that the SBU is different from that of STAM-1. According to the PDF data STAM-2 has a peak around 3 Å, which is related to the Cu – Cu distance of the material.
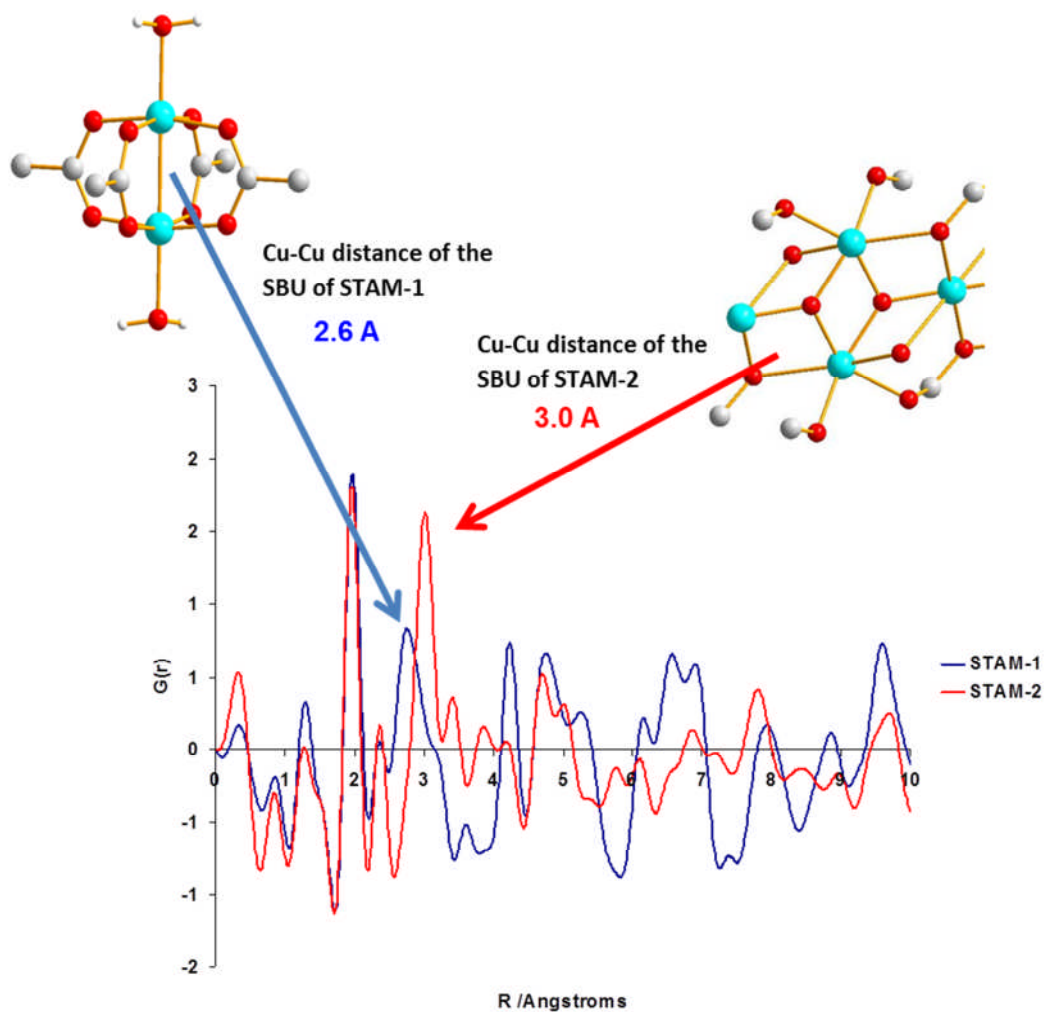
Figure 5.23.   A comparison of PDF data for STAM-1and STAM-2. This clearly

shows the difference in the Cu-Cu bond length in the SBU of both materials.

Although US was strong enough to break the interactions between the layers of

STAM-1, the energy released was not strong enough to hydrolyse the methyl ester

group present on the organic ligand. Both IR (Figure 5.24) and ^{13}C MAS NMR

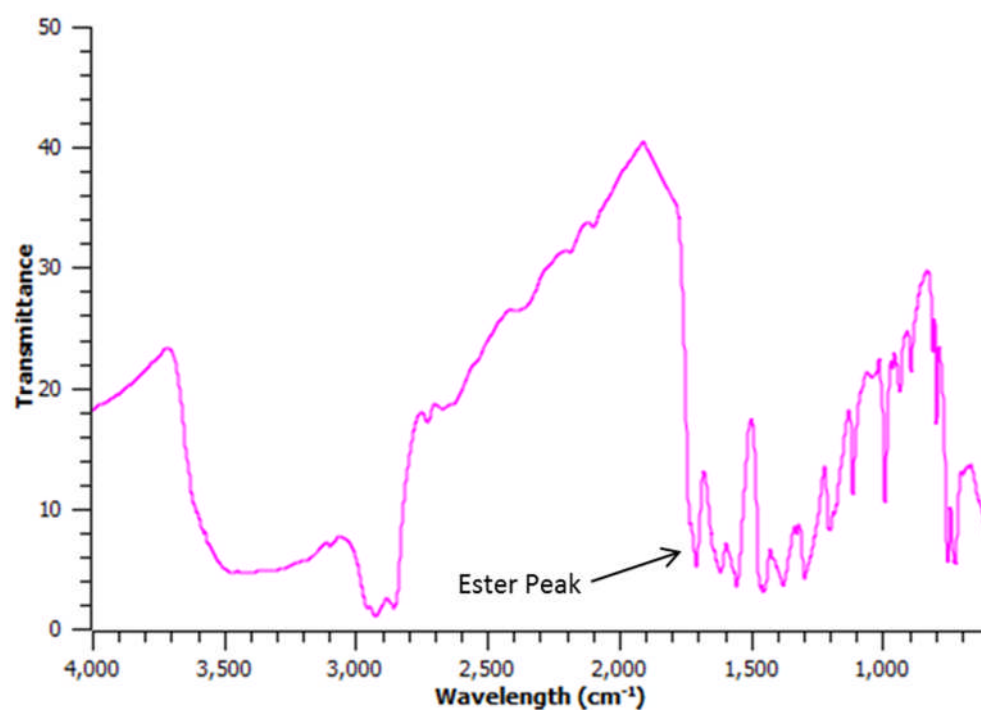(Figure 5.25) studies indicate that the ester group is still intact with the framework

of STAM-2.

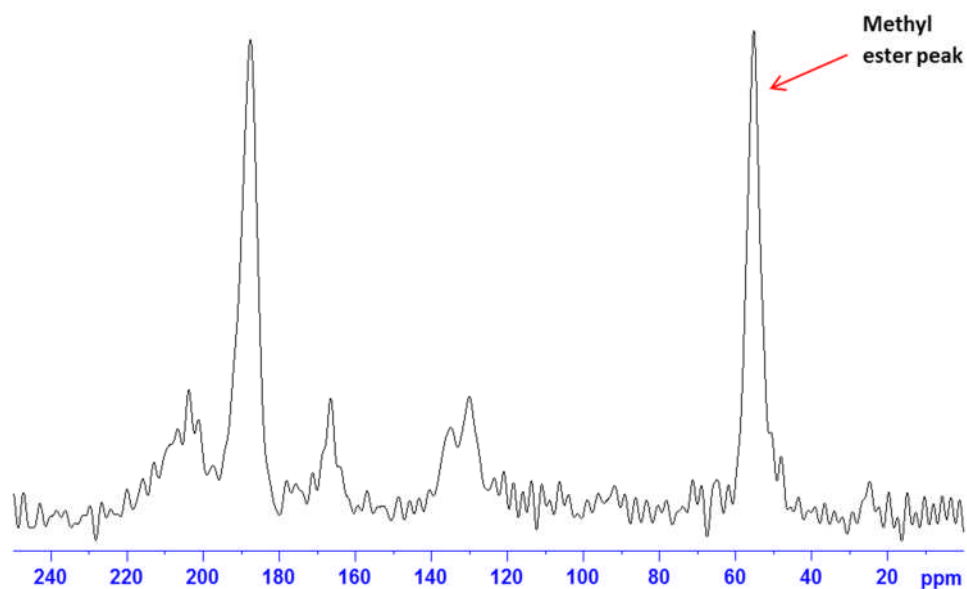**Figure 5.24.**   Infrared spectrum of STAM-2

Figure 5.25. ^{13}C MAS NMR spectrum of STAM-2

Interestingly STAM-2 also consists of layers with inter layer interactions. The inorganic chains are linked together with organic ligands in order to make the 2 D framework. These chains consist with edge-sharing Cu_2O_{10} octahedral dimers linked together with edge-sharing CuO_6 monomers in a recurring pattern. The linker binds with both dimer and monomer units in order to construct the 2D layers (Figure 5.26). Each copper centre adapts to the tetragonal distorted octahedral geometry by linking with 6 oxygens from either the linkers or from the water molecules (Figure 5.27). The binding pattern of the monomethyl benzene tri carboxylate (mmBTC) ligand into the inorganic cluster is interesting. Four O's of two carboxylates in mmBTC ligand are available for the coordination with the metal centres. When one oxygen of the carboxylate binds with the Cu of the dimer unit, the other binds to the Cu of the monomer unit of the same inorganic cluster which is labelled as Chain A (Figure 5.28). The other carboxylate of the same mmbtc ligand binds with Chain B. In this case only one oxygen binds to the dimer unit leaving the second oxygen unbound. The binding pattern is reversed in the second mmBTC. This sequence can be seen in the binding of the ligands leaving the ester groups in the anti-conformation, making each sheet to be built in sterically the most favourable conformation.
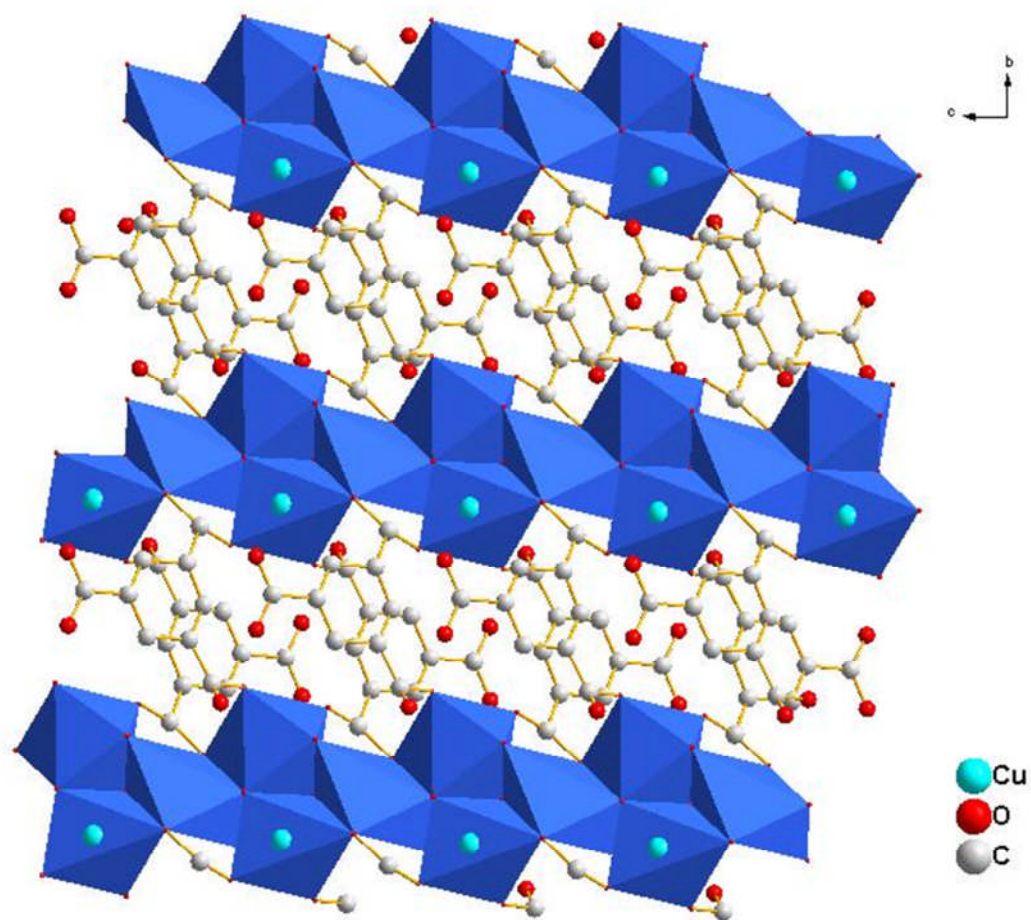
Figure 5.26.   Crystal structure of STAM-2 along the a-axis
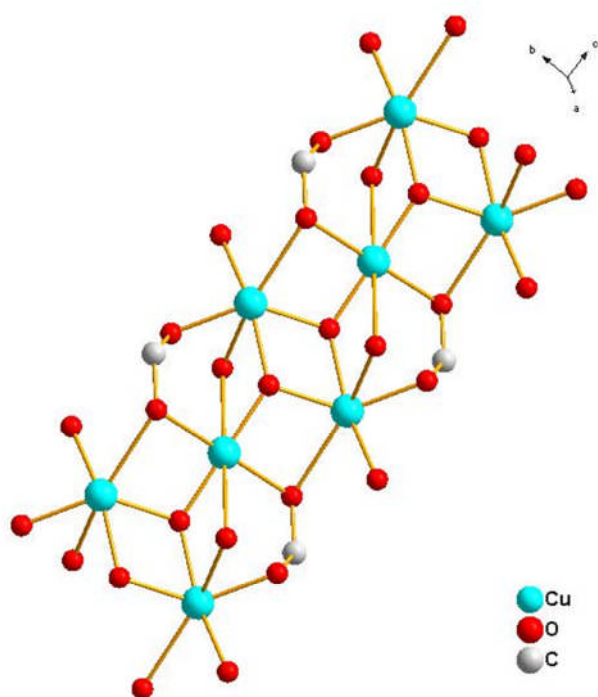
(Hydrogen atoms are omitted for clarity)

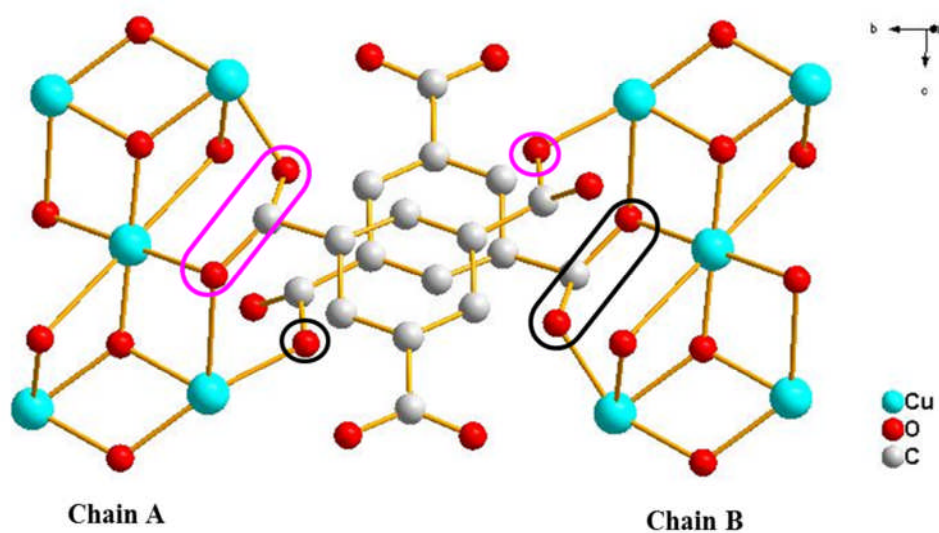**Figure 5.27.**   Inorganic cluster in STAM-2

Figure 5.28. Arrangement of mmBTC ligand in anti-conformation in STAM-2.The coordination of the front mmBTC is highlighted in pink whereas the coordination of the rear mmBTC is highlighted in black

Thermogravimetric analysis shows that STAM-2 also contains the same amount of water as STAM-1 (see Appendix 7, A7.2). Since STAM-2 does not contain any solvent accessible channels, the water molecules that count for STAM-2 should be chemically bound to the inorganic cluster.

US is not the only method that derives STAM-2. Instead, a hydrothermal application on STAM-1 also results STAM-2 suggesting that the material is in a more stable form. An attempt was made to heat STAM-1 at 80 °C in water for 2 hours in order to hydrolyze the methyl ester group. By hydrolizing the ester group, a modified version of STAM-1 can be obtained with two types of hydrophilic channels; with and without connecting to the open metal sites. Surprisingly the resultant framework gave a similar powder pattern as STAM-2 (Figure 5.29).
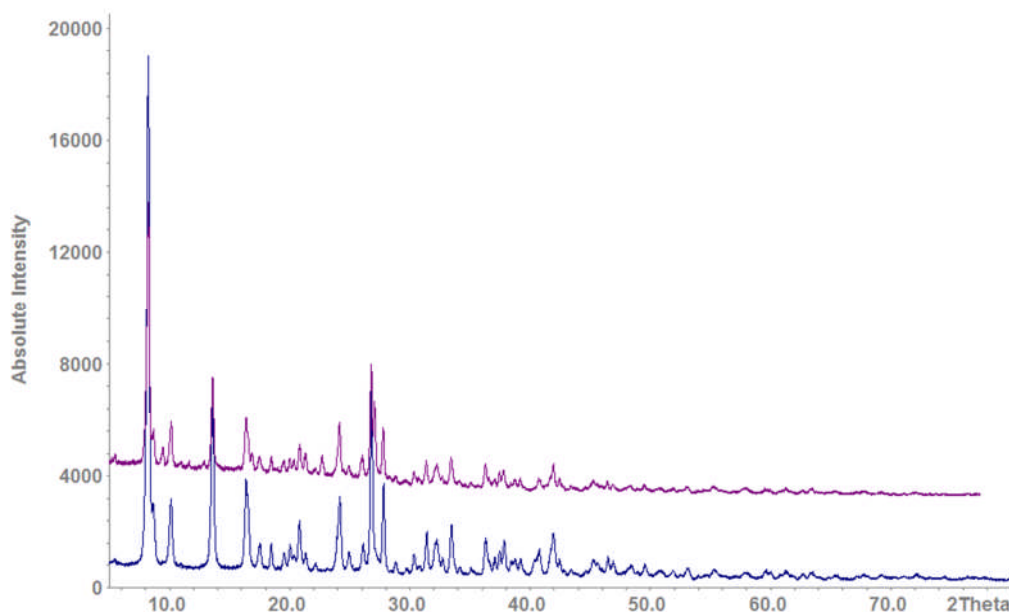
Figure 5.29. A comparison of PXRD obtained for STAM-2 by hydrothermal

application (top) and ultrasonication (bottom)

5.9.   Synthesis of STAM-3

STAM-3 was synthesized using copper nitrate and BTC in methanol and water by

direct irradiation with ultrasound at an ambient temperature and atmospheric

pressure for 64 minutes (see Chapter 4.5 for the exact conditions of the reaction).

The structure of the resultant product was then compared with STAM-1 and

STAM-2 using PXRD measurements (Figure 5.30). According to the PXRD data,

the product obtained was different from the hydrothermal product STAM-1 and

was named as STAM-3. Ultrasonication must have played an important role

during the formation of STAM-3 because no product was obtained by mixing

copper nitrate and BTC in the same reaction medium at ambient temperature and

pressure in the absence of US. The PXRD indicates that the unit cell of the

STAM-3 is smaller than that of STAM-1. Also according to the gas adsorption measurements (see Appendix 8, A8.1.2), STAM-3 does not contain any channels for gas adsorption where it appears to be more condensed than STAM-1. According to the infrared spectrum (Figure 5.31) STAM-3 does not contain a methyl ester on the BTC linker. This implies that US does not facilitate the monoesterification reaction. The structural comparative characterisation of this material is currently on going.
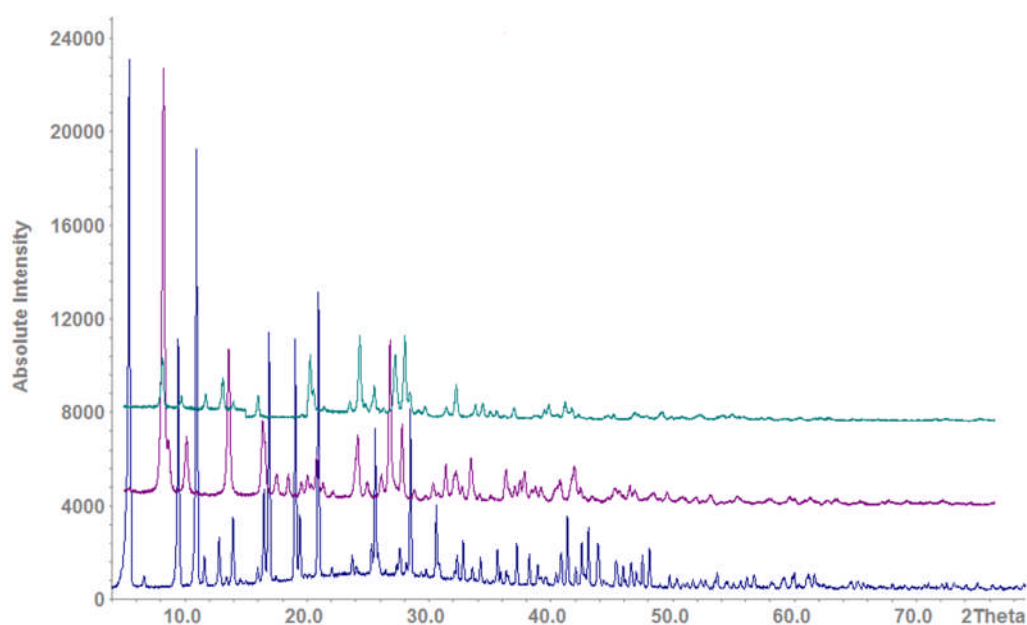

Figure 5.30.   A comparison of PXRD for STAM-3 (top), STAM-2 (middle) and
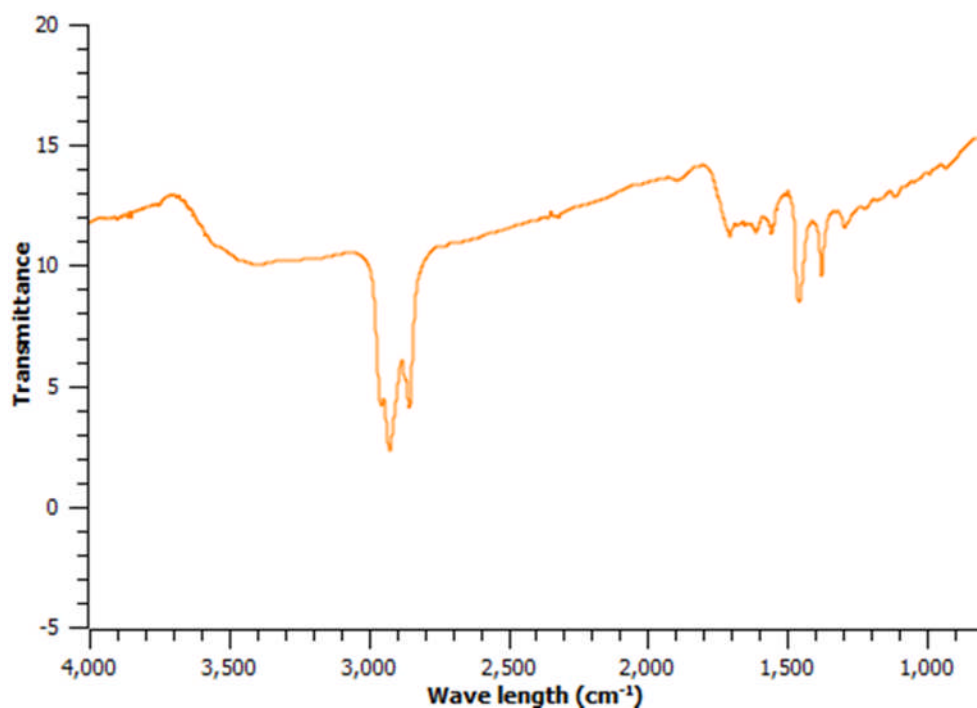
STAM-1 (bottom)

Figure 5.31.   Infrared spectrum of STAM-3

The effect of US on chemical reactions have been investigated and most theories imply that the chemical effect of US originates from acoustic cavitation within the collapsing bubbles, which can generate localized hot spots with an exceedingly high transient temperature (5000 K), pressure (1800 atm) and cooling rate (10^{10} K s^{-1}).[23] The rapid motions of molecules, high temperature and pressure in the interfacial region around the bubble lead to the production of excited states, bond breakage, free radicals, mechanical shocks and high shear gradients. Therefore many types of chemical reactions including the reactions that are difficult to process under traditional methods are easy to precede using ultrasonication.

5.10. Isolation of Monomethyl Ester of BTC

Since the reaction of STAM-1 undergoes *in situ* esterification which is difficult to accomplish using general synthetic routes, attempts were made to isolate the resulted mmBTC ligand from STAM-1 (Figure 5.32).
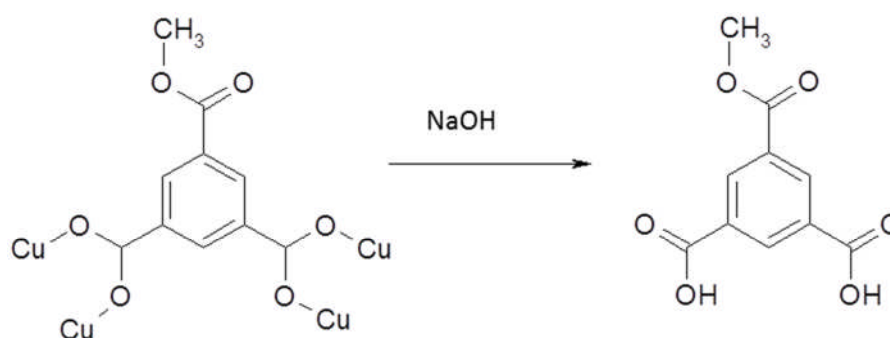

Figure 5.32. Isolation of mmBTC from STAM-1

The following attempts were made to isolate the monoester from STAM-1:

1. The material was dissolved in a minimum amount of HCl to hydrolyze the Cu-O bonds of STAM-1. This step was carried out carefully as it increases the chance of hydrolyzing the methyl ester bond. The resultant mixture was treated with a small amount of DOW-EX to get rid of all Cu^{2+} ions. After removing the solvent the crude product was recrystallized using ethyl acetate. The product was characterized using NMR and unfortunately the resultant product was 1,3,5-BTC. It is understood that the methyl ester bond has been hydrolysed during the process.

2. In the above step, even though a small amount of acid was used, when Cu^{2+} ions exchange with H^+ in DOW-EX, the medium becomes more acidic. Therefore direct exchange of Cu^{2+} with H^+ using Dow-Ex without adding any acid was attempted. The resultant product was then analysed using NMR, but unfortunately the result was the same.

3. NaOH was used to break the Cu-O bonds of the framework instead of HCl. Since $Cu(OH)_2$ is a precipitate, the idea behind the addition of NaOH was to have an exchange reaction with the MOF material. This reaction was successfully accomplished by precipitating the $Cu(OH)_2$ and leaving the sodium salt of the monoester in the solution. Then the solvent was evaporated and the resulting product was subjected for further analysis such as NMR studies (Figure 5.33).

When STAM-1 was treated with NaOH, it not only hydrolyzed the Cu-O bonds in the framework but a small amount of ester hydrolysis can also be seen. Therefore the end result was a mixture of BTC and mmBTC, but it always gave a higher yield (~ 90%) of mmBTC.
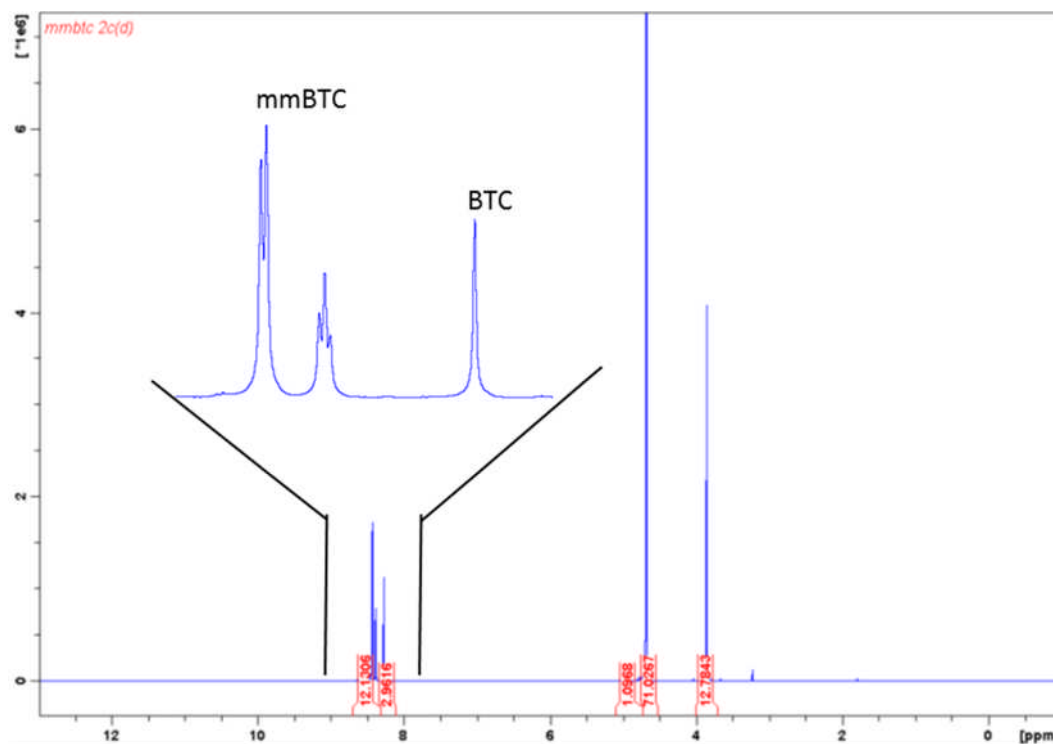
Figure 5.33. NMR spectrum of the isolated product from STAM-1 [^{1}**H-NMR**

(400 MHz, D$_2$O, 25 °C): δ = 3.80 (s, 3H), 8.28 (s, 3H), 8.39 (t, 1H), 8.44 (d,

2H)].

The full crystalline version of STAM-1 was made in 4 days and the yield was

increased from 40% at day 4 to 95% with a further 3 days heating (7 days in

total). In a similar way the yield of mmBTC was increased proportionally from 4

days to 7 days heating and the maximum yield of 95% of mmBTC was recovered

from the complete version of STAM-1 after 7 days.

The resultant solutions from day 1 to 7 days heating also were analysed in order to

get any evidence for the presence of mmbtc. The solvents were evaporated from

each solution and the resulted solids were subjected to, either, direct NMR analysis or first treated with 1M NaOH and then analysed by NMR.

The direct NMR analysis did not give clear spectra due to the presence of paramagnetic Cu ions. When the solids were treated with 1M NaOH and analysed by NMR the results were either the expected spectrum of BTC or messy spectra due to the presence of Cu ions. Since the exact stoichiometric amount of NaOH needed for the reaction cannot be calculated, the reaction was completed either by hydrolizing the Cu-O bonds as well as O-Me bonds giving BTC as the only product or it hydrolyzed some bonds by leaving Cu in the sample. Therefore the isolation of the mmbtc from the solution was not a success.

From the above results it is clear that the monomethyl ester BTC linker can be recovered from STAM-1 by careful dissolution of the MOF in aqueous NaOH (slow, dropwise addition – see Chapter 4.13) followed by the removal of the precipitated copper hydroxide by filtration and evaporation of the solvent. This step gives a high yield of mmBTC (typically 95%). STAM-1 therefore acts as a protecting group for two of the three carboxylic acid units of the BTC, enabling functionalisation for only one of the acid groups. The direct monoesterification of BTC is not known in the organic chemistry literature, and there are no reported protecting group strategies that can accomplish this transformation. The routes to the mono-methyl ester that have been developed require multi-step synthesis, beginning with the triesterification of BTC, followed by controlled hydrolysis of the ester groups, and by separation of the resulting mixtures of BTC itself, from

the mono-, di-ester and tri-ester derivatives. This type of procedure necessarily leads to considerably lower yields (<40%) for the overall process.[24,25] In contrast, the protecting group function of STAM-1 leads to a new and easily accessible high yielding (almost quantitative) synthetic methodology, which could be of use in the preparation of, for example, new cores for dendrimer synthesis,[26] synthons for supramolecular chemistry,[27] as well as of course in the synthesis of other MOFs.

5.11. Synthesis of new materials from mmBTC linker

New MOFs were prepared from the recovered sodium monomethyl BTC derivative. Since the mmbtc ligand has two coordination modes available, it can be coordinated with different metals in order to obtain complexes with novel structures. Chapter 4 illustrates the different synthetic procedures followed in this section. All the materials synthesized were characterized using PXRD and are shown in Figure 5.34.
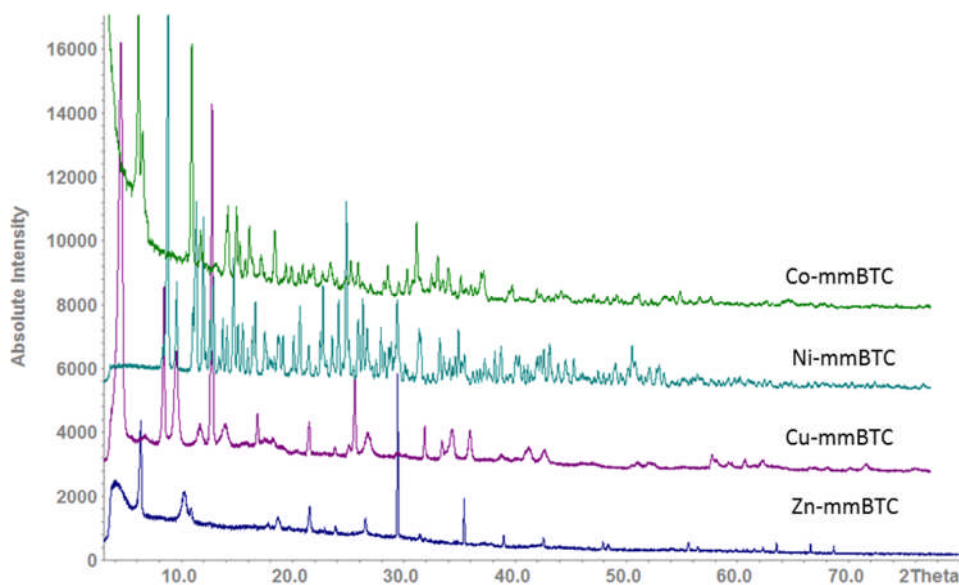
Figure 5.34.   PXRD patterns of the materials synthesized using mmBTC linker

The Ni-mmBTC and Cu-mmBTC were obtained as single crystal quality products whereas the Co-mmBTC and Zn-mmBTC were polycrystalline materials. The crystal structures of the Co-mmBTC and Zn-mmBTC are yet to be solved using the PXRDs obtained. Examination of the presence of the functional groups for all four Metal-mmBTC materials revealed that only the Zn-mmbtc contains the ester group in the MOF structure. Figure 5.35 shows the solid state NMR result of the Zn-mmbtc. The resonance at around 50 ppm (singlet) indicates the presence of the methyl ester moiety intact in the structure. The NMR also shows the presence of ethanol occluded in this material (the two coupled resonances around 50 ppm), which comes from the synthesis procedure.
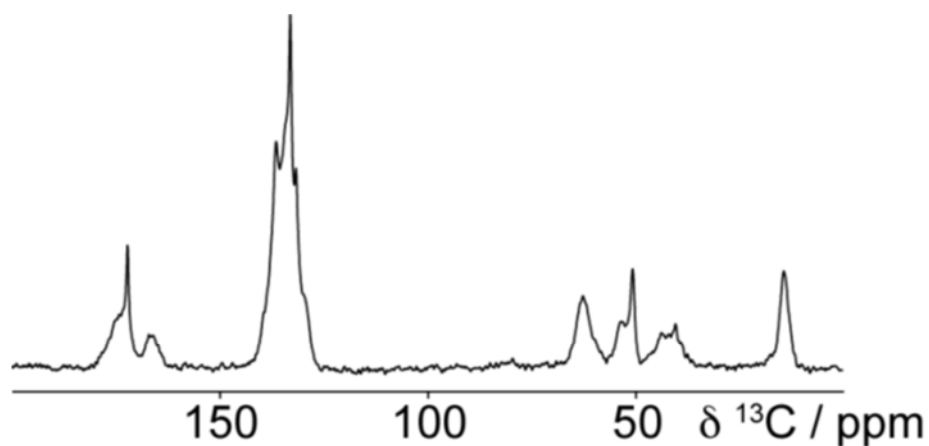
Figure 5.35. ^{13}C MAS NMR spectrum of Zn-Na$_2$mmBTC.

The structure of the Ni-Na$_2$mmbtc was solved using single crystal X-ray diffraction data shown in Table 5.3. As described in detail in Chapter 4.15, the reaction involved Ni(NO$_3$)$_2$ and Na$_2$mmbtc in methanol and water. The resulting product has a formula of Ni$_3$Na(OH)$_3$ (C$_9$O$_6$H$_4$)$_2$·10H$_2$O with both Ni and Na are incorporated in the structure giving a mix metal MOF. The methyl ester has been hydrolysed due to the hydrothermal conditions used in the preparation of the MOF. Therefore the ligand of the resulting structure is BTC. The PXRD of the as made material is well match with the theoretical pattern which was generated using the single crystal X-ray diffraction data (Figure 5.36).

Table 5.5.   Crystal data for structure determination of Ni-Na$_2$mmBTC (Full

details of the refinement can be found in the cif in the Appendix 2)

| Identification code	Ni-Na$_2$mmBTC
Empirical formula	Ni$_3$Na(OH)$_3$(C$_9$O$_6$H$_3$)$_2$·10H$_2$O
Formula weight	844
Temperature	150(2) K
Wavelength	0.7710 Å
Crystal system, space group	Orthorhombic, Pbca
Unit cell dimensions	a=14.4300(38) Å
	b= 18.8000(49) Å
	c= 21.3562(56) Å
Volume	5793.5(4) Å^3
Z	8
Calculated density	0.89 g cm^{-1}
Adsorption coefficient	2.583 mm^{-1}
F(000)	3272
Crystal size	0.07 x 0.07 x 0.03 mm
Theta range for data collection	2.36 to 33.52 deg
Limiting indices	0<=h<=20, 0<=k<=16, 0<=l<=23
Reflections collected/unique	5459/4486 [R(int) = 0.0832]
R1 (I > 2σ(I), wR2 (All data)	0.1382, 0.3608
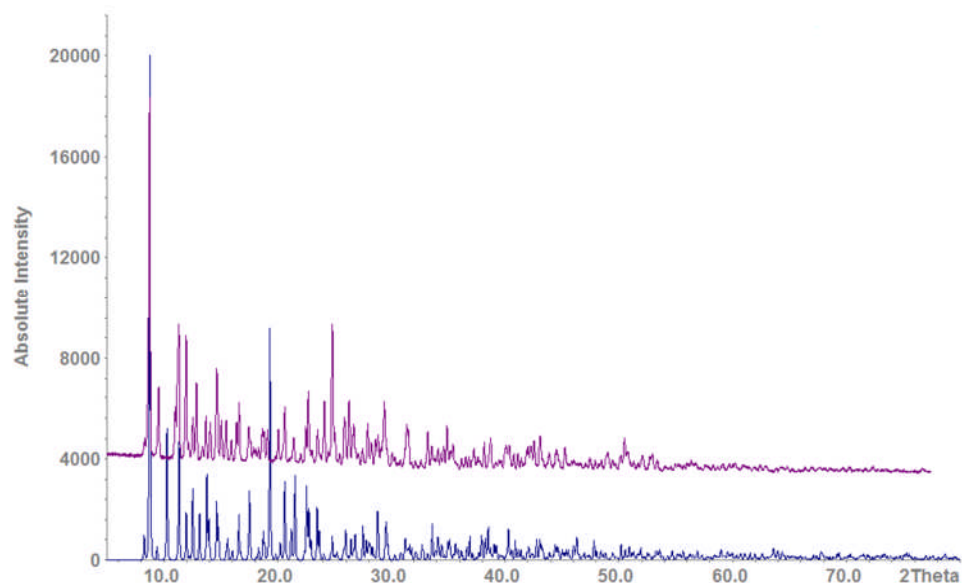
Figure 5.36. A PXRD comparison of the as made material of Ni-Na$_2$mmBTC

(top) and the simulated pattern based on the single crystal X-ray diffraction data

(bottom)

A nickel trimer can be seen in the structure, where each Ni adopts a distorted

octahedral geometry by coordinating with BTC and water molecules (Figure

5.37). Two types of BTC can be seen in the repeat unit (Figure 5.38) of the

material due to its coordination modes with metals. In one case two carboxylates

of BTC bind with four Ni centres leaving one carboxylic group unbound where as

in the other case only one carboxylate coordinates with two Ni centres leaving

two carboxylic groups chemically unbound. Ni and BTC make the 2D ridged

layers (Figure 5.39) while the water molecules bound to the axial positions of the

Ni centres prevent the 2D layers extend in to 3D. The Na species are solvated with
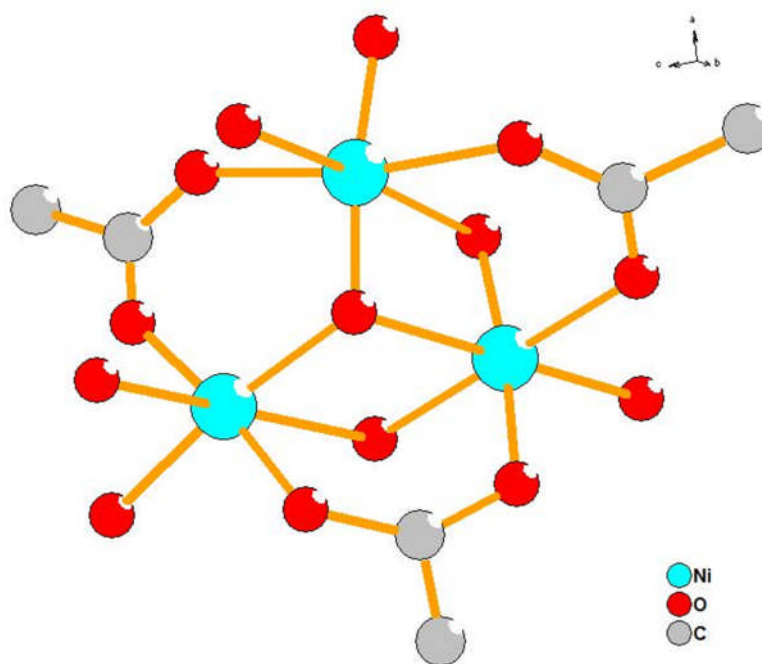
six water molecules.

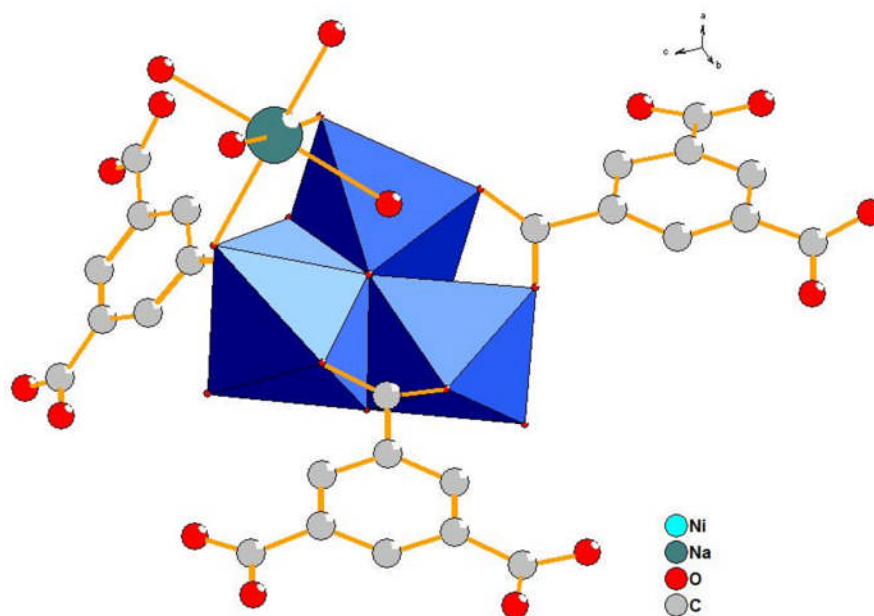**Figure 5.37.** Ni trimer in Ni-Na₂mmBTC

Figure 5.38. Repeat unit of Ni-Na₂mmBTC (Hydrogen atoms are omitted for
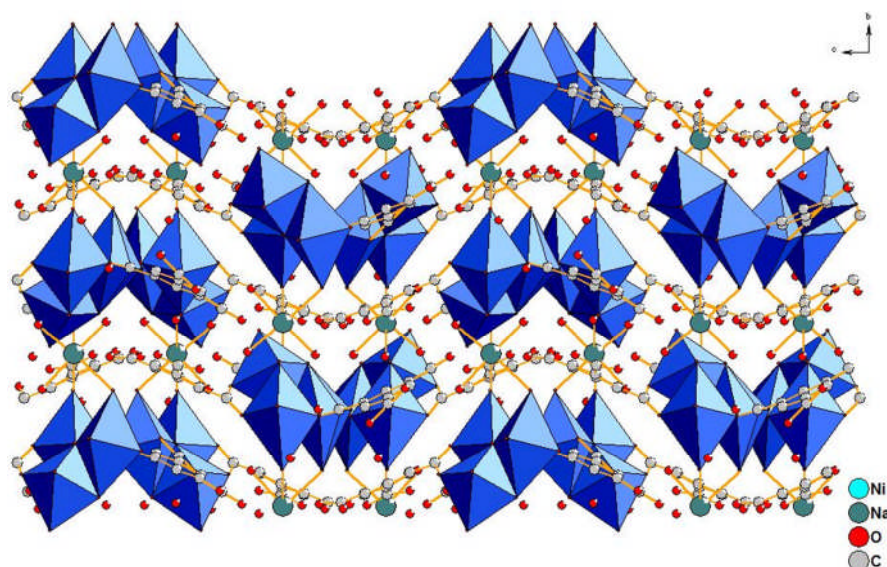
clarity)

Figure 5.39. Structure of Ni-Na$_2$mmBTC along the *a-axis*

The structure solution of Cu-mmBTC was attempted using single crystal XRD data but the size of the crystals was too small for the in house XRD analysis. Therefore these crystals are to be analysed using synchroton radiation source. The SEM image of the crystals can be seen in Figure 5.40. Various analyses were carried out in order to understand the structural features of this material. The EDX analysis (Figure 5.41) gives a clue of a mix metal MOF by showing presence of both Cu (16%) and Na (0.65%). Although EDX shows a low Na content in the material, ICP shows 22% of Cu and 8% of Na. Thermogravimetric analysis reveals that the material is stable until 573 K and about 7.46% of a mass loss is seen below 473 K without collapsing the framework (see Appendix 7, A7.4).
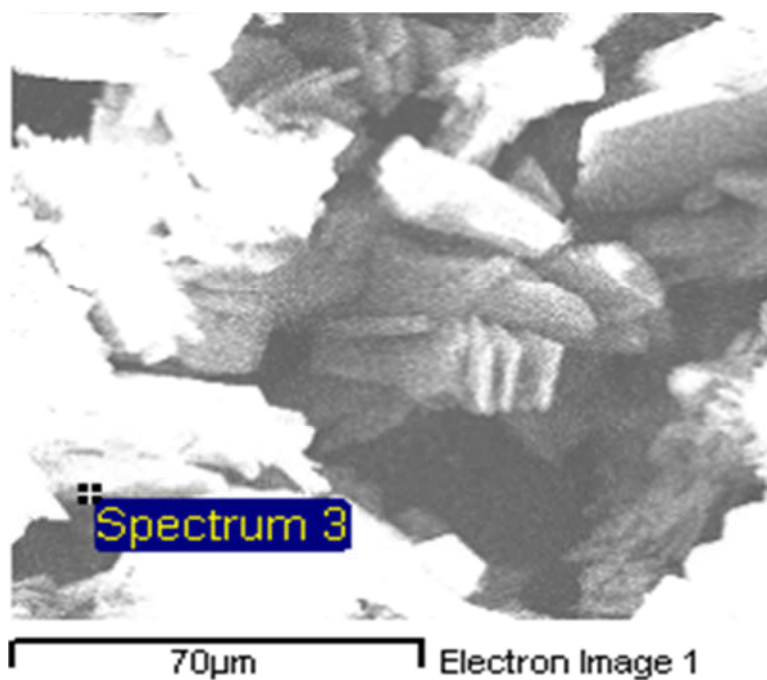
Figure 5.40. SEM micrograph of Cu-Na$_2$mmBTC
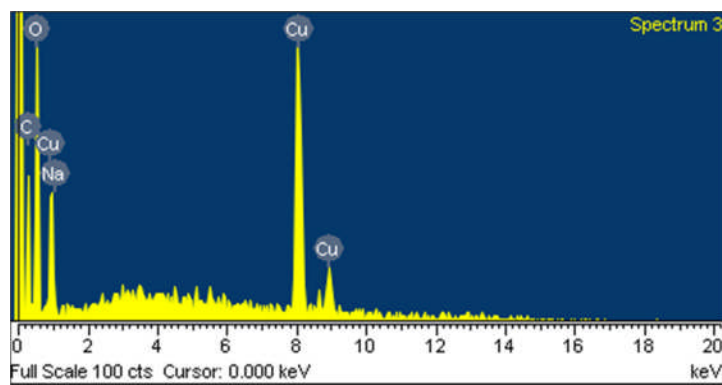
Element	Weight%	Atomic%
C	26.68	48.36
O	25.64	34.88
Na	0.69	0.65
Cu	46.99	16.10
Totals	100.00	

Figure 5.41. EDX analysis for Cu-Na$_2$mmBTC

5.12. Other Examples to Generalise *In situ* Esterification

The direct, high yield monoesterification of BTC is unknown adds to the considerable surprise that STAM-1 forms at all, and also opens up the use of MOFs as protecting groups to enable selectivity that is difficult to achieve in organic chemistry. An important question is whether the formation of STAM-1 is an oddity, or are there other examples where a MOF can be used as a protecting group in this manner? Equally important is the development of a strategy to find likely examples of such an effect without taking recourse to exhaustive exploration of chemical synthesis space. It is clear from our work presented here that the two criteria needed to be fulfilled to achieve the desired results are:

- Firstly, there must be a possible transformation of the ligand under conditions that are the same or similar to those used to prepare MOFs

- Secondly, if there is a mixture of products from such a transformation, the preferred product should crystallise preferentially

Clearly, if the first criterion is met with a high yielding reaction the second criterion will be moot, as the required MOF will crystallise out by default. In the preparation of STAM-1 the copper metal seems to be a vital part of the successful reaction. Using this methodology we have now identified two other methyl esterification reactions; one is a monoesterification of the 1,3,5-tris(4-carboxyphenyl) benzene (BTB) ligand (Figure 5.42), and the other is the

diesterification of pyromellitic dianhydride (Figure 5.43). Details are discussed in

the sections 5.12.1 and 5.12.2. The remaining example we have identified to date

is the selective monodecarboxylation of 1,3,4-BTC to benzenedicarboxyalate,

where again two of the carboxylate groups are protected (Figure 5.44).[28] This is of

lower interest as a synthetic procedure but serves as an additional 'proof of

concept' experiment. Therefore it seems that STAM-1 is not the only MOF that

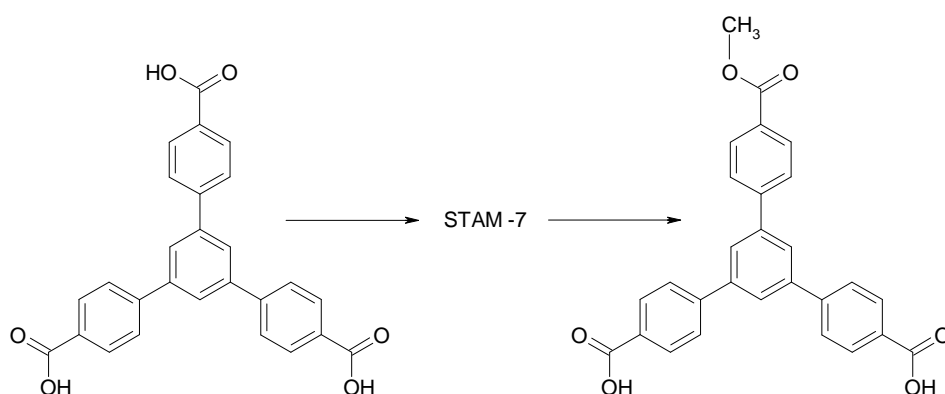could be used as a 'protecting group' but that others are possible.
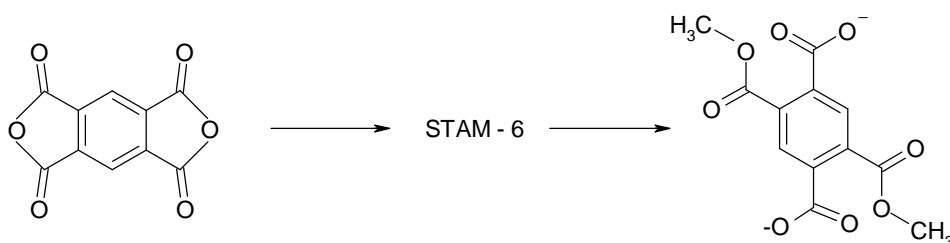

Figure 5.42. Selective monoesterification of BTB ligand

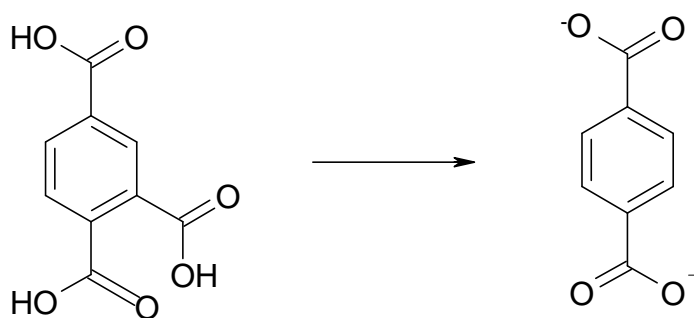**Figure 5.43.** Diesterification of pyromellitic dianhydride

Figure 5.44. Monodecarboxylation of 1,3,4-BTC[19]

5.12.1.   Synthesis of STAM-6

One of the ways to generate polycarboxylato anions *in situ* is by ring opening reactions of dianhydrides. The ring opening reaction of pyromellitic dianhydride by methanol is an effective method to prepare first row transition metal dicarboxylate complexes. The reactions of different first row transition metal salts with pyromellitic dianhydride in the presence of 1-10-phenanthroline or 2,2-bipyridine has been previously studied by Baruah *et al.*[29] The purpose of the addition of 1,10-phenanthroline or 2,2-bipyridine to the reaction medium should be to limit the metal coordination and to obtain simple metal complexes. Therefore MOF structures should be obtainable by replacing 2,2-bipyridine with 4,4-bipyridine which will then facilitate to extend the framework in to higher dimensionalities. By following this methodology STAM-6 was synthesized using nickel acetate and pyromellitic dianhydride in methanol in the presence of 4,4-bipyridine (see Chapter 4.7 for detailed experimental procedure).

The resulting product was obtained as small single X-ray quality crystals. The PXRD pattern of the material is shown in Figure 5.45. This product has IR adsorption at 1650 cm^{-1} (υ_{COO^-}) corresponding to the stretching frequency of coordinated carboxylate groups. This adsorption is lower in frequency than in free 1,2,4,5-benzenetetracarboxylic acid which lies around 1690 cm^{-1},[30] indicating the formation of the metal organic framework. Also the characteristic ester frequency can be seen at 1735 cm^{-1} (Figure 5.46), showing that the pyromellitic dianhydride ring has opened to form the corresponding ester. The structural characterisation of the material is currently on going.
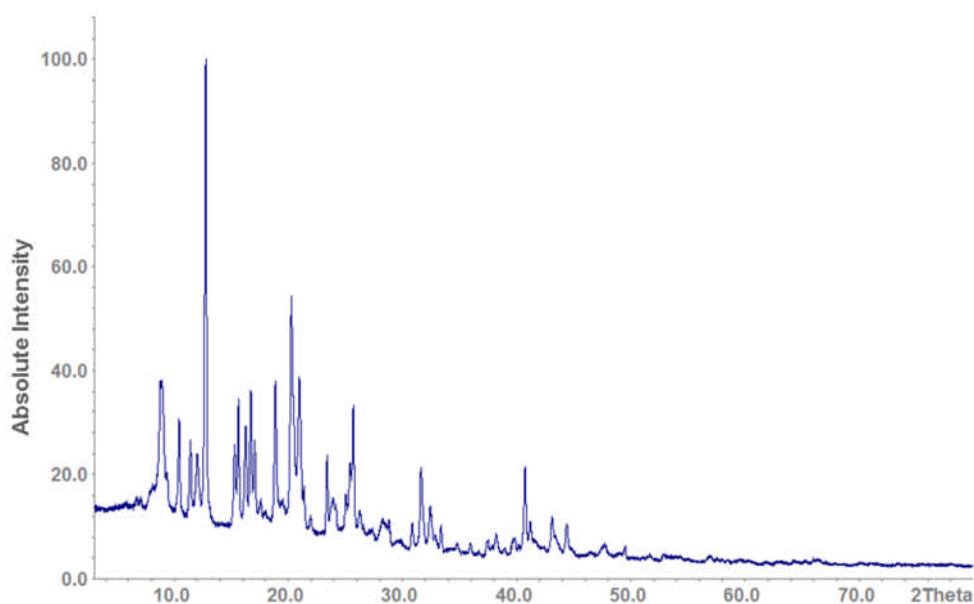

Figure 5.45. PXRD pattern of STAM-6
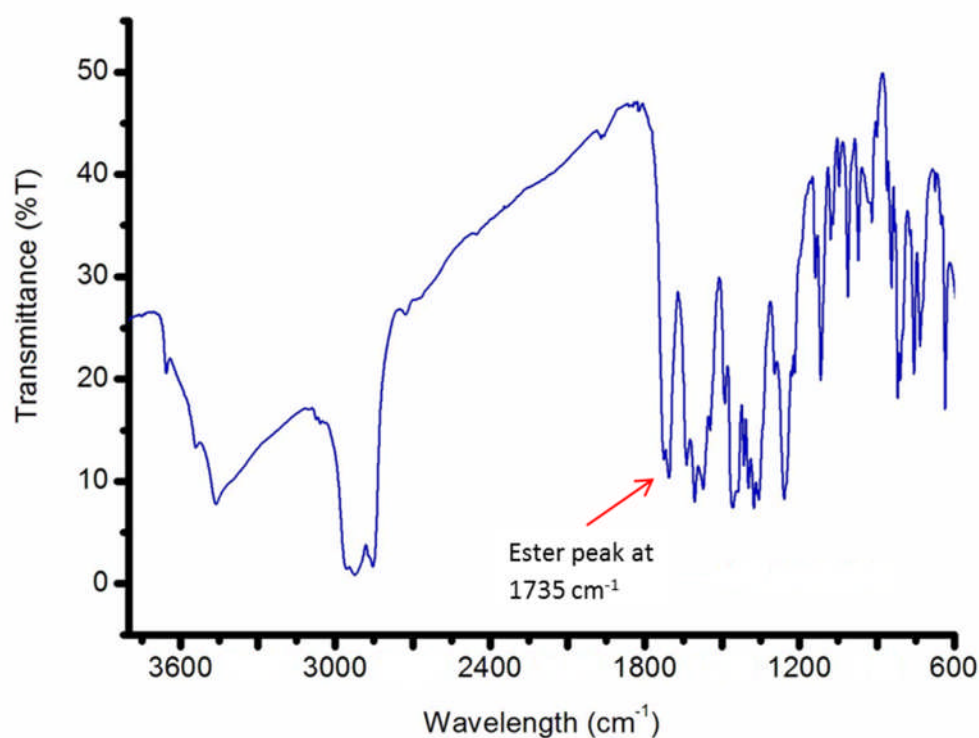
Figure 5.46. IR spectrum of STAM-6

5.12.2.   Synthesis of STAM-7

Yaghi *et al* designed IRMOF series based on MOF-5 to produce the octahedral cluster with a ditopic carboxylate link *in situ*.[31] The simplicity of the method and the facility with which IRMOF-1 was obtained indicated that the use of other carboxylate links under closely related, if not identical, conditions would yield the same type of frameworks with diverse pore sizes and functionalities. Based on the above fact, a MOF which has the same topology as STAM-1 should be able to obtain using BTB linker under same conditions. But increasing the length of the bridging ligand leads to larger natural cavity sizes, resulting in mutually interpenetrated networks. For example when BTB ligand is used instead of BTC

leaving all other synthetic conditions the same as applied in the synthesis of HKUST-1, the resulting framework was a unique interpenetrating 2D structure[32] instead of having the same topology as HKUST-1.

STAM-7 was synthesized using copper nitrate and BTB linker with the same conditions applied to STAM-1 (see Chapter 4.8 for detailed experimental procedure). The resulting product was then subjected to PXRD (Figure 5.47) and confirms that the material is in the crystalline form.
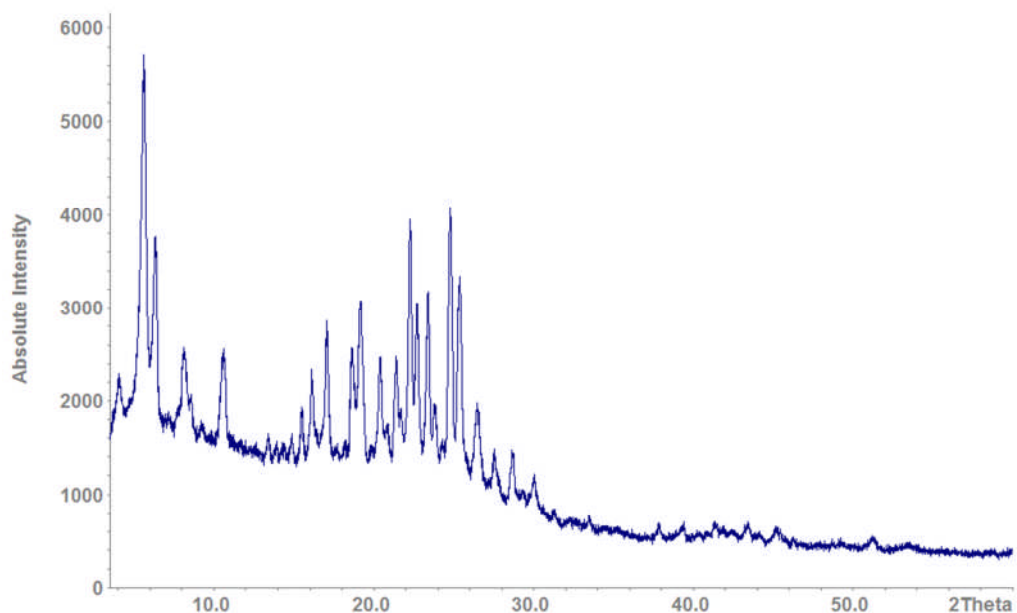
Figure 5.47. PXRD pattern for STAM-7

According to the IR analysis the adsorption at 1705 cm^{-1} (υ_{COO}-) corresponding to the stretching frequency of coordinated carboxylate groups. The characteristic ester frequency can be seen at 1726 cm^{-1} (Figure 5.48), indicating that the

esterification reaction has taken place *in situ*. The methyl peak at 52 ppm in the ^{13}C MAS NMR (Figure 5.49) further confirms the presence of the ester group. The peaks between 110 – 150 ppm are due to the aromatic rings present in the structure. The peak at 167 ppm is due to the ester carbon peak. The structural characterisation of this material is currently on going.

Figure 5.48.   Infrared spectrum of STAM-7
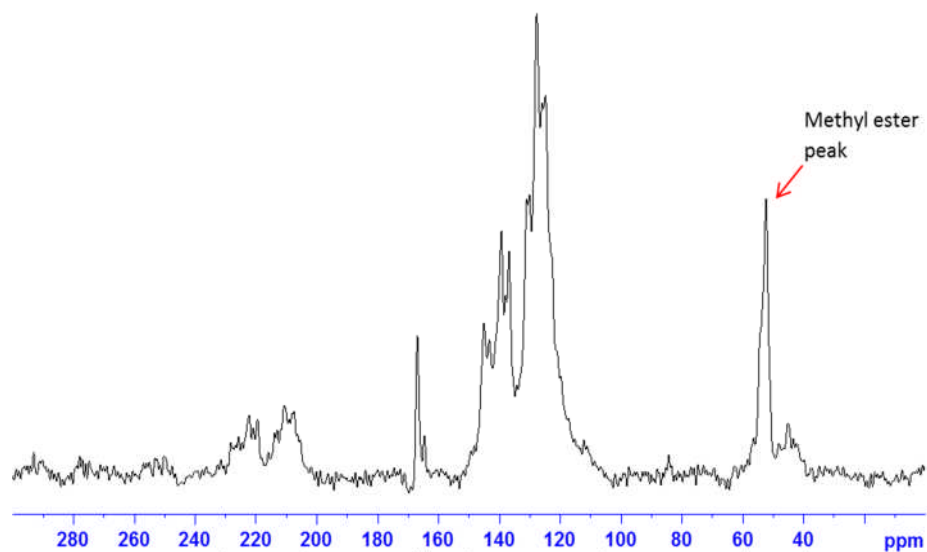
Figure 5.49. ^{13}C MAS NMR spectrum of STAM-7

5.12.3.   Effect of other Alcohols on Esterification

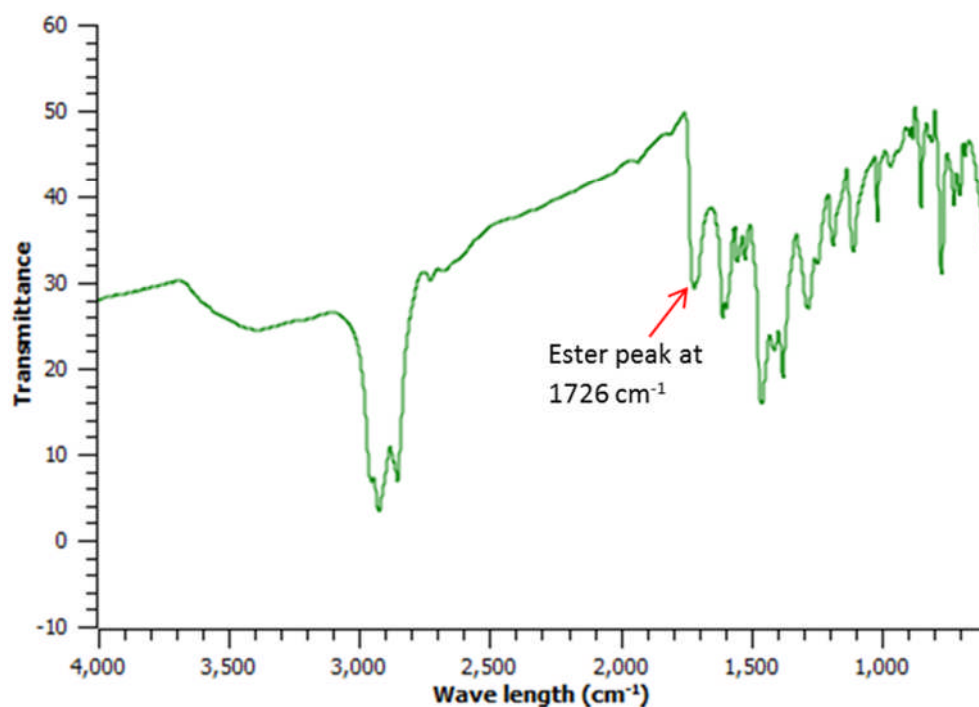Esterification using methanol is clearly successful in this type of synthesis. However, an important question is can the work be extended to other alcohols. Copper-catalyzed esterifications of simple aromatic carboxylic acids are known in the literature, at conditions that are not unlike those used to prepare MOFs (although using anhydrous alcohols as the solvent rather than alcohol:water mixtures).[33]The reports are that both methanol and ethanol give esterification products in good yields, but that the efficiency with which the esterification takes place diminishes rapidly as the size of the alcohol further increases, isopropyl alcohol gives lower yields and t-butyl alcohol gives only negligible amounts of the corresponding ester. In our work there is clear evidence, using conditions close to those in the work of Ho *et al*,[33] that ethyl esters form in the solution

rapidly in very good yield but as yet we have not been able to obtain an ethyl ester analogue of STAM-1 of sufficient crystallinity for structural characterisation and determination of its physical properties.

5.13. Conclusion

Here we have discussed the preparation of a MOF which undergoes selective linker derivatisation leading to the formation of a porous MOF with both hydrophilic and hydrophobic channels. The direct monoesterification of BTC formed by STAM-1 opens up MOFs to act as protecting tools in synthetic chemistry. Given that metal ions catalyze many organic chemistry transformations it is likely that there are several more examples of similar phenomena waiting to be discovered. Clearly, the potential for developing analogous reactions is great and further studies in this and related systems should enable synthetic routes to materials with different properties to those available at the present time.

Also preparation of STAM-2 from STAM-1 shows that materials of totally different architectures can be designed using physical and chemical techniques. STAM-3 appears to be more condensed structure than STAM-1. The ultrasonication which was employed to obtain STAM-2 and STAM-3 will be a good experimental technique for future material synthesis.

5.14. References

(1)   Zheng, N. F.; Bu, X. H.; Feng, P. Y. *J Am Chem Soc* **2002**, *124*, 9688.

(2)   Zhang, X. M.; Tong, M. L.; Chen, X. M. *Angew Chem Int Edit* **2002**, *41*, 1029.

(3)   Xiong, R. G.; Xue, X.; Zhao, H.; You, X. Z.; Abrahams, B. F.; Xue, Z. L. *Angew Chem Int Edit* **2002**, *41*, 3800.

(4)   Zhang, J. P.; Zheng, S. L.; Huang, X. C.; Chen, X. M. *Angew Chem Int Edit* **2004**, *43*, 206.

(5)   Hu, X. X.; Xu, J. Q.; Cheng, P.; Chen, X. Y.; Cui, X. B.; Song, J. F.; Yang, G. D.; Wang, T. G. *Inorg Chem* **2004**, *43*, 2261.

(6)   Xiao, D. R.; Hou, Y.; Wang, E. B.; Lu, J.; Li, Y. G.; Xu, L.; Hu, C. W. *Inorg Chem Commun* **2004**, *7*, 437.

(7)   Blake, A. J.; Champness, N. R.; Chung, S. S. M.; Li, W. S.; Schroder, M. *Chem Commun* **1997**, 1675.

(8)   Chui, S. S. Y.; Lo, S. M. F.; Charmant, J. P. H.; Orpen, A. G.; Williams, I. D. *Science* **1999**, *283*, 1148.

(9)   Seo, Y. K.; Hundal, G.; Jang, I. T.; Hwang, Y. K.; Jun, C. H.; Chang, J. S. *Micropor Mesopor Mat* **2009**, *119*, 331.

(10)   Mueller, U.; Schubert, M.; Teich, F.; Puetter, H.; Schierle-Arndt, K.; Pastre, J. *J Mater Chem* **2006**, *16*, 626.

(11)   Pech, R.; Pickardt, J. *Acta Crystallogr C* **1988**, *44*, 992.

(12)   Chui, S. S. Y.; Siu, A.; Williams, I. D. *Acta Crystallogr C* **1999**, *55*, 194.

(13)   Farha, O. K.; Spokoyny, A. M.; Mulfort, K. L.; Galli, S.; Hupp, J. T.; Mirkin, C. A. *Small* **2009**, *5*, 1727.

(14)   Barron, P. M.; Son, H. T.; Hu, C. H.; Choe, W. *Cryst Growth Des* **2009**, *9*, 1960.

(15)   Wang, L. Y.; Vysotsky, M. O.; Bogdan, A.; Bolte, M.; Bohmer, V. *Science* **2004**, *304*, 1312.

(16)   de Silva, N.; Ha, J. M.; Solovyov, A.; Nigra, M. M.; Ogino, I.; Yeh, S. W.; Durkin, K. A.; Katz, A. *Nat Chem* **2010**, *2*, 1062.

(17)   Jiang, Y. J.; Huang, J.; Kasumaj, B.; Jeschke, G.; Hunger, M.; Mallat, T.; Baiker, A. *J Am Chem Soc* **2009**, *131*, 2058.

(18)   Li, H.; Eddaoudi, M.; O'Keeffe, M.; Yaghi, O. M. *Nature* **1999**, *402*, 276.

(19)   Huang, L. M.; Wang, H. T.; Chen, J. X.; Wang, Z. B.; Sun, J. Y.; Zhao, D. Y.; Yan, Y. S. *Micropor Mesopor Mat* **2003**, *58*, 105.

(20)   Jee, B.; Eisinger, K.; Gul-E-Noor, F.; Bertmer, M.; Hartmann, M.; Himsl, D.; Poppl, A. *J Phys Chem C* **2010**, *114*, 16630.

(21)   Chalati, T.; Horcajada, P.; Gref, R.; Couvreur, P.; Serre, C. *J Mater Chem* **2011**, *21*, 2220.

(22)   Oszlanyi, G.; Suto, A. *Acta Crystallogr A* **2008**, *64*, 123.

(23)   Qiu, L. G.; Li, Z. Q.; Wu, Y.; Wang, W.; Xu, T.; Jiang, X. *Chem Commun* **2008**, 3642.

(24)   Roosma, J.; Mes, T.; Leclere, P.; Palmans, A. R. A.; Meijer, E. W. *J Am Chem Soc* **2008**, *130*, 1120.

(25)   Wallace, J. U.; Chen, S. H. *Ind Eng Chem Res* **2006**, *45*, 4494.

(26)   Grayson, S. M.; Frechet, J. M. J. *Abstr Pap Am Chem S* **2001**, *221*, U430.

(27)   Greig, L. M.; Philp, D. *Chem Soc Rev* **2001**, *30*, 287.

(28)   Han, Z. B.; Song, Y. J.; Ji, J. W.; Zhang, W.; Han, G. X. *J Solid State Chem* **2009**, *182*, 3067.

(29)   Baruah, A. M.; Karmakar, A.; Baruah, J. B. *Polyhedron* **2007**, *26*, 4479.

(30)   Kajimoto, T.; Tsuji, J. *J Org Chem* **1983**, *48*, 1685.

(31)   Eddaoudi, M.; Kim, J.; Rosi, N.; Vodak, D.; Wachter, J.; O'Keeffe, M.; Yaghi, O. M. *Science* **2002**, *295*, 469.

(32)   Mu, B.; Li, F.; Walton, K. S. *Chem Commun* **2009**, 2493.

(33)   Ho, T. L. *Synthetic Commun* **1989**, *19*, 2897.

Chapter 6   Gas Adsorption and Separation

Properties of STAM-1

6.1.   Introduction

Flexible MOFs have received increasing attention because of their unique molecular accommodation characteristics.[1-6] In contrast to robust porous frameworks; guest sorption processes with a structural change have a highly complex mechanism where both guest accommodation and the structural transformation occur at the same time. This ability suggests that these MOFs can exhibit a structural flexibility different from the zeolites or activated carbon. Moreover some of the MOFs reported today such as MIL-53[7] and MIL-88[8] produce the distinct structural transformation induced by guest molecules. This means that flexibility and transformability of the framework have significant influences on the sorption behaviour, which leads to unconventional opportunities to control the porous properties.

Since flexible MOFs are structurally transformable, the host guest interactions would act as a ''self-tuning mechanism'' in order to adjust the pore shape and size.[6] Selective sorption and separation is another advantage of flexible MOFs. Flexibility and a functional surface enable effective selectivity in the MOFs.[6] Structural flexibility, gas adsorption and separation properties of STAM-1 will be discussed in this Chapter. Some of the gas adsorption experiments discussed here

were carried out at the Newcastle University by Prof. Mark Thomas's group and the molecular modelling studies were carried out at University of Edinburgh by Dr Tina Düren's group as part of the collaboration.

6.2. Dehydrated STAM-1

In order to understand the porosity of materials, it is clear that the solvent molecules which are included in framework should be removed or exchanged without the loss of framework integrity. Sometimes people tend to describe the porosity of MOFs which have solely been characterized by crystallographic analysis.[9] This is clearly inappropriate since they have no idea about the stability of the framework after loss of solvent molecules. These ''open frameworks'' are described as materials which contain disordered, unbound solvent molecules in their channel systems and allow them to flow freely through the void spaces of the well-defined framework.[9] PXRD is the most common method to use to analyse the stability of the material after being subjected to heating or evacuation. Usually the result is compared with the calculated pattern of the host structure or experimental pattern of the as made material. Then these results can be correlated with the TGA analysis which gives an idea about the temperature at which desorption of the guest molecules occur as well as the temperature of the decomposition of the framework and any other transitions of the framework. Sometimes the solvent desorbed material is characterised using elemental analysis, IR and/or NMR techniques. In some cases if the quality of the crystals is still good enough after desolvation, single crystal specimens can be examined.[9]

Thermogravimetric analysis indicates that the guest molecules are lost from STAM-1 up to about 423 K (Figure 6.1) and PXRD confirms that the material after desolvation remains crystalline (Figure 6.2). Also the framework is stable until around 623 K. The guest molecules and the coordinated water molecules represent about 13% of the overall weight of the material. Mass spectrometry experiments indicate that only water and no methanol or carbon dioxide is given off below 573 – 623 K (Figure 6.1). High resolution X-ray diffraction reveals small but significant changes in the unit cell parameters and during the dehydration the shape of the unit changes slightly and the symmetry of the material is lowered from trigonal to triclinic (Figure 6.3).
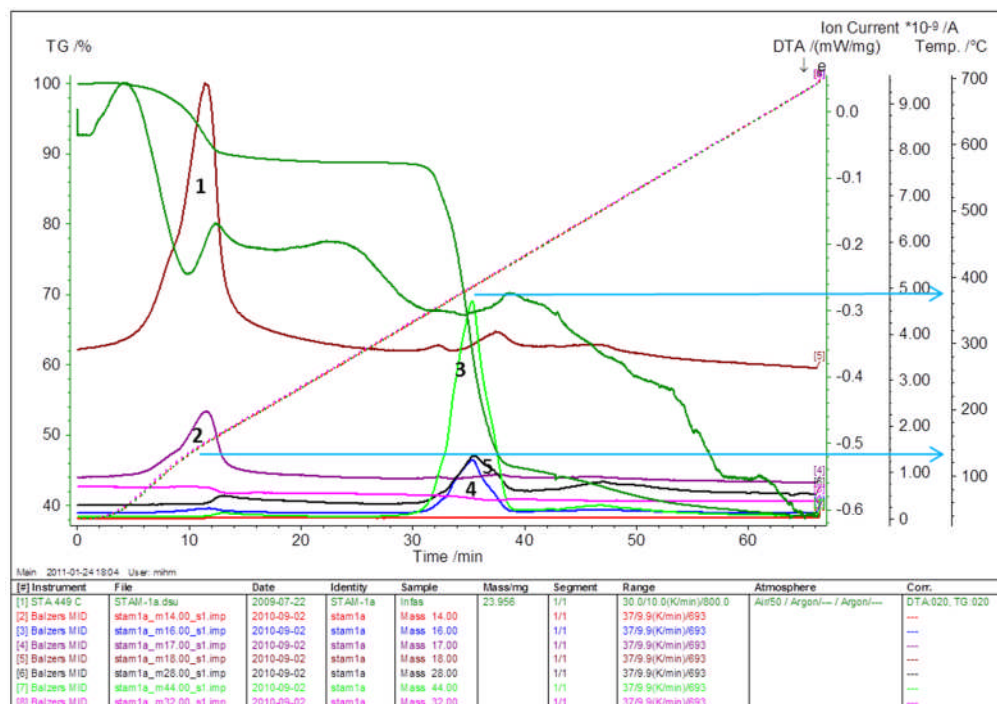
Figure 6.1.　　TG – MS spectrum of STAM-1. 1 and 2 peaks in the Figure refers

to H_2O and OH suggesting only water (guest water molecules include coordinated

water molecules) comes out below 423 K (150 ℃) and peaks 3, 4 and 5 are CO_2,

CO and O coming out around 673 K (400 ℃) . Figure 5.1 also shows that the

decomposition of the framework occurs at around 673 K (400 ℃). This

temperature is where the organic fractions come out, causing the framework to
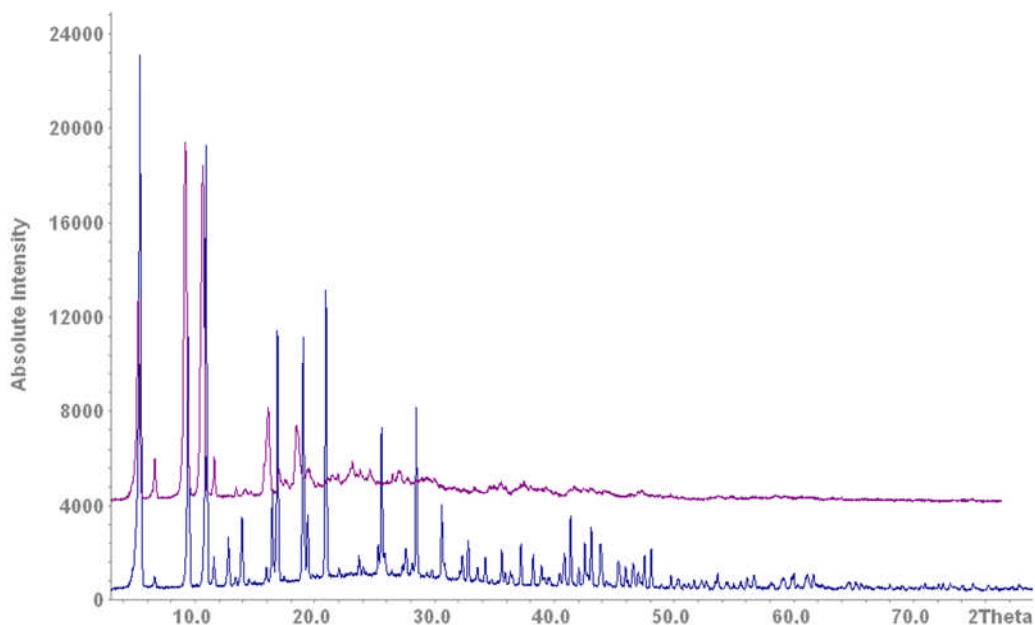
collapse.

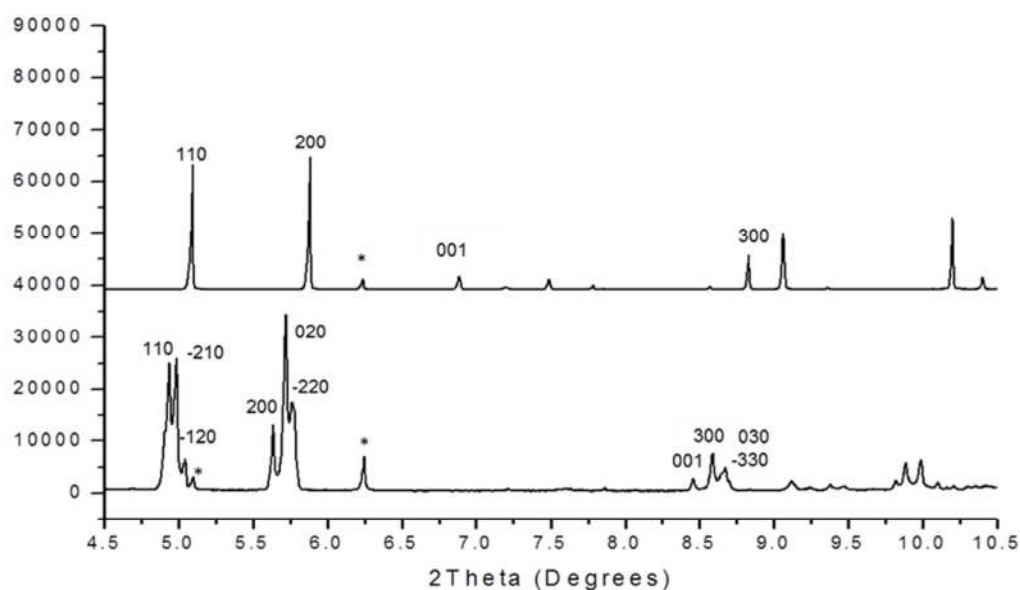**Figure 6.2.**   A comparison of PXRD of STAM-1 dehydrated (top) and STAM-1

as made (bottom).

Figure 6.3.   High resolution synchrotron X-ray (λ= 0.82744 Å) diffraction

pattern of as made STAM-1 (top) and dehydrated STAM-1 (bottom) collected at

the Diamond light source, Station I 11. * Represents the peaks resulted due to the

impurity HKUST-1.

A refined dehydrated unit cell gives a triclinic cell of a = 19.411 (2) Å, b = 19.512 (3) Å, c = 5.901 (1) Å α = 75.96 (1) °, β = 99.08 (1) °, γ = 120.23 (1) °. The changes show a slight increase in the *a* and *b* directions but a decrease in the *c* – direction. Overall the unit cell decreases in volume by slightly less than 10%. These changes are all consistent with adsorption into dehydrated STAM-1 which is described in the following sections. Diffraction from dehydrated STAM-1 dies off at around 2θ = 20° for this sample, making full unconstrained Rietveld analysis of the material unrealistic. Changes also occur in the solid state ^{13}C NMR of dehydrated STAM-1 with the methyl resonance slightly broadening and larger changes happening to the aromatic resonances, which is consistent with the aromatic carbons being closer to the hydrophilic pore and the site of water in the hydrated STAM-1 structure (Figure 6.4). The resonance at 227 ppm which was seen in the ^{13}C MAS solid state NMR spectrum obtained for STAM-1 at 600 MHz (Figure 5.12) was not observed in the slow (14 kHz) CP MAS NMR spectrum at 400 MHz shown below.
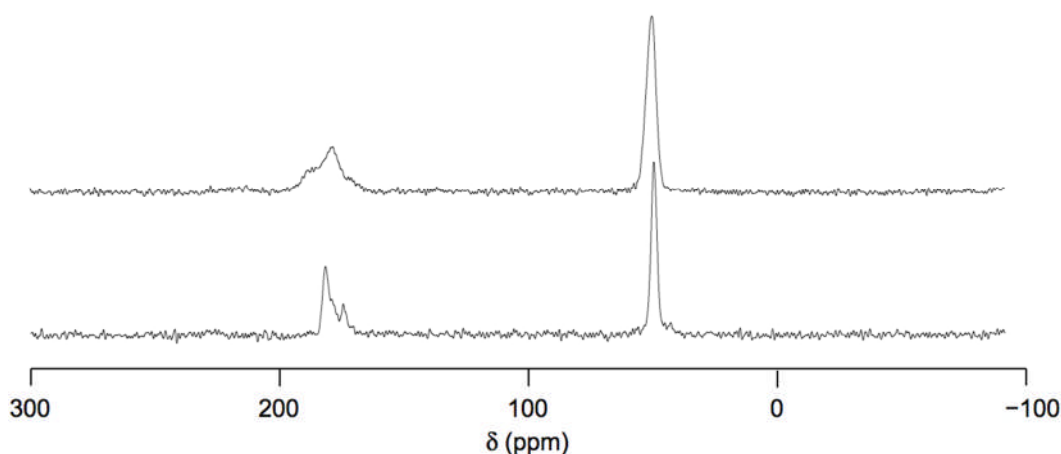
Figure 6.4. ^{13}C NMR spectrum of dehydrated STAM-1(top) and as made material (bottom).

Based on the above data the 'model' shown in Figure 6.5 was produced for the dehydrated STAM-1. This model was obtained *via* Molecular modelling studies by means of the minimal force field using Materials Studio.[10] The atomic coordinates of the model are given in Table 6.1.
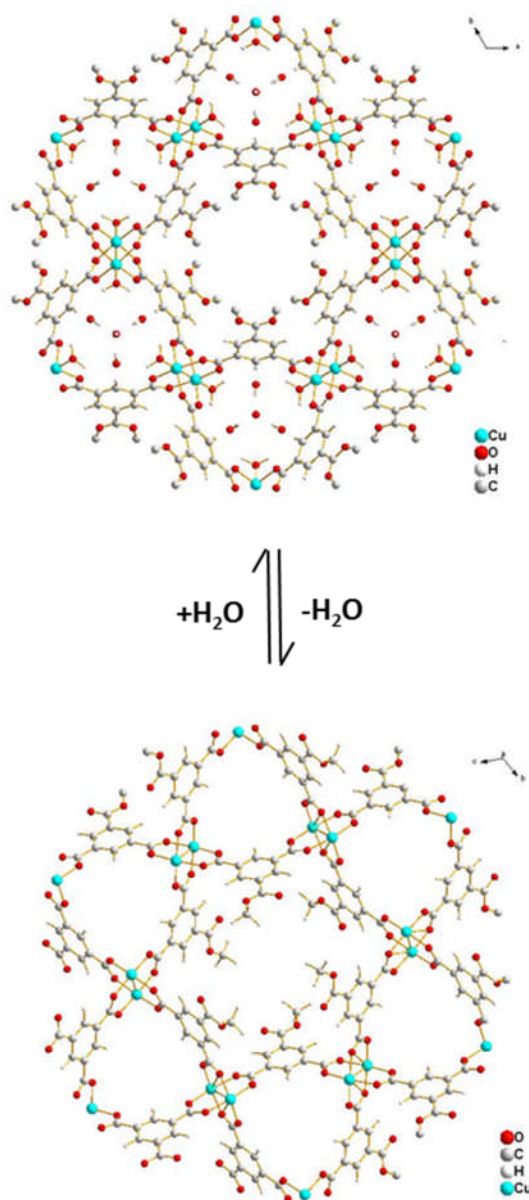

Figure 6.5.   STAM-1 as made (Top), a model of STAM-1 dehydrated (Bottom)

Table 6.1.   Atomic coordinates of the model for the dehydrated STAM-1

Atom	X	Y	Z	Occupancy	Uiso
O1	0.0612	0.2948	0.08319	1	0.06676
O2	-0.65879	0.47971	0.37269	1	0.04589
O3	-0.29582	0.44434	0.40617	1	0.02967
C4	-0.22327	0.38468	0.25321	1	0.02632
H5	-0.09674	0.36828	0.29226	1	0.033
C6	-0.42612	0.42549	0.27483	1	0.02178
C7	-0.46408	0.45078	0.35672	1	0.02061
C8	0.25363	0.24689	0.05208	0.5	0.085
H9	0.26632	0.19514	0.06554	0.5	0.127
H10	0.41493	0.28462	0.07998	0.5	0.127
O11	0.23479	0.80563	0.68594	1	0.06899
O12	-0.88717	0.88768	0.51765	1	0.04773
O13	-0.63315	0.97304	0.55002	1	0.03171
C14	-0.2961	0.87821	0.60567	1	0.02712
H15	-0.24433	0.94111	0.62163	1	0.033
C16	-0.51092	0.8545	0.56769	1	0.02138
C17	-0.68722	0.90864	0.54375	1	0.01937
C18	0.45868	0.82082	0.72565	0.5	0.085
H19	0.57586	0.82856	0.68878	0.5	0.127
H20	0.51792	0.76834	0.7354	0.5	0.127
H21	0.46435	0.87769	0.78519	0.5	0.127
O22	-0.4813	0.93954	0.17575	1	0.08068
O23	-1.07981	0.62433	0.11246	1	0.05406
O24	-0.82103	0.59548	0.03369	1	0.03268
C25	-0.72995	0.75694	0.1187	1	0.0282
H26	-0.66169	0.72347	0.06002	1	0.033
C27	-0.8654	0.72887	0.14589	1	0.02187
C28	-0.92205	0.64436	0.09353	1	0.01998
C29	-0.35929	0.96932	0.14486	0.5	0.085
H30	-0.28064	0.91898	0.09319	0.5	0.127
H31	-0.21907	2.00952	0.19127	0.5	0.127

Atom	X	Y	Z	Occupancy	Uiso
O32	-1.13018	0.07448	0.31565	1	0.0722
O33	-0.35478	0.37286	0.48254	1	0.04866
O34	-0.71966	0.40891	0.44995	1	0.03029
C35	-0.82283	0.24998	0.39331	1	0.0269
H36	-0.96117	0.28467	0.377	1	0.033
C37	-0.60766	0.27455	0.43162	1	0.02195
C38	-0.55996	0.35761	0.45542	1	0.02068
O39	-1.16253	0.70433	0.79698	1	0.06462
O40	-0.10246	0.52182	0.89047	1	0.04532
O41	-0.3571	0.55095	0.96875	1	0.03051
C42	-0.66774	0.61441	0.87438	1	0.02651
H43	-0.71164	0.63079	0.93509	1	0.033
C44	-0.46333	0.57341	0.85315	1	0.02144
C45	-0.29718	0.5469	0.90796	1	0.01983
O46	-0.50365	0.18487	0.93668	1	0.07961
O47	0.07702	0.11397	0.62782	1	0.05371
O48	-0.17928	0.02783	0.59472	1	0.03326
C49	-0.27159	0.11331	0.75572	1	0.02823
H50	-0.34162	0.04978	0.72018	1	0.033
C51	-0.13587	0.14207	0.72849	1	0.02165
C52	-0.07728	0.09099	0.64575	1	0.01945
Cu53	-0.28825	0.47885	0.51943	1	0.01638
Cu54	0.14005	0.04785	0.51834	1	0.01613
Cu55	0.14359	0.48313	0.955	1	0.01628
C56	0.03226	0.31519	0.15479	1	0.03836
C57	-0.18057	0.36345	0.17799	1	0.02846
C58	-0.5838	0.44514	0.2213	1	0.02077
H59	-0.74822	0.47727	0.24086	1	0.025
C60	0.09299	0.85532	0.66833	1	0.04063
C61	-0.13315	0.82745	0.62574	1	0.02995
C62	-0.55592	0.77798	0.5499	1	0.02079
H63	-0.72872	0.74901	0.51925	1	0.025
C64	-0.5395	0.86431	0.13311	1	0.04495
C65	-0.66837	0.83642	0.16753	1	0.03277
C66	-0.93164	0.78014	0.22047	1	0.02077
H67	-1.05421	0.75896	0.24626	1	0.025
H68	0.23177	0.22268	-0.01413	1	0
H69	-0.47121	3.00629	0.12225	1	0

6.3.   Gas adsorption

Permanent porosity is a key for MOFs to be useful for gas storage. These pores are available after removal of guest molecules under thermal application. Having two types of channel system, STAM-1 has an advantage of availability of one channel system, the hydrophobic channel without activation even at room temperature. The solvent molecules in the hydrophilic channel need to be cleared prior to gas adsorption. Therefore gas adsorption studies of STAM-1 were investigated after activation of the material at 393 K for 48 hours under vacuum. It should be noted that the initial synthetic conditions of the material has an influence on the properties of the product as some batches which contained good quality crystals have shown higher uptake of gases whereas the batches which resulted relatively poor quality crystals due to different synthetic conditions gave relatively lower uptake. However this variation is less when considering the total uptake of gases.

6.3.1. N_2 adsorption

Given the double-barrelled nature of the STAM-1 structure the expected difference in chemistry between the hydrophobic and hydrophilic channels should be visible in adsorption experiments, and this is indeed the case. As described below the experimental adsorption measurements have very much different result than the expected from molecular simulations. This difference has arisen due to the structural complexity of STAM-1.

Usually nitrogen molecules take part in physisorption in MOF materials and it is used as a characterisation technique to determine the porosity of materials. The porosity of STAM-1 was determined in a similar way using nitrogen adsorption which includes the surface area measurements. STAM-1 shows almost ideal Langmuir behaviour at 77 K (Figure 6.6), by giving a Langmuir surface area of 219 $m^2 g^{-1}$ and BET surface area of 203 $m^2 g^{-1}$. This was then compared with the surface area obtained using theoretical modelling studies (see Appendix 8, A8.2). In molecular simulations, the accessible surface area is determined geometrically by rolling a nitrogen sized probe molecule across the surface. According to the theoretical studies STAM-1 has an accessible surface area of 420 $m^2 g^{-1}$. This is almost double the value which was obtained experimentally. Therefore this suggests that only one type of channel system is available for nitrogen adsorption in STAM-1. Although the surface area of the material was calculated based on the nitrogen adsorption isotherm at 77 K, the activated diffusion effects of nitrogen adsorption make it not suitable for BET/Langmuir analysis.
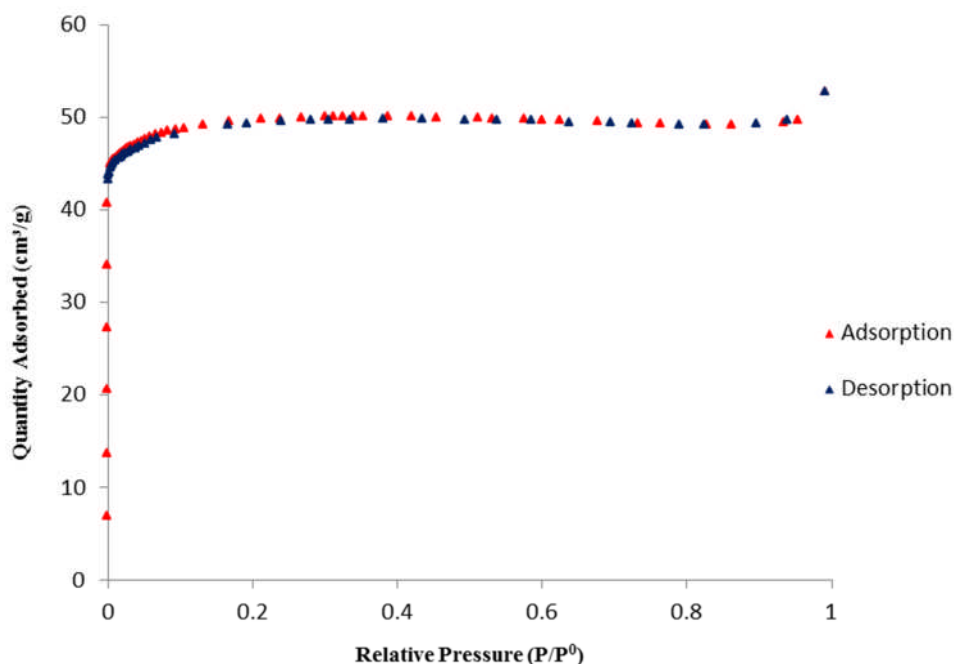
Figure 6.6.   Nitrogen adsorption on STAM-1 at 77 K.

6.3.2. CO_2 and N_2O adsorption

Another fundamental characterisation technique of MOFs is carbon dioxide (CO_2) physisorption, as it is used to determine porosity, including both surface area measurements and determination of pore volume. CO_2 isotherm at 195 K is type 1 in the IUPAC classification scheme and does not have diffusion limitations. Therefore the CO_2 adsorption isotherm (Figure 6.7) was used to calculate BET and Langmuir surface areas in order to verify the values obtained from the above mentioned nitrogen adsorption isotherm. According to the CO_2 adsorption and desorption isotherm, STAM-1 has a BET surface area of 196.2 ± 2.4 m^2 g^{-1} and a Langmuir surface area of 212.1 ± 3.7 m^2 g^{-1}. This surface area is consistent with

the results of the N_2 adsorption experiments and typical for a small pore material. However it should be noted that BET is not the ideal method for surface area measurements using CO_2.

CO_2 adsorption isotherm at 195 K shows a pore volume of ~0.11 cm^3 g^{-1}, which is much lower pore volume than would be expected (~0.24 cm^3 g^{-1}) by molecular simulations if both the hydrophobic and hydrophilic channels were accessible to CO_2. The isosteric enthalpy of adsorption for CO_2 (~30 kJ mol^{-1}) is similar to that seen on activated carbon,[11] but lower than observed in some other MOFs.[12] A similar result is seen for the adsorption of N_2O in STAM-1 at 195 K given in Figure 6.8.
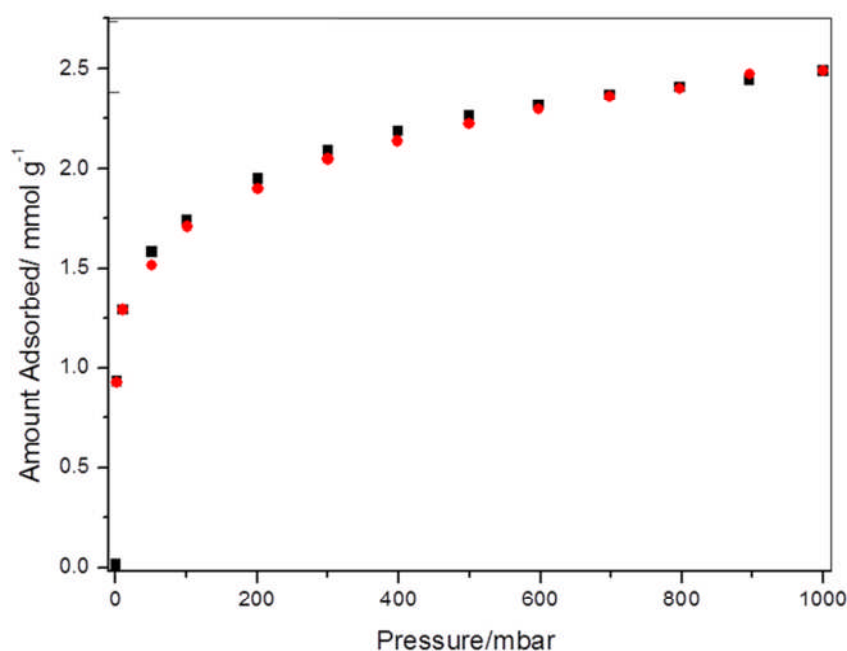

Figure 5.7.   The isotherm for adsorption (black) and desorption (red) of CO_2 on STAM- 1 at 195 K. The calculated pore volume from this isotherm is 0.11 cm^3 g^{-1}
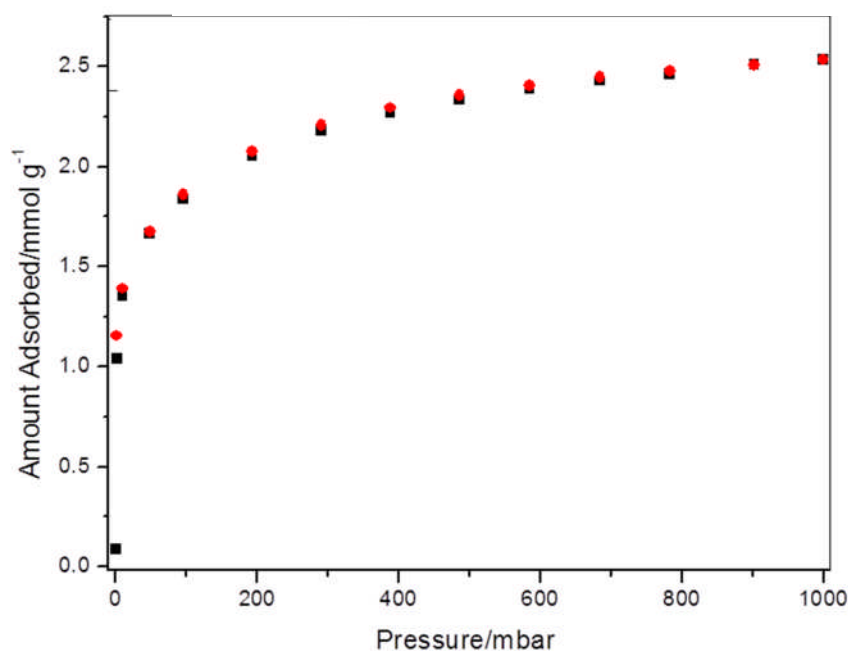
Figure 6.8. The isotherm for adsorption (black) and desorption (red) of N_2O on

STAM- 1 at 195 K.

6.3.3. Oxygen Adsorption

The experimental CO_2 pore volume is much less than what was obtained theoretically and it looks as though one type of pore is closed. To check on this, oxygen adsorption studies were carried out at temperatures between 195 – 298 K (Figure 6.9). The enthalpy of adsorption is constant over this range at $\sim$ 19.6 kJ mol^{-1}. The results obtained from the oxygen adsorption isotherms also aligns well with CO_2 adsorption results, suggesting that only one type of channel system is accessible for oxygen uptake.
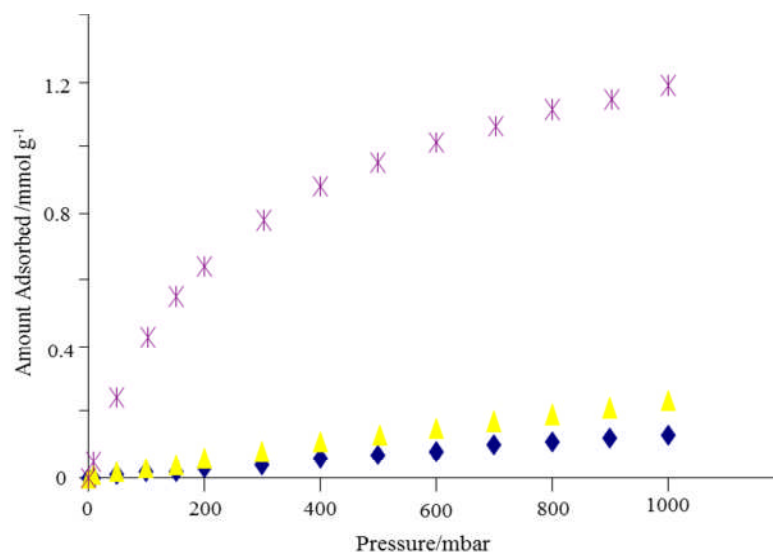
Figure 6.9. Adsorption Isotherms for Oxygen adsorption on STAM-1 at 298 K

(blue), 273 K (yellow) and 195 K (purple)

All the gases discussed so far seem to only have access to one particular type of

channel system which is accountable for half of the expected pore space. Then the

question arises whether this is true for all gases. Therefore gas adsorption

properties of STAM-1 were examined using some other gases and vapours in

order to understand how these behave within the material.

6.3.4. Gated Adsorption Process of methanol and water vapour

Vapours and gases would be expected to interact more strongly with the

hydrophilic channels in the structure, such as water vapour and methanol (Figure

6.10) which are adsorbed in considerably larger amounts. For example, methanol

adsorption on the same sample of STAM-1 as used for the CO_2 experiments

suggested a much higher available pore volume of 0.22 cm^3 g^{-1}, much closer to

the crystallographically expected value (0.24 cm^3 g^{-1}). This suggests that both hydrophilic and hydrophobic channels are accessible to methanol. For methanol adsorption, isosteric enthalpies of adsorption of 53 – 56 kJ mol^{-1} at coverage between 0.05 and 0.1 mmol g^{-1} were obtained. This range is similar to values observed for methanol adsorption on ethanol (**E**) and methanol (**M**) templated phases of hydrophilic Ni$_2$(bpy)$_3$(NO$_3$)$_4$.[2,13] Which means these values are consistent with hydrogen bonding of methanol to the surface. Methanol adsorption isotherms at high, intermediate and low pressure are shown in Figure 6.10 – Figure 6.12.
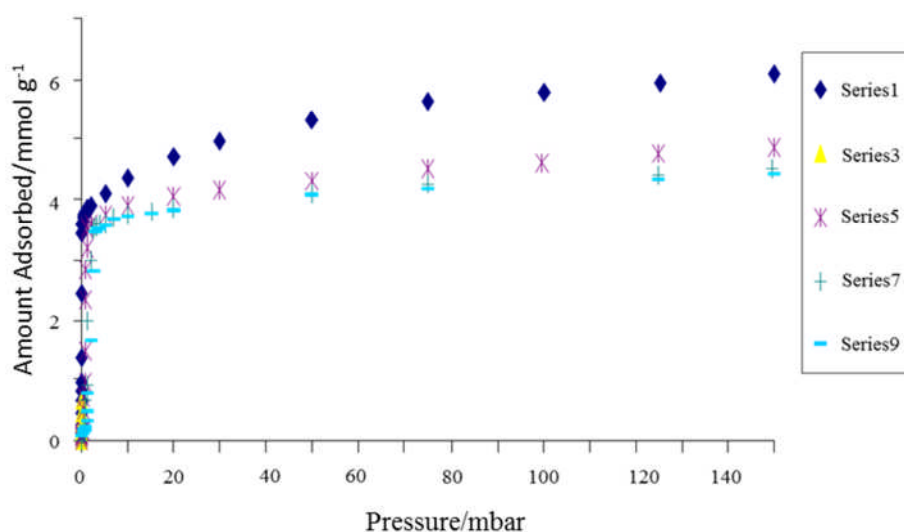

Figure 6.10.   Methanol Adsorption Isotherms on STAM-1 (Series 1(25 ℃); Series 3 (40 ℃); Series 5 (55 ℃); Series 7(65 ℃); Series 9 (70 ℃)
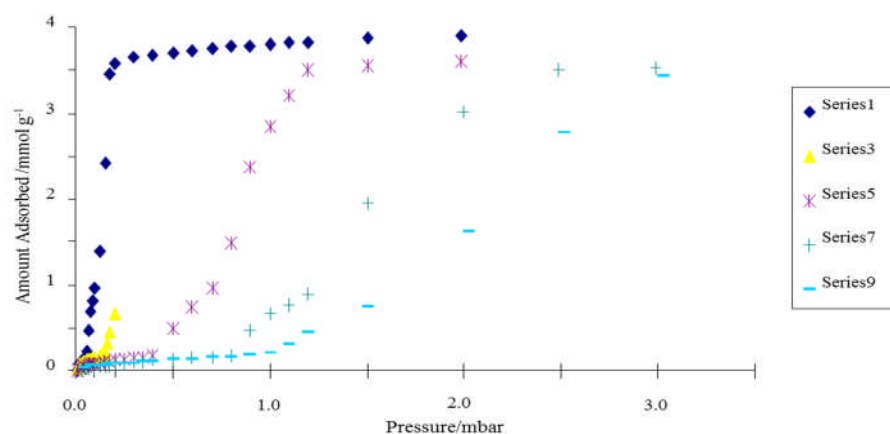
Figure 6.11.   Methanol Adsorption Isotherms on STAM-1, Intermediate

Pressure Range (Series 1(25 ºC); Series 3 (40 ºC); Series 5 (55 ºC); Series
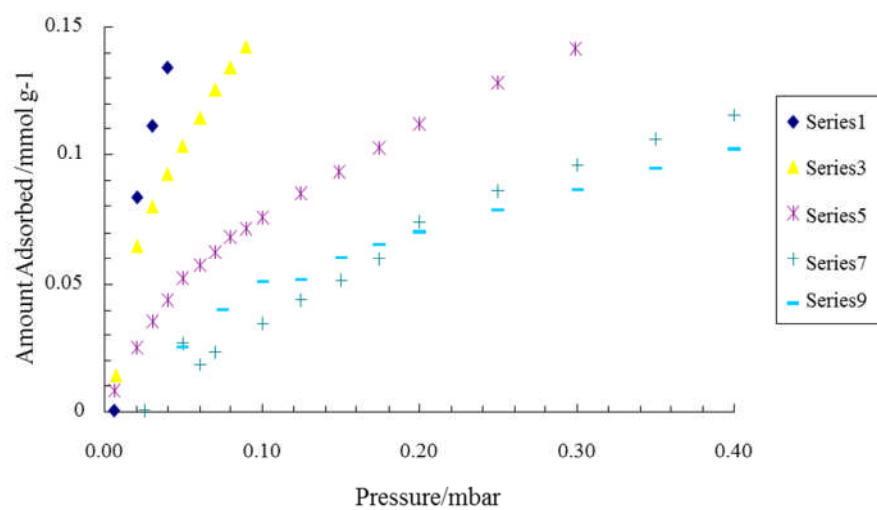
7(65 ºC); Series 9 (70 ºC)

Figure 6.12.   Methanol Adsorption Isotherms on STAM-1 Low Pressure

Range (Series 1(25 ºC); Series 3 (40 ºC); Series 5 (55 ºC); Series 7(65 ºC);

Series 9 (70 ºC)

Closer inspection of the methanol adsorption isotherms show a gated adsorption process[1]   (Figure 6.11) that leads to a large jump in the amount of adsorbed methanol. Methanol adsorption isotherms for STAM-1 have three distinct regions as illustrated by the isotherm at 353 K shown in Figure 6.13 and at 298 K shown in Figure 6.14. The adsorption kinetics for each of the regions was fitted using a stretched exponential-type model (Equation 6.1):

$$\frac{M_t}{M_e} = A_1(1 - e^{-(k_1 t)^{\beta_1}})\cdot$$

<div align="right">(6.1)</div>

Where; k is the rate constant and β the exponential.

Initial adsorption up to the gate opening pressure (P_{GO} ~ 1 mbar) is followed by a steep uptake region corresponding to the pore opening (1-4 mbar) and then gradual pore filling which occurs with increasing pressure. The adsorption kinetics are different for these isotherm regions. Adsorption is relatively fast below P_{GO} over the temperatures (298 – 382 K) investigated. At 353 K the adsorption kinetics show stretched exponential rate constants in the range 2.8 - 25 $\times 10^{-3}$ s^{-1} and exponent β values in the range 0.5 – 0.6. (see Appendix 8, A8.3) This implies that the kinetic model is a one–dimensional process with a distribution of relaxation times. This is consistent with the unidirectional pore structure.

However, above P_{GO} between pressures of 2.75 and ~ 6.5 mbar (uptake: 0.36 – 3.6 mmol g^{-1}) the adsorption isotherm kinetics (353 K) are very slow, corresponding to the steep part of the isotherm, which can be related to a structural change in the material. In this region the stretched exponential adsorption rate constants are in the range 4-30 × 10^{-5} s^{-1} and the exponent values are in the range 0.62 -0.98 (see Appendix 8, A8.4). The linear driving force model is obeyed (β ~1) in the middle region corresponding to uptakes in the range 1.5-2.5 mmol g^{-1} and this suggests a more complex, multi-dimensional process with a single relaxation time. In this region the isosteric enthalpies of adsorption are in the range 56 – 63 kJ mol^{-1}.

Detailed analysis of the adsorption kinetics for isotherm uptakes > 3.7 mmol g^{-1} up to pore filling at 353 K were not investigated because of instrument limitations on the vapour pressures that could be used before condensation in the cooler regions of the instrument. However, the isotherms for methanol adsorption at 298 K show that the adsorption kinetics for this high pressure regime up to 150 mbar (p/p^0 = 0.89, 98% of maximum uptake) return to being much faster, similar to the rates in the low pressure regime and considerably faster than they are just above P_{GO} even at 353 K. Where pore filling is completed the stretched exponential adsorption rate constants are in the range 5 – 10 × 10^{-3} s^{-1} and the exponent values are in the range 0.58 – 0.75. Adsorption in the region just above P_{GO} is too slow to be measured over a reasonable timescale at 298 K as equilibrium for the isotherm pressure increments could take 7-10 days. However, it is clear that adsorption kinetics both before and after the opening of the pores are faster by almost two

orders of magnitude than the adsorption occurring while the structural change occurs. Comparison of methanol adsorption isotherms at 348 and 382 K on a relative pressure basis shows that they are similar, indicating that surface interactions rather than temperature induces the structural change. The adsorption/desorption isotherm is hysteretic but the methanol desorbs at low pressure (Figure 6.15).
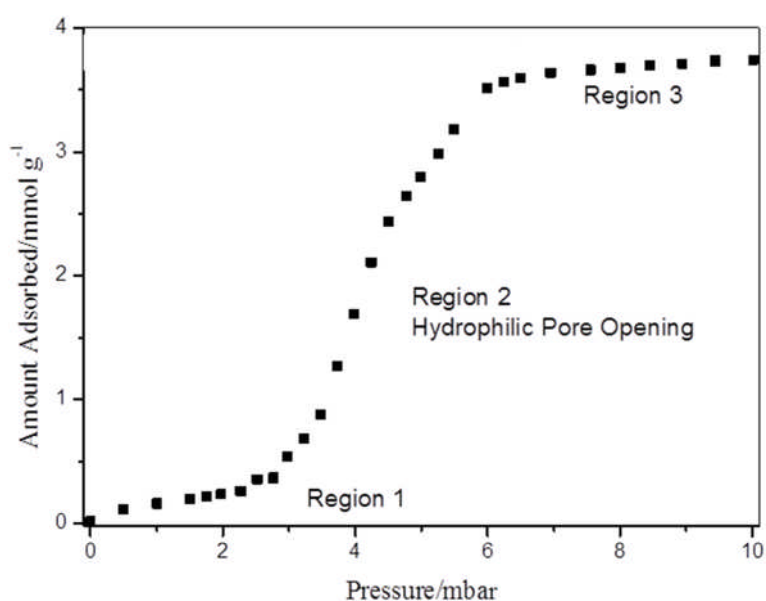

Figure 6.13. Isotherm for methanol adsorption on STAM-1 at 353 K showing the 3 regions, each has different adsorption kinetics. Region 2 corresponds to the opening of the hydrophilic pores.
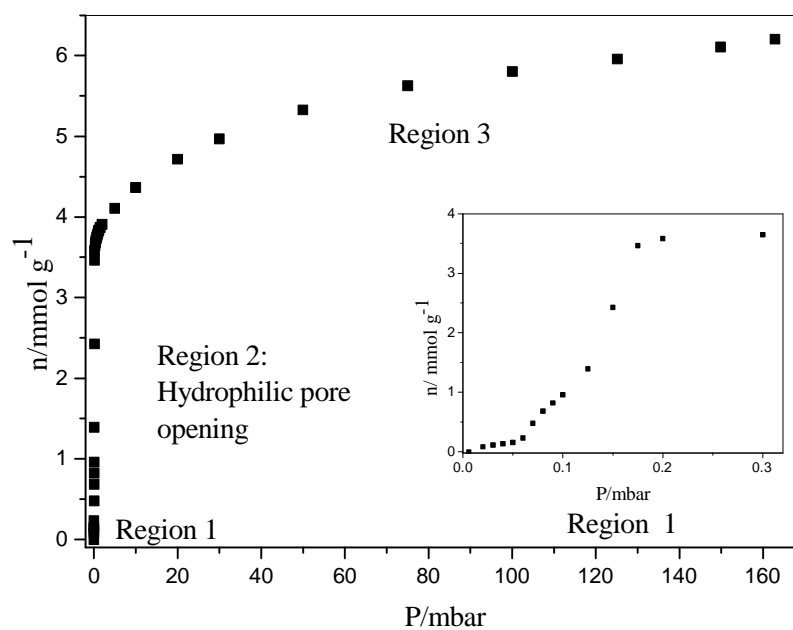
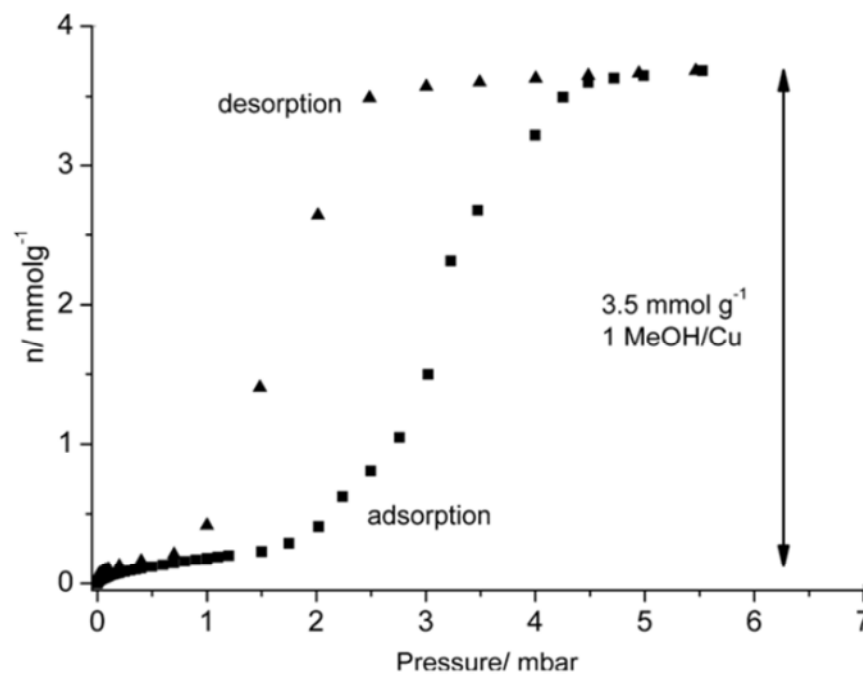**Figure 6.14**. Isotherm for methanol adsorption on STAM-1 at 298 K

Figure 6.15. The adsorption and desorption isotherm of methanol on STAM-1 at

353 K.

A very similar shaped isotherm is seen for water (Figure 6.16) where the kinetics of adsorption shows a very similar pattern. It is worth noting that the sample is stable towards water under these conditions, and the adsorption experiments are repeatable many times without the significant degradation that occurs with other MOFs.[14]
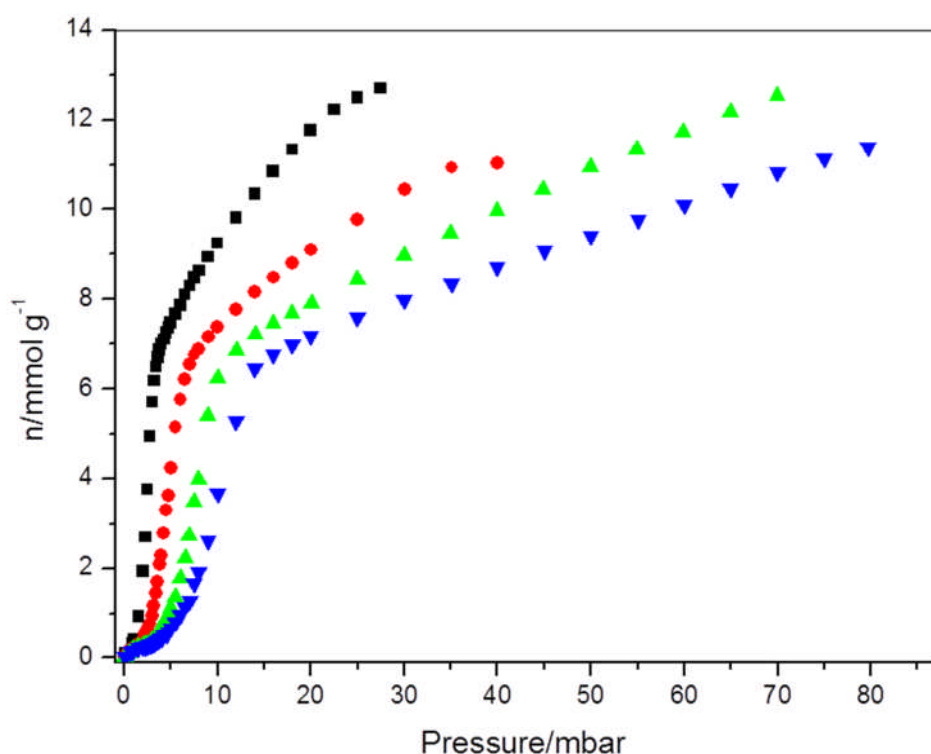

Figure 6.16. Water vapour adsorption isotherms for STAM-1 at 298 K (blue), 303 K (green), 308 K (red) 313 K (black).

6.3.5. Pore discriminating adsorption

STAM-1 is a member of an extremely small class of MOFs where different channels in the structure are lined by groups with opposite polarity.[15,16] In most

other solids that are bimodal, such as HKUST-1, all the pores have similar surface chemistry. The unidirectional hydrophobic and hydrophilic channels, combined with subtle flexibility, give STAM-1 unique adsorption characteristics. After the material has been desolvated (activated) at 393 K, CO_2 adsorption isotherms at temperatures between 195 K and 353 K all show a much lower total pore volume (0.11 cm^3 g^{-1}) than predicted as described in section 5.3.2. Similarly, lower than expected total pore volumes are also observed for the adsorption of other gases such as N_2O, N_2 and O_2. In contrast, methanol (pore volume 0.22 cm^3 g^{-1}) and water vapour (0.22 cm^3 g^{-1}) adsorption show much higher accessible volumes (see section 6.3.4), very close to those predicted for the crystallographic structure. The measured pore volumes suggest that only one channel is accessible to CO_2, N_2 and N_2O while both channels are accessible to methanol and water.

These results are all consistent with a structural change on dehydration that closes one of the pores so that some gases (N_2, N_2O, hexane) are only adsorbed in one type of pore. Adsorption of more strongly interacting adsorbates (methanol or water) induces a slow reversal of this structural change that allows the vapour to enter both types of pore. The observations regarding subtle structural flexibility are consistent with the changes seen in the PXRD experiments completed before and after adsorption, which show that the modifications seen on thermal activation are reversed on re-adsorption of methanol and water but are not reversed on adsorption of CO_2 (Figure 6.17).
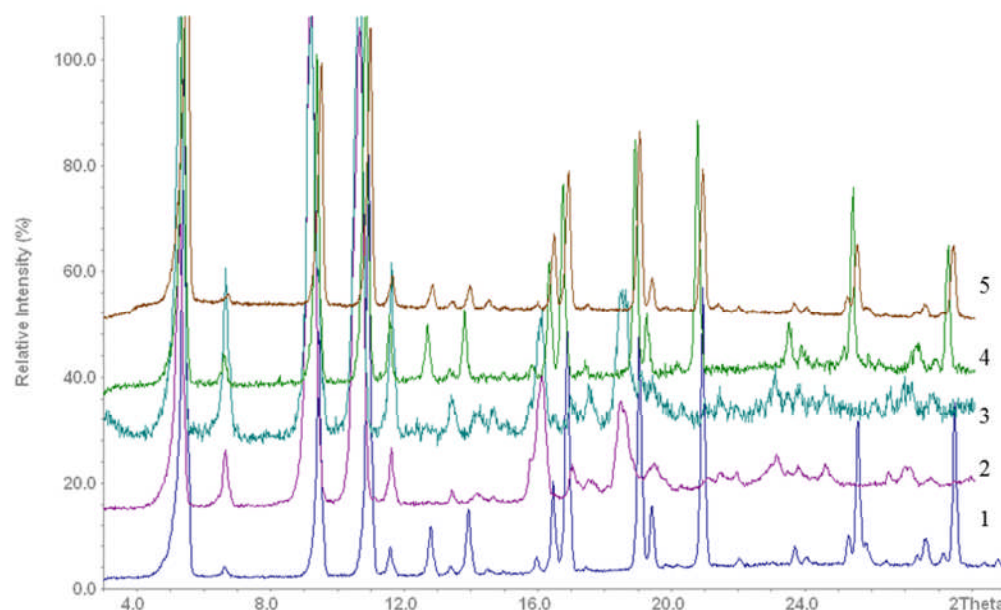
Figure 6.17. A comparison of PXRD of STAM-1 after introduced to gases and vapours. 1 – STAM-1 as made, 2 - STAM-1 dehydrated, 3 - dehydrated STAM-1 CO_2 adsorbed, 4 - dehydrated STAM-1 methanol adsorbed and 5- dehydrated STAM-1 water adsorbed.

Calculations of isosteric heats of adsorption (Q_{st}) versus coverage for both methanol (Figure 6.18) and water (Figure 6.19) clearly show the sharp change in Q_{st} that occurs after the hydrophilic channel is filled and as adsorption into the less favourable hydrophobic channel begins. The stoichiometry for the process shows that 3 methanol molecules are adsorbed per formula unit (one methanol per unsaturated copper centre) strongly suggesting that interaction with the open metal sites is the most important factor. Similarly, the pore opening process involves ~ 8 water molecules per formula unit adsorbed in the hydrophilic pores indicating both interactions with unsaturated metal centres and hydrogen bonding between water molecules. This agrees very well with the amount of water found in the hydrophilic channel in the single crystal X-ray diffraction data.

This suggests that the structural changes on activation hinder the adsorption of CO_2, N_2 and N_2O into one of the channels, which can only be reversed by a chemical opening using hydrophilic species that interact relatively strongly with the surface of the hydrophilic channel. Gated adsorption triggered by interaction with an adsorbate is known[1,17] but this is the first time it has occurred in only one constituent of a bimodal pore structure.
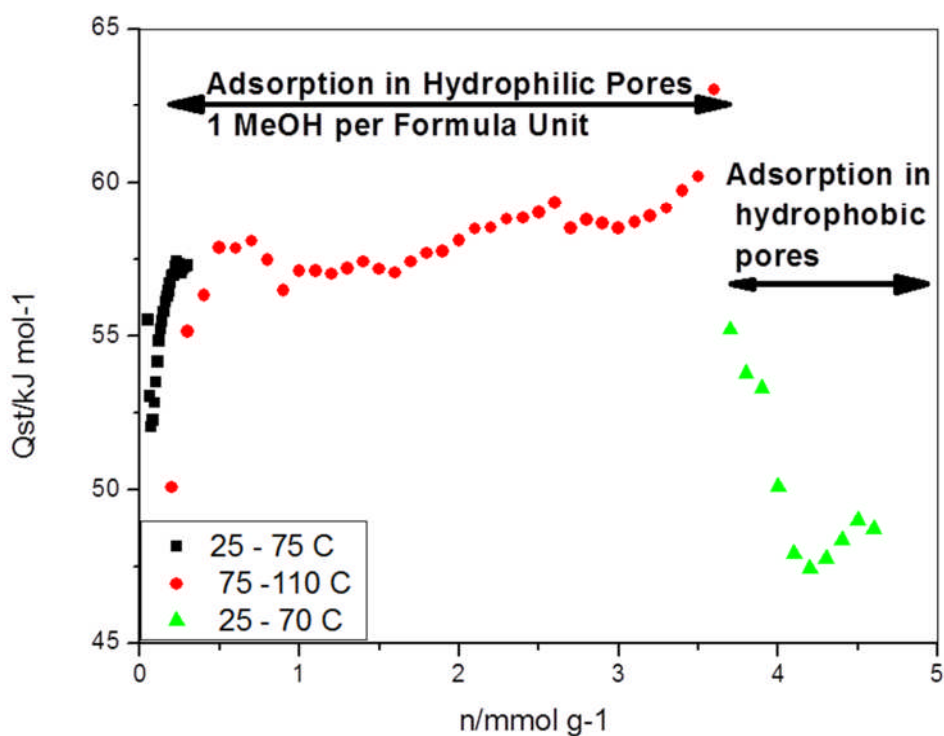

Figure 6.18. The isosteric enthalpies of adsorption calculated from adsorption isotherms between 298 and 383 K, showing the initial increase in Qst as the gate opening process occurs, followed by adsorption into the hydrophilic pores. This is then followed, after 1 MeOH per Cu has been adsorbed, by a sharp drop in Qst as the hydrophobic pores begin to be filled.
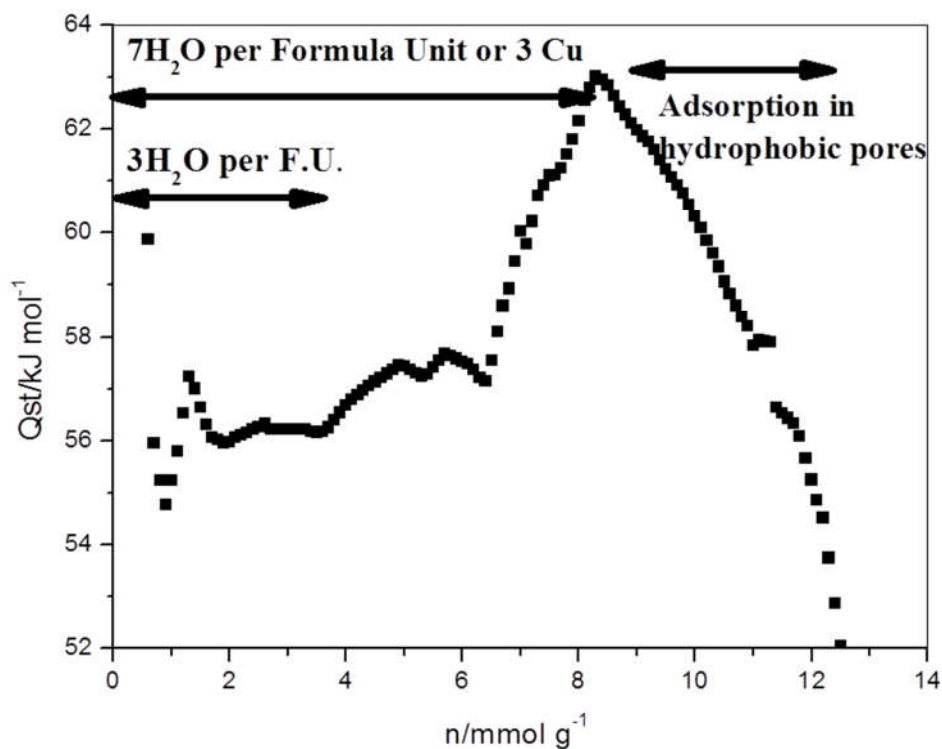
Figure 6.19. The isosteric heats of adsorption for water on STAM-1 calculated

from adsorption isotherms between 298 and 323 K, showing the initial increase in

Qst as the gate opening process occurs, followed by adsorption into the

hydrophilic pores (~2.3 waters per $Cu(C_{10}H_6O_6)(H_2O).1.66H_2O$ formula unit. This

shows an increasing Qst as the water adsorbs into the hydrophilic channel with

increasing amounts of hydrogen bonding, followed by a sharp drop in Qst as the

hydrophobic pores begin to be filled.

6.3.6.   Switchable adsorption

In the as made material, the hydrophilic channels of STAM-1 are occupied by water molecules and therefore hydrophobic channels are available for gas uptake. Whereas in the dehydrated material, the hydrophobic channels are not accessible for certain gases due to the structural changes that occur during the thermal activation and the hydrophilic channels are available after being cleared of water molecules. Therefore the double-barrelled nature of STAM-1 has made it a unique MOF which shows switchable properties under different conditions (Figure 6.20).   The switchable properties of STAM-1 were investigated using liquid phase and gas phase experiments.
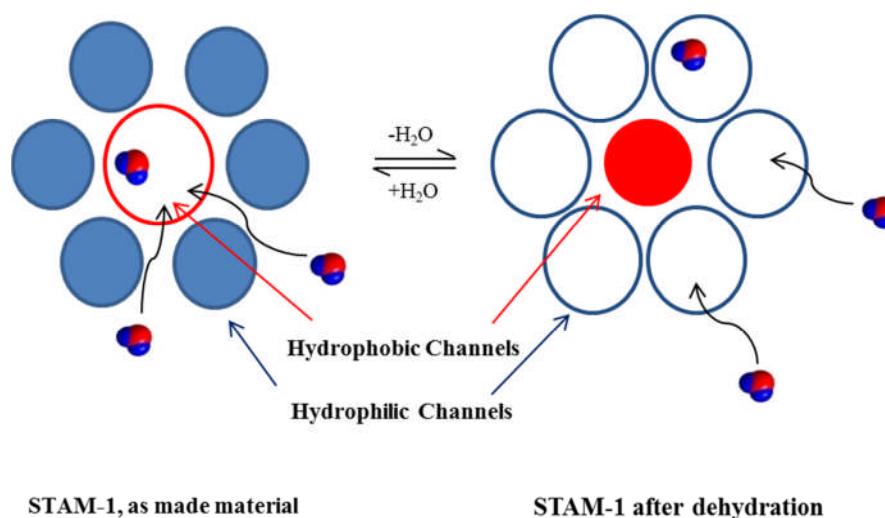

Figure 6.20.   A schematic model which shows the switchable properties of STAM-1. The shaded areas (blue in the as made and red in the dehydrated materials) show which channels are not accessible.

Importantly, the adsorption into the different pores seems essentially independent. Liquid phase experiments (which were carried out after dehydrating the material) using hexane, methanol and hexane/methanol mixtures show that both hexane and methanol are adsorbed in approximately 0.2 hexane and 1.9 methanol molecules per formula unit regardless of whether the methanol is adsorbed first and the hexane afterwards, or vice versa, or whether they are adsorbed at the same time from a mixture of the two liquids. The same is true for the water/hexane system (0.35 hexane and 3 water molecules per formula unit), although the two compounds are not very miscible adsorption from the mixture has to be completed with fairly vigorous stirring to ensure good contact with both liquids. Virtually all gas separations require dry gases as the competitive adsorption of even small amounts of water hinders the utility of the materials. In the case of STAM-1 however, it seems that at low water concentrations the adsorption into the different channels has no negative effect on performance.

The PXRD pattern of hexane adsorbed STAM-1 (Figure 6.21) is same as that of the dehydrated pattern, indicating hexane does not make any influence on structural changes to be reversible. But the methanol/hexane mixture and water/hexane mixture shows the PXRD pattern similar to that of the as made material (Figure 6.21) indicating that the structural changes were made reversible due to the adsorption of the mixture of liquids.
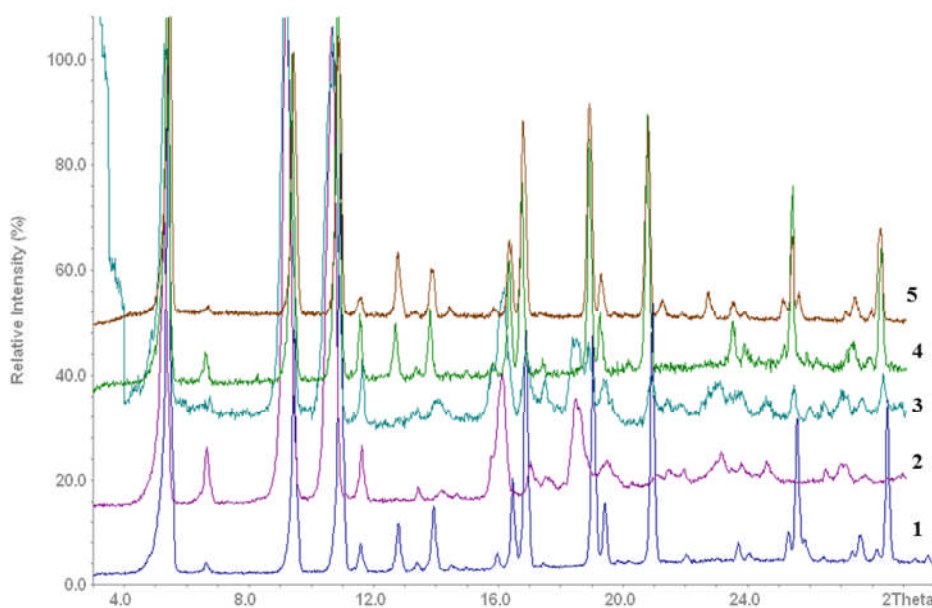
Figure 6.21. A comparison of PXRD of STAM-1 on liquid phase experiments.

1 – STAM-1 as made, 2 – dehydrated STAM-1, 3 – hexane adsorbed STAM-

1, 4 – hexane/methanol adsorbed STAM-1, 5 – hexane/water adsorbed

STAM-1.

The TG-MS of the methanol/hexane (Figure 6.22) and the water/hexane (see Appendix 7, A7.5) adsorbed STAM-1 clearly shows the presence of both components in the material. This result was further confirmed by elemental analysis: Calculated for $(CuC_{10}H_8O_7)_3(H_2O)_5$: C, 35.99; H, 3.42; found in as made material: C, 36.20; H, 3.44; found in hexane adsorbed STAM-1: C, 36.84; H, 3.48; found in hexane/methanol adsorbed STAM-1: C, 40.21; H, 3.52; found in hexane/water adsorbed STAM-1: C, 38.76; H, 3.60.
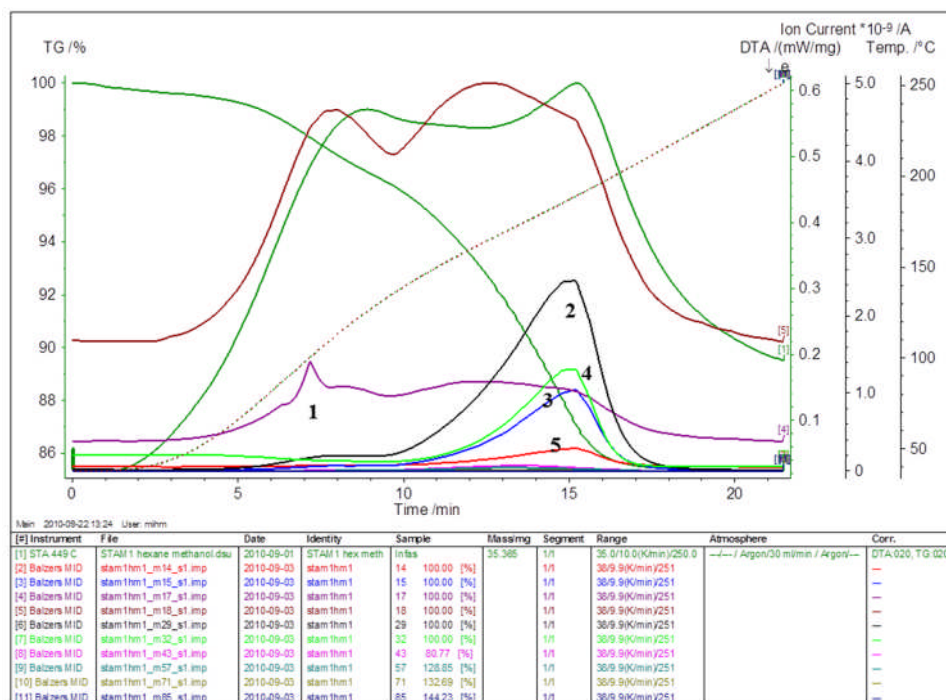
Figure 6.22. TG-MS of methanol/hexane loaded STAM-1. 1, 3 and 4 peaks in the Figure refers to OH, CH_3 and CH_3OH respectively, suggesting methanol and its fractions comes out from the framework. Peaks 2, 3 and 5 can be assigned for CH_3CH_2-, CH_3- and CH_2- coming out from the framework. This suggests both methanol and hexane was present in STAM-1 after the liquid phase experiments.

A similar effect can be seen in gas adsorption experiments. Activating the sample at 393 K to remove water results in the N_2 isotherm (77 K) described above. However, activation of the sample with no heating (298 K) under vacuum does not remove the water, but also allows uptake of N_2 at 77 K. The total uptake after the 298 K activation is in fact slightly greater than that after treatment at 393 K (Figure 6.24). Careful analyses of the low pressure regions of the respective isotherms show that the initial N_2 uptake of the 298 K

activated sample is much less steep than that for the 393 K sample. Furthermore, extrapolating the curves to $P/P^0 = 0$ for the 298 K activation would pass through the origin indicating a pure physisorption phenomenon as would be expected for adsorption into the hydrophobic channel. The steeper initial uptake for the 393 K activated sample is indicative of a stronger interaction, as would be expected for adsorption onto the hydrophilic channel containing the open metal sites. Therefore on activation at 298 K the hydrophobic channel is available for adsorption, whilst on activation at 393 K the water in the hydrophilic channel is lost, initiating the subtle framework flexibility described above which closes the hydrophobic channel, leaving only the hydrophilic channel available for adsorption (Figure 6.25).
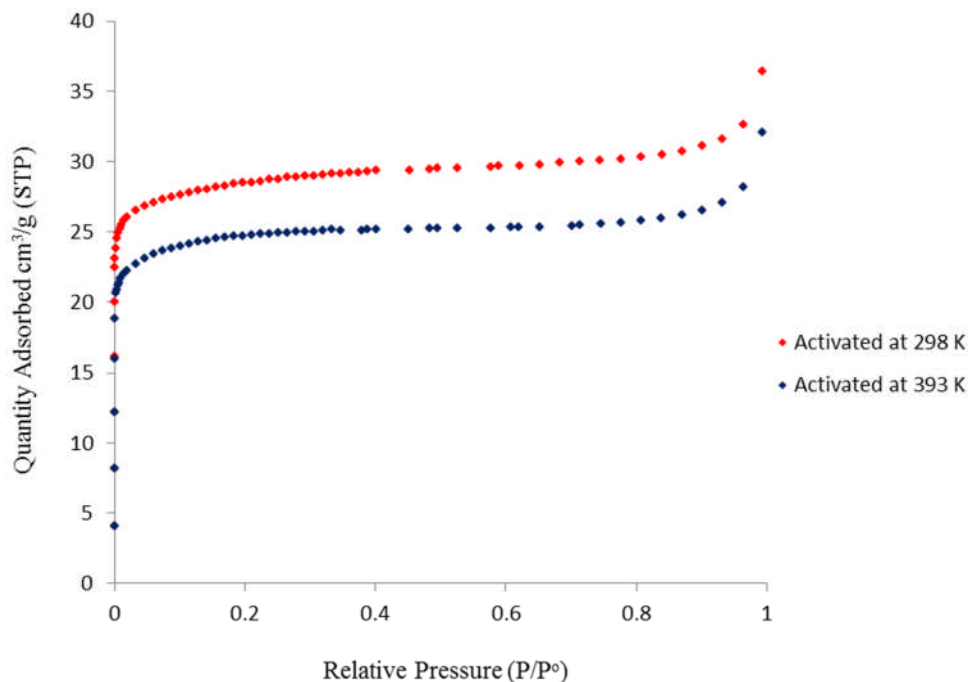

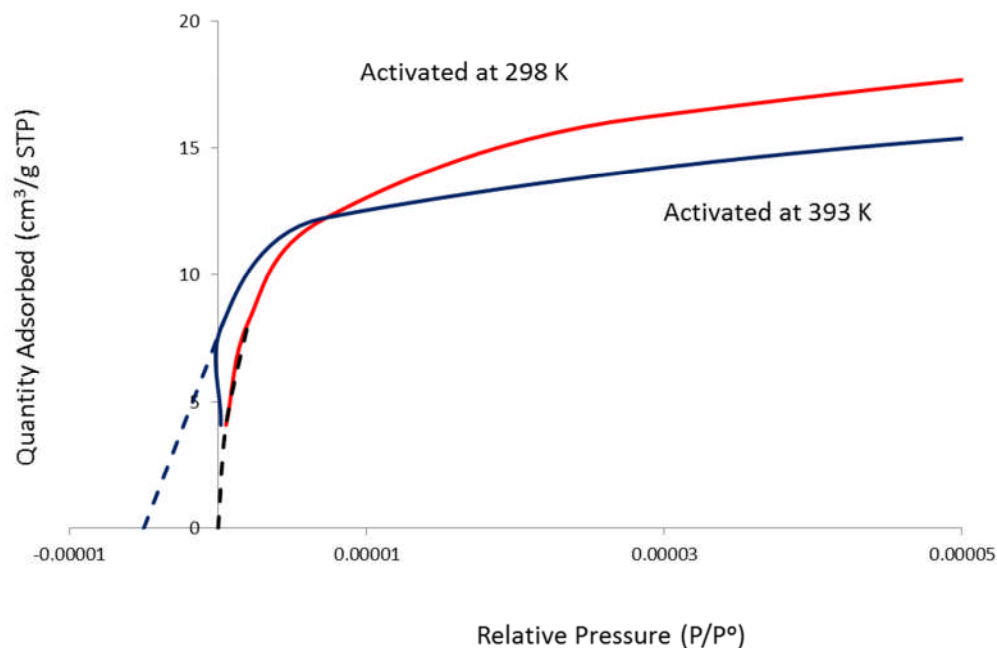**Figure 6.24.** Nitrogen adsorption experiments on STAM-1 at 77K.

Figure 6.25. The low pressure region of nitrogen adsorption experiments on STAM-1 at 77K. The steeper uptake of the 393 K activated sample indicates the presence of open metal sites while the shallower gradient of the 298 K activated sample indicates only physisorption. The dotted lines on the diagram indicate the extrapolation of the curves to zero adsorption.

The same effect is seen even more obviously in the adsorption of nitric oxide (NO) at room temperature after the two different activation treatments. The delivery of NO using porous materials is of interest for medical applications,[18] and one of its properties is its relatively strong interaction with open metal sites in MOF structures.[19,20] (More details about NO adsorption and release related to medical applications are discussed in Chapter 7). After activation at 298 K there are no open metal sites available, and only the hydrophobic

channel is available. The NO adsorption isotherm obtained at 298 K, (Figure 6.26) therefore shows a relatively shallow gradient on increase in NO pressure consistent with relatively weak physisorption. However, activation of STAM-1 at 393 K dehydrates the material and induces the structural change that closes the hydrophobic channel, leaving the hydrophilic channel with accessible open metal sites which are available for adsorption. The relatively strong interaction with the open metal sites is clearly seen in the steeper low pressure gradient in the NO adsorption isotherm (Figure 6.26).
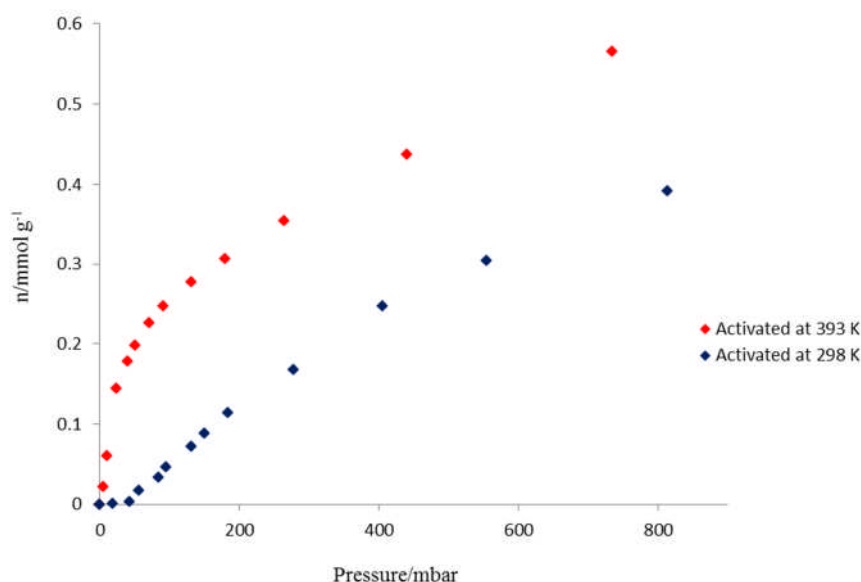
Figure 6.26. NO adsorption experiments on STAM-1 at 298 K. At low pressure the steeper uptake of the 393K activated sample indicates the presence of the relatively strong interactions with open metal sites while the shallow gradient of the 298 K activated sample indicates only physisorption.

PXRD indicates that NO does not interact with the material strongly enough to reverse the structural change in the solid (Figure 6.27). However, exposure to

moisture or methanol does reverse the structural change process and reopens the hydrophobic channel as described earlier. The PXRD pattern, as shown in Figure 6.3 provides a 'fingerprint' for which channel is open under any conditions. The 'as made' type pattern indicating that the hydrophobic channel is open, the 'dehydrated' type pattern indicating that the hydrophilic channel is open. The adsorption can therefore be controllably switched between the two channels simply by choosing the activation conditions and/or whether the material is exposed to water/methanol. This means a thermal trigger to open the hydrophilic channel and a chemical trigger to open the hydrophobic channel. Such observations of switchable pore adsorption are unprecedented and illustrate how different chemistries lining the channels in MOFs can lead to unique properties.
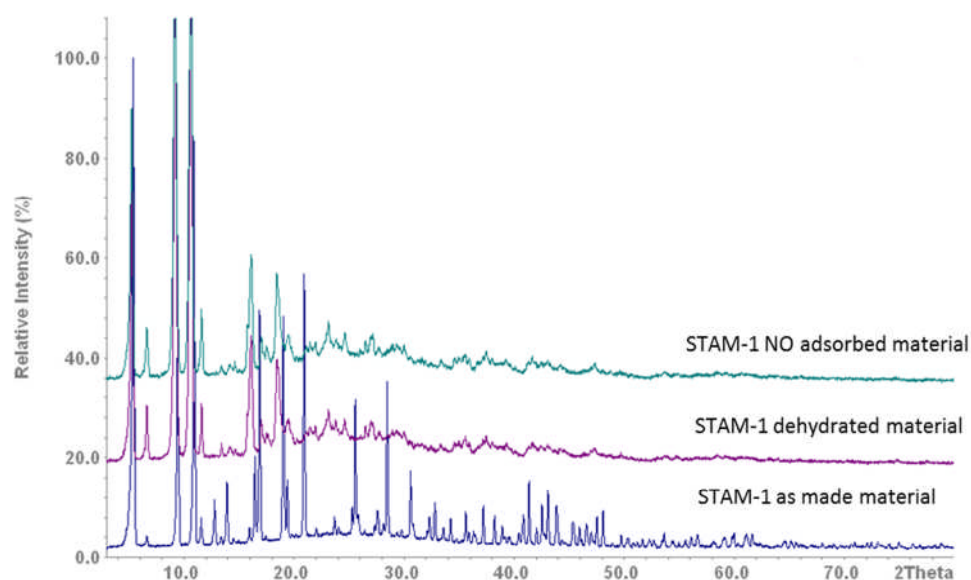

Figure 6.27. A comparison of the PXRD patterns of NO adsorbed STAM-1 with as made and dehydrated materials.

6.4.   STAM-1 for Energy Storage

The most intensively studied application of MOFs is gas storage towards alternative cleaner energy. The main two candidates used for this purpose are hydrogen gas and methane gas. Therefore the storage ability of these two gases in STAM-1 was investigated using molecular modelling studies. Molecular simulations are an ideal tool for screening MOFs. Using simulations the adsorption performance can be predicted quantitatively as well as a detailed picture on the molecular scale can be obtained.

6.4.1. Hydrogen Adsorption

Hydrogen represents the greener option but the safe storage difficulty limited its application. The difficulty of storage of hydrogen is mainly due to its low molecular weight and weak attractive forces. The storage capacity of hydrogen in a given space at a given temperature and pressure can be increased by physisorptive binding of hydrogen to a surface, which makes molecules pack closer by weakly attractive forces. The MOFs which show the highest surface area are the best materials to meet these requirements.[21] On the other hand by increasing the affinity of MOFs for hydrogen would increase the storage capability. This can be done by increasing the heat of hydrogen adsorption. The factors that govern the heat of adsorption are small pores, pore shape and coordinatively unsaturated metal centres.[22,23]

Although STAM-1 does not possess high surface area, its pore shape and size could have a positive effect on hydrogen adsorption. Therefore the molecular modelling studies were carried out on STAM-1 in order to understand the hydrogen adsorption and storage properties. Hydrogen was modelled as a united atom and, as such, represented by a single Lennard-Jones interaction site.[24] Hydrogen – hydrogen and hydrogen – STAM-1 interactions were modelled using the Lennard-Jones interaction potential. As shown in Figure 6.28, STAM-1 has an uptake of about 0.02 wt% of hydrogen at 77 K. This value is far below than the target set by the Department of Energy of U.S.[25,26] The low uptake of hydrogen implies that STAM-1 is not suitable for hydrogen storage.

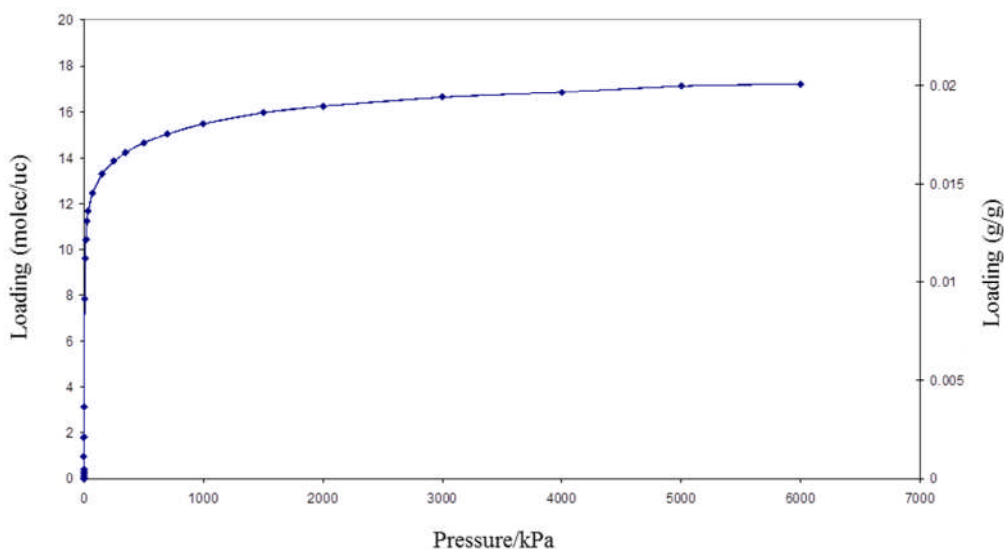

Figure 6.28. GCMC simulated adsorption isotherm of H_2 in STAM-1 at 77 K

As can be seen in Figure 6.29 the hydrogen molecules are distributed quite evenly throughout the pores at low pressure (0.1 bar). When pressure

increased up to 50 bar an induced ordering can be observed due to the high loading which is close to the saturation loading.
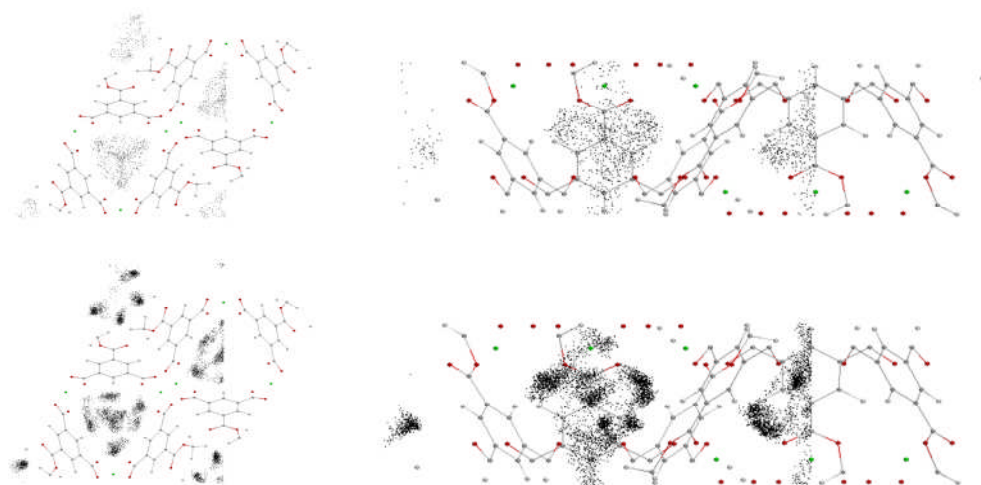

Figure 6.29. Distribution of hydrogen molecules during the simulation. Small black dots in the Figure represent the positions of hydrogen molecules at 0.1 bar (top) and black patches represents the distribution at higher pressure (50 bar) (bottom).

The preferential locations for the hydrogen molecules can be identified by using energy histograms at one particular pressure. Usually this gives an idea about which proportion of molecules experiences a certain potential energy at that particular pressure which helps to examine the adsorption mechanism. For example the small cavities in HKUST-1 result in much lower potential energy, which has high negative values compared to the rest of the framework.[27] These smaller cavities are the preferential locations for the hydrogen molecules in HKUST-1. In the case of STAM-1 nothing much can be seen as the pores are so small and only a single peak was observed which is shown for

hydrogen (Figure 6.30). Therefore the different chemical nature of the two different pores was not able to be examined.
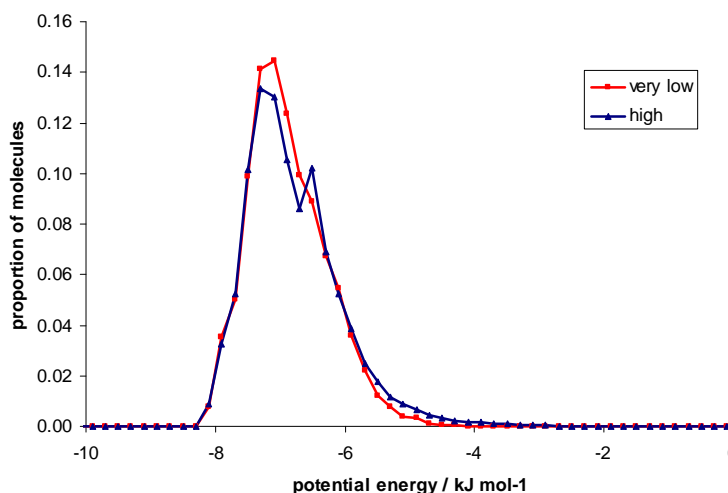

Figure 6.30. Energy histogram

6.4.2.   Simulation of Methane adsorption in STAM-1

As described in Chapter 1, methane is an abundant natural gas which is cleaner burning than gasoline.[28] Therefore methane is an attractive alternative to the internal combustion engine. However, similar to hydrogen, methane also faces many challenges such as storage in safe, cheap and convenient manner. Usually methane binding on MOFs is based on weak van der Waals forces.[28] Therefore the total uptake strongly correlates with the surface area. But according to the studies undertaken on PCN-14, two other types of factors have an influence on methane uptake. These factors are; coordinatively unsaturated metal sites and enhanced van der Waals potential pockets[29] (where the pore dimension is comparable to the kinetic diameter of methane ~3.8 Å).

Since the dehydrated STAM-1 contains open metal sites and the pore diameter of STAM-1 is only slightly higher than the kinetic diameter of methane, simulations on methane adsorption in STAM-1 was carried out.

In methane adsorption simulations, methane was modelled as a united atom such that it was represented by a single Lennard-Jones[24] interaction site. Methane-methane and methane-STAM-1 interactions were modelled with the Lennard-Jones[24] potential. The simulated adsorption isotherm of methane at 300 K on STAM-1 is shown in Figure 6.31. Methane adsorption is also similar to hydrogen adsorption. Only about 0.05 wt% of methane is adsorbed to the material according to the simulations. Again this value is far below the target set by the Department of Energy[28,30] of U.S., suggesting that STAM-1 is not a good material for energy storage applications.
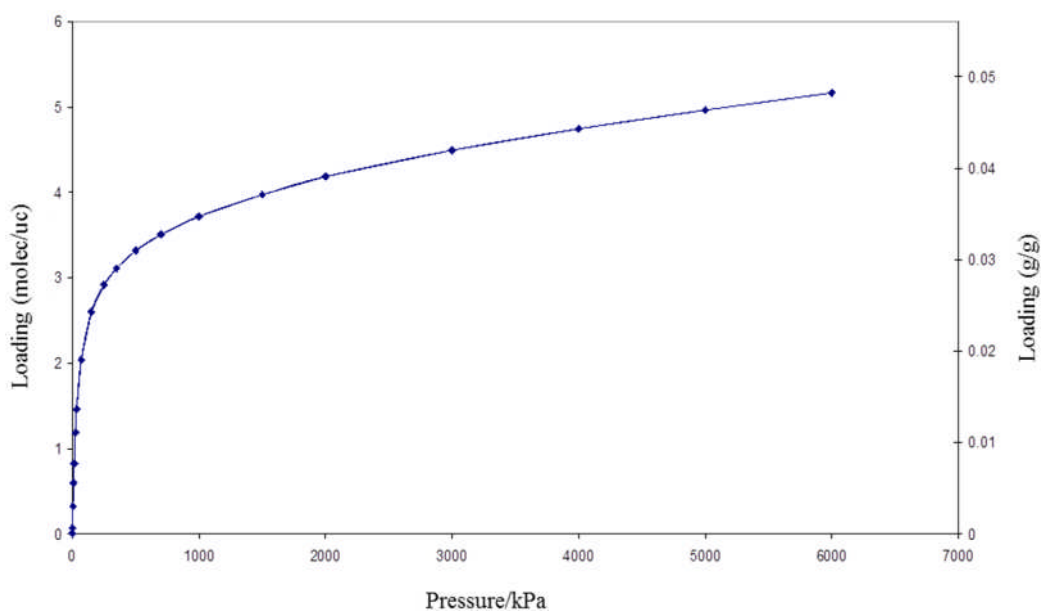

Figure 6.31. GCMC simulated adsorption isotherm for CH_4 in STAM-1 at 300 K

The location of the methane molecules is mainly determined by the potential energy between methane molecules and the framework. At higher loadings methane-methane interactions play an additional role along with the packing of the methane molecules inside the framework. Figure 6.32 shows contour plots of the potential energy for four cuts perpendicular to the pore axis for a methane molecule. It illustrates how much stronger the interactions in the centre of the cavity with a potential energy of -22 kJ mol^{-1}. The contour plots of the potential energy do not show much variation in the potential as the pores are quite small. These are rather random cuts which visualise the undulating nature of the pores. Snapshots (Figure 6.33) help to visualise how full the pores are. The preferential locations of the methane molecules can be observed using this method. Green represents the methane inside the pores which shows the distribution of methane inside the material. Due to low surface area and small size of pore, STAM-1 does not show a much potential for methane uptake.
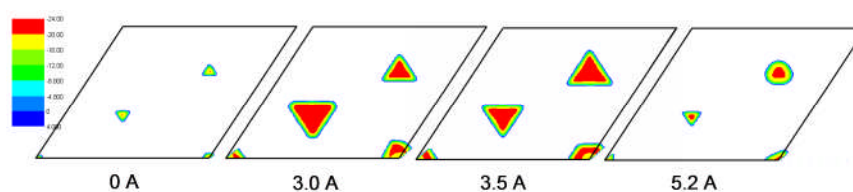

Figure 6.32. Contour plots of the potential energy between a methane molecule and the STAM-1 framework on a plane perpendicular to the pore axis of a methane molecule. Triangles correspond to the potential energy that the centre of mass of a methane molecule is experiencing. (i.e. the pore space that is accessible to methane molecules).
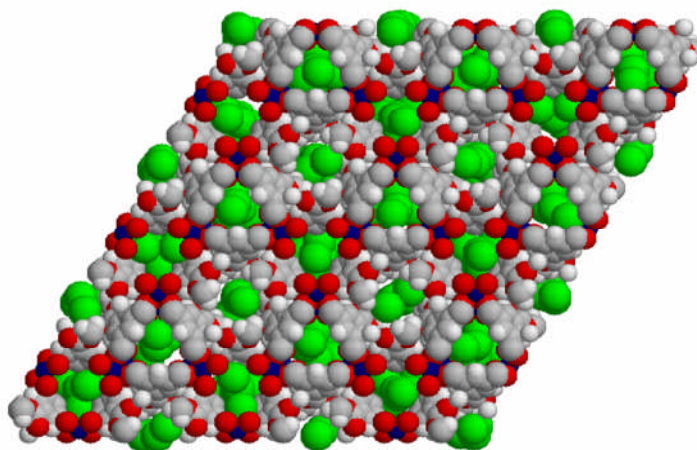
Figure 6.33. Snapshots at 50 bar. Distribution of methane in STAM-1 can be seen from the snap shot. Copper-blue, Carbon-grey, Oxygen- red, Methane-green.

6.5.   Kinetic separation of N_2 and O_2

The adsorption of N_2 in STAM-1 is significantly slower than the adsorption of O_2. Such kinetic effects on gas adsorption in porous solids have some important consequences in practice. One method of separating the O_2 from N_2 in air involves pressure swing adsorption using activated carbon molecular sieves based on the significantly faster diffusion of O_2 than N_2.[11,12] Reports of kinetic separation of gases using MOFs are still relatively rare,[31] and there have been no reports of air separation using this approach, although there has been a recent description of kinetic effects in a cyanometallate coordination polymer.[32] And some potential separation of O_2 from N_2 based on equilibrium measurements on MOFs have been published.[11] Figure 6.34 shows the kinetic data for the adsorption of O_2 and N_2 at 195 K in STAM-1.
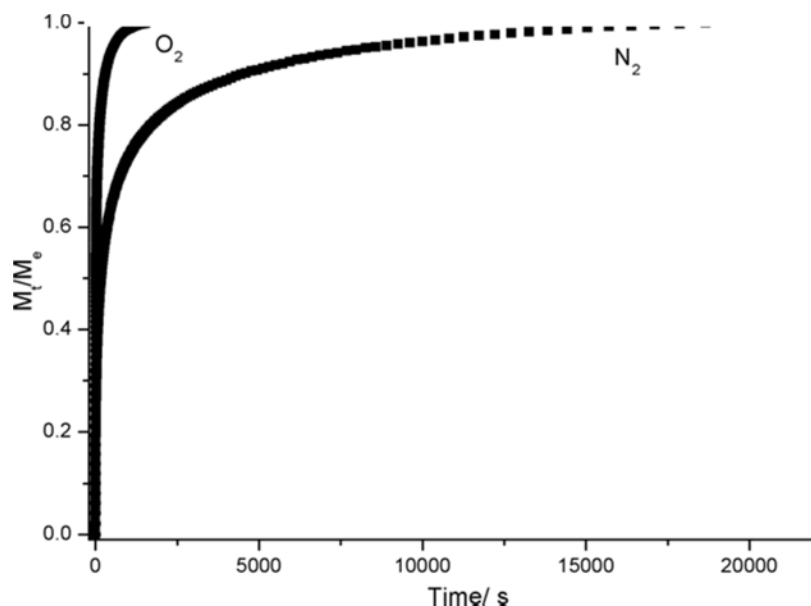
Figure 6.34. Comparison of O_2 and N_2 uptake rates on STAM-1 at 195 K.

Isosteric enthalpies of adsorption calculated from adsorption isotherms between 195 K and 295 K show that both N_2 and O_2 have heats of adsorption around 20 kJ mol^{-1}, which are similar to the values obtained for adsorption on carbon molecular sieves.[11]   The normalised kinetic profiles were analysed using the stretched exponential model, which is described by the Equation 6.2. The two component stretched exponential model was used here as it gave a 'good fit' with the experimental data obtained.

$$\frac{M_t}{M_e} = A_1(1-e^{-(k_1t)^{\beta_1}}) + A_2(1-e^{-(k_2t)^{\beta_2}})$$

(6.2)

where M_t is the mass at time t (mg), M_e is the mass at equilibrium (mg), k_1 and k_2 are rate constant (s^{-1}), β_1 and β_2 are material dependent parameters reflecting the width of the distribution of relaxation times and t is the time(s).

Since the kinetic profiles are normalised and there are equal number of both types of barrier in the crystal structure,

$$A_1 = A_2 = 0.5, \text{ i.e. } A_1 + A_2 = 1. \qquad \textbf{(6.3)}$$

The two components of the adsorption can be split into a slow and a fast component, and are described as follows.

a) Slow component of O_2/N_2 gas adsorption in STAM-1 at 195 K.
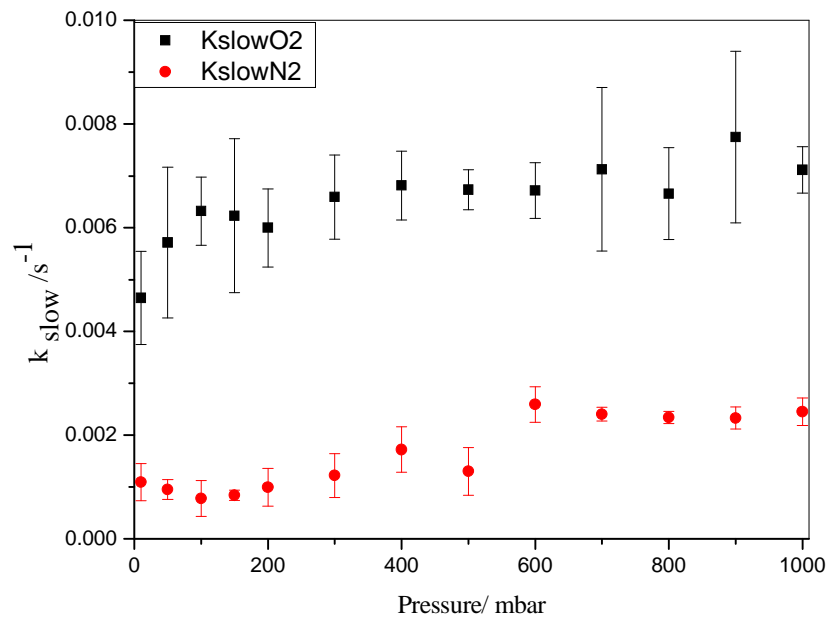
b) Fast component of O_2/N_2 gas adsorption in STAM-1 at 195 K.

c) Slow component of the exponent of O_2/N_2 gas adsorption in STAM-1 at 195 K.

d) Fast component of the exponent of O_2/N_2 gas adsorption in STAM-1 at 195 K.
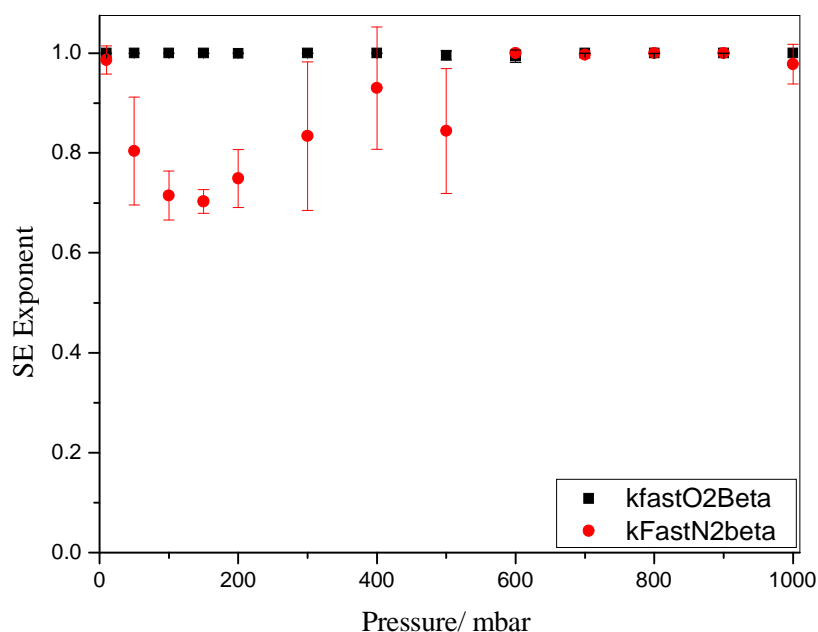
The values presented are the average of several runs with the corresponding uncertainties. The β values are the same for the fast components for oxygen and nitro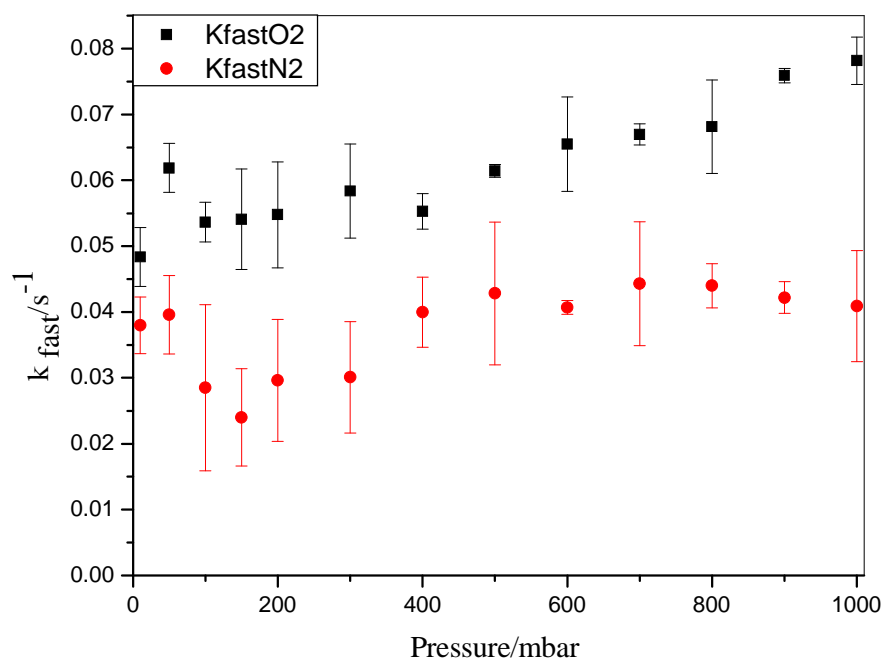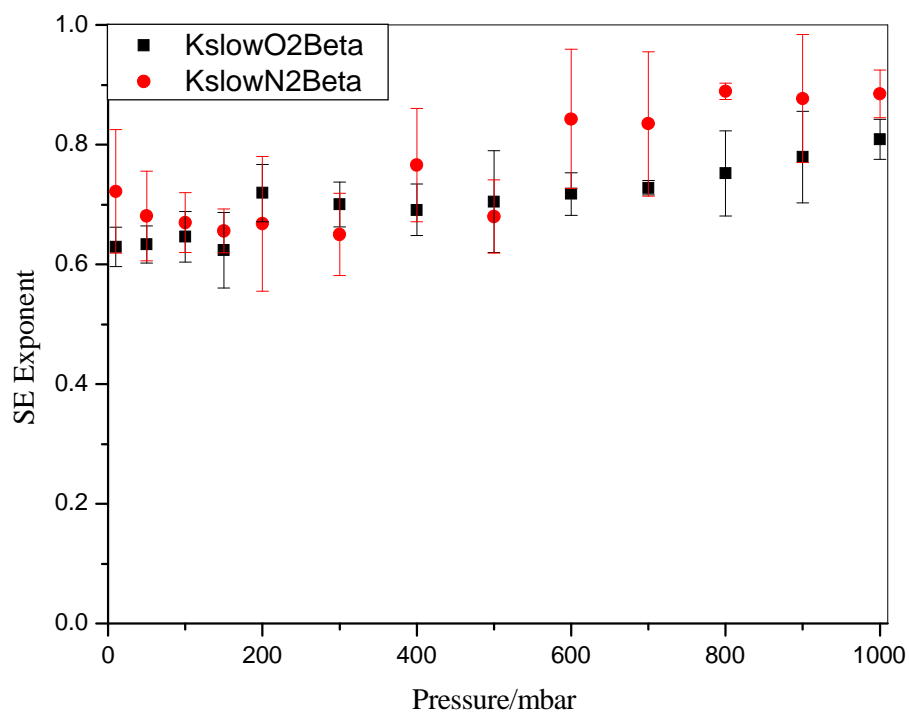gen are ~ 1 while the values for the slow components are ~0.7 and follow an upward trend with pressure. The k values show clear differences. The fast rate constant k_2 for oxygen are slightly faster than nitrogen. However the slower component for nitrogen is significantly smaller than that of oxygen and is clearly different. This demonstrates kinetic molecular sieving. This indicates an $O_2{:}N_2$ selectivity of around 4:1, which is lower than the very best carbon molecular sieves currently used in industry for the non-cryogenic separation of air (~20:1), but it should be remembered that these carbon results were only possible after several years of optimisation, and we hope that forthcoming optimisation of MOF properties, now that the concept of air separation using these materials has been proved, could lead to similar significant improvement in performance.

As with many important solids, the properties of STAM-1 are intimately connected with its structural architecture, which in turn can be traced directly back to the unprecedented *in situ* esterification during its synthesis of STAM-1. The demonstration of large differences in the kinetics of adsorption of O_2 and N_2 has obvious implications for air separation using MOFs. However, also of great interest is the development of materials that show extremely selective behaviour towards gases of different chemistry.[11,12]

6.6.   Conclusion

STAM-1 indicates clearly an unusual structure and flexibility. This can lead to new materials with unique properties that can be utilised in applications that are not possible with the current family of MOF materials. The development of materials that show extremely selective behaviour towards gases of different chemistry is of great interest for many gas adsorption/separation applications[11] and the demonstration of large differences in the kinetics of adsorption of O_2 and N_2 has obvious implications for air separation using STAM-1.

STAM-1 is a member of an extremely small class of MOFs in which different channels in the structure are lined by groups with opposite polarity.[15,16] These structural features combine with subtle flexibility give unique adsorption characteristics. The measured pore volume suggested that only one channel is accessible to CO_2, N_2 but both channels are accessible to methanol and water. Close inspection of the methanol and water adsorption isotherms reveals a gated

adsorption process that leads to a large increase in the amount of vapour adsorbed above the so-called gate opening pressure. The unique pore discriminating adsorption properties displayed by STAM-1 are unprecedented not only in other MOFs but also in any other class of adsorbent. This makes the adsorption properties of STAM-1 particularly novel and a potentially important new route down which MOF chemistry could be developed.

The adsorption into STAM-1 can be controllably switched between the two channels simply by choosing the activation conditions and/or whether the material is exposed to water/methanol; a thermal trigger to open the hydrophilic channel and a chemical trigger to open the hydrophobic channel. This unique switchable pore adsorption property of STAM-1 offers many possibilities for future studies as this is the first reported example of such behaviour in porous MOFs.

6.7. References

(1)   Kitaura, R.; Seki, K.; Akiyama, G.; Kitagawa, S. *Angew Chem Int Edit* **2003**, *42*, 428.

(2)   Fletcher, A. J.; Cussen, E. J.; Bradshaw, D.; Rosseinsky, M. J.; Thomas, K. M. *J Am Chem Soc* **2004**, *126*, 9750.

(3)   Li, D.; Kaneko, K. *Chem Phys Lett* **2001**, *335*, 50.

(4)   Kubota, Y.; Takata, M.; Matsuda, R.; Kitaura, R.; Kitagawa, S.; Kobayashi, T. C. *Angew Chem Int Edit* **2006**, *45*, 4932.

(5)   Matsuda, R.; Kitaura, R.; Kitagawa, S.; Kubota, Y.; Belosludov, R. V.; Kobayashi, T. C.; Sakamoto, H.; Chiba, T.; Takata, M.; Kawazoe, Y.; Mita, Y. *Nature* **2005**, *436*, 238.

(6)   Bureekaew, S.; Shimomura, S.; Kitagawa, S. *Sci Technol Adv Mat* **2008**, *9*.

(7)   Ferey, G.; Latroche, M.; Serre, C.; Millange, F.; Loiseau, T.; Percheron-Guegan, A. *Chem Commun* **2003**, 2976.

(8)   Chalati, T.; Horcajada, P.; Gref, R.; Couvreur, P.; Serre, C. *J Mater Chem* **2011**, *21*, 2220.

(9)   Rowsell, J. L. C.; Yaghi, O. M. *Micropor Mesopor Mat* **2004**, *73*, 3.

(10)   accelrys, p Materials Studio Software for molecular modelling studies.

(11)   Reid, C. R.; O'koye, I. P.; Thomas, K. M. *Langmuir* **1998**, *14*, 2415.

(12)   Caskey, S. R.; Wong-Foy, A. G.; Matzger, A. J. *J Am Chem Soc* **2008**, *130*, 10870.

(13)   Fletcher, A. J.; Cussen, E. J.; Prior, T. J.; Rosseinsky, M. J.; Kepert, C. J.; Thomas, K. M. *J Am Chem Soc* **2001**, *123*, 10001.

(14)   Huang, L. M.; Wang, H. T.; Chen, J. X.; Wang, Z. B.; Sun, J. Y.; Zhao, D. Y.; Yan, Y. S. *Micropor Mesopor Mat* **2003**, *58*, 105.

(15)   Kawano, M.; Kawamichi, T.; Haneda, T.; Kojima, T.; Fujita, M. *J Am Chem Soc* **2007**, *129*, 15418.

(16)   Xamena, F. X. L. I.; Abad, A.; Corma, A.; Garcia, H. *J Catal* **2007**, *250*, 294.

(17)   Xiao, B.; Byrne, P. J.; Wheatley, P. S.; Wragg, D. S.; Zhao, X. B.; Fletcher, A. J.; Thomas, K. M.; Peters, L.; Evans, J. S. O.; Warren, J. E.; Zhou, W. Z.; Morris, R. E. *Nat Chem* **2009**, *1*, 289.

(18)   Mowbray, M.; Tan, X. J.; Wheatley, P. S.; Morris, R. E.; Weller, R. B. *J Invest Dermatol* **2008**, *128*, 352.

(19)   McKinlay, A. C.; Xiao, B.; Wragg, D. S.; Wheatley, P. S.; Megson, I. L.; Morris, R. E. *J Am Chem Soc* **2008**, *130*, 10440.

(20)   Xiao, B.; Wheatley, P. S.; Zhao, X. B.; Fletcher, A. J.; Fox, S.; Rossi, A. G.; Megson, I. L.; Bordiga, S.; Regli, L.; Thomas, K. M.; Morris, R. E. *J Am Chem Soc* **2007**, *129*, 1203.

(21)   Dinca, M.; Yu, A. F.; Long, J. R. *J Am Chem Soc* **2006**, *128*, 8904.

(22)   Garrone, E.; Bonelli, B.; Arean, C. O. *Chem Phys Lett* **2008**, *456*, 68.

(23)   Rzepka, M.; Lamp, P.; de la Casa-Lillo, M. A. *J Phys Chem B* **1998**, *102*, 10894.

(24)   Lennard-Jones, J. E. *Proc. R. Soc. London, A* **1924**, *106*, 463.

(25)   Murray, L. J.; Dinca, M.; Long, J. R. *Chem Soc Rev* **2009**, *38*, 1294.

(26)   http://www.eere.energy.gov/hydrogenandfuelcells/mypp.

(27)   Getzschmann, J.; Senkovska, I.; Wallacher, D.; Tovar, M.; Fairen-Jimenez, D.; Duren, T.; van Baten, J. M.; Krishna, R.; Kaskel, S. *Micropor Mesopor Mat* **2010**, *136*, 50.

(28)   Zhou, W. *Chem Rec* **2010**, *10*, 200.

(29)   Wu, H.; Zhou, W.; Yildirim, T. *J Am Chem Soc* **2009**, *131*, 4995.

(30)   http://www.afdc.energy.gov/afdc/fuels/natural_gas.html.

(31)   Li, J. R.; Kuppler, R. J.; Zhou, H. C. *Chem Soc Rev* **2009**, *38*, 1477.

(32)   Zamora, B.; Autie, M.; Contreras, J. L.; Centeno, M.; Reguera, E. *Separ Sci Technol* **2010**, *45*, 692.

Chapter 7   Biomedical and Magnetic Properties

of STAM-1

7.1   Biomedical Properties of STAM-1

7.1.1. Introduction

Controlled drug delivery technology is one of the intensely studied areas of science related to health care. The conventional treatment of bacterial infection involves the administration of antibiotics. Not only is there a risk of toxicity associated with these methods but also there are chances to develop antibacterial resistant pathogens. There is high interest in this research area, currently focussed on engineered materials for localised delivery of anti-microbial compounds. Different delivery systems have been developed today which include, polymeric based systems, liposome based systems, mesoporous materials and microporous zeolites.[1-4] Some of these systems have the advantage of biocompatibility and uptake of many drugs but lack of a controlled release mechanism makes them inappropriate.[5] Whereas the others show controlled delivery of drugs but have poor loading capacity.[6] Therefore it is necessary to find better materials to overcome these issues and such systems should offer advantages in terms of improved efficacy and reduced toxicity.

Nitric Oxide (NO) has a number of well characterised immunomodulatory and antimicrobial effects.[7] As described in Chapter 1, NO can be impregnated into MOFs and its release controlled by the structure of the MOF.[8] Therefore, there is a potential for creating NO-containing MOFs for use in both the healthcare and community settings. STAM-1 was used for this purpose. The growth inhibitory and bactericidal effects of STAM-1 containing NO was studied against three different species of bacteria which are known to cause significant numbers of nosocomial and community-acquired infections. The results of this study will be discussed in this Chapter.

7.1.2. NO Adsorption and Release using STAM-1

The porosity of STAM-1 was discussed in Chapter 5 with its ability to take different gasses into the material. Apart from the porosity, STAM-1 has another advantage in particular for adsorption of NO. The hydrated version of STAM-1 has water molecules attached to the axial position of the metal centre in the paddlewheel unit. After activation of the material these water molecules disappear leaving coordinatively unsaturated metal sites (CUS) on the walls of the pores that are available for efficient binding of NO. An investigation was done in order to find out the affinity that STAM-1 has for NO and its ability to store and release significant amount of gas which can be possibly used in medical applications. STAM-1 was activated at 393 K under high vacuum, which eliminates the solvent molecules trapped inside the pores as well as the water molecules bound to the copper centres. The material was then cooled down to the room temperature and

NO adsorption was done at 298 K. NO adsorption and release profile is shown in Figure 7.1.1.
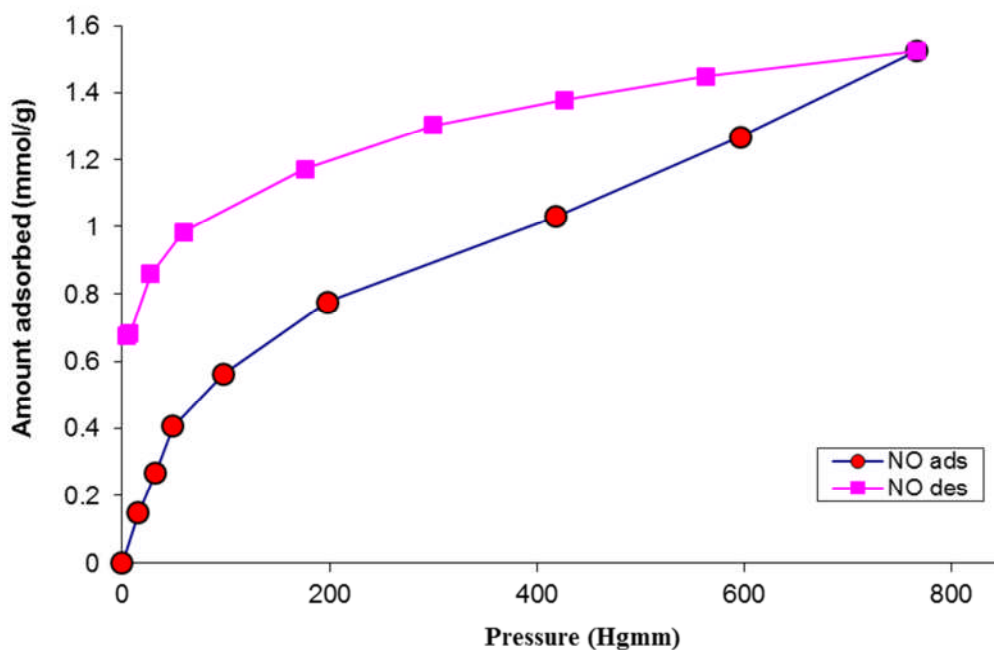

Figure 7.1.1. NO adsorption desorption isotherm of STAM-1 at 298 K.

Although the adsorption capacity is not the only consideration in determining the effectiveness of a material, it is advantageous to maximize the adsorption capacity of a material to increase the reservoir of stored gas. NO uptake occurs in two ways; it can physisorb in the pores as well as chemisorb to the open metal sites of STAM-1. According to the adsorption isotherm, STAM-1 adsorbs only about 1.6 mmol g^{-1} of NO. This amount is almost half of the uptake of NO shown in HKUST-1, which is 3 mmol g^{-1}.[9] As STAM-1 falls into the category of flexible MOFs, noticeable structural changes occur in the activation process. As described in Chapter 6, although relatively strong interactions with the open metal sites can be seen with NO, it does not interact strongly enough to reverse the structural

changes in the solid. Therefore the low uptake of NO is due to the availability of only one channel system of the material for NO adsorption. Although some reports suggests perfect desorption of NO in some MOFs such as in Ni-CPO-27,[10] the NO desorption in STAM-1 is very small which is similar to the desorption in HKUST-1.[9] A significant isotherm hysteresis (Figure 6.1) can be seen in the adsorption and desorption profiles which indicates a strong irreversible adsorption of some of the NO molecules on the open copper sites that line the walls of the hydrophilic pores in dehydrated STAM-1. About 0.65 mmol g^{-1} of NO is not desorbed when the pressure is reduced to almost zero.

For a material to qualify as a gas storage medium, it should not only adsorb the gas but also be able to release it when required. Particularly in biomedical applications the release should be within a controlled rate. The rate of NO release can be different according to the target application. For example some applications such as antibacterial effects need a greater flux of NO whereas for antithrombic applications need a slow rate of release.[10,11] The release of NO from a material is usually done by exposing the material to a flow of wet gas at a controlled relative humidity. The NO in the outlet stream then reacts with ozone which results in a chemiluminescence reaction. The amount of NO release can be measured by the intensity of the chemiluminescence.[9] Since water has a greater affinity for the metal it can easily replace and release NO.

A chemiluminescence NO analyser was used to investigate the release of NO from preloaded STAM-1. The measurement method for NO release used in the

NO analyser is same as described above. The experimental procedure has been described in Chapter 3. The NO release profiles of STAM-1 are shown in Figure 7.1.2 and 7.1.3.
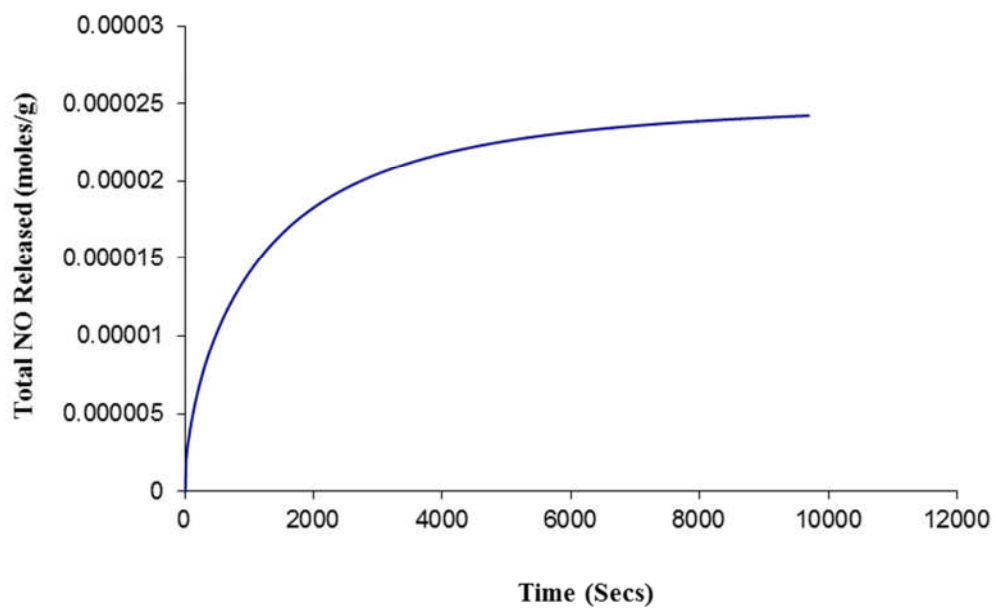

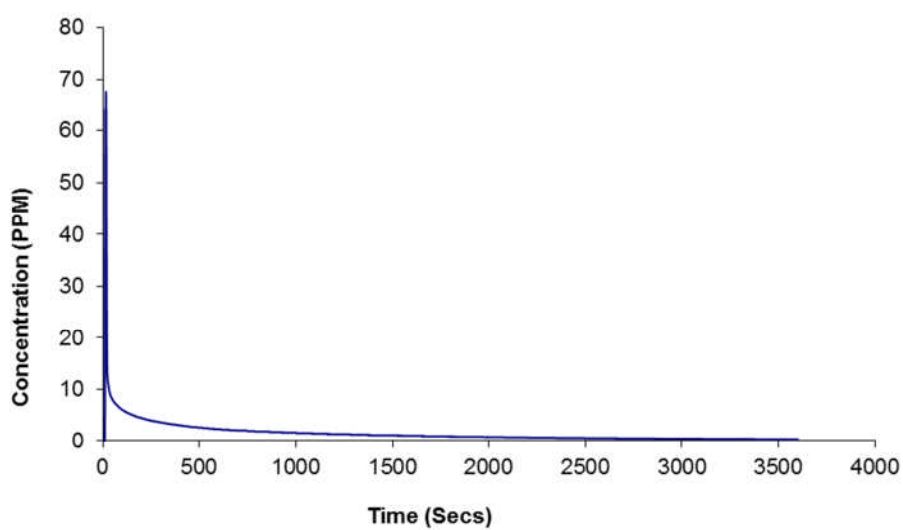**Figure 7.1.2.** The cumulative NO released per g of STAM-1

Figure 7.1.3. NO release profile for NO loaded STAM-1.

The total amount of NO released is about 25 μmol g^{-1} which is a lot less than the amount initially adsorbed. Although the initial amount of NO adsorbed by STAM-1 is about half of the amount adsorbed by HKUST-1, the NO release of STAM-1 is higher than that reported for HKUST-1 (2 μmol g^{-1}).[9] However the total amount of release seen for STAM-1 is significantly less than that of Ni or Co-CPO-27.[10] This is not a disadvantage as some of the biological applications need only a very low concentration of NO. As shown in the case of HKUST-1 the low flux of NO was sufficient to completely inhibit the platelet aggregation in biological experiments.[9]

7.1.3. The Antimicrobial Activity of NO-loaded STAM-1

Staphylococcus aureus and *Psedomonas aeruginosa* are prevalent nosocomial (hospital acquired) pathogens commonly found colonizing in medical devices including vascular lines, endotracheal tubes and urinary catheters.[12-14] *Clostridium difficile* is a widely publicized hospital ''superbug'' pathogen.[12-14] This is a major concern in hospitals and requires the development of new, efficient anti-bacterial protocols. A study was undertaken to investigate the anti-bacterial effects of NO-loaded STAM-1 and the NO-free STAM-1on these bacterial strains with a view to their suitability as bactericidal agents in medical applications. In the same study the anti-bacterial effect of NO-loaded HKUST-1 along with the NO free version also were compared with the anti-bacterial effect of STAM-1. The results which are discussed in this section were done by NovaBiotics Ltd. in Aberdeen, in a certified antibacterial testing laboratory.

Bacteria were cultured separately on three different media namely a cooked meat medium, Mueller Hinton agar and Brain Heart Infusion broth. The anti-bacterial effect of NO-loaded-STAM-1, NO free STAM-1, NO loaded-HKUST-1 and NO free HKUST-1 were studied separately in all three media. Prior to use, these MOFs were prepared as discs composed of the MOF material and polytetrafluoroethylene (PTFE) (1:1 w/w ratio in 20 mg pellets). PTFE was also used separately to see whether it has any effect on the results. Two water soluble antibiotics (Vancomycin and Ciprofloxacin) were used as positive controls for antibacterial activity.

The bactericidal or bacteriostatic effect of a treatment can be determined by estimating the number of bacteria present at t = 0. The growth potential of the bacteria in the experimental conditions also can be studied in same manner. Bactericidal effect is that the number of bacteria levels reduced after the treatment because the bacteria were killed. Bacteriostatic response is the capability of inhibition of the growth or the reproduction of bacteria, so that the numbers remain comparable to those estimated at t = 0.

7.1.3.1.   Results of anti-bacterial effect on *Clostridium difficile*.

The results in Table 7.1.1 demonstrate that both of the nitric oxide (NO)-containing MOFs (STAM-1-NO and HKUST-1-NO) as well as the non NO-impregnated discs (HKUST-1 and STAM-1) inhibited the growth of *C. difficile*

after 24 h incubation at 37 °C under anaerobic conditions and were bactericidal. The PTFE controls did not inhibit growth of *C. difficile*.

	Replicate A	Replicate B	Replicate C
STAM-1	No Growth	No Growth	No Growth
HKUST-1	No Growth	No Growth	No Growth
STAM-1-NO	No Growth	No Growth	No Growth
HKUST-1-NO	No Growth	No Growth	No Growth
PTFE	Growth	Growth	Growth
Vancomycin	No Growth	No Growth	No Growth
Negative Control	No Growth	No Growth	No Growth
Positive Control	Growth	Growth	Growth

Table 7.1.1.   Bactericidal Effects of Metal Organic Frameworks toward
C.difficile. Data are taken from three independent replicates.

7.1.3.2.   Results of anti-bacterial effect on *Staphylococcus aureus*.

The results in Figure 7.1.4 demonstrate that both of the nitric oxide (NO)-containing MOFs (STAM-1-NO and HKUST-1-NO) inhibit growth of *S. aureus* after 24 h incubation at 37 °C under aerobic conditions. Additionally, STAM-

1and HKUST-1 also inhibits growth of *S. aureus* without NO impregnation. The

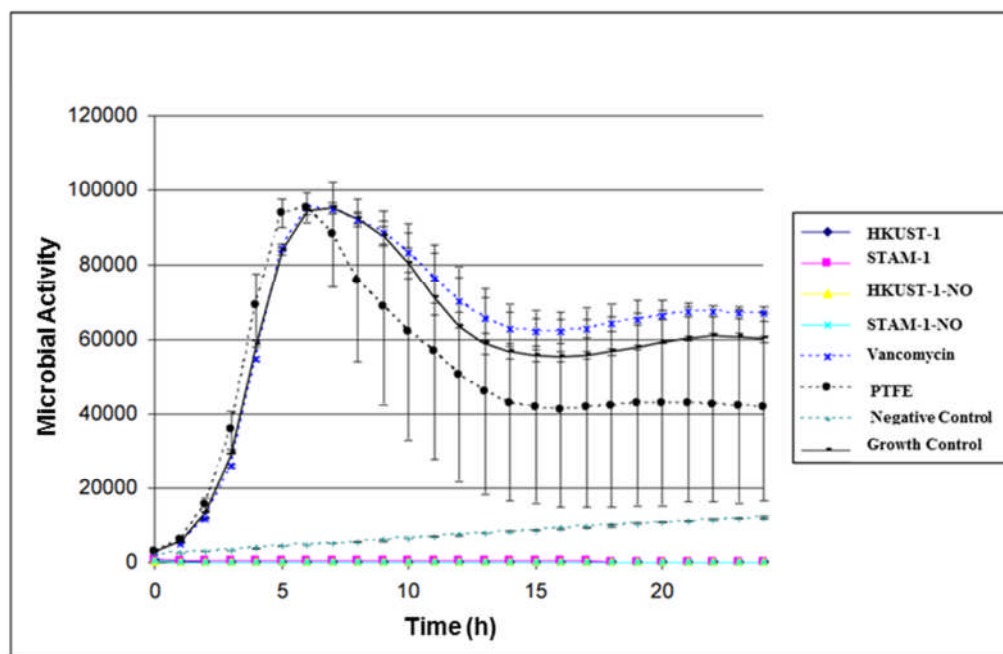PTFE controls had no effect on the growth of *S. aureus*.

Figure 7.1.4.   Growth inhibition of *S. aureus* by Metal Organic Frameworks.

The above results were summarized in Table 7.1.2 which demonstrates both nitric

oxide (NO)-containing MOFs (STAM-1-NO and HKUST-1-NO) and the NO

non-impregnated MOFs (STAM-1 and HKUST-1) were bactericidal towards *S.*

aureus.

	Replicate A	Replicate B	Replicate C
STAM-1	No Growth	No Growth	No Growth
HKUST-1	No Growth	No Growth	No Growth
STAM-1-NO	No Growth	No Growth	No Growth
HKUST-1-NO	No Growth	No Growth	No Growth
PTFE	Growth	Growth	Growth
Negative Control	No Growth	No Growth	No Growth
Positive Control	Growth	Growth	Growth

Table 7.1.2.   Bactericidal Effects of Metal Organic Frameworks toward

S.aureus.

7.1.3.3.   Results of anti-bacterial effect on *Pseudomonas aeruginosa*.

The antibacterial activity towards *Pseudomonas aeruginosa* was the same as presented in the previous two cases. The results are shown in Figure 7.1.5 which demonstrates that both the nitric oxide (NO)-containing MOFs (STAM-1-NO and HKUST-1-NO) and NO non-impregnated MOFs (STAM-1and HKUST-1) inhibit growth of *P.aeruginosa* after 24 h incubation at 37 Å under aerobic conditions. The Teflon controls did not inhibit growth of *P.aeruginosa*.
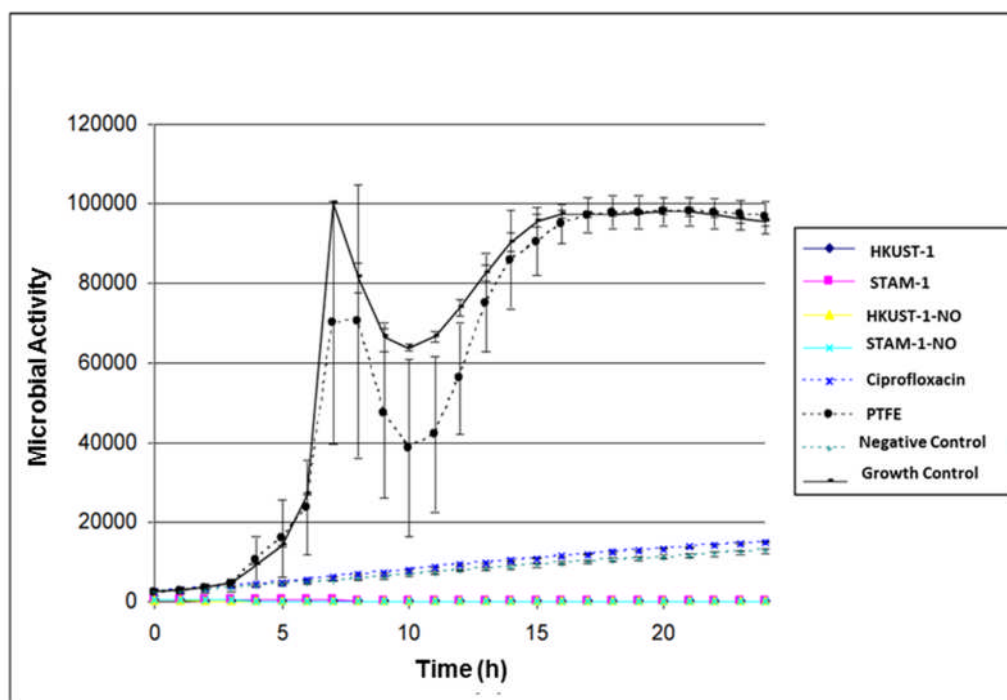
Figure 7.1.5. Growth inhibition of *P.aeruginosa* by Metal Organic Frameworks.

The above results were summarized in Table 7.1.3 which shows the successful antibacterial effects of NO containing as well NO free MOFs towards *Pseudomonas aeruginosa*.

	Replicate A	Replicate B	Replicate C
STAM-1	No Growth	No Growth	No Growth
HKUST-1	No Growth	No Growth	No Growth
STAM-1-NO	No Growth	No Growth	No Growth
HKUST-1-NO	No Growth	No Growth	No Growth
PTFE	Growth	Growth	Growth
Negative Control	No Growth	No Growth	No Growth
Positive Control	Growth	Growth	Growth

Table 7.1.3. Bactericidal Effects of Metal Organic Frameworks toward

P.aeruginosa.

According to the above results it is clear that both STAM-1 and HKUST-1 impregnated with Nitric Oxide (NO) have a significant bactericidal effect on *S.aureaus, P, aeruginosa* and *C. difficile* strains tested. These results are well matched with the previously reported work on bactericidal effects of NO and related species.[9,15] In addition, antibacterial activity was observed with NO free MOF discs towards these bacteria. In the NO free versions, the antibacterial properties arise from the Cu^{2+} ions which are present in both STAM-1 and HKUST-1.

Based on these results it appears that the non-impregnated MOF discs have antimicrobial activity. Impregnated with NO may promote or enhance the antimicrobial activity. However, no increase in metabolic activity inhibition was

observed for the *S.aureaus* and *P. aeruginosa* strains tested. The PTFE control did not inhibit the growth of any of the three strains and was not bactericidal either. The reduction in bacterial numbers compared to the control is a good indicator of the inhibition of bacterial growth in the MOF treatment.

7.1.4. The Antimicrobial Activity of Different Concentration of STAM-1

Since NO-free MOFs (STAM-1 and HKUST-1) show good antimicrobial properties the next step was to analyse the antimicrobial activity of different concentrations of NO free MOFs in order to determine the most effective concentration on the antimicrobial testing. STAM-1 was used for this purpose and the results are discussed in the following sections.

7.1.4.1.   Results of anti-bacterial effect on *Clostridium difficile*.

The results in Table 7.1.4 demonstrate that all the different concentrations of STAM-1 were bactericidal towards *C. difficile* after 24 h incubation at 37 $^{\circ}$C under anaerobic conditions, as was vancomycin. The growth controls demonstrated significant growth of *C. difficile*.

MOF	Replicate A	Replicate B	Replicate C
STAM-1 (5%)	No growth	No growth	No growth
STAM-1 (10%)	No growth	No growth	No growth
STAM-1 (25%)	No growth	No growth	No growth
STAM-1 (50%)	No growth	No growth	No growth
STAM-1 (75%)	No growth	No growth	No growth
160 µg/ml Vancomycin	No growth	No growth	No growth
Growth Control	Growth	Growth	Growth

Table 7.1.4. Bactericidal Effects of STAM-1 toward *C. difficile.* The data presented are from three independent replicates. The % represents the weight percentage. For example 10 % of a 20 mg pellet means 2mg of STAM-1 and 18 mg of PTFE.

7.1.4.2.   Results of anti-bacterial effect on *Staphylococcus aureus*.

Figure 7.1.6 shows the effect of different concentrations of STAM-1 towards the growth of *S. aureus* after 24 h incubation at 37°C under aerobic conditions. The vancomycin control completely inhibited growth of *S. aureus* and all the concentrations tested for STAM-1 also gave similar results as vancomycin

suggesting that even a low concentration of STAM-1 is bactericidal. These results were summarized in Table 7.1.5.
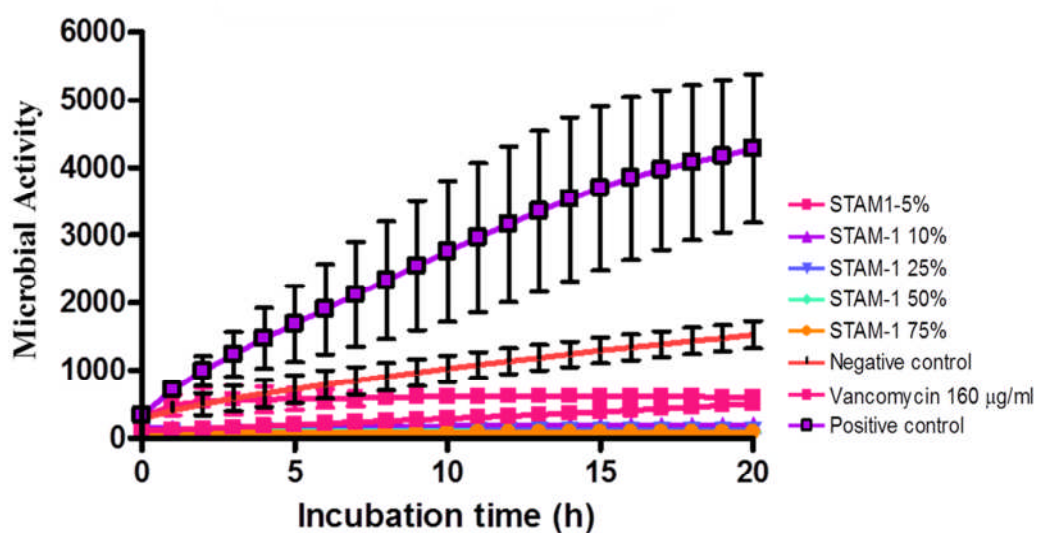

Figure 7.1.6. Growth inhibition of *S. aureus* by STAM-1.

MOF	Growth (cfu/ml)		
	Replicate A	Replicate B	Replicate C
STAM-1 (5%)	No Growth	No Growth	No Growth
STAM-1 (10%)	No Growth	No Growth	No Growth
STAM-1 (25%)	No Growth	No Growth	No Growth
STAM-1 (50%)	No Growth	No Growth	No Growth
STAM-1 (75%)	No Growth	No Growth	No Growth
160 µg/ml Vancomycin	No Growth	No Growth	No Growth
Negative Control	No Growth	No Growth	No Growth
Growth Control	>200	>200	>200

Table 7.1.5.   Bactericidal Effects of STAM-1 towards *S. aureus*. The % represents the weight percentage. For example 10 % of a 20 mg pellet means 2 mg of STAM-1 and 18 mg of PTFE.

7.1.4.3.   Results of anti-bacterial effect on *Pseudomonas aeruginosa*.

The results in Figure 7.1.7 demonstrate that MOFs containing STAM-1 inhibit growth of *P. aeruginosa* after 24 h incubation at 37°C under aerobic conditions. The MOF containing 5% STAM-1 partially inhibited growth (~80%), whereas all MOFs containing higher concentrations of STAM-1 inhibited growth completely.

Ciprofloxacin only partially inhibited growth of *P. aeruginosa*. The reason for this
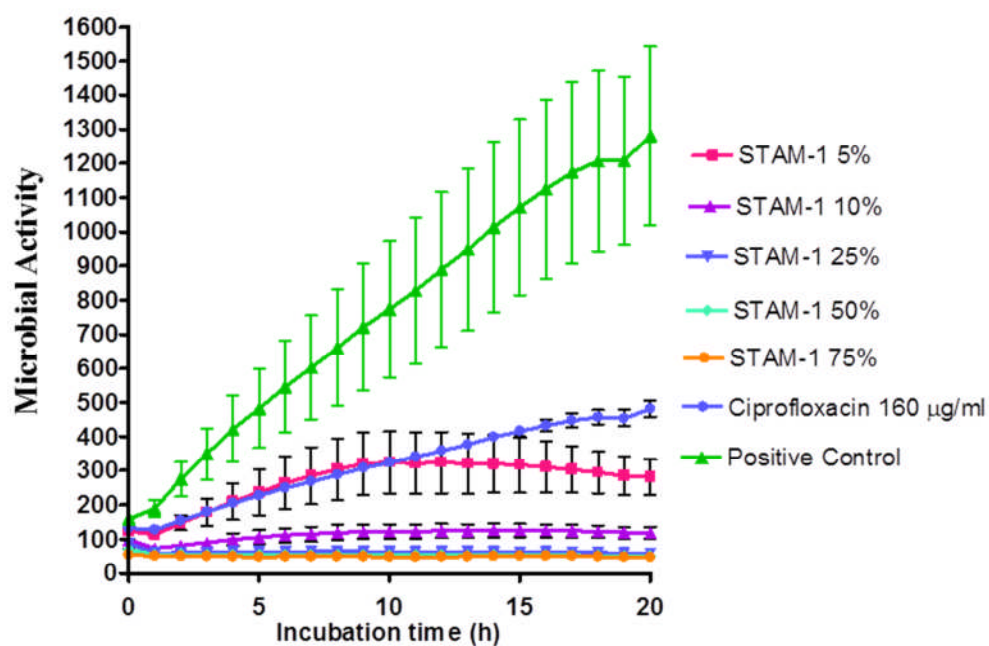
is not known. Table 7.1.6 summarized these results.

Figure 7.1.7. Growth inhibition of *P. aeruginosa* by STAM-1.

MOF	Replicate A	Replicate B	Replicate C
STAM-1 (5%)	Partially Inhibited	Partially Inhibited	Partially Inhibited
STAM-1 (10%)	No Growth	No Growth	No Growth
STAM-1 (25%)	No Growth	No Growth	No Growth
STAM-1 (50%)	No Growth	No Growth	No Growth
STAM-1 (75%)	No Growth	No Growth	No Growth
160 µg/ml Ciprofloxacin	No Growth	No Growth	No Growth
Growth Control	>200	>200	>200

Table 7.1.6.   Bactericidal Effects of STAM-1 towards *P. aeruginosa*. The %

represents the weight percentage. For example 10 % of a 20 mg pellet means 2 mg

of STAM-1 and 18 mg of PTFE.

These results show that STAM-1 was completely inhibitory to all three bacterial

strains tested. The discs containing 5% STAM-1 and 95% PTFE was not

completely inhibitory to growth of *P. aeruginosa* according to the testing, but was

bactericidal. The amount of metabolic activity demonstrated by *P. aeruginosa* in

the presence of 5% STAM-1 was very low (Figure 7.1.7). Since PTFE did not

inhibit growth of any of the tested strains, it is clear from these tests that only a

lower concentration of STAM-1 is required for growth inhibitions towards these

three strains. However, 5% STAM-1 would be a reasonable upper concentration to determine the appropriate concentration.

Fox *et al* has previously reported the bactericidal effect of NO-loaded zeolites and demonstrated that high concentrations of NO are required for bacterial killing.[15] This study was done using Zn^{2+} exchanged zeolites at 50 wt%.[15] In their study, despite Zn being an antibacterial agent, the material needed excess of NO to demonstrate the bactericidal effect. However by surpassing this, STAM-1 which contains Cu^{2+} as the metal source was able to show bactericidal effects in the NO non impregnated version. More interestingly even 5 % of the material was shown to be bactericidal.

7.1.5. Conclusion

Although the research on biomedical applications of MOFs has emerged recently, it has gained a good momentum. MOFs show excellent gas storage properties, particularly for NO. The amounts, rates and formulation of the delivery of NO from MOFs for different medical applications have been studied successfully.[8,9] Recently Hetrick *et al* reported possible uses of NO-loaded zeolites in preventing anti-infective strategies and treatment of established infections.[16] In their study they demonstrated the potential of NO-releasing particles in the clearance of bacterial biofilms.[16]

The bactericidal effects of STAM-1 on a wider range of bacterial strains together with potential anti-fungal and anti-viral effects remains to be investigated. However, the strength of the NO-releasing STAM-1 and HKUST-1 as well as NO free versions in the bacterial strains examined, together with their antibacterial activity provides promising results for their future development. The most important result from this study is that not only the NO releasing materials (STAM-1 and HKUST-1) are highly bactericidal but also the NO free version of STAM-1 and HKUST-1 are highly bactericidal. Furthermore, a very small concentration of STAM-1, such as 5 % of the material was shown to be bactericidal.

Despite this, inhibition of bacterial growth by STAM-1 could have excellent prospects in other areas. For example, the powdered STAM-1 could be used as surface disinfectants. The potential development of STAM-1 as anti-microbial coatings for use in medical devices needs further investigation. Especially about the mechanism and the cytotoxicity *in vivo* needs to be investigated. However, this study clearly highlights the anti-bacterial properties that might be exploited for biological and clinical use.

7.2 Magnetic Properties of STAM-1 and STAM-2

7.2.1. Introduction

The investigation of magneto-structural correlations in Metal Organic Frameworks has evoked considerable interest during the past few years.[17-19] As described in Chapter 1, these MOFs are constructed by linking paramagnetic metal ions with suitable ligands in order to transmit the magnetic interactions. The selection of bridging ligand is very important since it has a great effect on the magnetic properties of the resultant framework. Generally polycarboxylic ligands which are connected with different metal ions give rise to multidimensional systems with interesting properties.[20,21] The interactions between the d orbitals and the carboxylate bridge as well as the conformation of the carboxylate bridge are the main factors which determine the exchange coupling of these systems.[22] Some chain and layer compounds which consist of syn-anti carboxylate conformations have been characterized by weak ferromagnetic or antiferromagnetic interactions between their copper ions.[23,24] For example, a copper complex $\{[Cu(\mu\text{-papa})(H_2O)](ClO_4)\bullet 2H_2O\}n$, [where Hpapa = 2-(pyridylmethyl)amino-3-propoinic acid] was reported which showed weak ferromagnetic interactions between the neighbouring Cu(II) ions.[25] This complex has a helical chain structure with syn-anti carboxylate conformations. In contrast, another copper complex $[Cu(NH_3)_2Br(\mu\text{-CH}_3CO_2)]$ shows net antiferromagnetic interactions despite the fact that the carboxylate groups have syn-anti conformations within the chains.[24] In this case relatively strong inter chain

hydrogen bonding interactions were observed. This suggests that the magnetic behaviour is dependent not only on the intrinsic nature of the metal and the organic ligand but also with a particular level of organization created by the metal-ligand coordination environment.

As described in Chapter 4 both STAM-1 and STAM-2 are composed of Cu(II) ions and mmBTC ligands. Owing to their different topologies they are expected to show significantly different magnetic properties. Therefore the magnetic properties of STAM-1 and STAM-2 were investigated and are discussed in this chapter.

7.2.2. Magnetic Properties of STAM-1

Dimeric copper carboxylates ($Cu_2(O_2CR)_4L_2$) show some interesting magnetic behaviour.[26,27] The Cu-Cu separations of these metal centres are usually between 2.4 and 3.0 Å. The temperature dependent magnetizations of these compounds have been analysed and fitted using the Bleaney-Bowers equation.[26] The paramagnetic properties which they show at room temperature decrease with lowering temperature due to strong antiferromagnetic coupling of the unpaired electrons on the two Cu^{2+} d^9 centres and gives a coupling constant (-2J) of around 300 cm^{-1} in most compounds.[27] The coupling constant (-2J) is dependent on the nature of the carboxylate bridge and the axial ligand.[27] These compounds may form a Cu-Cu bond at lower temperatures (< 50 K) and are essentially diamagnetic in nature.[27]

The STAM-1 is also composed of dimeric copper tetracarboxylate units (Figure 7.2.1) with a Cu-Cu distance of 2.6 Å. Therefore the magnetic properties of STAM-1 were expected to be similar to the properties of these simple dimeric copper carboxylate units such as copper acetate. However since these dimeric units in STAM-1 are assembled into a 2D polymeric structure by virtue of the coordinating ability of the mmBTC linkers, they might show some additional magnetic interactions, which may be more complex in nature.

Magnetic susceptibility measurements for STAM-1 were performed on a Superconducting Quantum Interference Device (SQUID). The samples were sealed in a gelatine capsule inside a straw with a very weak magnetic signal ($< 10^{-6}$ emu), so that the magnetic signal of the samples can be accurately measured. The susceptibility was measured in the temperature range of 1.8 - 300 K as shown in Figure 7.2.2. The temperature dependency of χT is shown in Figure 7.2.3. All data has been normalised against the magnetic field (5000 Oe) and per mole of product.
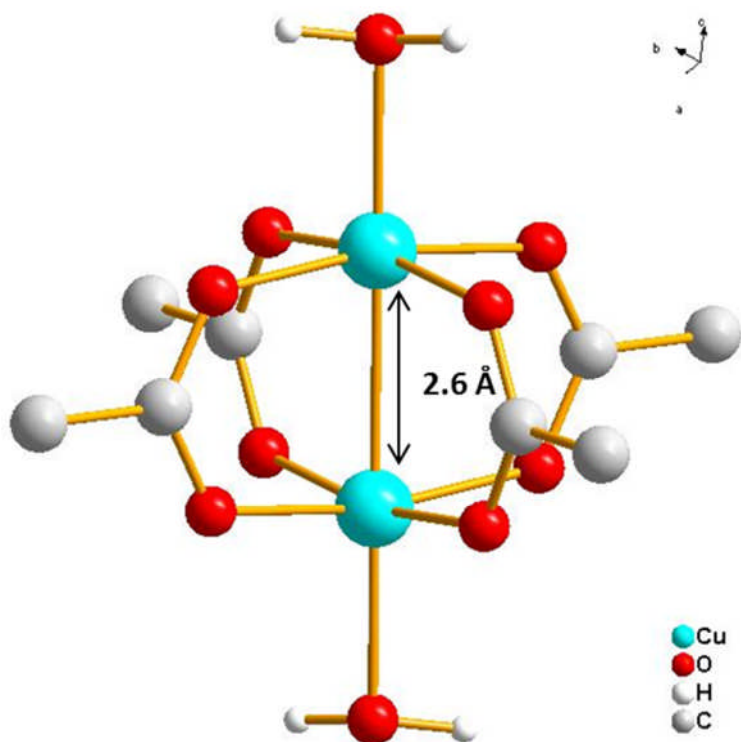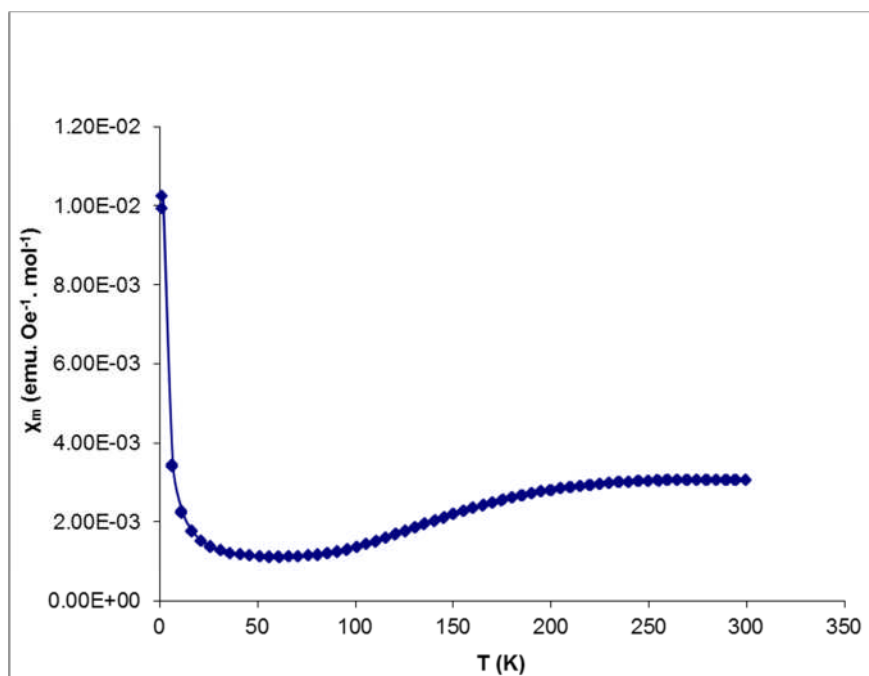
Figure 7.2.1. Copper dimeric unit in STAM-1

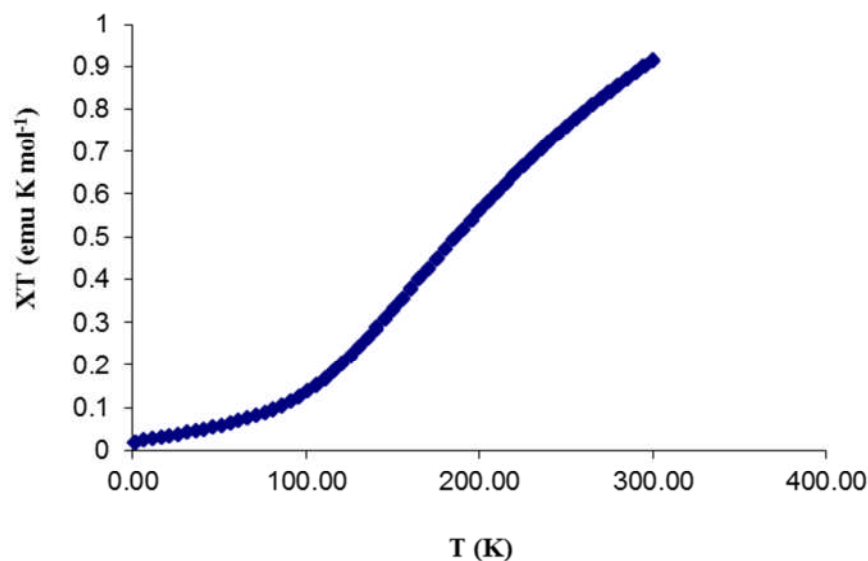**Figure 7.2.2.** The magnetic susceptibility of STAM-1 from 1.8 – 300 K.

Figure 7.2.3. The temperature dependency of χT of STAM-1 from 1.8 – 300 K.

The susceptibility curve shows a maximum at 250 K indicating a very strong antiferromagnetic coupling was involved. This is because of the two copper ions in the dimeric copper carboxylate cluster have opposite spins which results in zero total magnetic moment. Also it is well known that a carboxylato bridge is able to mediate very strong antiferromagnetic interactions in copper(II) complexes.[22-24] As can be seen in the curve the magnetic susceptibility decreases with lowering temperature and reach the minimum at around 50 -70 K and then begin to increase dramatically at lower temperature. This behaviour is similar to what is reported for HKUST-1[27] as both materials have some similarities in the organization of the structure but differ from the χ vs T plot of cupric acetate hydrate[26,27] where χ remains low until below 5 K.

The next step is to find a proper ''model'' to fit the data to the theoretical

expression for the magnetic susceptibility for two interacting spin (S = ½) centers,

which is based on the general Hamiltonian is; Ĥ = -JS1S2, in which the exchange

parameter J, is negative for antiferromagnetic and positive for ferromagnetic

interactions. Therefore the susceptibility per mole of isolated dimers is expressed

in Equation 7.2.1:

$$\chi_M = \frac{2Ng^2\beta^2}{3kT\left(1 + 0.333 * \exp(\frac{-J}{T})\right)} \qquad (7.2.1)$$

g = 2.16; N = $6.022144*10^{23}$ mol^{-1}; β_e= $4.66864*10^{-5}$ cm^{-1} Gauss^{-1}; k =

$1.38066*10^{-23}$ J.K^{-1}; k*T = 0.69504*T cm^{-1} for T in K; 1Gauss = 10^8cm^{-2}.

Where, $\dfrac{2N\beta^2}{3k} = 0.2498$.

g = Factor of spectroscopic splitting

N = Avagadro number

β = Bohr magneton

k = Boltzman constant

Figure 7.2.4 shows a comparison of the theoretical model obtained from the above

equation with the experimental data. Since the copper acetate hydrate complex has

a magnetic susceptibility decreasing with temperature and has a minimum until

below 5 K,[26,27] it might fit well with the model derived above. But unfortunately

the model obtained from the above equation does not fit well with the experimental pattern of STAM-1, below 100 K.
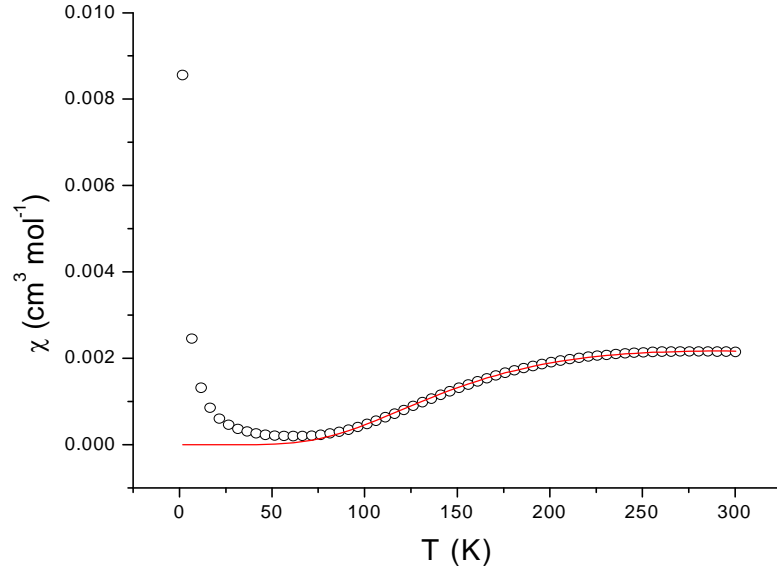

Figure 7.2.4. A comparison of the theoretical fit derived from the Equation 7.2.1 with the experimental data. The coupling constant (J) obtained from this fit is - 324 ± 50 cm^{-1}.

The above model was modified by including the other factors which could have an effect on the interactions. Therefore, the corrected susceptibility is expressed in the equation 7.2.2, which is known as Bleaney-Bowers equation.[26] The model obtained was fit with the experimental data and shown in Figure 7.2.5.

$$\chi_M = \frac{2Ng^2\beta^2}{3kT\left(1 + 0.333 * \exp(\frac{-J}{T})\right)}(1-\rho) + \frac{Ng^2\beta^2}{2kT}\rho \qquad (7.2.2.)$$

The parameter ρ denotes the percentage fraction of paramagnetic impurity in the sample. High values for ρ can lead to problems in fitting theoretical models to experimental data and should be minimised where possible.
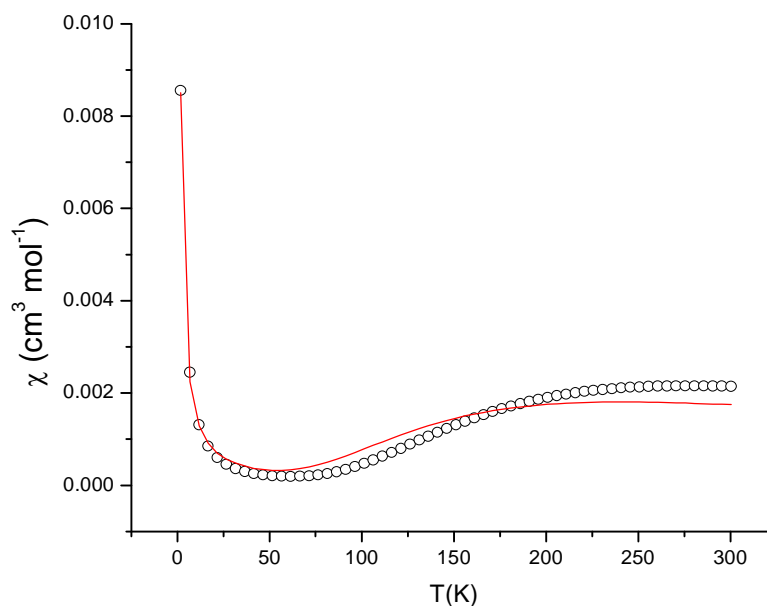

Figure 7.2.5. The experimental data fitted with the model derived from Bleaney-Bowers equation.[26] The coupling constant (*J*) obtained was -275±4 cm^{-1} and

$$\rho = 0.0174 \pm 0.0005.$$

The above model was derived by considering only the magnetic interactions within the copper dimeric units. For example a simple dimer such as copper acetate has interactions only within the dimer. However STAM-1 is formed into 2D layers (Figure 7.2.6) by the interconnection of these copper dimeric units. Therefore the neighboring effect should also be accounted as some additional

magnetic interactions might have been presented due to these neighboring copper dimers.
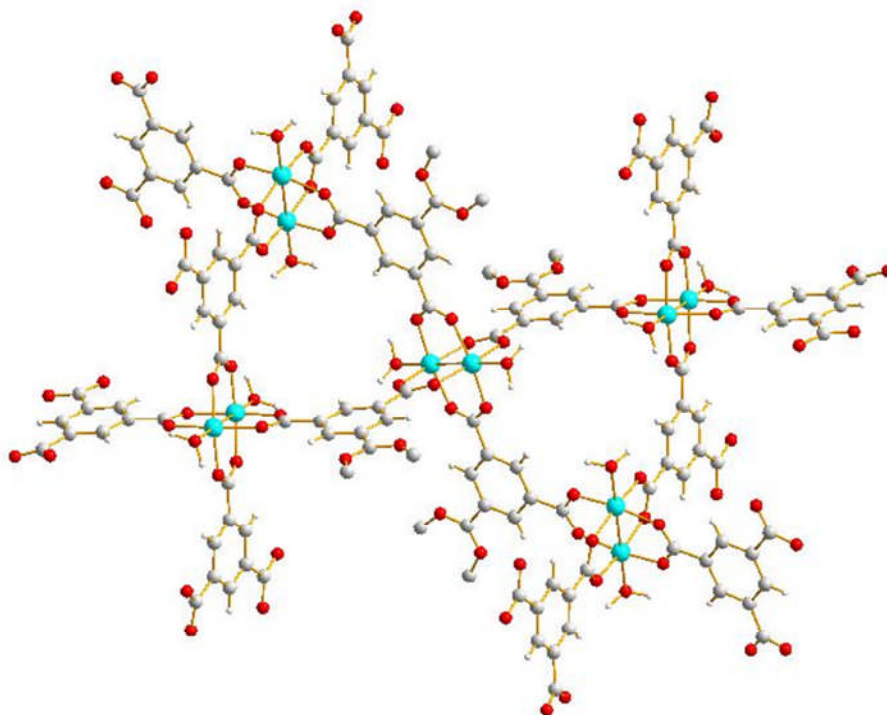

Figure 7.2.6.   Structure of STAM-1 showing neighboring copper dimer units.

Therefore the interactions between neighboring dinuclear identities are included by adding another term denoted J′z (where z is the number of nearest-neighboring dimers) and is shown in Equation 7.2.3. This was simplified and stated in Equation 7.2.4. Then the experimental data was fitted with the theoretical model obtained (Equation 7.2.4) and is shown in Figure 7.2.7.

$$\chi_M = \frac{2Ng^2\beta^2}{3kT\left(1+0.333*\exp(\frac{-2J}{kT})\right)-2J'z}(1-\rho)+\frac{Ng^2\beta^2}{2kT}\rho$$

<div align="right">(7.2.3.)</div>

$$\chi_M = \frac{1.165\times(1-\rho)}{T\left(1+0.333*\exp\left(\frac{-p_2}{T}\right)\right)-2p_3}+\frac{0.874\times\rho}{T}$$
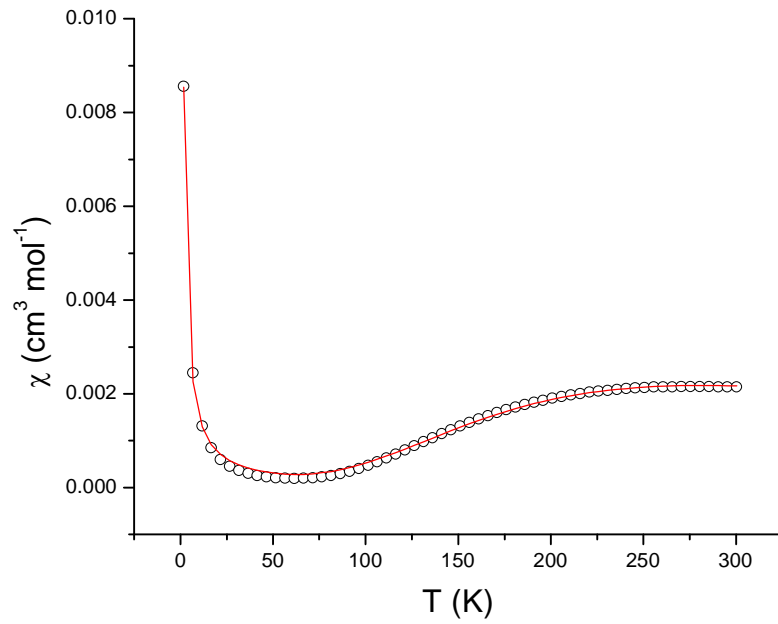
<div align="right">(7.2.4)</div>

Figure 7.2.7. A better fit derived from equation 7.2.4 for the experimental results. (Values obtained from this fit are; J= -317±2 cm^{-1} ; J′z= 108±4 cm^{-1} and $\rho = 0.0175\pm0.0001$)

Although the above model fits well with the experimental results, it can still be improved by introducing a temperature independent contribution (N_α) to the susceptibility. This induces the paramagnetic and diamagnetic constant contribution of the ligands and anions. The model and its simplified version are shown in Equation 7.2.5 and 7.2.6. The comparison of the experimental fit with the theoretical model (Equation 7.2.6) is shown in Figure 7.2.8.

$$\chi_M = \frac{2Ng^2\beta^2}{3kT\left(1+0.333*\exp(\frac{-2J}{kT})-2J'z\right)}(1-\rho)+\frac{Ng^2\beta^2}{2kT}\rho+N_\alpha$$

(7.2.5.)

$$\chi_M = \frac{1.165\times(1-\rho)}{T\left(1+0.333*\exp\left(\frac{-p_2}{T}\right)\right)-2p_3}+\frac{0.874\times\rho}{T}+p_4$$

(7.2.6.)

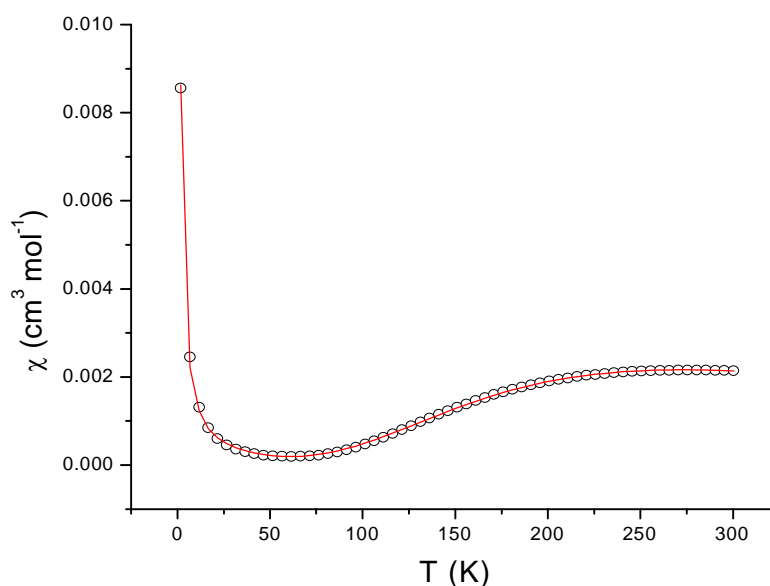**Figure 7.2.8.** The model derived from the equation 7.2.6 fits with the experimental pattern of STAM-1. The values obtained are, J=-308±1 cm^{-1}; J′z= 107±2 cm^{-1} ; N$_\alpha$ = -10^{-4} and ρ = 0.01784±0.00008.

According to the ''best fit'', the *J* value obtained was -308 cm^{-1} which suggests a strong antiferromagnetic interactions. *J*′z is 107 cm^{-1} suggesting strong ferromagnetic interactions. Taken together, these factors support a model of strong antiferromagnetic coupling within the dimer and strong ferromagnetic coupling between the dimers. This behavior has a good agreement with the results reported for HKUST-1 as it also shows both ferromagnetic and antiferromagnetic interactions.[27]

Although both materials show some similarities, the comparison of zero field cooling (ZFC) and field cooling (FC) susceptibilities of STAM-1 are different from that of HKUST-1. The shape of the plot of ZFC of HKUST-1 was similar to

that of STAM-1 and has a minimum at around 90 K whereas FC has a different

shape and gives a maximum at the same temperature (Figure 7.2.9).[27] Although

the author in the case of HKUST-1 has not explained the exact reason to have a

maximum at 90 K in the results of FC susceptibility, it was claimed that if there is

a dip as in the case of ''normal'' ZFC as the applied field will tend to act against

the antiferromagnetic ordering within the dimers.[27] However in the case of

STAM-1 there is no difference between the ZFC and FC susceptibilities (Figure

7.2.10), which suggests that the magnetic property in STAM-1 is not affected by
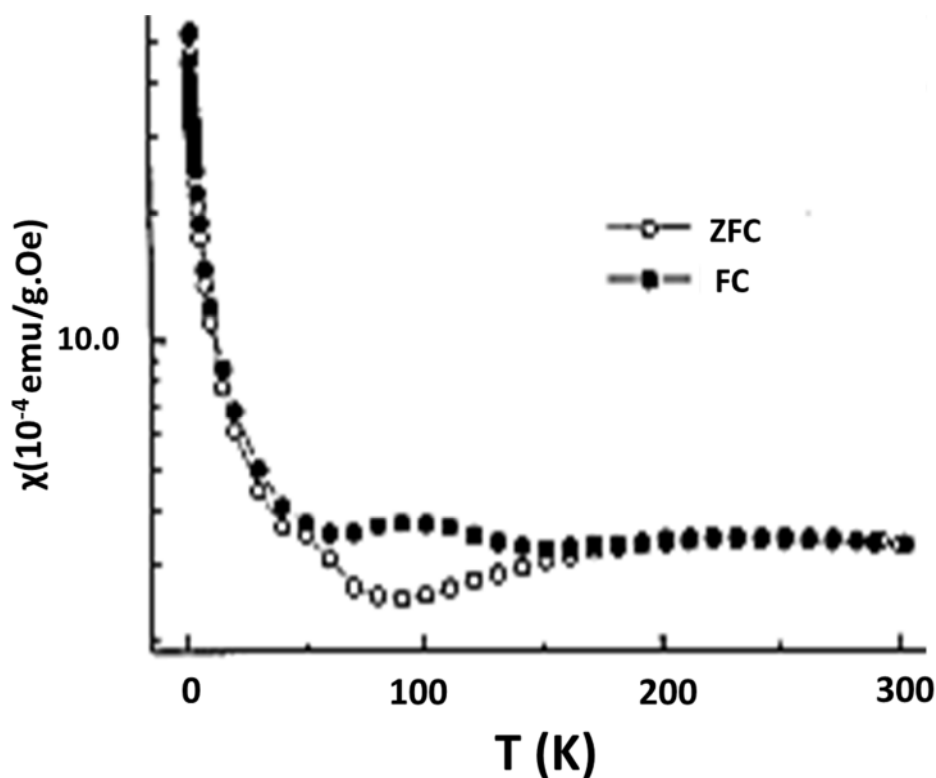
the applied magnetic field.

Figure 7.2.9. ZFC Vs FC temperature dependant magnetic susceptibility of
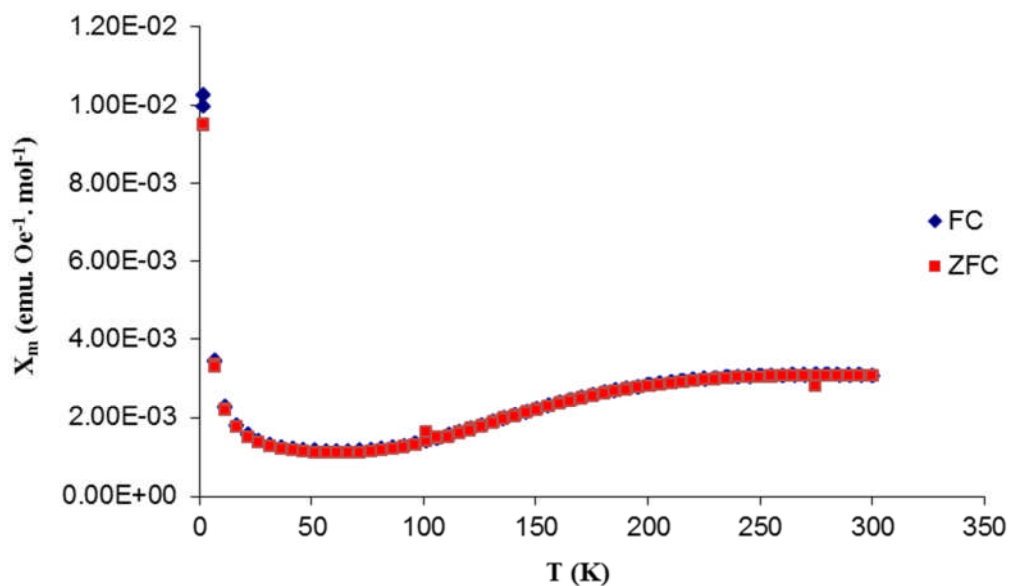
HKUST-1.[27]

Figure 7.2.10. ZFC Vs FC temperature dependant magnetic susceptibility of

STAM-1.

This can be attributed to the difference in the structural organizations of STAM-1

and HKUST-1. The crystal structure in HKUST-1 is of high symmetry (cubic

*Fm*3*m*) and possesses copper dimers at its six vertices and has four of its eight

faces paneled by the BTC ligands (Figure 7.2.11).[20] Each octahedron shares a

corner with its neighbors through the dimeric vertices to form the framework.[20]

But in STAM-1 the dimeric units are arranged in a triangular manner (Figure

7.2.12). Therefore even though these two materials built with the same building

units and show some similarities in magnetic properties, when assembling into the

supra molecular structures they might show some key differences in the magnetic

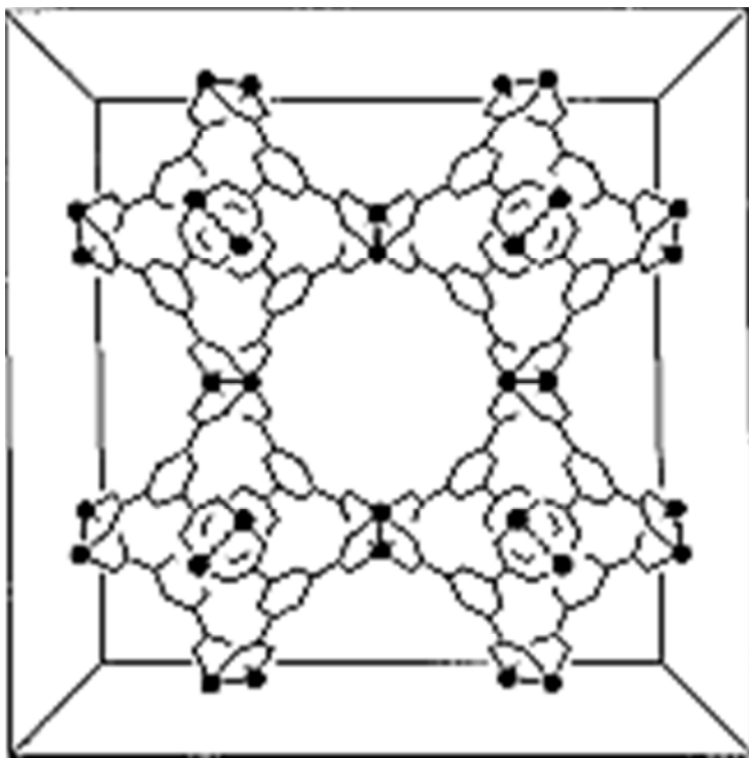properties due to the complex nature of the organization.

Figure 7.2.11. Supramolecular assembly of HKUST-1 showing the neighboring
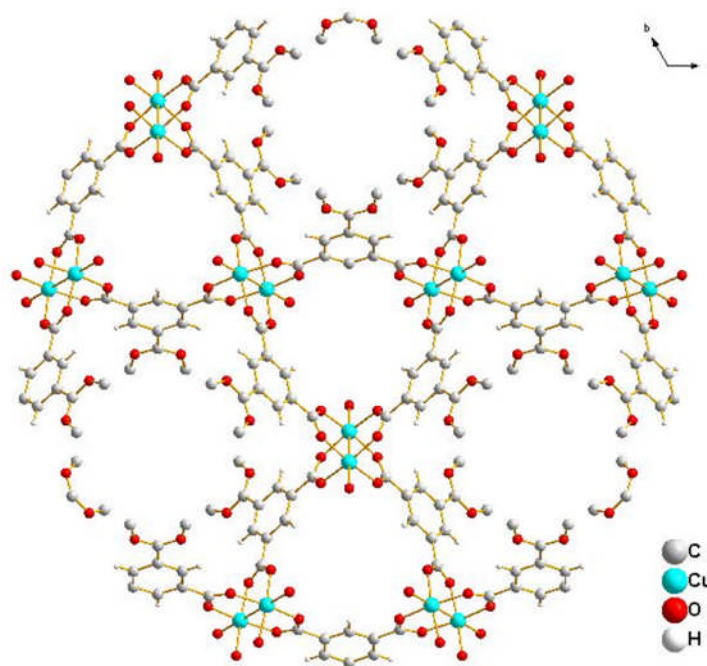
dimers.[27]

Figure 7.2.12. Supramolecular assembly of STAM-1 showing the triangular

arrangement of the dimeric units.

This magnetic study of STAM-1 clearly states the importance of the hierarchical structure. On some occasions the magnetic behaviour was clearly dominated by the copper dimers, which are the simple building units of the structure. However during the formation of Metal Organic Frameworks, these dimeric units interact differently than isolated molecular complexes. The mmBTC ligand of STAM-1 also plays an important role by assisting the electronic exchange and thus magnetic communication between the dimers.

7.2.3. Magnetic Properties of STAM-2

Synthesis and characterization of STAM-2 was described in Chapter 5. Although STAM-2 was obtained from STAM-1 *via* an ultrasonic method, the structural organization of STAM-2 is totally different from that of STAM-1. STAM-2 is consisted with inorganic clusters linked together with mmBTC ligands. The arrangement of copper ions in the inorganic cluster is shown in Figure 7.2.13. It is clear that STAM-2 does not contain any copper dimeric units. Therefore the magnetic properties of STAM-2 should be different from that of STAM-1. Magnetic susceptibility measurements for STAM-2 were performed with the same procedure to that of STAM-1 on the SQUID magnetometer. The susceptibility was measured in the temperature range of 1.8 - 300 K and with an applied field of 5000 Oe as shown in Figure 7.2.14.
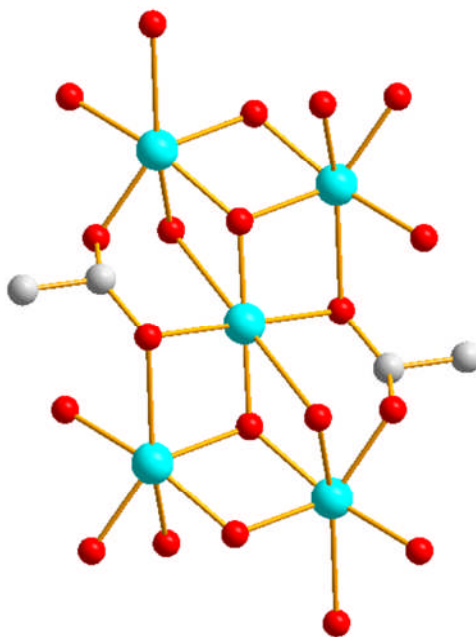

Figure 7.2.13. Arrangement of copper ions in the inorganic cluster of STAM-2.
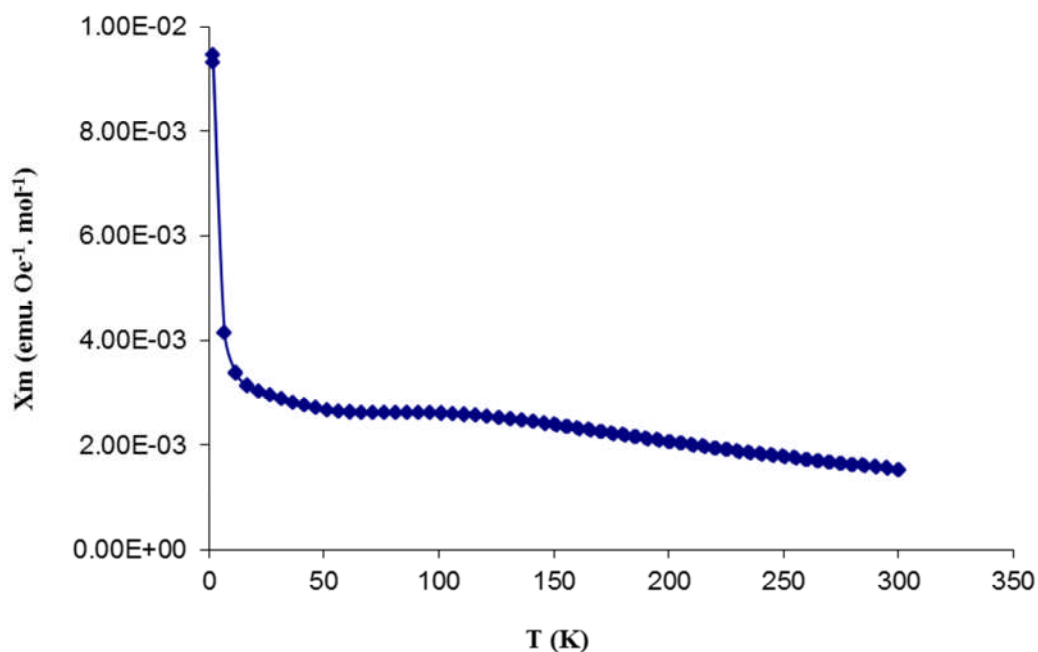
Figure 7.2.14. Magnetic susceptibility of STAM-1

According to the experimental data the magnetic susceptibility increases gradually with lowering temperature till 150 K and below that it remains almost constant until 50 K. To understand this behaviour the temperature dependence of the $1/\chi$ was used and is shown in Figure 7.2.15. According to the data obtained the susceptibility above 150 K is paramagnetic.
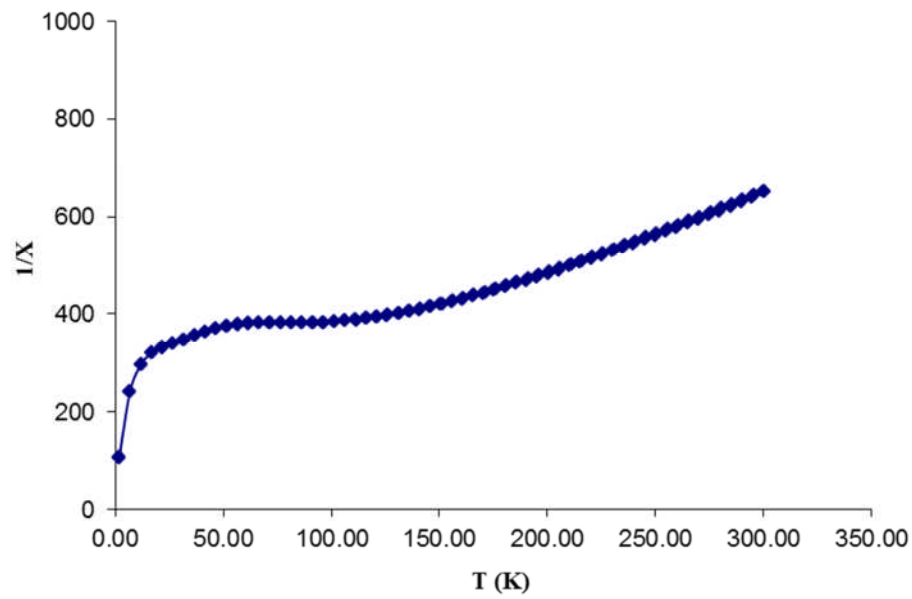
Figure 7.2.15. $1/\chi$ Vs T plot for STAM-2. This plot is useful to analyse the data before using Curie-Weiss Law, to locate the temperature above which the sample is paramagnetic, which in this case is above 150 K

Therefore this was analysed using Curie-Weiss Law (Equation 7.2.7)[26] and fitted the data for the high temperature range (Figure 7.2.16).

Curie-Weiss Law:[26]

$$\chi = C\,/(T - Tc) \qquad\qquad \textbf{(7.2.7.)}$$

χ – Magnetic susceptibility

C – Curie constant
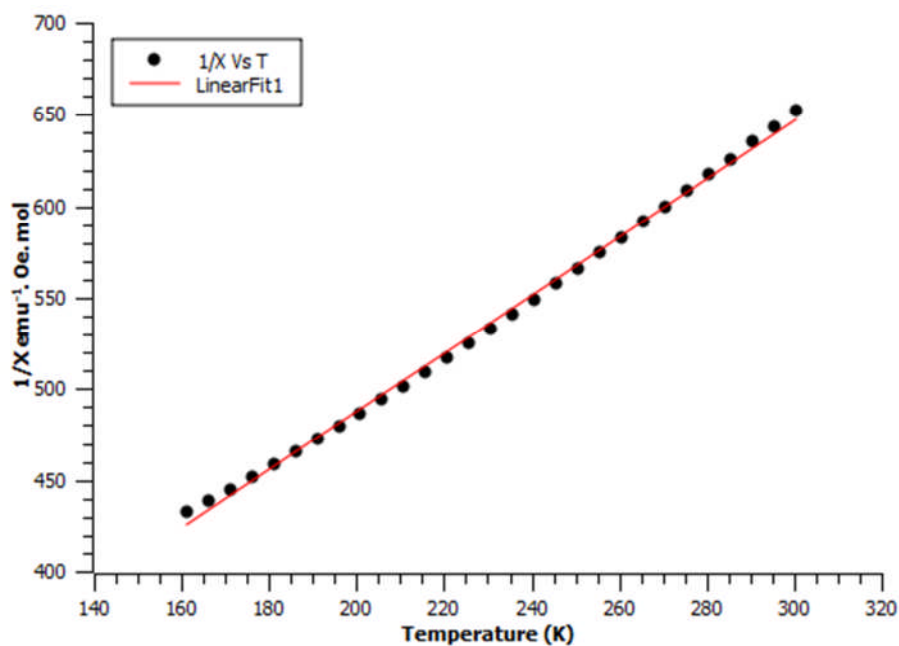
T – Absolute Temperature

Tc – Curie temperature

Figur 7.2.16. 1/χ vs T plot for STAM-2 above 150 K fitted with Curie Weiss

law.

STAM-2 shows Curie-Weiss paramagnetism at high temperature (above 150 K). The values obtained were; Tc = -103 K and C = 0.625. This suggests that STAM-2 shows strong paramagnetic properties at room temperature. This can be attributed to the short distances between the copper ions in the inorganic cluster (Figure 7.2.17). Each copper ion in the cluster is separated only by the oxygen atoms. Each of these clusters is then connected through mmBTC ligands to make the 2D layered network. Below 150 K the material tends to show antiferromagnetic properties.
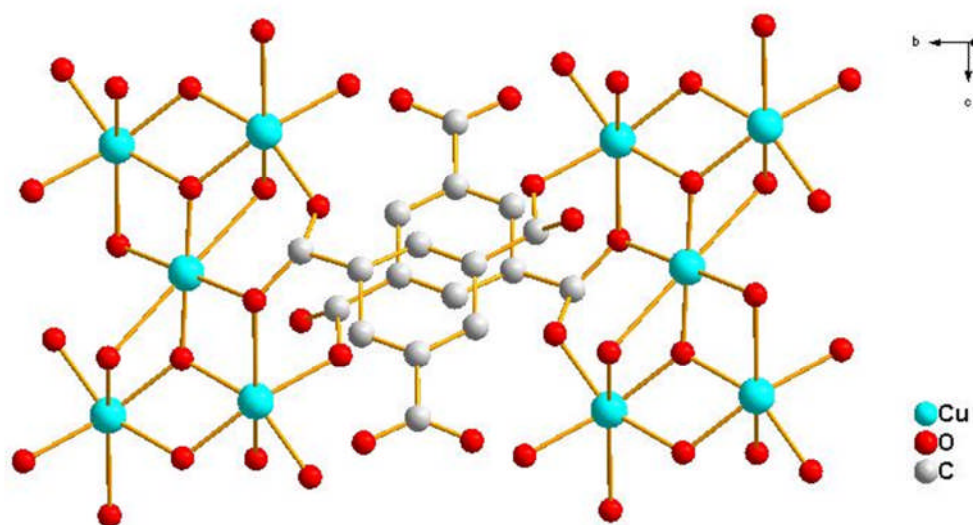
Figure 7.2.17. Structure of STAM-2, showing the inorganic clusters joined

together by the organic ligands.

7.2.4. Conclusion

Magnetism as an application of MOFs has received considerable attention recently. It is interesting that these properties can be controlled through design of MOFs. The improvement of magnetic properties combined with other useful phenomena should be a future goal. For example Kahn *et al* reported a MOF system with Fe spin transition that can be used as memory materials by incorporating into ''smart cards''.[28] Interestingly in another recent report, Wasuke *et al* has used the magnetic data in the absence of single crystal X-ray diffraction data to support the hypothesis that the SBU of the structure of a Copper terephthalate should be $[Cu_2(O_2CR)_4]$.[29]

In contrast to magnetic studies of individual dimers such as copper acetate, STAM-1 shows a complex magnetic behaviour. It shows strong antiferromagnetic coupling within the dimers as well as ferromagnetic coupling between the dimers. This property of ferromagnetism can only be attributed to the incorporation of magnetic dimers in the framework.

STAM-2 has a totally different behaviour than STAM-1. It shows strong paramagnetic properties above 150 K while weak antiferromagnetic coupling below 150 K. The paramagnetic properties arise from the inorganic clusters.

7.3.   References

(1)   Parzuchowski, P. G.; Frost, M. C.; Meyerhoff, M. E. *J Am Chem Soc* **2002**, *124*, 12182.

(2)   Gabizon, A. A. *Clin Cancer Res* **2001**, *7*, 223.

(3)   Zhang, H. P.; Annich, G. M.; Miskulin, J.; Stankiewicz, K.; Osterholzer, K.; Merz, S. I.; Bartlett, R. H.; Meyerhoff, M. E. *J Am Chem Soc* **2003**, *125*, 5015.

(4)   Wheatley, P. S.; Butler, A. R.; Crane, M. S.; Fox, S.; Xiao, B.; Rossi, A. G.; Megson, I. L.; Morris, R. E. *J Am Chem Soc* **2006**, *128*, 502.

(5)   Peer, D.; Karp, J. M.; Hong, S.; FaroKHzad, O. C.; Margalit, R.; Langer, R. *Nat Nanotechnol* **2007**, *2*, 751.

(6)   Colilla, M.; Manzano, M.; Vallet-Regi, M. *Int J Nanomed* **2008**, *3*, 403.

(7) Zhu, H. F.; Ka, B.; Murad, F. *World J Surg* **2007**, *31*, 624.

(8) McKinlay, A. C.; Morris, R. E.; Horcajada, P.; Ferey, G.; Gref, R.; Couvreur, P.; Serre, C. *Angew Chem Int Edit* **2010**, *49*, 6260.

(9) Xiao, B.; Wheatley, P. S.; Zhao, X. B.; Fletcher, A. J.; Fox, S.; Rossi, A. G.; Megson, I. L.; Bordiga, S.; Regli, L.; Thomas, K. M.; Morris, R. E. *J Am Chem Soc* **2007**, *129*, 1203.

(10) McKinlay, A. C.; Xiao, B.; Wragg, D. S.; Wheatley, P. S.; Megson, I. L.; Morris, R. E. *J Am Chem Soc* **2008**, *130*, 10440.

(11) Keefer, L. K. *Nat Mater* **2003**, *2*, 357.

(12) Warren, J. W. *Int J Antimicrob Ag* **2001**, *17*, 299.

(13) Maki, D. G.; Tambyah, P. A. *Emerg Infect Dis* **2001**, *7*, 342.

(14) Plumridge, R. J.; Golledge, C. L. *Pharmacoeconomics* **1996**, *9*, 295.

(15) Fox, S.; Wilkinson, T. S.; Wheatley, P. S.; Xiao, B.; Morris, R. E.; Sutherland, A.; Simpson, A. J.; Barlow, P. G.; Butler, A. R.; Megson, I. L.; Rossi, A. G. *Acta Biomater* **2010**, *6*, 1515.

(16) Hetrick, E. M.; Shin, J. H.; Paul, H. S.; Schoenfisch, M. H. *Biomaterials* **2009**, *30*, 2782.

(17) Kurmoo, M. *Chem Soc Rev* **2009**, *38*, 1353.

(18) Qi, C. M.; Zhang, D.; Gao, S.; Ma, H.; He, Y.; Ma, S. L.; Chen, Y. F.; Yang, X. J. *J Mol Struct* **2008**, *891*, 357.

(19) Guillou, N.; Livage, C.; Drillon, M.; Ferey, G. *Angew Chem Int Edit* **2003**, *42*, 5314.

(20)   Chui, S. S. Y.; Lo, S. M. F.; Charmant, J. P. H.; Orpen, A. G.; Williams, I. D. *Science* **1999**, *283*, 1148.

(21)   Livage, C.; Egger, C.; Nogues, M.; Ferey, G. *J Mater Chem* **1998**, *8*, 2743.

(22)   Chen, X. M.; Wu, Y. L.; Yang, Y. Y.; Aubin, S. M. J.; Hendrickson, D. N. *Inorg Chem* **1998**, *37*, 6186.

(23)   Colacio, E.; Ghazi, M.; Kivekas, R.; Moreno, J. M. *Inorg Chem* **2000**, *39*, 2882.

(24)   Carlin, R. L.; Kopinga, K.; Kahn, O.; Verdaguer, M. *Inorg Chem* **1986**, *25*, 1786.

(25)   Colacio, E.; Dominguez-Vera, J. M.; Ghazi, M.; Kivekas, R.; Klinga, M.; Moreno, J. M. *Eur J Inorg Chem* **1999**, 441.

(26)   Blundell, S. *Magnetism in condensed matter*; Oxford University Press: Oxford ; New York, **2001**.

(27)   Zhang, X. X.; Chui, S. S. Y.; Williams, I. D. *J Appl Phys* 2000, *87*, **6007**.

(28)   Kahn, O.; Martinez, C. J. *Science* **1998**, *279*, 44.

(29)   Mori, W.; Inoue, F.; Yoshida, K.; Nakayama, H.; Takamizawa, S.; Kishita, M. *Chem Lett* **1997**, 1219.

Chapter 8   Other Novel MOFs

8.1.   Introduction

Considerable effort has been focused on the synthesis of new functional materials and supramolecules with novel topologies using BTC and BDC as linkers owing to their ability to coordinate to metal centres through the carboxylate group and their aromaticity.[1,2] Moreover, the rigidity of H_3BTC and H_2BDC may facilitate the formation of inorganic–organic materials with high thermal stability.[1,2] These linkers are sometimes used in combination with 4,4-bipyridyl type ligands in order to obtain pillared networks.[3]   On synthesising these new materials their properties are examined using a number of different characterisation techniques and modifications to the synthetic procedure were carried out to enhance any novel qualities.

In this work MOFs have been synthesized by using both solvothermal and ionothermal techniques. Since ionic liquids are composed of only ions, they show very high ionic conductivity, nonflammability and very low vapour pressure.[4] Ionic liquids, therefore have provided a safe method to prepare MOFs.[4] Ionic liquids are multi-purpose materials; they act not only as a solvent in preparing MOFs but also can act as structure directing agents in the crystallization of the MOFs.[4] At present most of the interest in ionic liquids are centred on the design of 'new solvents'.[5] While the development of 'new solvents' has led to new materials with different

properties, there is still potential for the more commonly used ionic liquids to produce

novel MOFs. Three commonly used ionic liquids were employed in the preparation

of MOFs in this course of study, 1-ethyl-3-methylimidazolium bromide (EmimBr), 1-

butyl-3-methylimidazolium   bromide   (BmimBr)   and   1-isopropyl-3-

methylimidazolium bromide (IospropylmimBr) (Figure 8.1). These were prepared by

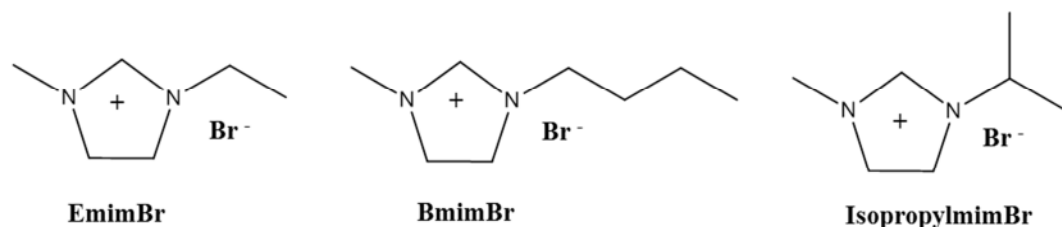following the literature methods which were described in Chapter 4.18.[5]

Figure 8.1.   Ionic liquids used in the preparation of MOFs in this work.

The focus of this chapter is to present the synthesis and characterisation of four novel

materials.

Three were synthesized using solvothermal methods and the other synthesized using

an ionothermal method; these synthetic procedures will be discussed in detail later.

Although the MOFs produced do not show any particularly novel properties, the

design and synthesis of these MOFs might help for the development of new materials

with potentially important product applications in the future.

8.2   Synthesis and characterisation of STAM-8

As described in Chapter 4.9, blue crystals were produced from the reaction between $Cu(CH_3COO)_2$ and 1,3,5-BTC in pyridine (py) and water. Single crystal X-ray diffraction analysis revealed that the network consisted of 2D layers and indicates that the compound crystallizes in the space group R-3c. The single crystal X-ray diffraction data and the final crystallographic parameters are shown in Table 8.1.

The molecular formula is $[Cu_3(BTC)_2(Py)_3 \cdot 3(H_2O)]$ and the repeat unit is shown in Figure 8.2. Cu(II) centre has a distorted square pyramidal geometry where two pyridine molecules and two BTC molecules bind in the equatorial positions and the remaining pyridine molecule binds in the axial position.

Table 8.1. Crystal data from the structural determination of STAM-8 (Full details of

the refinement can be found in the cif in the Appendix 3)

| Identification code	STAM-8
Empirical formula	$Cu_3(BTC)_2(Py)_3 \cdot 3(H_2O)$
Formula weight	904.5
Temperature	293(2) K
Wavelength	0.71073 Å
Crystal system, space group	Trigonal,R-3c
Unit cell dimensions	a=19.0447(15) Å
	b= 19.0447(15) Å
	c= 41.538(6) Å
Volume	13047.41(2) Å^3
Z	18
Calculated density	1.189 g cm^{-1}
Absorption coefficient	0.798 mm^{-1}
F(000)	4842
Theta range for data collection	3.15 to 27.48 deg.
Limiting indices	-22<=h<=24, -24<=k<=17, -53<=l<=48
Reflections collected/unique	30599/3249 [R(int) = 0.0561]
Completeness to theta = 27.38	97.4 %
R1 (I > 2σ(I), wR2 (All data)	0.089, 0.3183
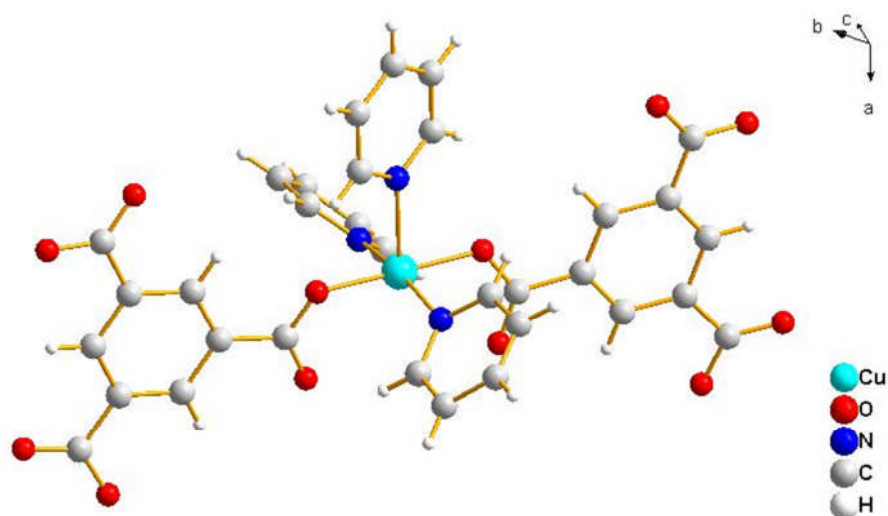
Figure 8.2.   Repeat unit of STAM-8.

While the carboxylates of the BTC forms the 2-D layered network, the pyridine molecules which coordinated in the axial position prevents the 2-D layers from being extended into a higher dimensional network. Solvent accessible channels can be seen when considering a single layer (Figure 8.3). However, owing to the steric repulsions these layers are oriented in such a way that the final packing structure does not contain any solvent accessible channels (Figure 8.4). Water molecules can be seen between the layers which possess H-bonds with the adjacent layers.
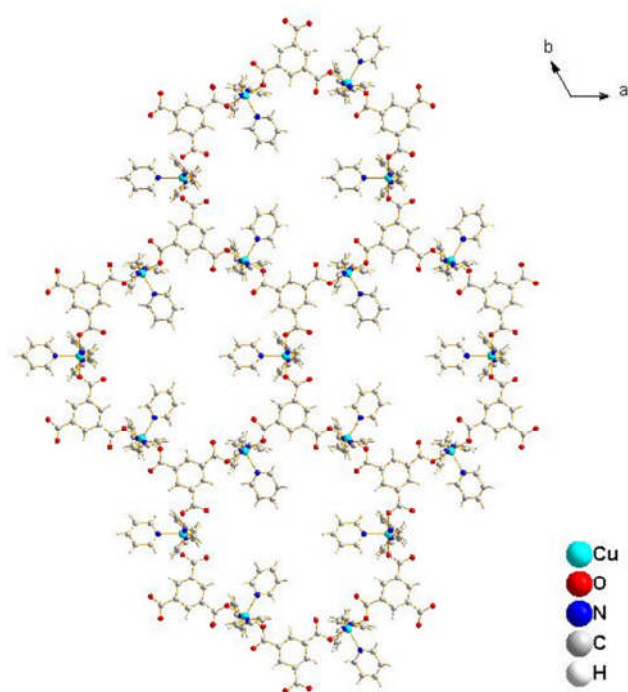
Figure 8.3.   View of a single layer of STAM-8 along the *c*-axis.
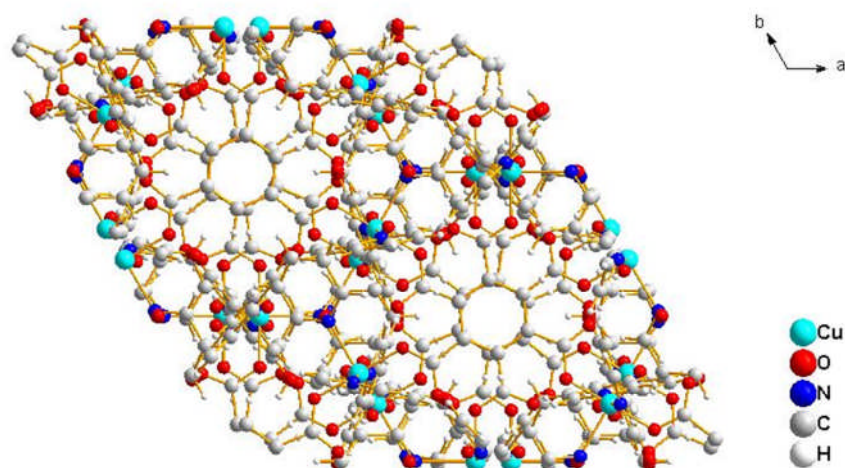

Figure 8.4.   View of STAM-8 along the *c*-axis where channels have been

disappeared.

As can be seen from Figure 8.5, the comparison of the experimental and simulated PXRD patterns shows that there are two phases present in the product; STAM-8 is the minor product and the major product unfortunately could not be identified.
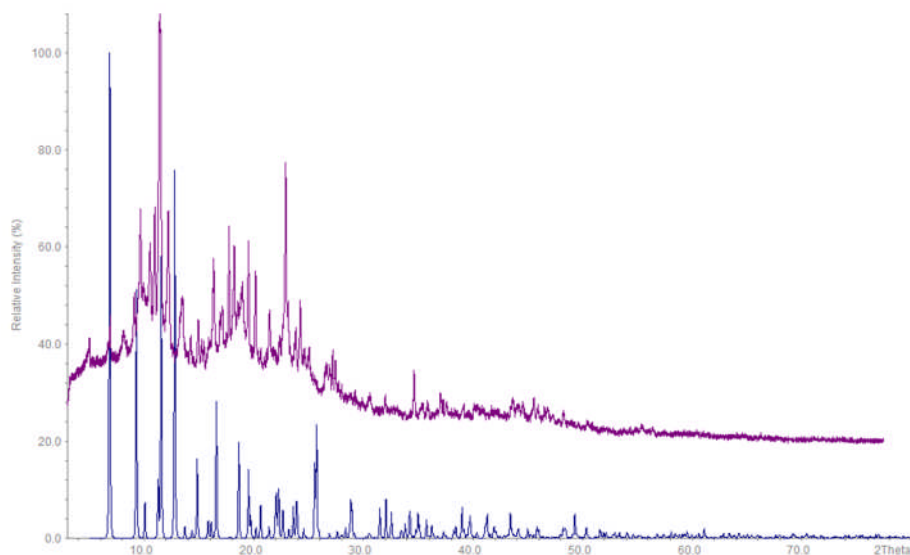

Figure 8.5.   A comparison of experimental (top) and calculated (bottom) PXRD patterns for STAM-8. The calculated pattern is based upon the single crystal X-ray diffraction data; See the relevant cif in the appendix for details.

8.3.   Synthesis and Characterization of STAM-9

The use of mixed ligands to prepare MOF materials is a well-studied area since combining organic ligands of different connectivity, charge and donor functionality can introduce additional levels of structural complexity into the resulting

frameworks.[6] This approach has made access to materials with enhanced properties and thus potential novel applications. A powerful strategy to identify and prepare new complex structural topologies is the combination of small structure-directing agents (SDAs) or template molecules with ligand systems.[7] Template molecules are often small organic species or alkyl ammonium salts. These have been successfully employed in MOF synthesis to influence network topology and pore shape.[8]

Templates such as 4,4-bipyridine and its derivatives have attracted considerable interest for the formation of extended structures by bridging metal nodes.[9] However, the template effects of 4,4-bipyridine are also very important for the preparation of open frameworks containing various dimensionalities.[7] Much work still needs to be carried out in order to have a better understanding of the role of these templates in the formation of novel functional materials. According to the design strategy, a combination of 4,4-bipyridine along with 1,3,5-BTC should prove to be a formulation which would result in the formation of new functional MOFs. Indeed, a 2D MOF has been synthesized which was named STAM-9.

As described in Chapter 4.10, solvothermal reaction of $Cu(NO_3)_2$ with H_2BTC and 4,4-biyridyl (bpy) yields a previously unreported X-ray quality single crystal of STAM-9 $[Cu_3(HBTC)_2(bpy)(NO_3)(OH)]$. The single crystal X-ray diffraction data and the final crystallographic parameters are shown in Table 8.2.

Table 8.2. Crystal data from the structural determination of STAM-9 (Full details of

the refinement can be found in the cif in the Appendix 4)

Identification code	STAM-9
Empirical formula	$Cu_3(HBTC)(bpy)(NO_3)(OH)$
Formula weight	621.81
Temperature	293(2) K
Wavelength	0.71073 Å
Crystal system, space group	Triclinic, P-1
Unit cell dimensions	a = 7.1589 (75) Å
	b = 10.7910 (98) Å
	c = 13.4228 (118) Å
	α = 88.958 (18)°
	β = 84.60 (3)°
	γ = 87.59 (2)°
Volume	1010.0 (11) Å^3
Z	2
Calculated density	1.34 g cm^{-1}
Absorption coefficient	2.171 mm^{-1}
F(000)	548
Theta range for data collection	3.06 to 27.41 deg.
Limiting indices	-5<=h<=8, -10<=k<=12, -15<=l<=16
Reflections collected/unique	3746/2864[R(int) = 0.0333]
Completeness to theta = 27.38	81.7 %
R1 (I > 2σ(I), wR2 (All data)	0.068, 0.2126

STAM-9 possesses an extended 2D structure consisting of corrugated layers (Figure 8.6). These layers are composed of Cu-BTC units connected by the bpy ligands with a crystallographically imposed symmetry of inversion (Figure 8.7). Edge sharing copper tetramers can be seen in the asymmetric unit of STAM-9, with two symmetrical equivalent Cu(II) centres, each possessing a six coordinated geometry. The importance of bpy is not only as a connector but also it plays the important role of template in the crystallization process of the compound. The templated bpy molecules are oriented between the layers in a parallel fashion, blocking each pore (Figure 8.8).
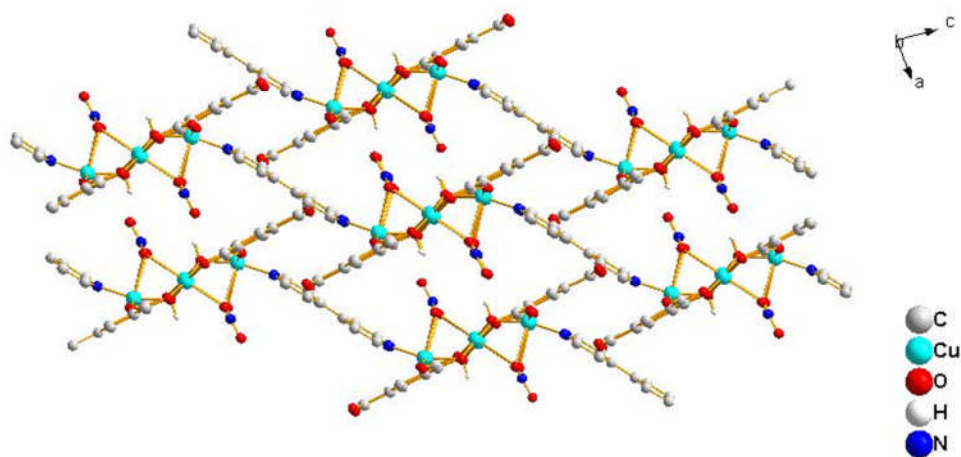

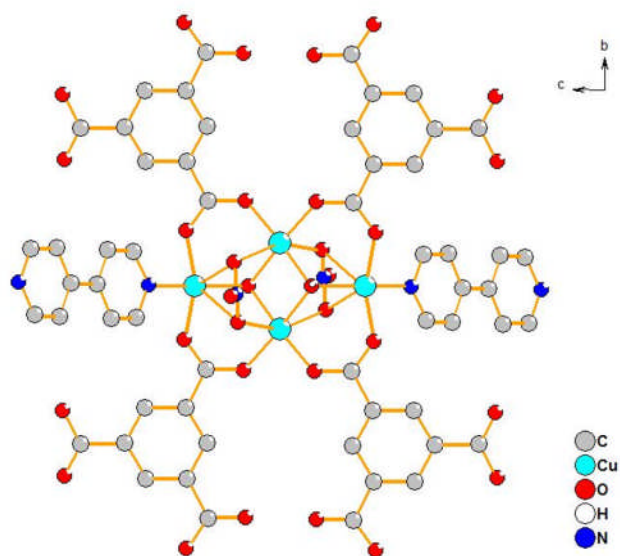**Figure 8.6**. Structure of STAM-9 consisting of Cu-BTC corrugated layers.

Figure 8.7. View of crystallographically imposed symmetry of the structure.
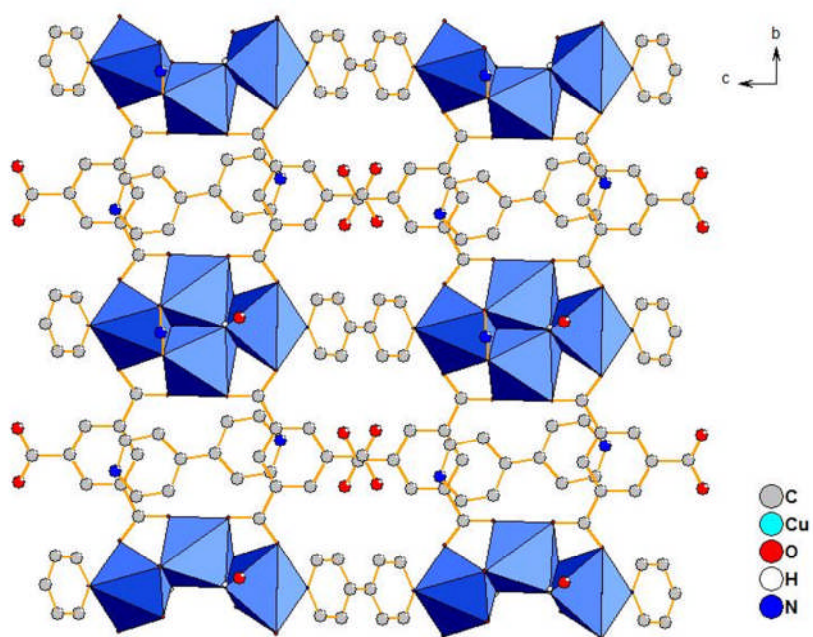

Figure 8.8.   Structure of STAM-9 along the a-axis showing the templated bpy

blocking the pores.

The BTC ligands are partially deprotonated and two of the carboxylate groups contribute to extend the network. Carboxylates of BTC bond in a monodentate fashion to each copper atom. Cu1 is bonded to a bpy, two carboxylates and a hydroxyl group, whereas Cu2 is bonded to two carboxylates and two hydroxyl groups. Carboxylates are bonded in a planar fashion that allows propagation of the layer structure (Figure 8.9). The oxygen of the hydroxyl group has coordination geometry of four and is coordinated to three copper atoms and a hydrogen atom. Oxygen atoms of the nitrate groups possess interactions with both Cu centres. These interactions are not in the range of normal bond distances. Two oxygens of the nitrate group have interactions with Cu1 at distances of 2.6002 Å and 2.7140 Å (Figure 8.9-left) and two oxygens from two nitrate groups possess interactions with Cu2 at distances of 2.7612 Å and 2.4448 Å (Figure 8.9-right).
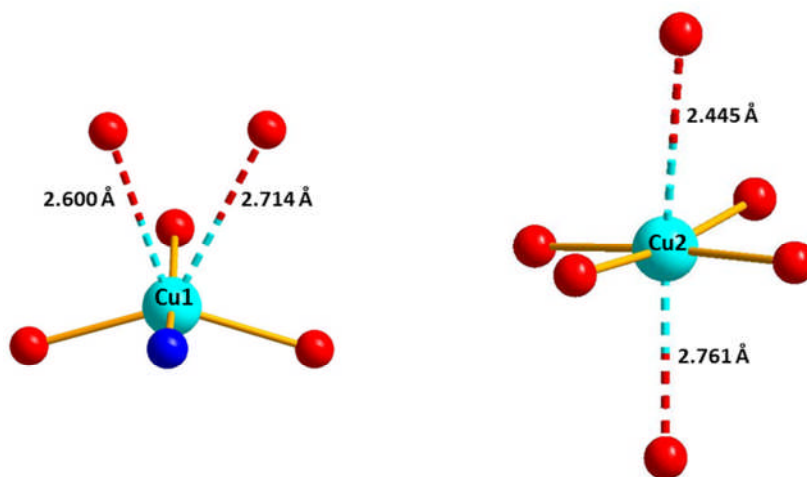

Figure 8.9.   Coordination geometry around Cu1 centre (left) and Cu2 centre (right).

In order to investigate whether these interactions have any contribution towards geometry, the oxidation states of both Cu1 and Cu2 were calculated according to the bond valence method. The basic concept of this method is that the valence V of an atom is the sum of the individual bond valences v_i surrounding the atom (Equation 8.1).[10]

$$V = \sum(v_i) \qquad\qquad (8.1)$$

The individual bond valences in turn are calculated from the observed bond lengths (Equation 8.2).

$$v_i = \exp\left(\frac{R_0 - R}{b}\right) \qquad\qquad (8.2)$$

Where,

R_0 – Tabulated bond length (Cu-O = 1.649 Å and Cu-N = 1.751 Å)

R- observed bond length

b – constant (0.37)

The calculations have shown that even though the interactions are weak they are necessary in order to maintain a valence of two in both Cu centres. Table 8.3 below gives the bond valence sum analysis.

Table 8.3.   Bond valence sum analysis.

Bond	Bond Length (Å)	Bond valences (v_i)
Cu1 O004	1.946(5)	0.448
Cu1 O012	1.944(5)	0.4505
Cu1 O001	1.955(5)	0.4373
Cu1 N009	2.023(7)	0.4794
Cu1 O3	2.7303(13)	0.05380
Cu1 O2	2.5981(13)	0.07690
Cu1		**1.95**
Cu2 O008	1.931(5)	0.4666
Cu2 O007	1.928(5)	0.4705
Cu2 O001	1.968(5)	0.4222
Cu2 O001	1.985(5)	0.4033
Cu2 O3	2.4496(12)	0.1148
Cu2 O2	2.7448(13)	0.0517
Cu2		**1.93**

Figure 8.10 shows a comparison of the experimental PXRD pattern of the as synthesized material with the simulated pattern (taken from single crystal XRD data). Although there is good agreement of the PXRD patterns; a small amount of un-identified impurity is present. Thermogravimetric analysis was carried out in order to investigate the thermal properties of the material (Figure 8.112) in particular to ascertain the stability of the framework after removal of the template.

Only one defined step can be seen in TGA related to weight loss around 300 ℃ in the temperature range of 0 – 400 ℃. Therefore the material was heated to 300 ℃ and subjected to PXRD in order to investigate the stability of the framework after the weight loss. PXRD reveals loss in crystallinity of the product. This means that the framework is not stable at the temperature in which the template is removed.
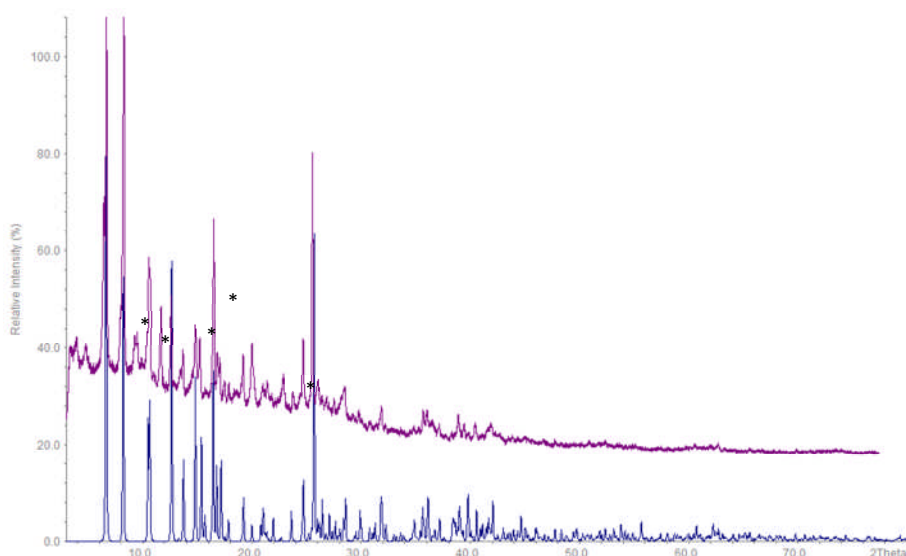

Figure 8.10.   A comparison of experimental (top) and calculated (bottom) PXRD patterns for STAM-9. The calculated pattern is based upon the single crystal X-ray diffraction data; See the relevant cif in the appendix for details. * shows the impurities present in STAM-9.
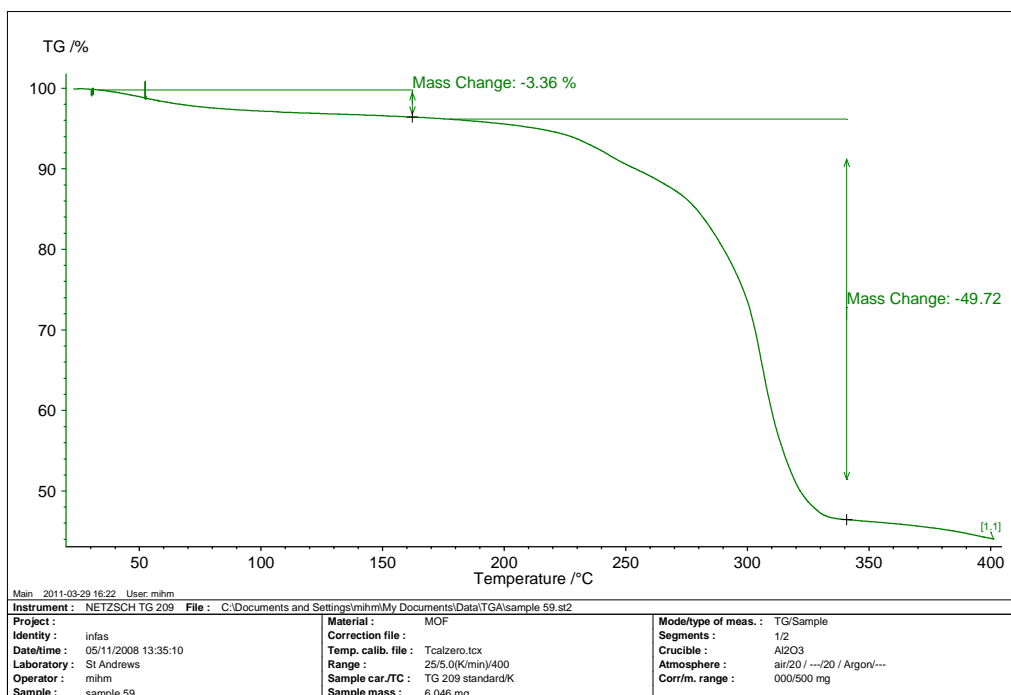
Figure 8.11.   Thermogravimetric analysis of STAM-9.

8.4.   Synthesis and Characterization of STAM-10

As described in Chapter 4.11, STAM-10 was synthesized by the solvothermal reaction of $Zn(NO_3)_2$, BDC and bpy in a mixture of ethanol and water at 110 ºC for 3 days as colourless crystals. It was formulated as $Zn_2(BDC)_2(bpy)_2$ by single crystal X-ray diffraction studies, and the phase purity of the bulk material was examined by PXRD (Figure 8.12). On comparing the experimental PXRD with the simulated pattern; it is clear that there is an un-identified impurity present in the product. However, according to the comparison of PXRD, STAM-10 is the minor product. The single crystal X-ray diffraction data and the final crystallographic parameters are shown in Table 8.4.
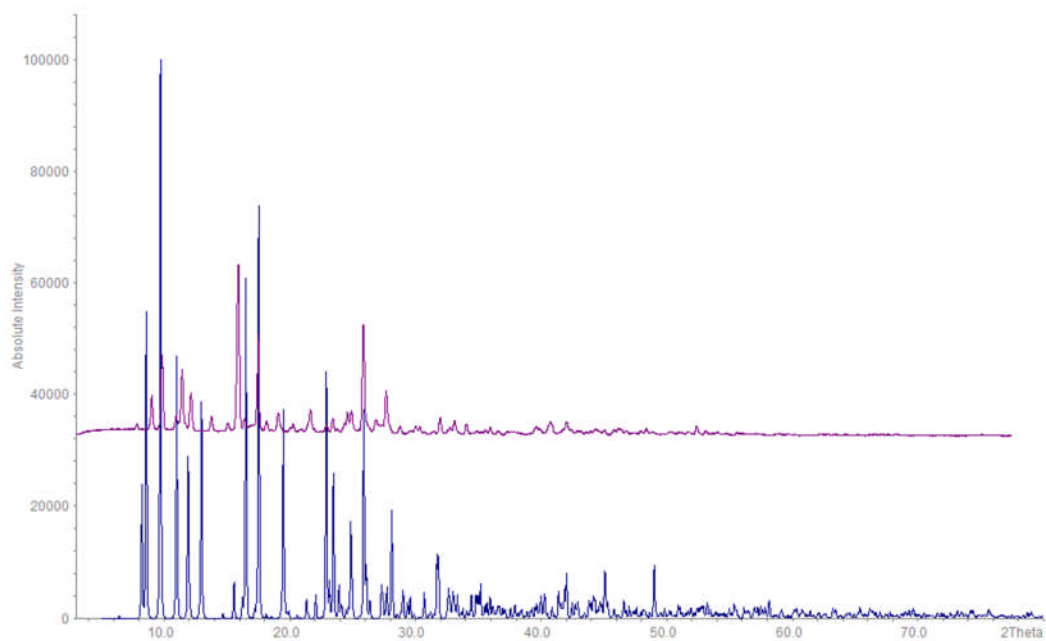
Figure 8.12.   A comparison of experimental (top) and calculated (bottom) PXRD

patterns for STAM-10. The calculated pattern is based upon the single crystal X-

ray diffraction data; See the relevant cif in the appendix for details.

Table 8.4. Crystal data from the structural determination of STAM-10 (Full

details of the refinement can be found in the cif in the Appendix 5)

Identification code	STAM-10
Empirical formula	$Zn_2(BDC)_2(bpy)_2$
Formula weight	771.33
Temperature	293(2) K
Wavelength	0.71069 Å
Crystal system, space group	triclinic, P-1
Unit cell dimensions	a = 10.399 (5) Å
	b = 11.460 (5) Å
	c = 14.812 (5) Å
	α = 108.171 (5)°
	β = 99.646 (5)°
	γ = 95.795 (5)°
Volume	1631.2(12) Å^3
Z	2
Calculated density	0.945 g cm^{-1}
Absorption coefficient	1.53 mm^{-1}
F(000)	784
Theta range for data collection	2.74 to 30.62 deg.
Limiting indices	-14<=h<=14, -16<=k<=16, -21<=l<=20
Reflections collected/unique	9788/5610[R(int) = 0.3615]
Completeness to theta = 27.38	97.3 %
R1 (I > 2σ(I), wR2 (All data)	0.1189, 0.3397

Single crystal X-ray diffraction data reveals that STAM-10 crystallises in the triclinic space group, P-1. It is a 3D network containing two trigonal bipyramidal Zn centres in the repeat unit, the Zn centres have the same coordination environment (Figure 8.13). Each Zn centre is attached to 3 carboxylic oxygens of the BDC linker in a trigonal plane and the axial positions of the trigonal bipyramid are occupied by two bpy ligands. Two different types of bonding are present for the BDC ligand; the carboxylate groups of BDC are attached to the Zn centre as both a monodentate and bidentate fashion.
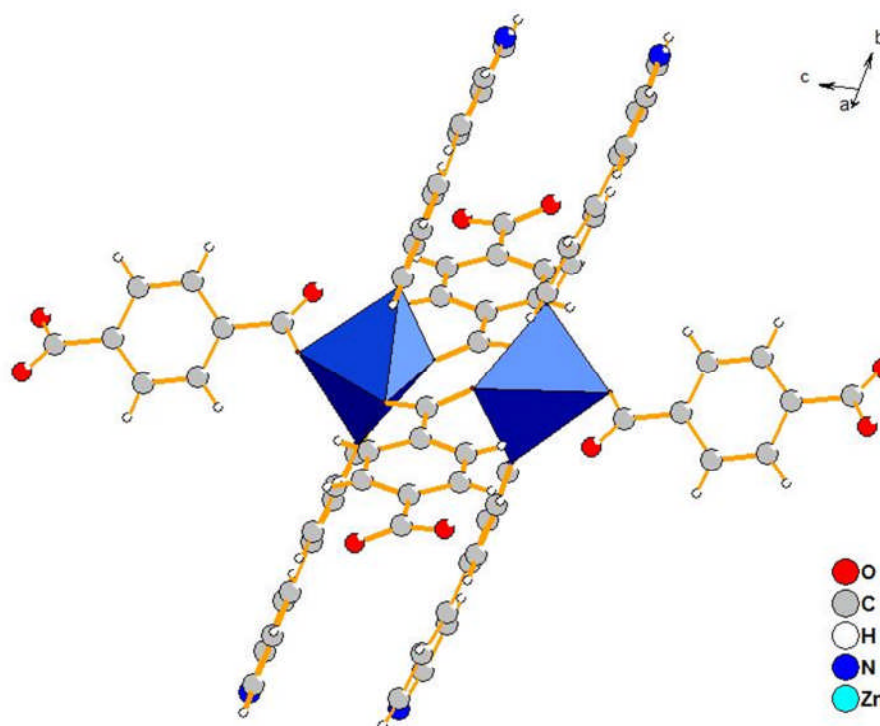

Figure 8.13.   Repeat unit of STAM-10.

There are reports that the introduction of longer dicarboxylates and bidentate pillar linkers lead to the formation of multiple interpenetrated frameworks.[11]

Similarly, the spacious nature of the single network of STAM-10 allows another identical network to interpenetrate it. This interpenetration has occurred as a result of the larger voids (13.47 X 16.23 Å) generated by the BDC-Zn-BPy combination (Figure 8.14). The resulting framework therefore does not contain solvent accessible channels.
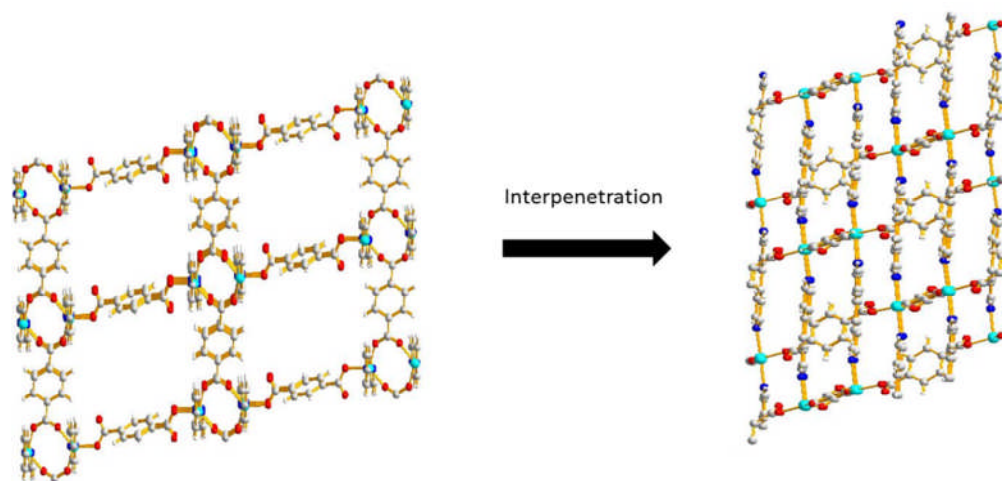

Figure 8.14.   Interpenetration of networks in STAM-10

8.5.   Synthesis of STAM-11

Solvent effect is a vital factor in determining the structure of a MOF. In Chapter 5, the importance of the solvent effect was discussed in relation to the copper nitrate and BTC system. It was shown that an exchange of ethanol for methanol resulted in a different framework structure, HKUST-1 and STAM-1 respectively. Similarly the zinc nitrate and BDC system has been studied under different solvent conditions. This system is very sensitive to variation in the water content and the solvent employed. For example, $Zn(BDC) \cdot DMF \cdot H_2O$ (MOF-2), $Zn_3(BDC)_3 \cdot 6CH_3OH$ (MOF-3) and $Zn_4O(BDC)_3$ (MOF-5) were synthesized by

Yaghi *et al* from the same starting materials but under differing solvent conditions.[2,12,13] In addition, another MOF was reported for the same system by Burrows *et al* which has a formula of $[NH_2ET_2]_2[Zn_3(BDC)_4 \cdot 2.5DEF.[7]$ Interestingly, MOF-5 was reported for the Zn^{2+} and BDC system using fresh Diethylformamide (DEF) whereas $[NH_2ET_2]_2[Zn_3(BDC)_4 \cdot 2.5DEF$ was reported for the same system under the same conditions with hydrolysed DEF which has been in the lab for several weeks.[2,7] This means the solvent has been hydrolysed and has participated as a solvent as well as a template in the synthesis of MOF.

As described in Chapter 4.12, STAM-11 was synthesised in $Zn(NO_3)_2 \cdot 6H_2O$ and H_2BDC under ionothermal conditions, using EmimBr as the solvent. The resultant structure has a formula of $Zn_3Br_2(BDC)_3 \cdot 2(C_6H_{11}N_2)$. The structure consists of trimetallic zinc building units that are interconnected by six BDC units each. A 2D framework is formed as the two bromide ions connected to the terminal zinc centres prevent the further extension of the framework. The single crystal X-ray diffraction data and the final crystallographic parameters are shown in Table 8.5.

Table 8.5. Crystal data from the structural determination of STAM-11 (Full

details of the refinement can be found in the cif in the Appendix 6)

Identification code	STAM-11
Empirical formula	$Zn_3Br_2(BDC)_3 \cdot 2(C_6H_{11}N_2)$
Formula weight	1070.60
Temperature	125(2) K
Wavelength	0.71073 Å
Crystal system, space group	monoclinic, P 2_1/n
Unit cell dimensions	a= 12.869 (4) Å
	b= 9.345 (2) Å
	c= 18.308 (5) Å
	β = 108.094 (5)º
Volume	2092.9(10) Å^3
Z	2
Calculated density	1.042 g cm^{-1}
Absorption coefficient	3.678 mm^{-1}
F(000)	1068
Theta range for data collection	1.71 to 26.37 deg.
Limiting indices	-16<=h<=15, -9<=k<=11, -18<=l<=22
Reflections collected/unique	4219/3599[R(int) = 0.0992]
Completeness to theta = 27.38	98.5 %
R1 (I > 2σ(I), wR2 (All data)	0.0852, 0.2274

The repeat unit of the network is shown in Figure 8.16. There are two symmetrically independent Zn^{2+} ions. Zn1 is tetrahedrally coordinated to three carboxylate oxygen atoms belonging to three distinct carboxylate groups and to a bromide ion. Zn2 is octahedrally connected to six different carboxylate groups. It is possible to distinguish two different coordination modes of the carboxylate groups in the trimetallic units (Figure 8.17). The first one (Type A), both oxygen atoms of the carboxylate group are involved in the coordination of two zinc atoms, forming bridging $Zn(1)O_3Br$ tetrahedra and $Zn(2)O_6$ octahedra. In the second coordination mode (Type B), just one of the two oxygen atoms of the carboxylate groups is coordinated to both Zn(1) and Zn(2) at the same time, thus bridging the two metal centres.
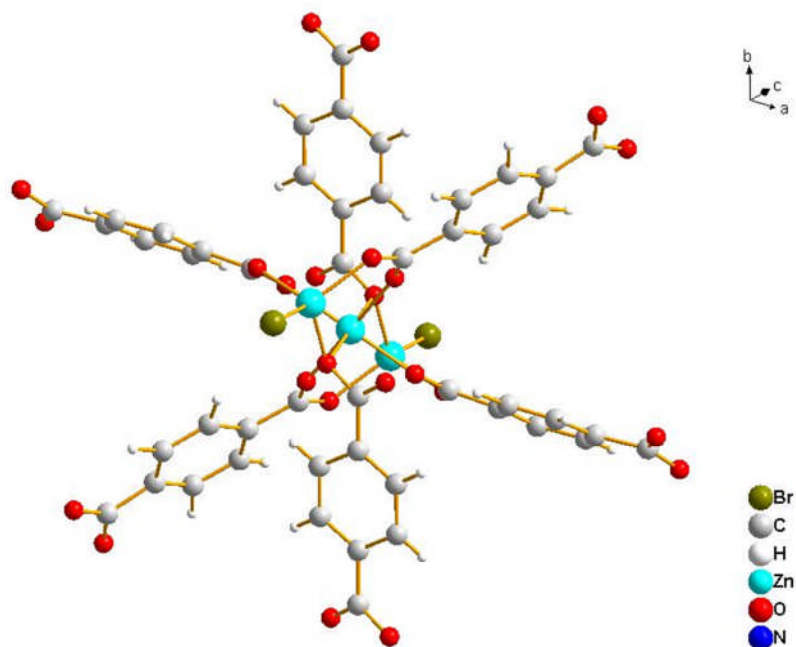

Figure 8.16. Repeat unit of STAM-11.

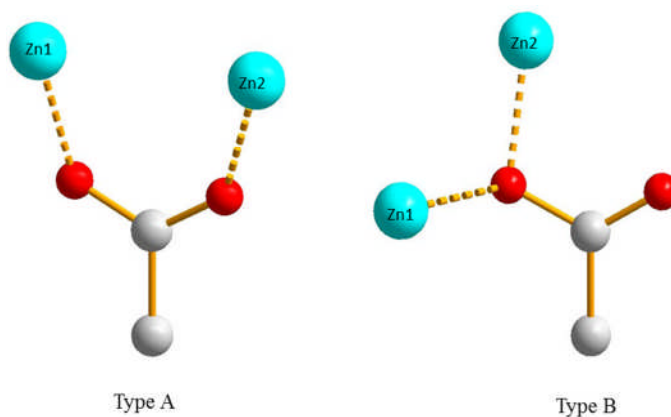Type A   Type B

Figure 8.17. Coordination modes observed in STAM-11. Type A: both oxygen

atoms of the carboxylic group bridge with two metal ions. Type B: only one

carboxylic oxygen atom is coordinating both tetrahedral and octahedral Zn

centres.

Since each trimetallic unit is connected with six terephthalates, they are found to

be formed an interconnected 2D framework in the *bc*-plane using these different

coordination modes of the carboxylates (Figure 8.18). An extension of the

network through the terminal Zn(1) tetrahedral in the *a* direction is prevented by

the coordination of the bromide ions. The resultant structure therefore, is a 2D

layered network. The pores are blocked due to the entrapment of the 1-ethyl-3-

methylimidazolium ions between the layers. This suggests that imidazolium ions

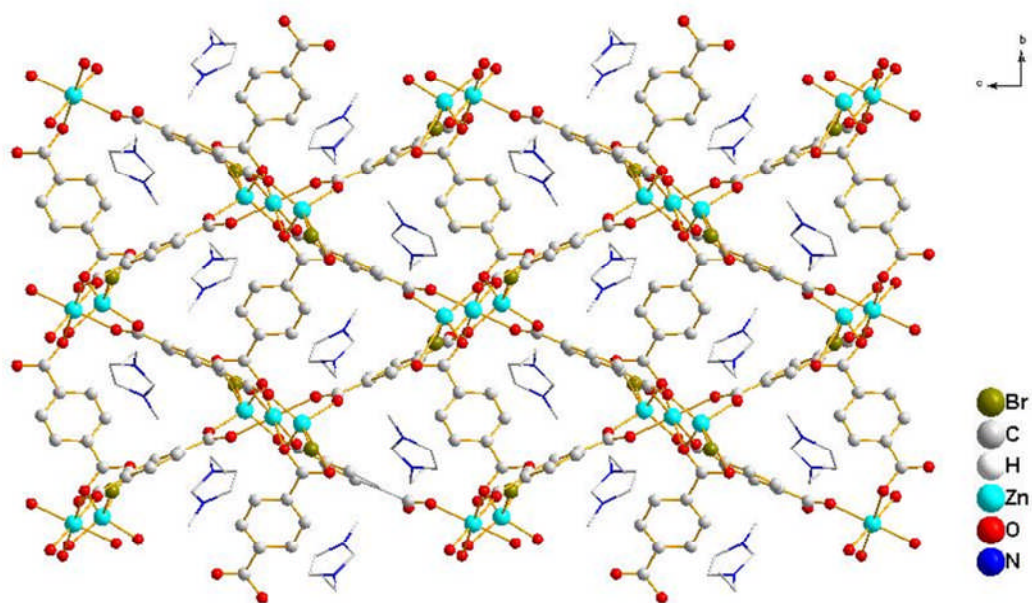play a templating role in the crystallization of this material.

Figure 8.18. Extended structure of STAM-11 in *bc* plane. H-atoms are omitted

for clarity. Templating imidazolium cations are shown in wire and stick

representation.

The structure of STAM-11 is quite similar to that of

$[NH_2ET_2]_2[Zn_3(BDC)_4] \cdot 2.5DEF$, in this particular case it was shown that NH_2Et^{2+}

acted as the templating agent.[7] Both these materials consist of the same Zn

trimetallic cluster with same coordination environment. The two coordination

modes of terephthalates (type A and B) can also be seen in both materials.

However, $[NH_2ET_2]_2[Zn_3(BDC)_4] \cdot 2.5DEF$[7] consists with eight terephthalates in

its trimetallic cluster whereas STAM-11 consists with six terephthalates in the

trimetallic cluster. The main difference between these two structures is that the

bromide ions which are bound to the terminal Zn centres in STAM-11 restrict the

network to 2D layers, while the terminal terephthalates which are in the same

position as the bromide ions in $[NH_2ET_2]_2[Zn_3(BDC)_4]\cdot2.5DEF^7$ allow the network to extend into a 3D framework due to its higher coordination ability.

Figure 8.19 shows a comparison of the experimental PXRD pattern of the as synthesized material with the simulated pattern (from single crystal XRD data). There is a good agreement between the PXRD patterns which shows that a single phase product has been synthesised.
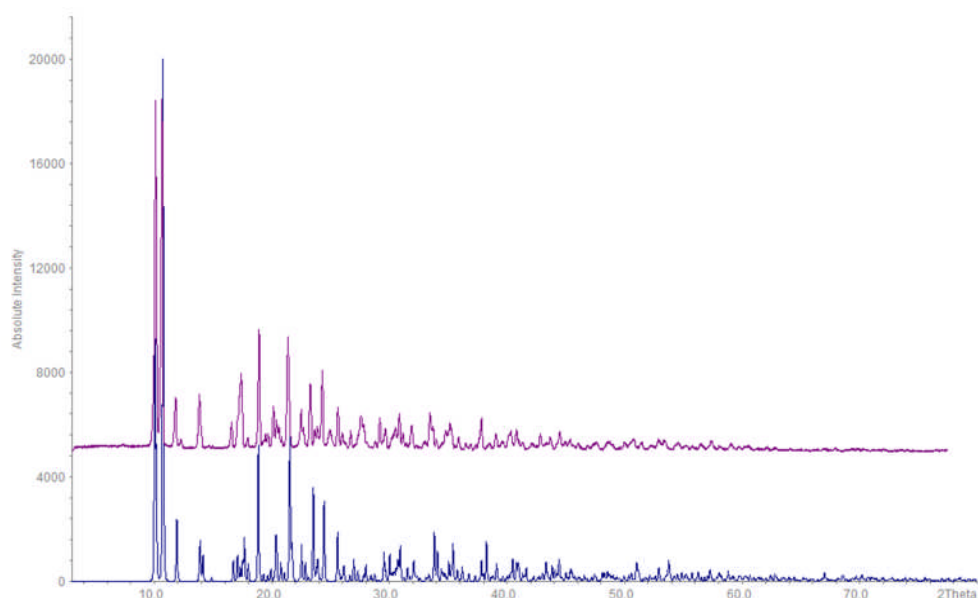
Figure 8.19.   A comparison of experimental (top) and calculated (bottom) PXRD patterns for STAM-11. The calculated pattern is based upon the single crystal X-ray diffraction data; See the relevant cif in the appendix for details.

The thermogravimetric analysis (Figure 8.20) shows a well-defined step, accounting for a weight loss of 15 % at ~340 ºC. This weight loss can be assigned to the removal of the 1-ethyl-3-methylimidazolium template present in between

the layers of the structure. Following the thermal treatment, the structural integrity of the material was examined using PXRD. As shown in the PXRD pattern, Figure 8.21, STAM-11 remains highly crystalline and retains the main structural features of the as synthesised material. However, there is broadening of the peaks and several peaks are shifted. In addition there is the disappearance of some peaks which is shown by * symbol. These changes can be attributed to distortion of the crystal lattice in response to the removal of the template molecules. This is commonly observed in many MOF structures.
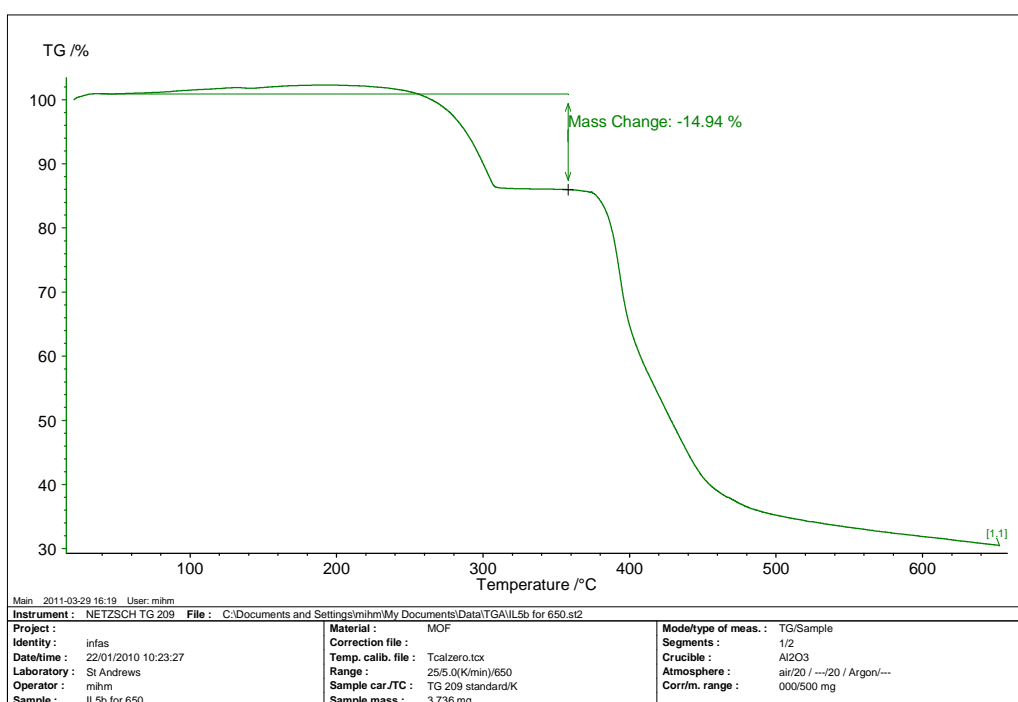
Figure 8.20.   Thermogravimetric analysis of STAM-11
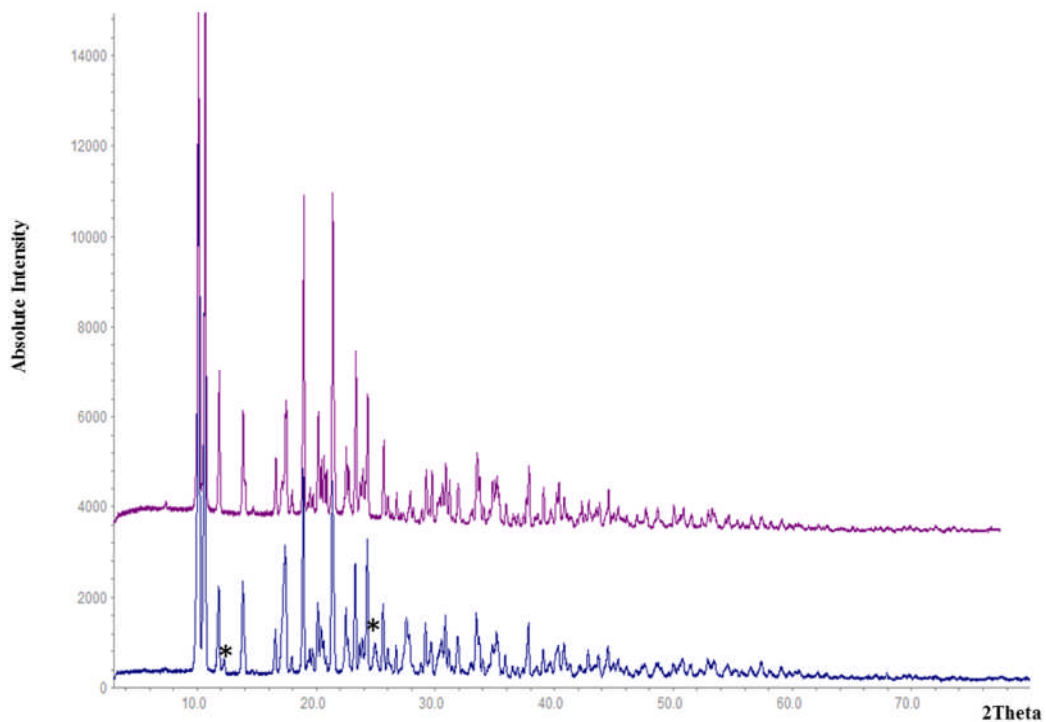
Figure 8.21.   A comparison of PXRD of the material after the thermal treatment

at 340 ºC (top) and the as synthesised material of STAM-11 (bottom). * Shows the

peaks which can be seen in the as made material whereas disappeared in the

heated material

Gas adsorption studies were undertaken after removal of template from the
material in order to determine the porosity of STAM-11. The N_2 adsorption
experiments show that the material does not uptake any gas and thus suggest that
the material is non-porous.

8.6.   Conclusion

MOFs are a diverse and rapidly growing class of functional materials. The use of organic bridging ligands has allowed the design and functionalization of new structures and allows the properties of MOFs to be rationally tuned.

The synthetic strategy of STAM-9 incorporating mixed ligands with a metal source gives obvious choices. Bonding motifs of different coordinating strengths of different linkers in one 'reaction pot' offer many opportunities to design advanced materials that show new and interesting dynamic properties. Although STAM-9 does not show any porosity due to the pore blocking process of the template, it shows some interesting structural features due to the mixed ligand system and the cage like structure resulting from the copper tetramer. Variation of the reactant concentrations or application of different conditions may give rise to STAM-9 without its templates.

When long linear linkers are used to synthesize MOFs, it will generate larger voids. If the voids in a structure are larger enough to accommodate another framework, the interpenetration is resulted. The effect of interpenetration can be seen in STAM-10, which has led to diminish the porosity of the material.

The ionothermal synthesis resulted STAM-11 which has a 2D layered structure. It shows interesting structural features and high thermal stability even after removal of templates. This is quite surprising because of the interactions between

imidazolium ions and the framework is expected to be strong due to the ionic nature of the template. However the stability of the framework is maintained at higher temperature as well as after removal of template ions.

8.7. References

(1)   Chui, S. S. Y.; Lo, S. M. F.; Charmant, J. P. H.; Orpen, A. G.; Williams, I. D. *Science* **1999**, *283*, 1148.

(2)   Li, H.; Eddaoudi, M.; O'Keeffe, M.; Yaghi, O. M. *Nature* **1999**, *402*, 276.

(3)   Kondo, M.; Okubo, T.; Asami, A.; Noro, S.; Yoshitomi, T.; Kitagawa, S.; Ishii, T.; Matsuzaka, H.; Seki, K. *Angew Chem Int Edit* **1999**, *38*, 140.

(4)   Parnham, E. R.; Morris, R. E. *Accounts Chem Res* **2007**, *40*, 1005.

(5)   Bonhote, P.; Dias, A. P.; Papageorgiou, N.; Kalyanasundaram, K.; Gratzel, M. *Inorg Chem* **1996**, *35*, 1168.

(6)   Tanaka, D.; Kitagawa, S. *Chem Mater* **2008**, *20*, 922.

(7)   Burrows, A. D.; Cassar, K.; Friend, R. M. W.; Mahon, M. F.; Rigby, S. P.; Warren, J. E. *Crystengcomm* **2005**, *7*, 548.

(8)   de Lill, D. T.; Gunning, N. S.; Cahill, C. L. *Inorg Chem* **2005**, *44*, 258.

(9)   Heck, R.; Bacsa, J.; Warren, J. E.; Rosseinsky, M. J.; Bradshaw, D. *CrystEngComm* **2008**, *10*, 1687.

(10)   Brown, I. D.; Altermatt, D. *Acta Crystallogr B* **1985**, *41*, 244.

(11)   Horike, S.; Tanaka, D.; Nakagawa, K.; Kitagawa, S. *Chem Commun* **2007**, 3395.

(12)   Li, H.; Eddaoudi, M.; Groy, T. L.; Yaghi, O. M. *J Am Chem Soc* **1998**, *120*, 8571.

(13)   Eddaoudi, M.; Li, H. L.; Yaghi, O. M. *J Am Chem Soc* **2000**, *122*, 1391.

Chapter 9   Conclusion and Further Work

9.1.   Conclusion

The overall aim of this project was to design and synthesize novel Metal Organic Frameworks and examine their properties for application in a variety of fields. A number of novel MOFs were prepared during this course of study as has been discussed earlier in this thesis. STAM-1 was the only material to show permanent porosity with some interesting properties for different applications among the MOFs synthesized and hence was fully characterised. STAM-2 also showed some interesting molecular magnetism properties.

In STAM-1, one carboxylate of the BTC linker undergoes monomethyl esterification *in situ* while the other two carboxylate groups are protected by the MOF compound. This opens up a new application for MOFs as they now could be considered as protecting tools in synthetic organic chemistry.

In as synthesised STAM-1 there are two types of channel systems; one where there are open metal sites which results in the channels being hydrophilic in nature and the other channel is hydrophobic due to methyl ester groupings coating the internal surface. On dehydrating STAM-1 there are structural changes, however these changes are reversible when the open metal sites bond strongly with molecules such as water or methanol. On adsorption of gases in the dehydrated material such as N_2 and CO_2 only one channel system is open and thus

the structure is not reversible. This unique pore discriminating adsorption properties displayed by STAM-1 are unprecedented not only in other MOFs but also in any other class of adsorbent. STAM-1 shows extremely selective behaviour towards gases of different chemistry which gives promising properties for applications in the field of gas separation. The large differences in the kinetics of adsorption of O_2 and N_2 shown by STAM-1 have obvious implications for air separation.

When the material is dehydrated only the hydrophilic channels are available to guest molecules and however for the as synthesised material now it is only the hydrophobic channels that are available. These switchable pore adsorption properties shown by STAM-1 offer many possibilities for future studies as this property is reported for the first time in the field of MOFs.

STAM-1 shows promising antibacterial effects even at low concentrations of 5 wt% of the material in a polymer matrix. The active bactericidal agent in this case will be the copper ions which are incorporated in the framework structure of STAM-1. However with NO-loaded STAM-1 there is a combined antibacterial effect of both NO gas being released from the pores and the presence of Cu^{2+} ions in the framework. This combination could prove to be very effective for the inhibition of the growth of bacteria.

The dimeric copper paddlewheel units which are linked together with mmBTC ligands in STAM-1 show a complex magnetic behaviour. Antiferromagnetic

coupling can be seen within the dimers at room temperature however on lowering the temperature the dimers couple to give strong ferromagnetic properties. This ferromagnetic property arises due to cooperation between neighbouring dimers.

Using different techniques, totally different architectures can be designed as shown by the preparation of STAM-2 from STAM-1. STAM-2 was characterized as a non-porous solid in contrast to STAM-1 which is a porous material. STAM-2 exhibits different magnetic behaviour to STAM-1 although it was derived from STAM-1. It shows strong paramagnetic properties above 150 K while weak antiferromagnetic coupling below 150 K. The paramagnetic properties arise from a different arrangement of the copper ions in the framework of STAM-2 compared with STAM-1.

It has been shown that good design applied to the synthetic procedure can result in specific properties exhibited by the MOFs. In addition, the MOFs prepared have shown good structural properties combined with high stability which makes them useful in many applications in different fields.

9.2.   Further Work

A successful synthesis and characterisation of STAM-1 with its possible applications in different fields was discussed in this thesis. The synthesis and characterisation of a number of other novel MOFs using different methods and techniques were also discussed. In order to complete this work presented here several other investigations could be performed.

The bactericidal effects of STAM-1 on a wider range of bacterial strains together with potential anti-fungal and anti-viral effects remains to be investigated. However, on the strength of results of the NO-releasing STAM-1 as well as the NO free version on the bacterial strains examined, their antibacterial activity provides promising results for their future wider development. The inhibition of bacterial growth shown by STAM-1 may result in excellent new products in the future. For example, STAM-1 could be used for *in vitro* applications such as wound healing or as a surface disinfectant.

It would be interesting to try and incorporate a higher percentage of Zn^{2+} in to the STAM-1 structure as although a catalytic amount of Cu^{2+} is necessary to favour the monoesterification reaction, a pure Zn-STAM-1 may exhibit interesting and different gas adsorption properties. Modifications to the synthetic procedure used to obtain the mixed Cu-Zn-STAM-1 may result in a pure Zn-STAM-1 but these still have to be investigated.

More investigations need to be carried out on STAM-3 in order to obtain a better structural model for the framework. Different characterisation techniques such as elemental analysis will be required to supplement the data already collected in order to try and solve the structure. Since the size of the crystals of STAM-6 and STAM-7 are too small for in house single crystal XRD analysis, the use of synchrotron radiation (Diamond light source Ltd.) will be necessary for single crystal structural analysis.

To understand and identify the products which were not single phase, more characterisation should be carried out on the powder product which in some cases was the major component (see Chapter 8). For example, STAM-8 is the minor phase of the product. If the major phase was identified then this may lead to ideas on how to synthesise STAM-8 as a pure phase. In addition, in STAM-8 the channels are blocked by pyridine molecules; it may be possible to exchange these molecules with a primary amine using a solvent exchange technique and therefore open up the channels. On calcining STAM-9, the framework collapses, thus a less aggressive technique could be explored to remove the template in the framework without this structural change occurring. Again, a solvent exchange method could be employed for this purpose. The interpenetration of the frameworks in STAM-10 is a result of the formation of large voids. This material was synthesised using linear linkers (BDC, bpy), thus by changing to branched or shorter linkers for example, 4-NO$_2$-BDC or 4-amino-BDC this could be avoided. Furthermore, recent reports have shown that the control of the interpenetration can be achieved by liquid phase epitaxial growth,[1] use of template molecules in synthetic

solution,[2] or by changing the concentration of reagents.[3] STAM-11 shows interesting structural features and high thermal stability even after removal of template. Different conditions or the use of different ionic liquids could be used to modify STAM-11 in order to obtain higher dimensional networks with higher porosity and higher thermal stability.

9.3 References

(1)   Shekhah, O.; Wang, H.; Paradinas, M.; Ocal, C.; Schupbach, B.; Terfort, A.; Zacher, D.; Fischer, R. A.; Woll, C. *Nat Mater* **2009**, *8*, 481.

(2)   Tanaka, D.; Kitagawa, S. *Chem Mater* **2008**, *20*, 922.

(3)   Hunt, J. R.; Doonan, C. J.; LeVangie, J. D.; Cote, A. P.; Yaghi, O. M. *J Am Chem Soc* **2008**, *130*, 11872.